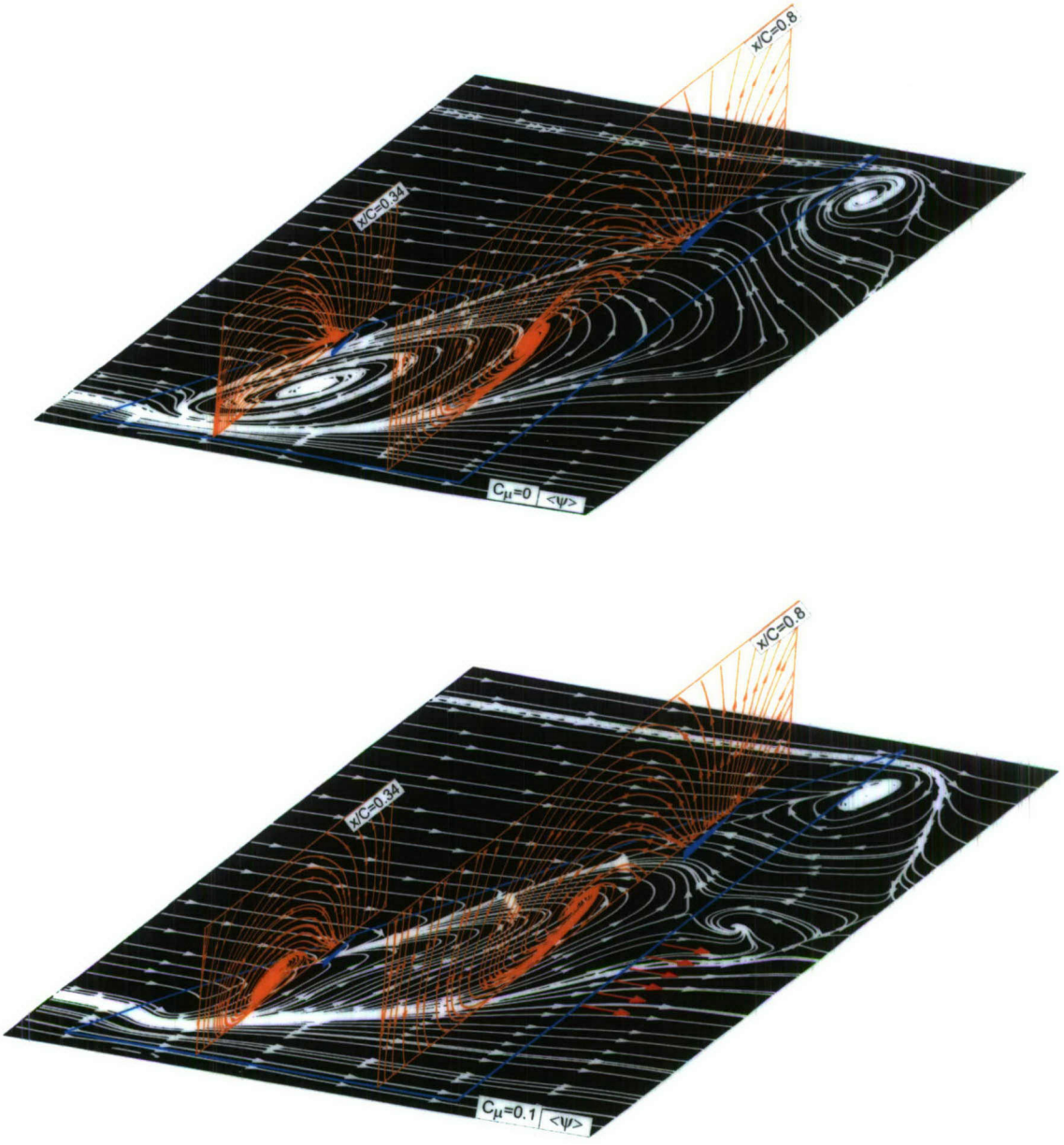
ORIGIN AND CONTROL OF THE FLOW STRUCTURE ON UNMANNED COMBAT AIR VEHICLES

AFOSR GRANT #FA9550-05-1-0072
1 January 2005 to 31 December 2007

Donald Rockwell
Department of Mechanical Engineering and Mechanics
356 Packard Laboratory, 19 Memorial Drive West
Lehigh University
Bethlehem, PA 18015



REPORT DOCUMENTATION PAGE

Form Approved
OMB No. 0704-0188

Public reporting burden for this collection of information is estimated to average 1 hour per response, including the time for reviewing instructions, searching existing data sources, gathering and maintaining the data needed, and completing and reviewing this collection of information. Send comments regarding this burden estimate or any other aspect of this collection of information, including suggestions for reducing this burden to Department of Defense, Washington Headquarters Services, Directorate for Information Operations and Reports (0704-0188), 1215 Jefferson Davis Highway, Suite 1204, Arlington, VA 22202-4302. Respondents should be aware that notwithstanding any other provision of law, no person shall be subject to any penalty for failing to comply with a collection of information if it does not display a currently valid OMB control number. **PLEASE DO NOT RETURN YOUR FORM TO THE ABOVE ADDRESS.**

1. REPORT DATE *(DD-MM-YYYY)*	2. REPORT TYPE	3. DATES COVERED *(From - To)*
January 24, 2008	Final	1 January 2005 to 31 December 2007

4. TITLE AND SUBTITLE
Origin and Control of the Flow Structure on Unmanned Combat Air Vehicles

5a. CONTRACT NUMBER

5b. GRANT NUMBER
FA9550-05-1-0072

5c. PROGRAM ELEMENT NUMBER

6. AUTHOR(S)
Donald Rockwell

5d. PROJECT NUMBER

5e. TASK NUMBER

5f. WORK UNIT NUMBER

7. PERFORMING ORGANIZATION NAME(S) AND ADDRESS(ES)

Professor Donald Rockwell
Department of Mechanical Engineering and Mechanics
356 Packard Laboratory, 19 Memorial Drive West
Lehigh University
Bethlehem, PA 18015

8. PERFORMING ORGANIZATION REPORT NUMBER

9. SPONSORING / MONITORING AGENCY NAME(S) AND ADDRESS(ES)
Dr. John Schmisseur /NA
Unsteady Aerodynamics and Hypersonics
Air Force Office of Scientific Research
801 N. Randolph Street, Room 732
Arlington VA 22203-1977

10. SPONSOR/MONITOR'S ACRONYM(S)
AFOSR/NA

11. SPONSOR/MONITOR'S REPORT NUMBER(S)

12. DISTRIBUTION / AVAILABILITY STATEMENT

Approved for public release,
distribution unlimited

AFRL-SR-AR-TR-08-0110

13. SUPPLEMENTARY NOTES

14. ABSTRACT

Flow structure on delta wings having low sweep angle, representative of those used in UCAVs and MAVs, is characterized in detail using a technique of quantitative imaging, high-image-density particle image velocimetry. Cases of stationary wings, wings subjected to control at their trailing-edges, and wings undergoing prescribed pitching maneuvers have been addressed as part of this investigation. The sweep angle of each wing is sufficiently small, such that the patterns of the flow structure exhibit elongated separation layers in the crossflow plane. These patterns can be interpreted in conjunction with patterns of streamline topology in the crossflow plane, as well as patterns of root-mean-square velocity fluctuation and velocity spectra, in order to provide insight into the origin of unsteady loading of the aerodynamic surface. As an adjunct to the series of investigations of flow past delta wings in absence of a tail, the interaction of vortex breakdown with the simulated tail of a wing has been characterized using quantitative imaging and evaluated using a technique of proper orthogonal decomposition (POD).

15. SUBJECT TERMS

Vortex, topology, flow separation ·

16. SECURITY CLASSIFICATION OF:			17. LIMITATION OF ABSTRACT	18. NUMBER OF PAGES	19a. NAME OF RESPONSIBLE PERSON
a. REPORT	b. ABSTRACT	c. THIS PAGE			Donald Rockwell
Approved for public release; distribution is unlimited	Approved for public release; distribution is unlimited	Approved for public release; distribution is unlimited			19b. TELEPHONE NUMBER *(include area code)* 610-758-4107

Standard Form 298 (Rev. 8-98)
Prescribed by ANSI Std. Z39.18

ORIGIN AND CONTROL OF THE FLOW STRUCTURE ON UNMANNED COMBAT AIR VEHICLES

AFOSR GRANT #FA9550-05-1-0072
1 January 2005 to 31 December 2007

Donald Rockwell
Department of Mechanical Engineering and Mechanics
356 Packard Laboratory, 19 Memorial Drive West
Lehigh University
Bethlehem, PA 18015

SUMMARY

Flow structure on delta wings having low sweep angle, representative of those used in UCAVs and MAVs, is characterized in detail using a technique of quantitative imaging, high-image-density particle image velocimetry. Cases of stationary wings, wings subjected to control at their trailing-edges, and wings undergoing prescribed pitching maneuvers have been addressed as part of this investigation.

The sweep angle of each wing is sufficiently small, such that the patterns of the flow structure exhibit elongated separation layers in the crossflow plane. These patterns can be interpreted in conjunction with patterns of streamline topology in the crossflow plane, as well as patterns of root-mean-square velocity fluctuation and velocity spectra, in order to provide insight into the origin of unsteady loading of the aerodynamic surface.

In the event that blowing is applied at the trailing-edge of the wing to simulate, for example, a thrust vectoring system, it is demonstrated that the global influence of blowing occurs well upstream of the trailing-edge, including the apex of the wing. Depending upon the dimensionless blowing coefficient, various topological patterns in the near-surface region are attainable. It has been demonstrated that it is possible to eradicate the large-scale three-dimensional separation region in the vicinity of the apex. The relationship between the topological patterns along the near-surface has been interpreted in conjunction with the alteration of the crossflow topology due to the application of trailing-edge blowing.

When a wing is subjected to a transient pitching motion, the near-surface topology passes through a sequence of highly ordered states, which can be shown to have a universal form, irrespective of the pitch rate. The states are classified according to the patterns of near-surface topology.

As an adjunct to the series of investigations of flow past delta wings in absence of a tail, the interaction of vortex breakdown with the simulated tail of a wing has been addressed. The patterns of flow structure are evaluated using a technique of proper orthogonal decomposition (POD). The eigenmodes required to describe the flow structure were critically evaluated.

20080313321

A full description and illustration of the experimental systems employed in the foregoing investigations, as well as all acquired images and data, are included in the publications referred to in this report.

A central focus of the present research program is detailed characterization of the patterns of quantitative flow structure, both in the near-surface and crossflow planes. These types of approaches are employed for planforms having various trailing-edge configurations in absence of any type of control, as well as the application of trailing-edge control in the form of jet blowing and a form of controlled motion of the wing involving transient, pitch-up maneuvers. Patterns of topology are complemented by patterns of out-of-plane vorticity and root-mean-square velocity fluctuations that yield insight into the origin of surface loading. The sequential phases of this research program are described in the following in the form of brief synopses. They correspond to journal articles that have either been published, submitted, or, in one case, in preparation.

"Flow Structure on Diamond and Lambda Planforms: Trailing-Edge Region" by B. Yaniktepe and D. Rockwell

The instantaneous and averaged flow structure on diamond and lambda planforms is characterized using a technique of high-image-density particle image velocimetry. Emphasis is on the structure in the trailing-edge region, over a range of angle of attack. Elongated layers of vorticity in the crossflow plane exhibit well-defined mean (time-averaged) and instantaneous concentrations of vorticity. These features are interpreted in conjunction with patterns of streamline topology, as well as images of root-mean-square velocity fluctuation and velocity spectra obtained from space-time imaging.

This investigation is described in Appendix A.

"Control of Near-Surface Flow Structure on Low Swept Delta Wing with Steady Trailing Edge Blowing" by M. Yavuz and D. Rockwell

The near-surface flow structure and topology are characterized on a delta wing of low sweep angle, which is subjected to trialing-edge blowing. A technique of high-image-density particle image velocimetry is employed to determine the topological critical points adjacent to the surface and in the near wake of the wing, in relation to the dimensionless magnitude of the blowing coefficient. These topological features are, in turn, interpreted in conjunction with patterns of surface-normal vorticity and near-surface velocity fluctuations, which provide an indication of buffet loading. Even thought the jet blowing is at the trailing edge, it has a remarkable, global influence on the surface patterns located well upstream; at high angle of attack, it leads to eradication of large-scale, three-dimensional separation on the vicinity of the apex.

This investigation is described in Appendix B.

"Identification and Control of Three-Dimensional Separation on Low Swept Delta Wing" by M. Yavuz and D. Rockwell

For the case of a delta wing having small sweep angle, the flow structure on crossflow planes is related to patterns of the flow on near-surface planes, in relation to the application of localized blowing from the trailing-edge of the wing. When such blowing

is applied, the surface patterns show eradication of the large-scale, three-dimensional separation zone and, correspondingly, the crossflow patterns show recovery of both the swirl pattern of streamlines and the pronounced axial vorticity concentration in the crossflow plane closest to the apex. When the blowing coefficient is increased at successively larger values, the center of the vortex structure in the crossflow plane moves closer to the leading-edge of the wing. When the blowing coefficient is sufficiently high, a dual vortex structure occurs, as opposed to a classical single leading-edge vortex. Such a vortex pattern can occur at low angle-of-attack, as determined from both numerical and experimental investigations.

This investigation is described in Appendix C.

"Near-Surface Topology on a Delta Wing of Low Sweep Angle: Relaxation Processes Following a Transient Maneuver" by T. Goruney and D. Rockwell

A delta wing of low sweep angle is subjected to a linear pitch-up maneuver for a range of values of dimensionless pitch rate. The near-surface flow structure and streamline topology are characterized during the relaxation process, following cessation of the wing motion. It is demonstrated that identifiable states of the flow topology occur in succession until a steady-state flow structure is achieved. Remarkably, the same states of near-surface topology occur, irrespective of the value of dimensionless pitch rate, though these states are delayed to varying degrees, depending upon the pitch rate.

This investigation is described in Appendix D.

"Flow Structure along a 1303 Unmanned Combat Air Vehicle" by M. A. Kosoglu and D. Rockwell

The flow structure along a three-dimensional model of a 1303 UCAV is characterized in detail. Dye visualization shows the onset of leading-edge vortex formation, vortex breakdown and regions of separation/stall as a function of angle-of-attack and Reynolds number. Quantitative imaging, using the technique of high-image-density particle image velocimetry, is employed to characterize the time-dependent structure of regions of separation/stall using cinema PIV acquisition. The regions of separation/stall can exhibit substantial large-scale unsteadiness.

This investigation is described in Appendix E.

"Vortex Buffeting of Aircraft Tail: Interpretation via Proper Orthogonal Decomposition" by Y. Kim, D. Rockwell and A. Liakopoulos

The Proper Orthogonal Decomposition (POD) method is applied to PIV data to extract the most energetic flow structures of vortex-tail interaction. The reconstructed flow fields, in conjunction with patterns of vorticity and streamline topology are compared with the original PIV data on a crossflow plane. The reconstructed flow fields using a small number of eigenfunctions can predict the largest-scale features of the original flow field. However, the smaller-scale flow structures, which are evident in the original PIV image, are lost. Furthermore, patterns of instantaneous streamline topology clearly show that the reconstructed flow fields from a small number of eigenmodes can represent the most dominant characteristics of the original flow field.

This investigation is described in Appendix F.

THESES AND DISSERTATIONS*

M.S. Theses

Tunc Goruney, "Time Evolution of Surface Topology and Flow Structure on Delta Wing of Moderate Sweep Angle", 2006.

Mehmet Alparslan Kosoglu, "Flow Structure along a 1303 Unmanned Combat Air Vehicle", 2007.

Ph.D. Dissertations

Mehmet Metin Yavuz, "Origin and Control of the Flow Structure and Topology on Delta Wings", 2006.

Tunc Goruney, " Investigation of Flow Structure on a Pitching Delta Wing of Moderate Sweep Angle using Stereoscopic Particle Image Velocimetry: Passive Control of Flow Structure via Leading Edge Protuberances", to be completed May, 2008.

* All theses and dissertations are available from the Department of Mechanical Engineering and Mechanics, Lehigh University, Bethlehem, PA 18015

PUBLICATIONS

Yavuz, M. and Rockwell, D. 2006 "Identification and Control of Three-Dimensional Separation on Low Swept Delta Wing Angle", *AIAA Journal*, Vol. 44, No. 11, November, pp. 2805-2811.

Yavuz, M. and Rockwell, D. 2006 "Control of Flow Structure on Delta Wing with Steady Trailing Edge Blowing", *AIAA Journal*, Vol. 44, No. 3, March, pp. 493-501.

Elkhoury, M., Yavuz, M. and Rockwell, D. 2005 "Near-Surface Topology of an Unmanned Combat Air Vehicle Planform: Reynolds Number Dependence", *AIAA Journal of Aircraft*, Vol. 42, No. 5, September/October, pp. 1318-1330.

Westerweel, J., Rockwell, D. and Tropea, C. 2006 Experiments in Fluids Editorial, *Experiments in Fluids*, Vol. 41, No. 2, August, p. 145.

Naudascher, E. and Rockwell, D. 2005 Flow-Induced Vibrations: An Engineering Guide, (book), Dover Press (reprinting of book originally published in 1994), August.

Yaniktepe, B. and Rockwell, D. 2005 "Flow Structure on Diamond and Lambda Planforms: Trailing-Edge Region", *AIAA Journal*, Vol. 43, No. 7, July, pp. 1490-1512.

Kim, Y., Rockwell, D. and Liakopoulos, A. 2005 "Vortex Buffeting of Aircraft Tail: Interpretation via Proper Orthogonal Decomposition", *AIAA Journal*, Vol. 43, No. 3, March, pp. 550-559.

Appendix A

FLOW STRUCTURE ON DIAMOND AND LAMBDA PLANFORMS: TRAILING-EDGE REGION

by

B. Yaniktepe[**]
Cukurova University

D. Rockwell[†]
Lehigh University

[**] On leave as Visiting Scientist at Lehigh University.

ABSTRACT

The instantaneous and averaged flow structure on diamond and lambda planforms is characterized using a technique of high-image-density particle image velocimetry. Emphasis is on the structure in the trailing-edge region, over a range of angle of attack. Elongated layers of vorticity in the crossflow plane exhibit well-defined mean (time-averaged) and instantaneous concentrations of vorticity. These features are interpreted in conjunction with patterns of streamline topology, as well as images of root-mean-square velocity fluctuation and velocity spectra obtained from space-time imaging.

NOMENCLATURE

C = Root chord of entire planform (mm)
C' = Root chord of leading (delta wing) portion of planform (mm)
f = Frequency (Hz)
S = Local semi-span of wing (mm)
S_w = Spectrum of w component of velocity fluctuation
U = Freestream velocity (mm/sec)
v' = Instantaneous velocity fluctuation in direction parallel to surface of wing (mm/sec)
V = Magnitude of velocity vector (mm/sec)
w' = Instantaneous velocity fluctuation normal to surface of wing (mm/sec)
w_{rms} = Root-mean-square of velocity fluctuation (mm/sec)
x = Distance from apex measured along plane of symmetry of wing (mm)
y = Distance from apex measured normal to plane of symmetry of wing (mm)
$< >$ = Time-averaged value of quantity
α = Angle-of-attack (degrees)
Λ = Sweep angle (degrees)
ψ = Streamfunction (mm^2)
ω = Vorticity (1/sec)

1. INTRODUCTION

Recent interest in unmanned combat air vehicles (UCAVs), has stimulated investigation of the flow structure on delta wings having low and moderate values of

[†] Professor Donald Rockwell, Department of Mechanical Engineering and Mechanics, 356 Packard Laboratory, 19 Memorial Drive West, Lehigh University, Bethlehem, PA 18015

sweep angle, as well as on planforms that represent the actual UCAV configuration or simplifications thereof. Summaries of recent investigations, as well as unresolved issues, are given in the following.

1.1 FLOW STRUCTURE ON DELTA WINGS OF MODERATE AND LOW SWEEP ANGLE

The distinctive features of the instantaneous and averaged flow structure on a delta wing of sweep angle $\Lambda = 50°$ have been numerically computed by Gordnier and Visbal[1]. At low angle-of-attack, a dual primary vortex system is established, whereas at higher angles-of-attack, this dual structure gives way to a single, larger-scale vortex. Furthermore, the unsteadiness of the vortex core can involve a type of organized wandering at locations upstream of vortex breakdown. The form of vortex breakdown is more complex than for wings of relatively large sweep angle.

Ol and Gharib[2,3] undertook an experimental investigations of wings of sweep angle $\Lambda = 50°$ and 65°. They characterized the onset of vortex breakdown using dye visualization and, via a stereo PIV technique, characterized various features of the leading-edge vortex structure, including a large-scale collapse of the rolled-up, leading-edge vortex. Yaniktepe and Rockwell[4] considered a wing of sweep angle $\Lambda = 38.7°$ and focused on the flow structure well into the region of vortex breakdown including, at high angle-of-attack, the onset of a large-scale region of disordered flow structure beneath a highly organized vorticity layer. With the intent of characterizing the origin of buffet loading, patterns of the averaged and instantaneous flow structure were interpreted in conjunction with velocity spectra, which provided dimensionless frequencies along the elongated vorticity layer adjacent to the wing surface.

1.2 FLOW STRUCTURE ON HIGHLY SWEPT WINGS

For wings of relatively large sweep angle, a single, large-scale vortex dominates the crossflow pattern. Well-defined vortical substructures can, however, occur about the periphery of this primary vortex. Visbal and Gordnier[5] summarize recent investigations of vortical substructures, and describe the physical origin based on their high resolution numerical simulations. In addition, they assess three different interpretations of the substructures.

In recent decades, a range of experimental investigations have provided insight into the nature of these substructures. Early studies employed qualitative flow visualization to identify them, in unsteady and/or stationary forms. They include Squire et al.[6], Gad-el-Hak and Blackwelder[7,8], Payne et al.[9], Lowson[10] and Reynolds and Abtahi[11]. Further, time-averaged quantitative characterizations of vortical substructures involve the work of Verhaagen et al.[12], Washburn and Visser[13], Lowson et al.[14], Riley and Lowson[15], and Mitchell et al.[16].

The occurrence of vortical substructures was first computed by Gordnier and Visbal[17, 18] who demonstrated their existence in the absence of external forcing. Mitchell et al.[19] and Mitchell and Molton[20] also have computed patterns of vortical substructures using a different numerical approach.

1.3 FLOW STRUCTURE ON UCAV PLANFORMS

Gursul et al.[21] summarized recent investigations of low aspect ratio wings and planforms and, furthermore, provide insight into the phenomena of vortex breakdown visualized by dye injection. The consequences of low sweep angle were clearly evident.

1.4 UNRESOLVED ISSUES

The emphasis of the present investigation is on the unsteady flow structure, which serves as the origin of buffeting, with emphasis on the configurations of diamond and lambda planforms. A central, generic feature of these planforms is an abrupt change in sweep angle of the leading-edge, from a relatively low value to a value of 90°. The consequence of this sudden change on both the averaged flow structure and the flow unsteadiness has not been clarified. In particular, the following issues have not been addressed.

Crossflow topology on diamond and lambda planforms. The patterns of averaged streamline topology over crossflow planes on lambda and delta planforms are expected to be substantially different from those on a simple delta wing of low sweep angle. The possibility of a well-defined focus (apparent center) of a tightly wound spiral pattern of streamlines, which might be located at the leading-edge, rather than well inboard of it, would be an indication of the rapid flow distortion in the leading-edge region. In addition, the possibility of a saddle point, i.e., an apparent intersection of streamlines, located outboard of the leading-edge, has not been pursued in relation to the detailed geometry of the diamond and lambda planforms, including the geometry of the trailing-edge.

Moreover, corresponding patterns of time-averaged vorticity, in relation to the streamline topology, have not been defined. It is expected, on the basis of investigations of a simple delta wing by Yaniktepe and Rockwell[4], that an elongated layer of vorticity will form adjacent to the wing. The possibility, however, of a highly concentrated region of vorticity at the leading-edge, which may be associated with the abrupt transformation of sweep angle, has not been addressed. Furthermore, the averaged patterns of vorticity may exhibit well-defined vortical substructures within the elongated layer from a diamond or lambda planform. For the case of a wing of relatively large sweep angle, where the flow pattern is dominated by a single large-scale vortex, the occurrence of such substructures is well established, as defined in the references given in the Introduction. The possibility that analogous, time-averaged vortical substructures may occur on wings with an abrupt change in sweep angle has not been pursued.

Instantaneous/unsteady flow structure. The time-averaged features described in the foregoing are, of course, a consequence of the instantaneous flow structure. In particular, the instantaneous patterns of vorticity adjacent to the surface of the wing, in relation to possible time-averaged structures, have not been addressed for the wing planforms of interest herein. An important consequence of the instantaneous patterns of vorticity, as well as sequences of them, is the root-mean-square velocity fluctuation along the separated region adjacent to the surface of the wing. These patterns of rms velocity,

along with the corresponding spectra, define the physical origin of unsteady (buffet) loading of the wing surface.

Objectives. The overall aim of the present investigation is to address the issues defined in the foregoing using a technique of high-image-density particle image velocimetry, which allows wholefield representations of both the time-averaged and instantaneous structure. Furthermore, a cinema mode of image acquisition allows, in effect, time records of the flow at a large number of locations, and thereby determination of the corresponding spectra of the fluctuating velocity field.

2. EXPERIMENTAL SYSTEM AND TECHNIQUES

Experiments were performed in a large-scale water channel, which had a test section 4,928 mm long, 927 mm wide, and 610 mm high. This test section was preceded by a settling tank, a honeycomb screen arrangement, and a 2:1 contraction. The turbulence intensity at the entrance to the test section was less than 0.3%.

The wings involved two basic planforms designated as diamond and lambda; they are shown in Figures A1a and A1b. These figures show the system coordinates and critical length scales for each of the wings. The fore regions of the wings were matched. That is, the delta wing portion of the leading region of each wing, having a chord C' = 101.6 mm, was maintained the same for each planform, in order to allow a direct comparison of the consequence of trailing-edge configuration on the flow development. The chords C of the diamond and lambda wings had values respectively of 195 mm and 167 mm. This dimension C allows determination of all other dimensions of the wing via the schematics of Figure A1b. In addition, each wing had a thickness t of 3 mm, and was beveled on the windward side at an angle of 30°. The value of Reynolds number based on chord C was maintained at 10,000 for both wings. The corresponding values of free-stream velocity for the diamond and lambda wings were U_∞ = 51.4 mm/sec and U_∞ = 60.1 mm/sec respectively. The values of angle-of-attack were α = 7°, 13°, 17° and 25°.

Emphasis is on global patterns of instantaneous flow structure and cinema sequences of these patterns, which allow characterization of the timewise evolution of the flow, as well as determination of the time-averaged structure. A technique of high-image-density particle image velocimetry was employed. Illumination was provided by a dual-pulsed Yag laser system, having a maximum output of 90 mJ. The colinear beam from this dual system was transmitted through a system of cylindrical and spherical lenses, in order to generate a vertical laser sheet, which illuminated a desired crossflow plane, as indicated in Figure A1a. The laser sheet was located at the trailing-edge; in this region, it is anticipated that the unsteady (buffet) loading will be severe. This location corresponds to the streamwise distance x/C' = 1.4, in which C' is the chord of the leading delta wing configuration in each of the planforms, as designated in Figure A1b. Based on preliminary dye visualization, it is estimated that the angle between the centerline of the predominant leading-edge vortex and the plane of the laser sheet is 60°. The flow was seeded with 12 micron, metallic-coated, hollow plastic spheres, which were essentially neutrally buoyant. Patterns of these particle images were recorded on a high-resolution camera, having 1,024 pixels × 1,024 pixels. The effective framing rate of the camera was 15 cycles per second. This framing rate, relative to the characteristic

frequencies of the major events of the flow structure allowed a technique of cinema PIV for determination of spectra and cross-spectra of the fluctuating flow field.

The pattern of instantaneous velocity vectors was obtained by a cross-correlation technique involving successive frames of the patterns of particle images. Two sizes of interrogation windows were employed: 32 × 32 pixels and 16 × 16 pixels. In both cases, an effective overlap of 50% was employed, in order to satisfy the Nyquist criterion. The effective grid size for the larger interrogation window, in the plane of the laser sheet, was 2.65 mm. In order to ensure that the high-image-density criterion was satisfied, the number of particle images within the interrogation window was, at minimum, 15 to 20.

3. DYE VISUALIZATION OF FLOW PATTERNS

Representative patterns of the flow, visualized by dye injection, are shown in Figure A2. At the lowest angle of attack angle-of-attack $\alpha = 7°$, the dye was injected from two localized ports located at the apex of the wing. These ports were positioned to identify the locus of the vortex with the largest circulation formed from the leading-edge. Substantial distortions of the dye marker are evident well upstream of the trailing-edge of each wing; in an approximate sense, this distortion sets in at about $x/C' = 1.0$, corresponding to the coordinates given in Figure A1b. These distortions, or undulations, are highly nonstationary, and are similar to the undulations prior to the onset of vortex breakdown calculated numerically by Gordnier and Visbal[1] on a delta wing of low sweep angle.

At the higher angle of attack $\alpha = 13°$, the dye was injected along the windward side of the leading-edge. The central portion of each wing is unmarked by dye, as it is continuously swept away by the streamwise velocity adjacent to the wing surface. On the other hand, exterior to this region, the dye is distributed over a large portion of the wing surface.

At higher angles of attack $\alpha = 17°$ and $25°$ considered in this investigation, the dye flooded the entire surface of the wing, and therefore these images are not shown.

4. PATTERNS OF AVERAGED VELOCITY AND STREAMLINE TOPOLOGY

Velocity patterns. Figure A3 shows patterns of averaged velocity $\langle V \rangle$ at angles-of-attack $\alpha = 7°$, 13°, 17° and 25°. The patterns for the diamond and lambda planforms are directly compared at each angle-of-attack. At $\alpha = 7°$, a common feature of the flow structure on both planforms is existence of a well-defined, small-scale swirl pattern at the leading-edge. Furthermore, both wings exhibit relatively narrow, elongated patterns of velocity vectors, with a recirculation flow towards the leading-edge of the wing. For the case of the lambda planform, the pattern is significantly distorted, apparently due to the gap occurring in the wing segment.

At $\alpha = 13°$, the intense, small-scale swirl pattern located at the leading-edge, which was predominant at $\alpha = 7°$, no longer exists. For each wing, well-defined swirl patterns are evident, however, at the interface between: (i) the recirculating flow that

returns to the leading-edge region; and (ii) the flow exterior to this region. Furthermore, it is evident that the scale of the recirculation zone is smaller for the lambda planform.

At $\alpha = 17°$, small-scale swirl patterns are again evident at the interface between the elongated recirculation zone and the exterior flow. The predominant pattern for the lambda planform is closer to the leading-edge than that for the diamond planform. This relative position of the swirl pattern is also evident at $\alpha = 13°$.

Finally, for the angle-of-attack $\alpha = 25°$, a well-defined, elongated swirl pattern no longer exists. Rather, flow is away from the wing surface towards the interface with the exterior flow. The overall spatial extent of this grossly separated flow pattern is approximately the same for both the diamond and lambda planforms.

Streamline Topology. Corresponding patterns of streamline topology, based on the averaged velocity patterns of Figure A3, are shown in Figure A4. At $\alpha = 7°$, for the diamond planform, the streamlines form a small-scale limit cycle immediately adjacent to the leading-edge, while for the lambda planform, a localized swirl pattern occurs in this region. It is evident that the focus (apparent center) of both streamline patterns is located very close to the leading-edge.

Furthermore, at $\alpha = 7°$, a saddle point, i.e., the locus of an apparent intersection of streamlines, is located outboard of the leading-edge of the diamond planform; no such saddle occurs for the diamond planform. These differences indicate that the trailing-edge configuration of the planform has a global influence on the streamline topology. A common feature of the streamline topology of both planforms, however, is the flow adjacent to the surface of the wing towards the leading-edge; this return flow occurs over a relatively small width, in accord with the location of the interface of the corresponding patterns of averaged velocity $< V >$ shown at $\alpha = 7°$ in Figure A3. Just inboard of the leading-edge, this return flow merges with the small-scale swirl pattern at the leading-edge to form a system of convergent streamlines known as a bifurcation line; it has not been observed previously in the cross-sectional topology of wings of either large or small sweep angle.

At $\alpha = 13°$, foci are no longer evident at the leading-edge of either planform, and the streamline topology reverts to a more classical form, which involves a single-large-scale swirl inboard of the leading-edge. For the lambda planform, the focus (apparent center) of this pattern is located closer to both the leading-edge and the surface of the wing. Moreover, the saddle point evident at $\alpha = 7°$ in the outboard region still persists at this angle-of-attack, although it is located further from the surface of the wing.

At $\alpha = 17°$, the overall characteristics of the patterns at $\alpha = 13°$ are generally retained. On the other hand, at $\alpha = 25°$, the streamline patterns are indicative of a highly separated region adjacent to the surface of the wing, and it is not possible to identify a single, well-defined, large-scale swirl pattern.

The patterns of the averaged velocity $<V>$ and streamline topology $<\Psi>$ shown in Figures A3 and A4 are associated with distinctive patterns of averaged vorticity $<\omega>$ and velocity fluctuations w_{rms}/U, which are addressed in the next section.

5. PATTERNS OF AVERAGED VORTICITY AND FLUCTUATING VELOCITY

The images of Figures A5a and A5b show a direct comparison of the averaged vorticity $<\omega>$ and root-mean-square velocity w_{rms}/U at angles-of-attack $\alpha = 7°$, 13°, 17°, and 25°, for both the diamond and lambda planforms.

Consider the patterns of averaged vorticity $<\omega>$ at $\alpha = 7°$ in Figure A5a. Both planforms exhibit a cluster of concentrated vorticity at the leading-edge, which is associated with the localized swirl pattern of velocity shown at $\alpha = 7°$ in Figure A3, and the focus of the streamline topology at the leading-edge at $\alpha = 7°$ in Figure A4. Furthermore, the patterns of vorticity are relatively elongated and contain two identifiable cells, or local concentrations of vorticity, designated as *a* and *b*, in addition to the vorticity concentrations appearing at the leading-edge. These substructures are similar in form to those identified in the numerical simulation of Gordnier and Visbal[1] on a simple delta wing of low sweep angle. The corresponding patterns of transverse velocity fluctuation w_{rms}/U are generally similar for both planforms. The peak values are $[w_{rms}/U]_{max} = 0.12$ and 0.13 for the diamond and lambda planforms respectively.

At $\alpha = 13°$, the region of highly-concentrated vorticity in the vicinity of the leading-edge becomes even more pronounced, relative to that at $\alpha = 7°$, for both planforms. These concentrations at $\alpha = 13°$ are, however, displaced further from the edge than those at $\alpha = 7°$. For this reason, they are not detectable in the corresponding streamline topology of Figure A4. Furthermore, the vorticity layers appear as relatively elongated, and have a substantially larger spanwise extent and width than at $\alpha = 7°$. Within these large-scale elongated layers, a number of smaller-scale concentrations of vorticity are evident at both $\alpha = 7°$ and 13°. They are more clearly defined, however, for the lambda planform, and for purposes of simplicity in describing their existence, individual structures are designated for this planform at $\alpha = 13°$ and at $\alpha = 17°$. The predominant, distinctive concentrations at $\alpha = 13°$ are indicated as *a*, *b*, and *c*. The corresponding patterns of root-mean-square velocity w_{rms}/U occupy a relatively large spatial extent, relative to the vorticity layer. Generally speaking, the maximum values of w_{rms}/U approximately correspond to the outer edge of the averaged patterns of vorticity $<\omega>$. The peak value of velocity fluctuation is significantly high, i.e., $[w_{rms}/U]_{max} = 0.24$ and 0.20 respectively for the diamond and lambda planforms.

Patterns corresponding to higher angles-of-attack $\alpha = 17°$ and 25° are shown in Figure A5b. At $\alpha = 17°$, the patterns of averaged vorticity $<\omega>$ exhibit a generally similar, large-scale, elongated form as at $\alpha = 13°$. The pronounced concentration of vorticity adjacent to the leading-edge persists for both planforms. Furthermore, identifiable concentrations of vorticity are evident in the large-scale, elongated layer. The most prominent are designated as *a*, *b*, *c* and *d* on the lambda planform. The respective patterns of velocity fluctuation w_{rms}/U occupy a still larger spatial extent than at $\alpha = 13°$. The peak values are generally at the same spatial position as at the outer region of each of

the large-scale patterns of averaged vorticity $<\omega>$. The peak values of the velocity fluctuation are $[w_{rms}/U]_{max}$ = 0.24 and 0.22 respectively for the diamond and lambda planforms.

For the highest angle-of-attack $\alpha = 25°$, the patterns of averaged vorticity $<\omega>$ take on a fundamentally different form. They are displaced a substantial distance from the surface of the wing and, moreover, contain identifiable concentrations of smaller-scale vorticity, specified as *a*, *b*, *c* and *d*. The locations of these smaller-scale concentrations are generally coincident with the peak values of velocity fluctuation w_{rms}/U. The peak values are $[w_{rms}/U]$ = 0.24 and 0.2 respectively for the diamond and lambda planforms. It is apparent that the layers of vorticity shown in Figure A5b are formed at the interface between the highly-separated region and the exterior flow indicated in the patterns of averaged velocity $<V>$ at $\alpha = 25°$ in Figure A3. That is, this layer of relatively high vorticity exists adjacent to a large-scale region of separated flow.

6. PATTERNS OF AVERAGED VORTICITY AND STREAMLINE TOPOLOGY: A COMPARISON

Certain of the patterns of averaged streamline topology shown in Figure A4 suggests existence of a single, large-scale leading-edge vortex, especially the patterns corresponding to the diamond planform at α = 13° and 17°. This type of pattern, however, must be interpreted in conjunction with the corresponding pattern of averaged vorticity $<\omega>$, as shown in Figures A5a and A5b. The comparisons of Figure A6 involve superposition of patterns of averaged vorticity $<\omega>$ and averaged $<\Psi>$ topology at $\alpha = 17°$ for the diamond and lambda planforms. As emphasized previously, the vorticity layer exhibits a narrow, elongated form, in contrast to the classical, nearly circular pattern of vorticity which occurs on highly swept wings at sufficiently large angle-of-attack. For the diamond planform, the focus (apparent center) of the streamline pattern lies approximately midway along the elongated layer of vorticity. For the lambda planform, however, the focus is actually closer to the leading-edge of the wing. In an overall sense, these streamlines pattern do not indicate the presence of the well-defined, smaller-scale concentrations of vorticity.

The aforementioned coexistence of an elongated vorticity layer and a single spiral pattern of streamlines (with a single focus) appears to be an inherent feature of rapidly distorting flows separating from a solid boundary. For the case of vortex formation in the very near-wake of a cylinder, Akilli and Rockwell[22] observe conceptually similar patterns of streamline topology and vorticity layers. In this region, the boundary layer from the cylinder separates to form the elongated free shear layer.

7. PATTERNS OF INSTANTANEOUS VORTICITY

Patterns of instantaneous vorticity are shown relative to instantaneous velocity vectors in Figure A7. In the left column, these patterns are compared at an angle-of-attack $\alpha = 7°$, along with the corresponding pattern of the averaged velocity $<V>$, while in the right column, they are compared for α = 25°. Generally speaking, the identifiable

clusters of vorticity are associated with well-defined swirls of patterns of velocity vectors.

In order to indicate the degree of variability of the instantaneous patterns of vorticity, Figure A8a shows two images at each angle-of-attack α, and for both the diamond and lambda planforms. Angles-of-attack α = 13° and 17° are represented in Figure A8a, while α = 17° and 25° are shown in Figure A8b. All patterns exhibit, from one instant to the next, significant variability in the precise location and level of the vorticity concentrations. Nevertheless, a quasi-ordered structure is apparent in each of the images and, furthermore, it is possible to discern, in an approximate sense, the spacing between identifiable concentrations of vorticity. For each of the sets of instantaneous images, at each value of angle-of-attack α and each planform, the spacing between concentrations is, in most cases, roughly commensurate with the spacing between the time-averaged patterns of substructures *a*, *b*, *c* and *d* shown in Figures A5a and A5b. During the averaging process that yields the patterns of Figures A5a and A5b, the instantaneous patterns of Figures A8a and A8b are, in effect, smeared due to the variation in spatial position of the patterns of vorticity concentrations over the entire time sequence of instantaneous images. As a result, the peak values of vorticity and the patterns of Figures A5a and A5b are typically much lower than the peak values in the corresponding instantaneous images.

8. SPECTRA OF FLUCTUATING VELOCITY

The organized patterns of instantaneous vorticity shown in Figures A8a and A8b are associated with definable spectral components of the velocity fluctuation w. These spectra $S_w(f)$ are shown in Figure A9 for α = 7° and 25°. Each spectrum is referenced to a specified location in the corresponding pattern of constant contours of root-mean-square velocity fluctuation w_{rms}/U. At α = 7°, for the diamond planform, a well-defined spectral component emerges just inboard of the leading-edge; its frequency is f = 0.49 Hz. Further along the separated layer, a higher frequency component occurs; its value is f = 1.49 Hz and it coexists with the aforementioned component at f = 0.95 Hz. For the lambda wing, organized spectral components are also detectable. They have values in the range f = 0.77 to 1.37 Hz.

As the vorticity layer tends to reattach to the surface of both lambda and diamond planforms, the degree of organization, as well as the peak amplitude of the spectral component, both decrease. In fact, for the diamond planform, the organized component is nearly entirely attenuated.

For the highest angle-of-attack α = 25° (diamond planform), an organized spectral component is clearly detectable at a significant distance from the leading-edge. It has a value f = 0.95 Hz. This spectral component persists along the separated layer, and at the furthest location from the leading-edge, components at f = 0.71 and 0.95 Hz are evident. For the lambda planform, at the location closest to the leading-edge, the spectral component is f = 1.43 Hz, and at locations further along the layer, a single, well-defined component no longer occurs. Rather, the general peak is relatively broadband. The center frequencies of these rather broad distributions of peaks are indicated and have spectral components in the range f = 0.83 to 1.31 Hz.

For the diamond planform, the identifiable spectral peaks in Figure A9 are in the range $0.71 \leq f \leq 0.95$ Hz, which corresponds to $2.69 \leq fC/U \leq 3.60$. For the lambda planform, the identifiable spectral peaks are in the range $0.77 \leq f \leq 1.43$ Hz, which corresponds to $2.13 \leq fC/U \leq 3.97$. For the case of a simple delta wing, Yaniktepe and Rockwell[4] found values of dimensionless frequency, based on spectral analysis, extending over the range of $0.51 \leq fC/U \leq 3.29$ and, for a simple delta wing of sweep angle $\Lambda = 50°$, Gordnier and Visbal[1] computed a band of frequencies in the surface pressure spectrum extending over the approximate range $1 \leq fC/U \leq 4.5$. Taken together, all of the foregoing results suggest that the organized unsteadiness associated with undulations or breakdown of the vortex core extend approximately over the range $0.5 \leq fC/U \leq 4.5$ for wings having relatively low sweep angle. Remarkably, this range of frequencies approximates frequencies associated with the helical mode of instability of vortex breakdown of wings having relatively high sweep angle $1.0 \leq fC/U \leq 4$, as assessed by Menke et al.[23] and earlier works cited therein.

9. CONCLUDING REMARKS

The abrupt change in sweep angle, which is characteristic of both diamond and lambda planforms, along with the different trailing-edge configurations of these planforms, yields distinctive features of the flow patterns, relative to the case of a simple delta wing.

The streamline topology for both the diamond and lambda planforms shows, at low angle of attack, a focus (apparent center) of a spiral pattern of streamlines at, rather than inboard of, the leading-edge. At moderate angles-of-attack this focus shifts inboard of the leading-edge, and at high-angle-attack, where a large-scale separated zone occurs adjacent to the wing surface, the pattern of streamline topology loses its ordered definition. Furthermore, the occurrence of saddle points (apparent intersection of streamlines) is influenced by a global effect of the trailing-edge configuration. For the lambda planform, a saddle point is located outboard of the leading-edge; for the diamond planform, it is absent.

Corresponding patterns of vorticity show, at all values of angle of attack, a high concentration of vorticity in either the vicinity of, or even at, the leading-edge. In the limiting case of low angle-of-attack, this concentration is nearly centered at the edge, while at larger angles-of-attack, it is displaced significantly away from the edge. Furthermore, well-defined vortical substructures are identifiable in the elongated layers of time-averaged vorticity adjacent to the surface of the wing. These substructures appear to be analogous to those about the periphery of the single, large-scale region of vorticity on a wing of high sweep angle. Corresponding images of instantaneous vorticity show that the elongated layer of average vorticity is actually made up of well-defined vorticity concentrations, whose spacing is very approximately commensurate with those of time-averaged patterns. The spatial positions of these instantaneous vorticity concentrations exhibit substantial modulation from one instantaneous image to the next.

Contours of constant root-mean-square velocity fluctuation adjacent to the wing have extrema that are generally coincident with the outer regions of the elongated, time-averaged vorticity layers. The spectral content of these fluctuations, evaluated from space-time imaging, shows well-defined peaks, which are associated with the aforementioned modulation of instantaneous vorticity patterns. For extreme values of low and high angle-of-attack, the dimensionless frequencies of the spectral peaks lie in the range of $2.13 \leq fC/U \leq 3.97$.

10. ACKNOWLEDGEMENTS

The authors are grateful to the Air Force Office of Scientific Research, Grant #F49620-02-1-0061 for support of this research program, which was monitored by Dr. John Schmisseur. The first author was supported jointly by AFOSR and Cukurova University during his research stay as a Visiting Scientist at Lehigh University. Prior to and subsequent to his stay at Lehigh, he has been supported as a Research Assistant at Cukurova University.

11. LIST OF REFERENCES

[1]Gordnier, R. E., and Visbal, M. R. "Higher-Order Compact-Difference Scheme Applied to the Simulation of the Low Sweep Delta Wing Flow", AIAA Paper 2003-0620, 41st AIAA Aerospace Sciences Meeting and Exhibit, 6-9 January, 2003, Reno, NV.

[2]Ol, M. V., and Gharib, M. "The Passage Towards Stall of Nonslender Delta Wings at Low Reynolds Number", AIAA Paper 2001-2843, 2001.

[3]Ol, M. V. and Gharib, M. "Leading-Edge Vortex Structure of Nonslender Delta Wings at Low Reynolds Number", *AIAA Journal*, Vol. 41, No. 1, 2003, pp. 16-26.

[4]Yaniktepe, B., and Rockwell, D. "Flow Structure in Regions of Vortex Breakdown and Stall on a Delta Wing at Low Sweep Angle", *AIAA Journal*, Vol. 42, No. 1, January, 2004 (in press) .

[5]Visbal, M. R., and Gordnier, R. E. "On the Structure of the Shear Layer Emanating from a Swept Leading Edge at Angle of Attack", AIAA Paper No. 2003-4016, 33rd Fluid Dynamics Conference and Exhibit, 23-26 June, 2003, Orlando, FL.

[6]Squire, B. II, Jones, J. G., and Stanbrook, A. "Investigation of the Characteristics of Some Plane and Cambered 65 Deg Delta Wings at Mach Numbers from 0.7 to 2.0", *ARC, R.M. No. 3305*, 1961.

[7]Gad-el-Hak, M., and Blackwelder, R. F. "The Discrete Vortices from a Delta Wing", *AIAA Journal*, Vol. 23, No. 6, 1985, pp. 961-962.

[8]Gad-el-Hak, M., and Blackwelder, R. F. "Control of the Discrete Vortices from a Delta Wing", *AIAA Journal*, Vol. 25 No. 8, 1987, pp. 1042-1049.

[9]Payne, F.M., Ng, T.T., Nelson, R.C., and Schiff, L.B. "Visualization and Wake Surveys of Vortical Flow Over Delta Wing", *AIAA Journal*, Vol. 26, No. 2, 1988, pp. 137-143.

[10]Lowson, M. V. "The Three-Dimensional Vortex Sheet Structure on Delta Wings". In *Fluid Dynamics of Three-Dimensional Turbulent Shear Flows and Transition*, October, Agard-CP-438, 1988.

[11]Reynolds, G. A., and Abtahi, A. A. "Three-Dimensional Vortex Development, Breakdown and Control", AIAA-89-0998, March, 1989.

[12]Verhaagen, N. G., Meeder, J. P., and Verhelst, J. M. "Boundary Layer Effects on the Flow of a Leading Edge Vortex", AIAA Paper 93-3463-CP, 1993.

[13]Washburn, A. E., and Visser, K. D. Evolution of Vortical Structures in the Shear Layer of Delta Wings", AIAA Paper No. 94-2317, 1994.

[14]Lowson, M. V., Riley, A. J., and Swales, C. "Flow Structure over Delta Wings", AIAA Paper No. 95-0586, 1995.

[15]Riley, A. J., and Lowson, M. V. "Development of a Three-Dimensional Free Shear Layer", *Journal of Fluid Mechanics*, Vol. 369, 1998, pp. 49-89.

[16]Mitchell, A., Molton, P., Barbaris, D., and Delery, J. "Vortical Substructures in the Shear Layers Forming Leading-Edge Vortices", AIAA Paper No. 2001-2424, 2001.

[17]Gordnier, R. E., and Visbal, M. R. "Numerical Simulation of the Unsteady Vortex Structure over a Delta Wing", AIAA Paper No. 91-1811, 1991.

[18]Gordner, R. E., and Visbal, M. R. "Unsteady Vortex Structure over a Delta Wing", *Journal of Aircraft*, Vol. 31, No. 1, 1994, pp. 243-248.

[19]Mitchell, A., Morton, S., and Forsythe, J. "Analysis of Delta Wing Vortical Substructure Using Detached-Eddy Simulation", AIAA Paper No. 2002-2968, 2002.

[20]Mitchell, A. M., and Molton, P. "Vortical Substructures in the Shear Layers Forming Leading-Edge Vortices" *AIAA Journal*, Vol. 40, 2002, pp. 1689-1692.

[21]Gursul, I, Taylor, G., and Wooding, C. L. "Vortex Flows over Fixed-Wing Micro Air Vehicles", AIAA Paper A02-14137, 2002.

[23]Menke, M., Yang, H., and Gursul, I. "Experiments on the Unsteady Nature of Vortex Breakdown over Delta Wings", *Experiments in Fluids*, Vol. 27, 1999, pp. 262-272.

[22]Akilli, H., and Rockwell, D. 2002 "Vortex Formation from a Cylinder in Shallow Water", *Physics of Fluids*, Vol. 14, No. 9, 2002, pp. 2957-2967.

LIST OF FIGURES

Figure A1a: Schematic of experimental system showing a representative wing, laser sheet location and direction of view.

Figure A1b: Direct comparison of diamond and lambda planforms and locations of laser sheets employed for quantitative imaging.

Figure A2: Dye visualization at angles-of-attack $\alpha = 7°$ and 13°. At $\alpha = 7°$, dye is injected from two localized ports at the apex of the wing, while at $\alpha = 13°$, it is injected along the leading-edge on the windward side.

Figure A3: Patterns of time-averaged velocity $< V >$ at $\alpha = 7°$, 13°, 17° and 25°. For both the diamond and lambda planforms, laser sheet is located at $x/C' = 1.4$, immediately downstream of abrupt change of sweep angle. Scale shown above planform cross-section is y/S, in which $y/S = 1.0$ corresponds to plane of symmetry of wing; S is the semi-span at $x/C' = 1.4$.

Figure A4: Patterns of time-averaged streamline $< \Psi >$ topology at angles-of-attack $\alpha =$ 7°, 13°, 17° and 25° for the diamond and lambda planforms. For both planforms, the laser sheet is located at $x/C' = 1.4$, immediately downstream of abrupt change of sweep angle. Spanwise extent of each planform cross-section is same as in Figure 3.

Figure A5a: Patterns of time-averaged vorticity $< \omega >$ and corresponding patterns of root-mean-square velocity fluctuation w_{rms}/U (normal to the wing). At angle-of-attack α = 7°, minimum and incremental values of vorticity contours are $[< \omega >]_{min} = -0.2$ sec^{-1} and $\Delta[< \omega >] = -0.15$ sec^{-1}. At $\alpha = 13°$, $[< \omega >]_{min} = -0.35$ sec^{-1} and $\Delta[< \omega >] =$ -0.15 sec^{-1}. For patterns of root-mean-square velocity, minimum and incremental values at $\alpha = 7°$ are $[w_{rms}/U]_{min} = 0.02$ and $\Delta[w_{rms}/U] = 0.01$. For $\alpha = 13°$, $[w_{rms}/U]_{min} = 0.04$ and $\Delta[w_{rms}/U] = 0.01$. For both the diamond and lambda planforms, laser sheet is located at $x/C' = 1.4$, immediately downstream of abrupt change of sweep angle. In each image, spanwise extent of planform cross-section corresponds to the semi-span S of the wing at $x/C' = 1.4$.

Figure A5b: Patterns of time-averaged vorticity $< \omega >$ and corresponding patterns of root-mean-square velocity fluctuation w_{rms}/U (normal to the wing). At angle-of-attack α = 17°, minimum and incremental values of vorticity contours are $[< \omega >]_{min} = -0.35$ sec^{-1} and $\Delta[< \omega >] = -0.15$ sec^{-1}. At $\alpha = 25°$, $[< \omega >]_{min} = -0.2$ sec^{-1} and $\Delta[< \omega >] =$ -0.15 sec^{-1}. For contours of root-mean-square vertical velocity, at $\alpha = 17°$, $[w_{rms}/U]_{min} =$ 0.03 and $\Delta[w_{rms}/U] = 0.01$. For $\alpha = 25°$, $[w_{rms}/U]_{min} = 0.02$ and $\Delta[w_{rms}/U] = 0.01$. For both the diamond and lambda planforms, laser sheet is located at $x/C' = 1.4$, immediately downstream of abrupt change of sweep angle. In each image, spanwise extent of planform cross-section corresponds to the semi-span S of the wing at $x/C' =$ 1.4.

Figure A6: Superposition of patterns of averaged vorticity $< \omega >$ and streamline $< \Psi >$ topology at $\alpha = 17°$ for the diamond and lambda planforms. The laser sheet is located at $x/C' = 1.4$.

Figure A7: Comparison of patterns of instantaneous velocity V and vorticity ω at angles-of-attack $\alpha = 7°$ and 25° for the diamond planform. At $\alpha = 7°$, minimum and incremental values of vorticity are $\omega_{min} = -1.5$ sec^{-1} and $\Delta\omega = -0.5$ sec^{-1}. At $\alpha = 25°$, minimum and incremental values of vorticity are $\omega_{min} = -0.5$ sec^{-1} and $\Delta\omega = -0.5$ sec^{-1}. For both the diamond and lambda planforms, laser sheet is located at $x/C' = 1.4$, immediately downstream of abrupt change of sweep angle. Spanwise extent of each planform cross-section extends from $y/S = 0$ to 0.62 ($\alpha = 7°$) and to 1.0 ($\alpha = 25°$).

Figure A8a: Patterns of instantaneous vorticity ω at angles-of-attack $\alpha = 7°$ and 13° for the diamond and lambda planforms. At $\alpha = 7°$, values of minimum and incremental levels of vorticity are $\omega_{min} = -1.5$ sec^{-1} and $\Delta\omega = -0.5$ sec^{-1}. At $\alpha = 13°$, values of minimum and incremental levels of vorticity are $\omega_{min} = -0.5$ sec^{-1} and $\Delta\omega = -0.5$ sec^{-1}. For both the diamond and lambda planforms, laser sheet is located at $x/C' = 1.4$, immediately downstream of abrupt change of sweep angle. At $\alpha = 7°$ (diamond and lambda planforms), spanwise extent of planform cross-section extends from $y/S = 0$ (leading-edge) to $y/S = 0.62$. For all other images, it extends from $y/S = 0$ to $y/S = 1.0$, where S is the semi-span at $x/C' = 1.4$.

Figure A8b: Patterns of instantaneous vorticity ω at angles-of-attack $\alpha = 17°$ and 25° for the diamond and lambda planforms. Values of minimum and incremental levels of vorticity are $\omega_{min} = -0.5$ sec^{-1} and $\Delta\omega = -0.5$ sec^{-1}. For both the diamond and lambda planforms, laser sheet is located at $x/C' = 1.4$, immediately downstream of abrupt change of sweep angle.

Figure A9: Spectra $S_w(f)$ of the vertical velocity fluctuation w at locations corresponding to maxima of the root-mean-square value of the transverse (vertical) velocity fluctuation w_{rms}/U at angles-of-attack $\alpha = 7°$ and 25° for the diamond and lambda planforms. The laser sheet is located at $x/C' = 1.4$.

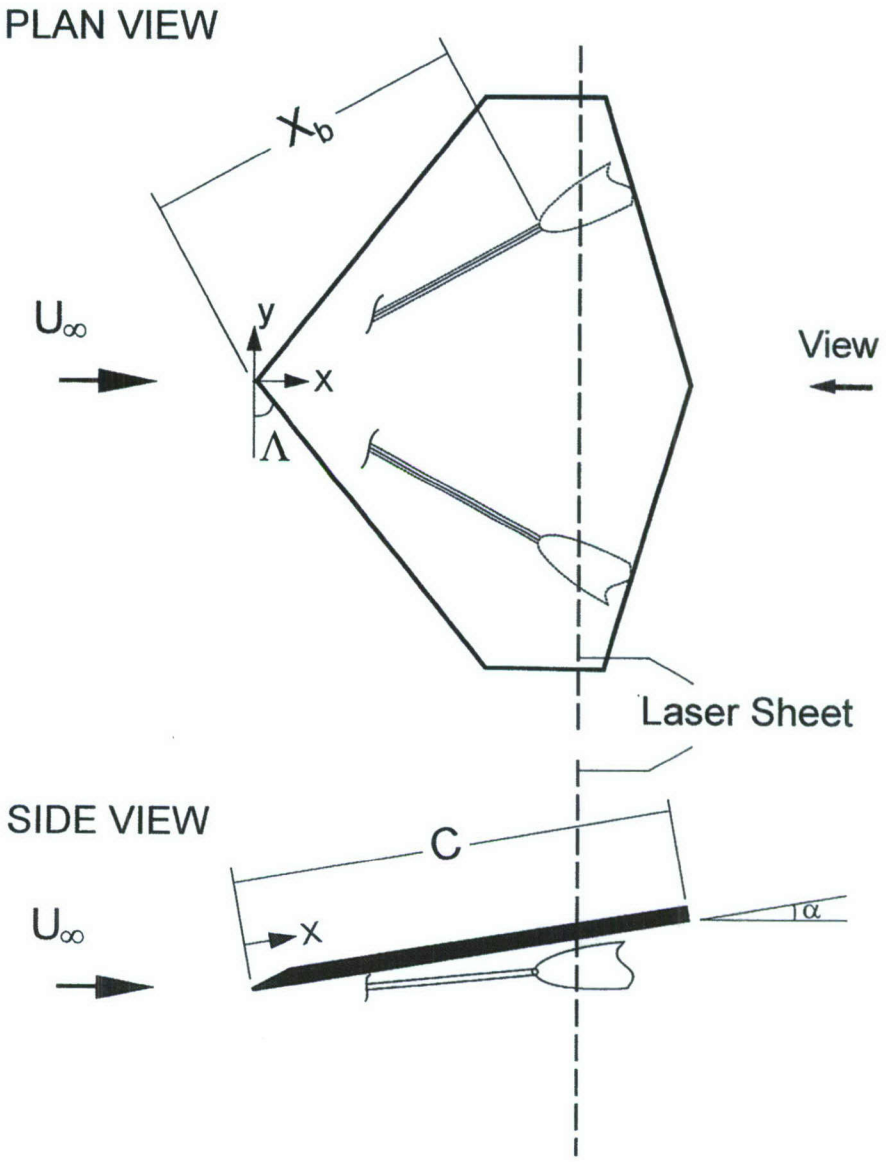


Figure A1a: Schematic of experimental system showing a representative wing, laser sheet location and direction of view.

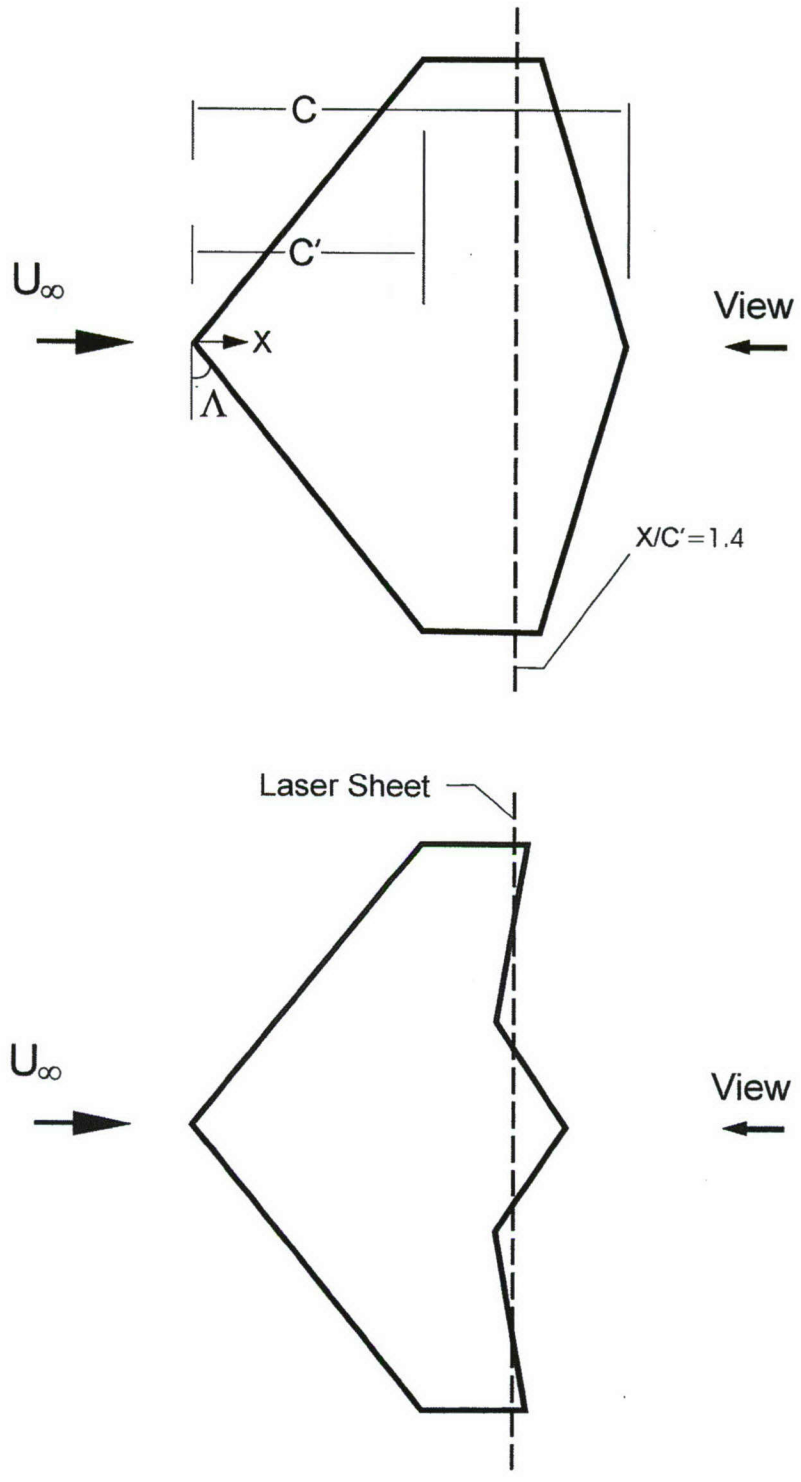


Figure A1b: Direct comparison of diamond and lambda planforms and locations of laser sheets employed for quantitative imaging.

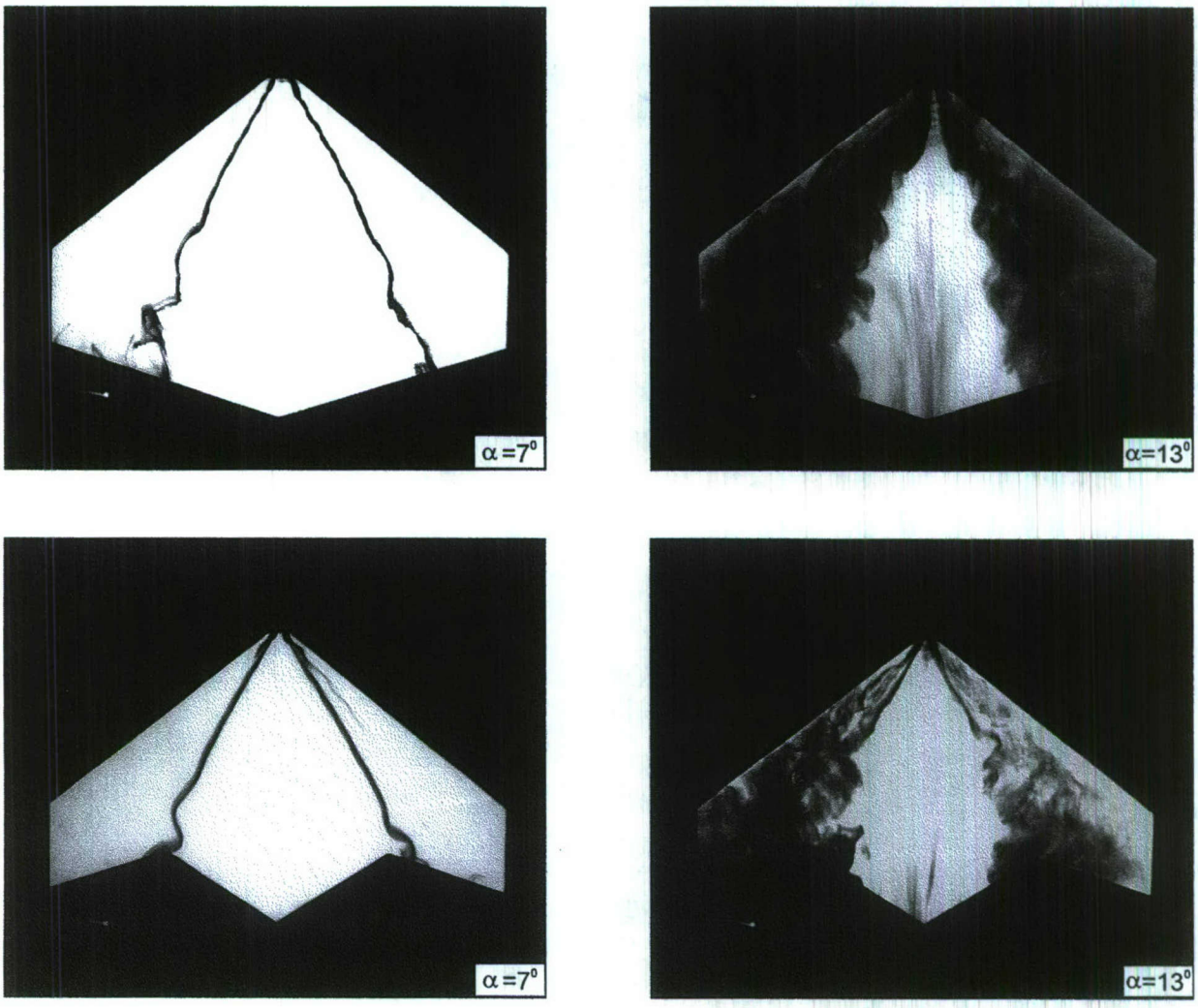


Figure A2: Dye visualization at angles-of-attack $\alpha = 7°$ and 13°. At $\alpha = 7°$, dye is injected from two localized ports at the apex of the wing, while at $\alpha = 13°$, it is injected along the leading-edge on the windward side.

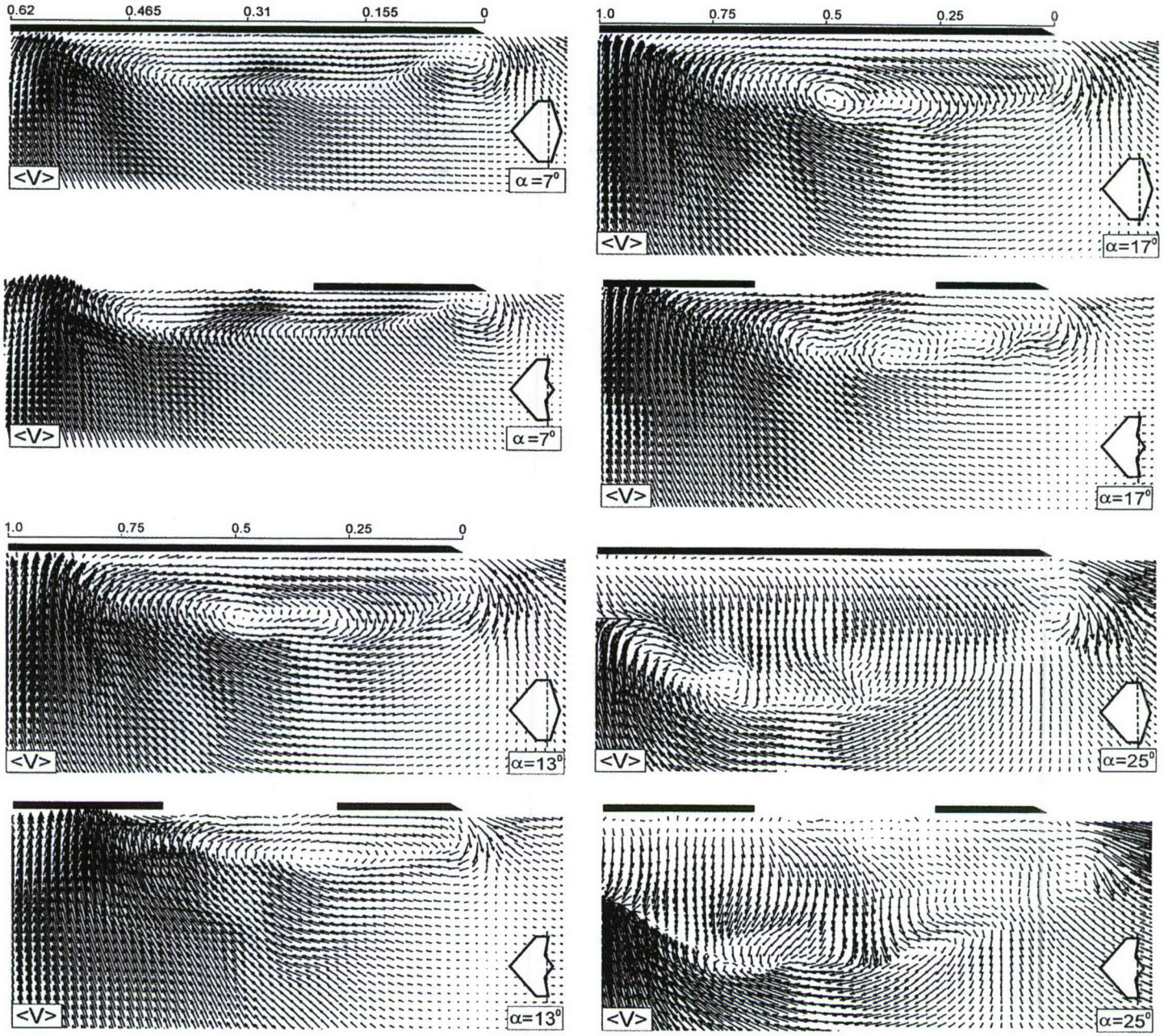


Figure A3: Patterns of time-averaged velocity $< V >$ at α = 7°, 13°, 17° and 25°. For both the diamond and lambda planforms, laser sheet is located at $x / C' = 1.4$, immediately downstream of abrupt change of sweep angle. Scale shown above planform cross-section is *y/S*, in which *y/S* = 1.0 corresponds to plane of symmetry of wing; *S* is the semi-span at $x / C' = 1.4$.

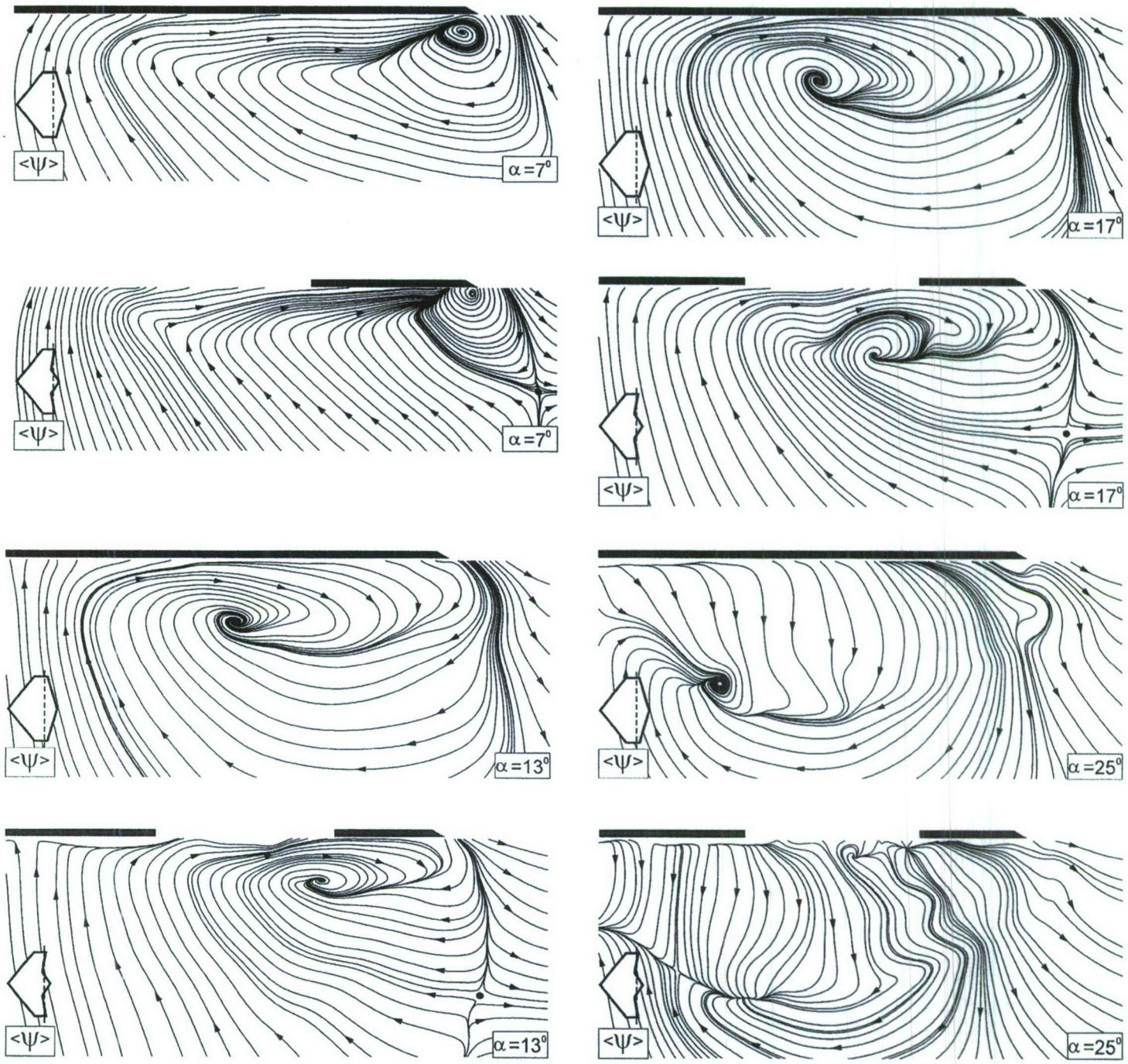


Figure A4: Patterns of time-averaged streamline $<\Psi>$ topology at angles-of-attack $\alpha = 7°$, 13°, 17° and 25° for the diamond and lambda planforms. For both planforms, the laser sheet is located at $x/C' = 1.4$, immediately downstream of abrupt change of sweep angle. Spanwise extent of each planform cross-section is same as in Figure 3.

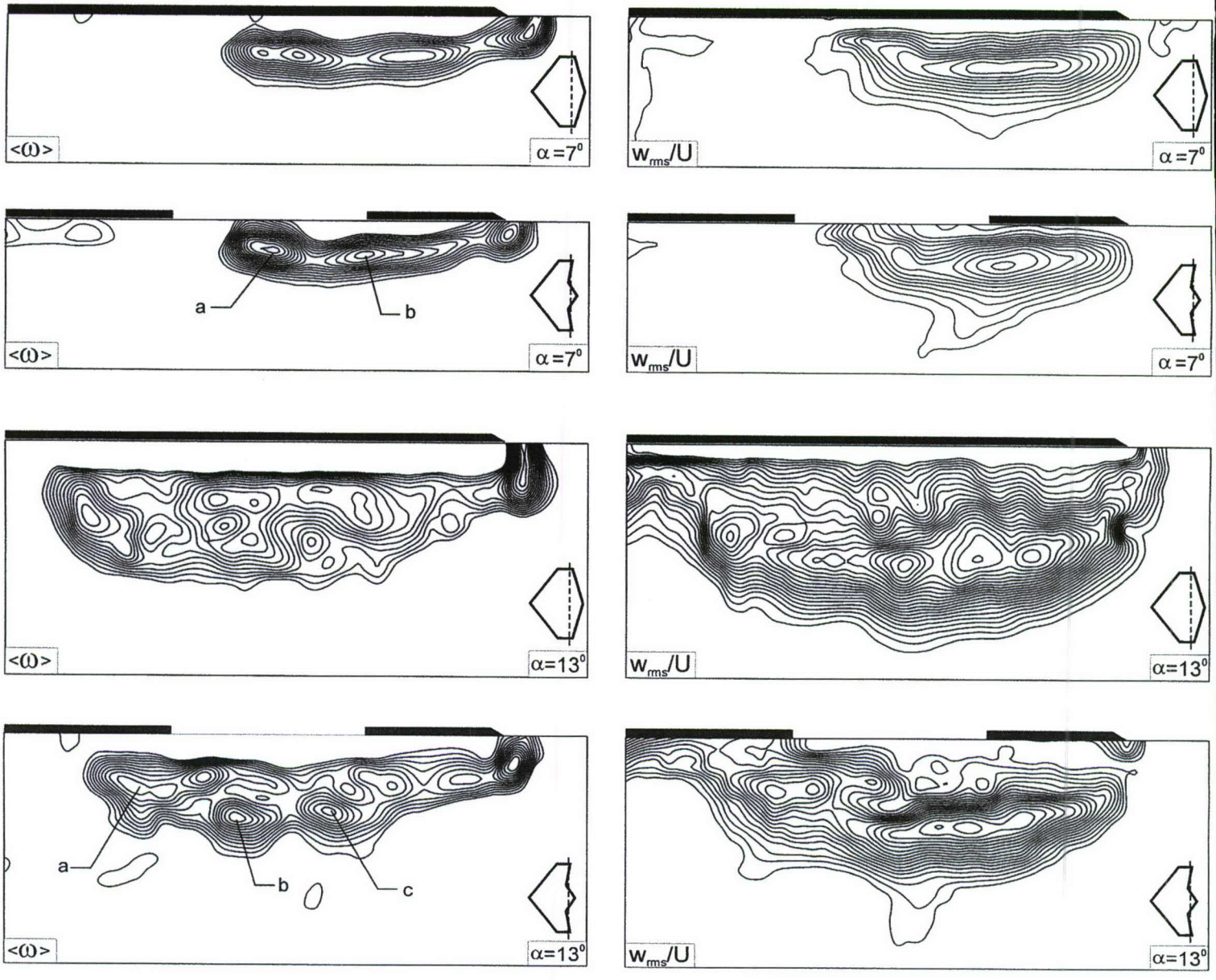


Figure A5a: Patterns of time-averaged vorticity $< \omega >$ and corresponding patterns of root-mean-square velocity fluctuation w_{rms}/U (normal to the wing). At angle-of-attack α = 7°, minimum and incremental values of vorticity contours are $[< \omega >]_{min}$ = –0.2 sec^{-1} and $\Delta[< \omega >]$ = –0.15 sec^{-1}. At α = 13°, $[< \omega >]_{min}$ = –0.35 sec^{-1} and $\Delta[< \omega >]$ = –0.15 sec^{-1}. For patterns of root-mean-square velocity, minimum and incremental values at α = 7° are $[w_{rms}/U]_{min}$ = 0.02 and $\Delta[w_{rms}/U]$ = 0.01. For α = 13°, $[w_{rms}/U]_{min}$ = 0.04 and $\Delta[w_{rms}/U]$ = 0.01. For both the diamond and lambda planforms, laser sheet is located at x/C' = 1.4, immediately downstream of abrupt change of sweep angle. In each image, spanwise extent of planform cross-section corresponds to the semi-span S of the wing at x/C' = 1.4.

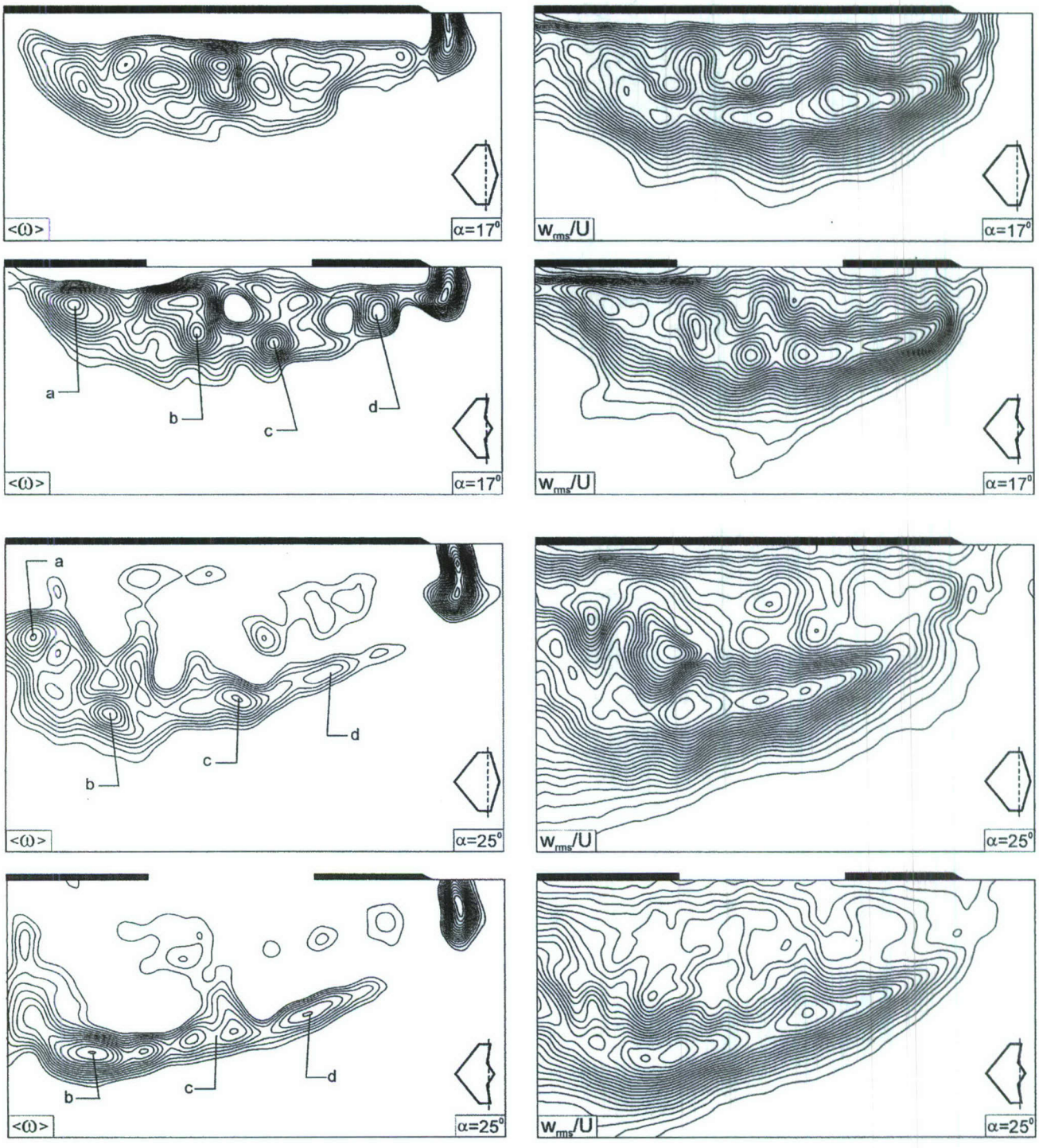


Figure A5b: Patterns of time-averaged vorticity $< \omega >$ and corresponding patterns of root-mean-square velocity fluctuation w_{rms}/U (normal to the wing). At angle-of-attack $\alpha = 17°$, minimum and incremental values of vorticity contours are $[< \omega >]_{min} = -0.35$ sec^{-1} and $\Delta[< \omega >] = -0.15$ sec^{-1}. At $\alpha = 25°$, $[< \omega >]_{min} = -0.2$ sec^{-1} and $\Delta[< \omega >] = -0.15$ sec^{-1}. For contours of root-mean-square vertical velocity, at $\alpha = 17°$, $[w_{rms}/U]_{min} = 0.03$ and $\Delta[w_{rms}/U] = 0.01$. For $\alpha = 25°$, $[w_{rms}/U]_{min} = 0.02$ and $\Delta[w_{rms}/U] = 0.01$. For both the diamond and lambda planforms, laser sheet is located at $x/C' = 1.4$, immediately downstream of abrupt change of sweep angle. In each image, spanwise extent of planform cross-section corresponds to the semi-span S of the wing at $x/C' = 1.4$.

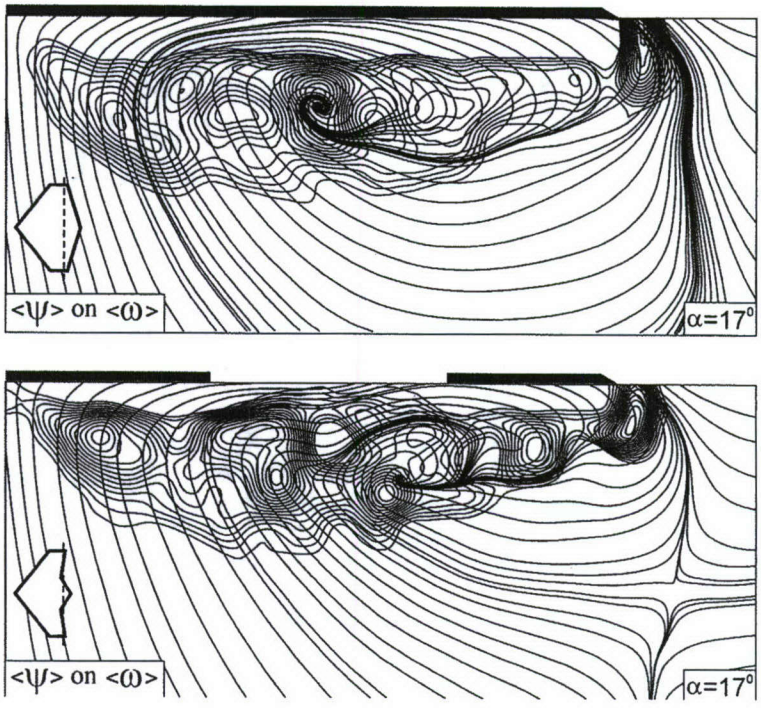


Figure A6: Superposition of patterns of averaged vorticity $< \omega >$ and streamline $< \Psi >$ topology at α = 17° for the diamond and lambda planforms. The laser sheet is located at $x / C' = 1.4$.

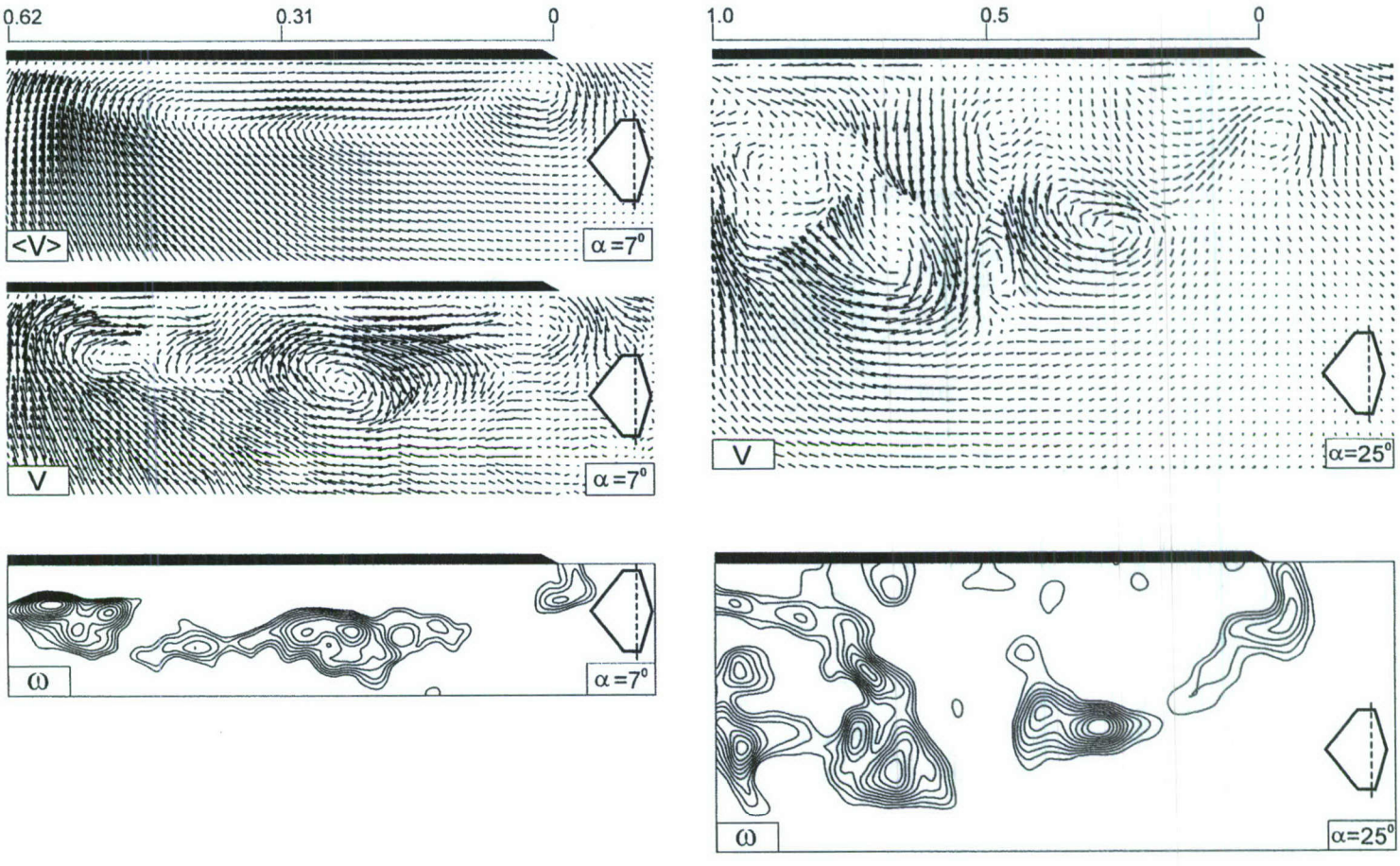


Figure A7: Comparison of patterns of instantaneous velocity V and vorticity ω at angles-of-attack $\alpha = 7°$ and 25° for the diamond planform. At $\alpha = 7°$, minimum and incremental values of vorticity are $\omega_{min} = -1.5$ sec^{-1} and $\Delta\omega = -0.5$ sec^{-1}. At $\alpha = 25°$, minimum and incremental values of vorticity are $\omega_{min} = -0.5$ sec^{-1} and $\Delta\omega = -0.5$ sec^{-1}. For both the diamond and lambda planforms, laser sheet is located at $x / C' = 1.4$, immediately downstream of abrupt change of sweep angle. Spanwise extent of each planform cross-section extends from $y/S = 0$ to 0.62 ($\alpha = 7°$) and to 1.0 ($\alpha = 25°$).

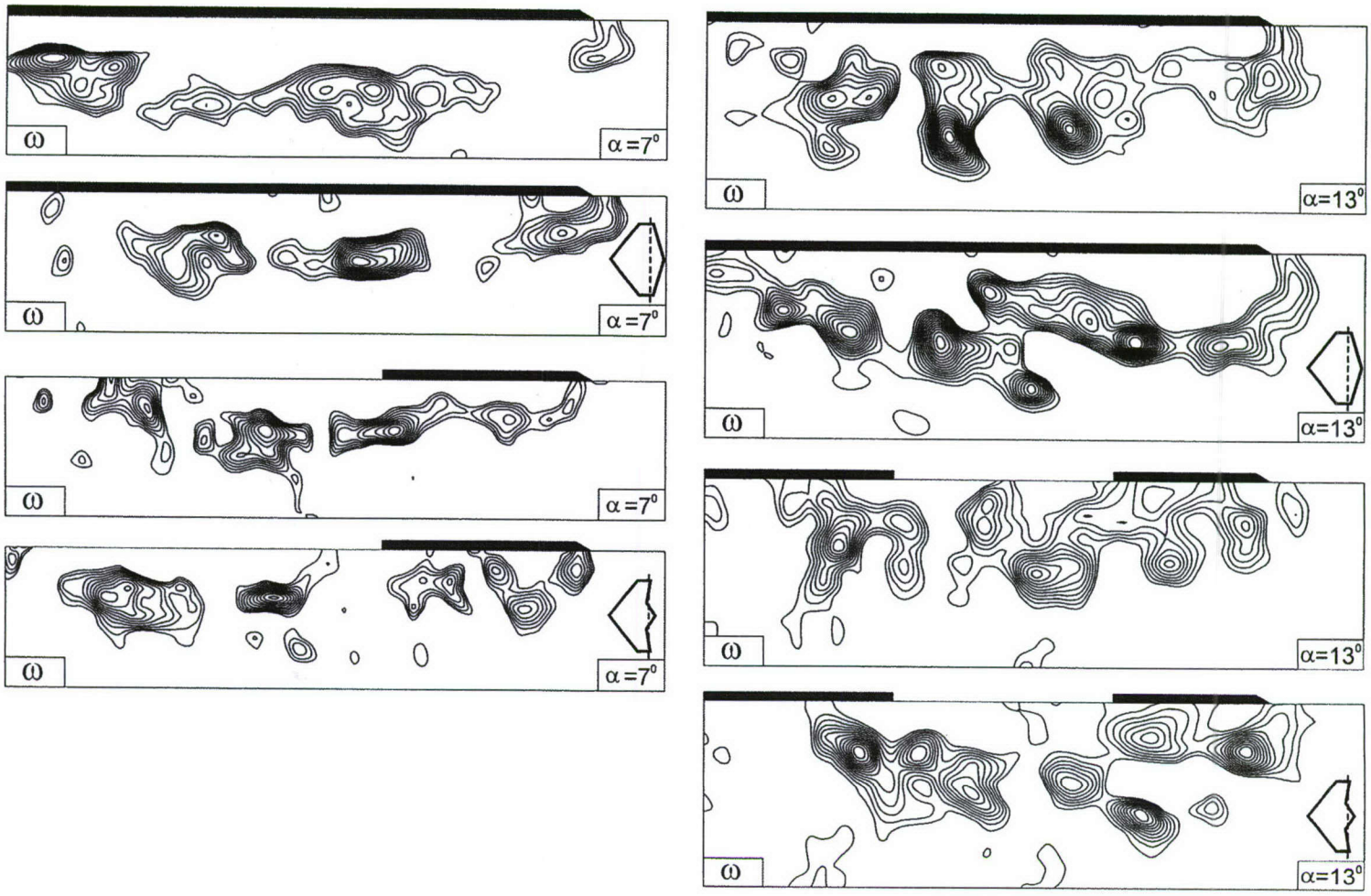


Figure A8a:
Patterns of instantaneous vorticity ω at angles-of-attack $\alpha = 7°$ and 13° for the diamond and lambda planforms. At $\alpha = 7°$, values of minimum and incremental levels of vorticity are $\omega_{min} = -1.5$ sec^{-1} and $\Delta\omega = -0.5$ sec^{-1}. At $\alpha = 13°$, values of minimum and incremental levels of vorticity are $\omega_{min} = -0.5$ sec^{-1} and $\Delta\omega = -0.5$ sec^{-1}. For both the diamond and lambda planforms, laser sheet is located at $x/C' = 1.4$, immediately downstream of abrupt change of sweep angle. At $\alpha = 7°$ (diamond and lambda planforms), spanwise extent of planform cross-section extends from $y/S = 0$ (leading-edge) to $y/S = 0.62$. For all other images, it extends from $y/S = 0$ to $y/S = 1.0$, where S is the semi-span at $x/C' = 1.4$.

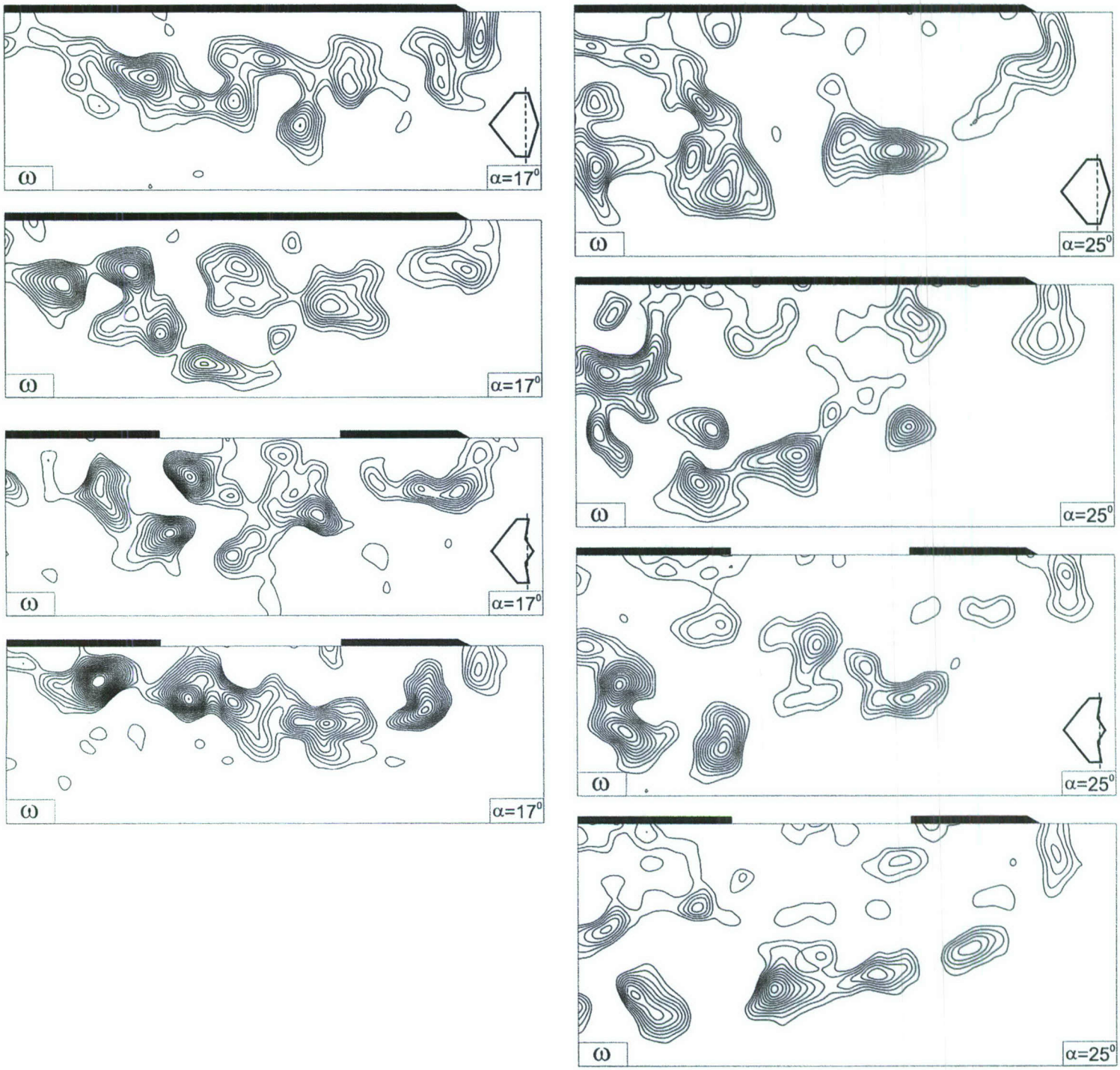


Figure A8b: Patterns of instantaneous vorticity ω at angles-of-attack α = 17° and 25° for the diamond and lambda planforms. Values of minimum and incremental levels of vorticity are $\omega_{min} = -0.5$ sec^{-1} and $\Delta\omega = -0.5$ sec^{-1}. For both the diamond and lambda planforms, laser sheet is located at $x / C' = 1.4$, immediately downstream of abrupt change of sweep angle.

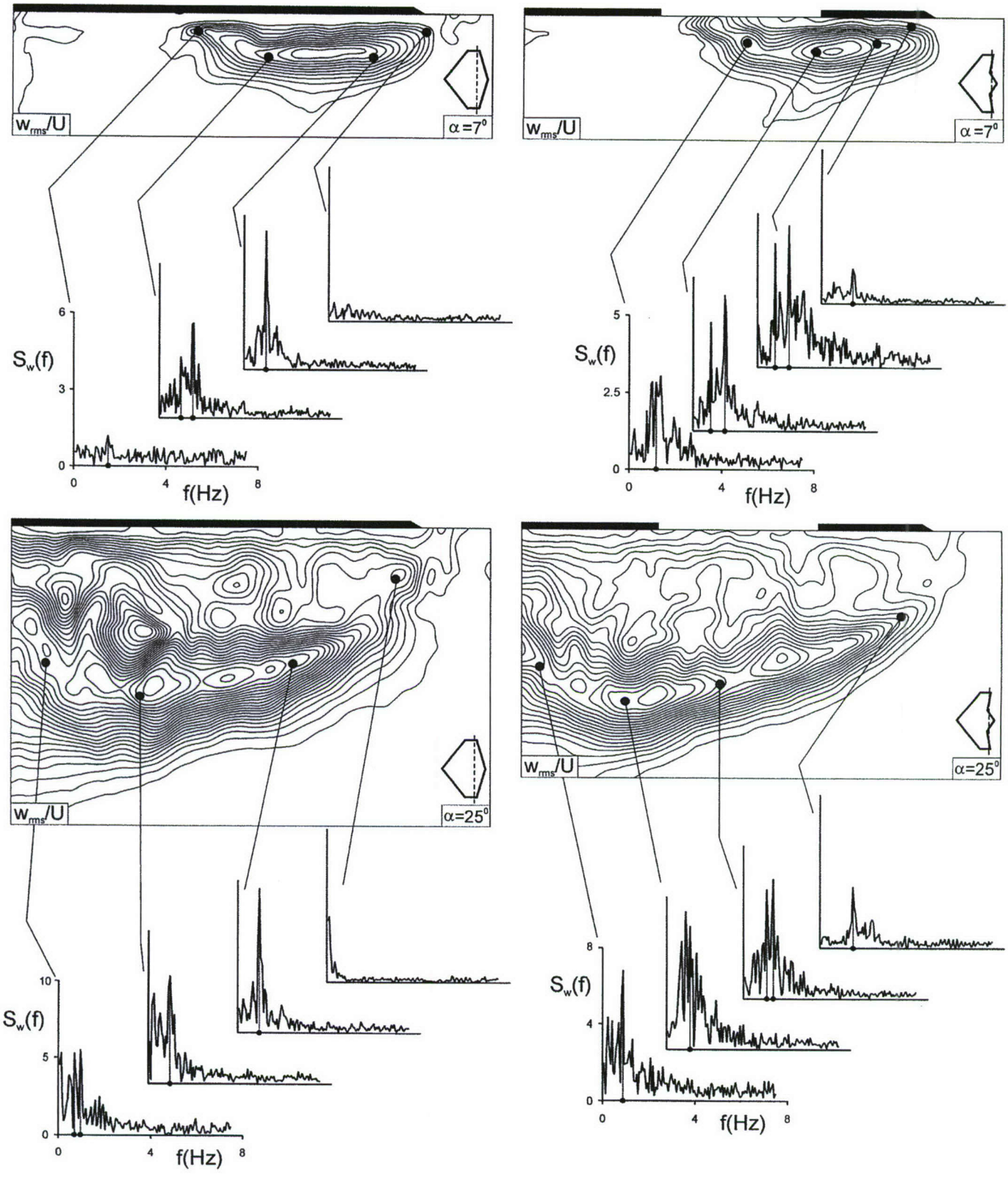


Figure A9: Spectra $S_w(f)$ of the vertical velocity fluctuation w at locations corresponding to maxima of the root-mean-square value of the transverse (vertical) velocity fluctuation w_{rms}/U at angles-of-attack $\alpha =$ 7° and 25° for the diamond and lambda planforms. The laser sheet is located at $x / C' = 1.4$.

Appendix B

CONTROL OF NEAR-SURFACE FLOW STRUCTURE ON LOW SWEPT DELTA WING WITH STEADY TRAILING EDGE BLOWING

by

M. M. Yavuz and D. Rockwell
Department of Mechanical Engineering and Mechanics
Lehigh University
Bethlehem, PA 18015
Email: dor0@lehigh.edu

ABSTRACT

The near-surface flow structure and topology are characterized on a delta wing of low sweep angle, which is subjected to trailing-edge blowing. A technique of high-image-density particle image velocimetry is employed to determine the topological critical points adjacent to the surface and in the near-wake of the wing, in relation to the dimensionless magnitude of the blowing coefficient. These topological features are, in turn, interpreted in conjunction with patterns of surface-normal vorticity and near-surface velocity fluctuations, which provide an indication of buffet loading. Even though the jet blowing is at the trailing-edge, it has a remarkable, global influence on the surface patterns located well upstream; at high angle-of-attack, it leads to eradication of large-scale, three-dimensional separation in the vicinity of the apex.

1. INTRODUCTION

Recent interest in unmanned combat air vehicles (UCAVs), has motivated the investigation of the flow structure on delta wings having low and moderate values of sweep angle. This interest leads us to investigate present study which is; the control of near surface flow topology of delta wings having a low sweep angle with steady trailing edge blowing, the effect of angle-of-attack of planform and different blowing locations on flow structure. Related investigations that were previously done include: experimental and numerical studies of the flow structure above wings of low- and moderate sweep angle and investigations of blowing concept and its effects on flow structures of delta wings. These are included in the summaries that follow.

1.1 FLOW STRUCTURE AND NEAR SURFACE TOPOLOGY ON DELTA WINGS OF MODERATE AND LOW SWEEP ANGLES

The generic features of UCAV configurations can be represented by delta wings having low and moderate values of sweep angle. They are associated with distinctive types of flow patterns above and at the surface of the wing, which have been the subject of recent investigations. Ol and Gharib[1,2] undertook experimental investigations of wings of sweep angle $\Lambda = 50°$ and 65°. They determined the onset of vortex breakdown using dye visualization and, via a stereo PIV technique, characterized various features of the leading-edge vortex structure. Honkan and Adreopoulos[3] determined patterns of instantaneous vorticity on a delta wing of sweep angle $\Lambda = 45°$ with triple orthogonal hot wire probes, and identified the existence of discrete stationary vortices in the feeding shear layer as well as the primary vortex. They also

showed that high turbulence activity is associated with the regions of shear layer reattachment and secondary separation. Miau, Kuo, Liu, Hsieh, Chou and Lin[4] investigated the flow patterns on a wing of sweep angle $\Lambda = 50°$, with a focus on the consequences of leading-edge profile. The detailed characteristics of the instantaneous and averaged flow structure, as well as the surface flow topology on a delta wing of sweep angle $\Lambda = 50°$ were numerically computed by Gordnier and Visbal[5]. Taylor, Schnorbus and Gursul[6] employed a dye technique, along with complementary particle image velocimetry, to visualize the vortex cores on wings of low swept $\Lambda = 50°$ wing, and Taylor and Gursul[7] investigated the near-surface topology and buffeting phenomena on the same planform. Both of the foregoing experimental and numerical studies have demonstrated that, for the $\Lambda = 50°$ wing, at low angle-of-attack, a dual primary vortex system exists, whereas at higher angle-of-attack, this dual structure gives way to a single, larger-scale vortex which is a basic feature of highly swept wings.

Investigations at lower values of sweep angle include Yaniktepe and Rockwell[8], who considered a wing of sweep angle $\Lambda = 38.7°$ and addressed the flow structure well into the region of vortex breakdown via particle image velocimetry (PIV). Yavuz, Elkhoury and Rockwell[9] investigated the near-surface topology and flow structure for a wing of sweep angle $\Lambda = 38.7°$, including the effect of wing perturbations and transient motion of the wing; a near-surface technique of PIV was employed.

For complex geometries such as an actual X-45 planform, both the fuselage and the wing extensions have low sweep angle. Elkhoury and Rockwell[10] and Elkhoury, Yavuz and Rockwell[11] employed dye visualization in conjunction with PIV on crossflow and near-surface planes to determine mean and unsteady representations of the flow structure.

1.2 CONTROL OF FLOW STRUCTURE VIA SUCTION AND BLOWING

Different methods of control of the flow structure on a delta wing have been pursued, in order to delay the onset of vortex breakdown, with the aim of reducing its undesired effects on the aerodynamic surface(s), as well as altering the overall performance characteristics of the planform. Suction and blowing in the tangential direction along the leading edge of a wing have been investigated by a number of researchers, with emphasis on highly swept wings. Wood, Roberts and Celik[12] and McCormick and Gursul[13] employed the steady blowing and suction, whereas Gu, Robinson and Rockwell[14] applied periodic suction and blowing along the leading edge of the planform/wing. Intermittent trailing-edge blowing was studied by Vorobieff and Rockwell[15]. Parmenter and Rockwell[16] provided a different method, i.e., suction along the vortex axis at a location of downstream of the onset of vortex breakdown, for delaying the onset of vortex breakdown. A unique approach to blowing is that of Johari, Olinger and Fitzpatrick[17], who provided blowing from surface ports oriented at different angles and located beneath the vortex core. Helin and Watry[18], Shih and Ding[19], Mitchell, Molton, Barberis and Delery[20], and Phillips, Lambert, and Gursul[21] demonstrated the effectiveness of trailing-edge blowing on the flow characteristics and onset of vortex breakdown. Further investigation on a closely related approach, which involved jet vectoring, was investigated by Wang, Li and Liu[22].

1.3 UNRESOLVED ISSUES

Generally speaking, very little effort has been devoted to control of the flow structure on wings having low sweep angle, which are representative of UCAV planforms. In particular, the following issues have not been addressed.

(a) The flow structure on delta wings of low sweep angle, in absence of a control technique, should be defined in a systematic fashion, e.g., by variations of angle-of-attack, with particular attention to the occurrence of vortex breakdown, surface buffeting and stall, all interpreted in terms of quantitative representations of the surface flow topology, in particular classes of critical points. This approach can potentially lead to definition of a critical angle-of-attack, at which the onset of three-dimensional separation occurs.

(b) A particularly effective form of control may involve blowing at the trailing-edge of a delta wing of low sweep angle. The anticipated onset of large-scale, three-dimensional surface separation and stall at relatively low angle-of-attack provides a flow state that may be sensitive to control by trailing-edge blowing. The minimum dimensionless blowing coefficient that yields a significant transformation of the near-surface flow structure and topology should be determined.

(c) Trailing-edge blowing represents a form of control that is localized at the trailing-edge, yet it may have a substantial, global influence over the entire surface of the wing. This concept of global alteration of the flow structure in presence of localized control at a downstream location is a potentially important concept that may extend to other types of control approaches. Quantitative interpretation of patterns of the flow structure and topology at the wing surface can allow assessment of this concept.

(d) Potential control of the mean (time-averaged) patterns of the flow along the near-surface of the wing is expected to have implications for surface buffeting phenomena, which can be represented in terms of patterns of velocity fluctuation amplitude along the surface. The interrelationship between the mean streamline topology (critical points) that indicate the onset of three-dimensional separation should be interpreted in terms of these patterns of fluctuation intensity.

This investigation aims to address these points using a technique of high-image-density particle image velocimetry to characterize the flow patterns in the near-surface region of the wing.

2. EXPERIMENTAL SYSTEM AND TECHNIQUES

Experiments were performed in a large-scale water channel, with a test section 927 mm wide, 610 mm deep and 4,928 mm long. This test section was preceded by a settling tank, a honeycomb screen arrangement, and a 2:1 contraction. The turbulence intensity at the entrance to the test section was less than 0.3%. The walls of this section were optically transparent. The free-surface of the water was maintained at a height of 559 mm. The value of Reynolds number Re based on chord C was maintained at 10,000. The corresponding value of free-stream velocity was $U_\infty = 96.8$ mm/sec

The delta wing had a sweep angle of $\Lambda = 35°$, a chord C of 98 mm and a total span at the trailing-edge of 280 mm. The thickness of the wing was 12.7 mm, and its leading-edges were beveled on the windward side at an angle of 15°. The angles-of-attack of the wing were $\alpha = 5°$, 8° and 10°.

The inside of the delta wing was machined in the form of a cavity, in order to allow generation of uniform blowing from the trailing-edge; this blowing is represented in the schematic of Figure B1a. A water pump, control and bypass valves, and a volumetric flow meter were located outside of the water channel, in order to generate, measure and control the flow rate of the blowing. Two different configurations of trailing-edge blowing were used in the experiments: single and dual jets. For the case of the single jet, its slit was located at midspan, i.e. at the plane of symmetry of the wing. . The width and the thickness of the slit were 25.4 mm and 1.6 mm respectively. For the dual jet system, the center of each slit was located 50.8 mm from the plane of symmetry of the wing. Each slit had width of 25.4 mm and thickness of 0.8 mm. Both for single and dual jet configurations, seven different jet velocities were employed. These velocities corresponded to seven different momentum coefficients, $C_\mu = 0.006$, 0.025, 0.1, 0.23, 0.4, 0.92 and 1.63. The momentum coefficient was calculated as follows: $C_\mu = (V_j^2 * A_j)/(U^2 * A_s)$, in which V_j is the mean velocity of blowing at the trailing edge, A_j is the total area of both blowing slots the trailing edge, A_s is the surface area of the planform, and U is the freestream velocity. The wide range of momentum coefficients employed herein allowed examination of the possible regimes of response of the flow patterns induced by the trailing-edge blowing, taking into account values attainable in practical applications, as well as values employed in previous related investigations. Regarding previous studies, the maximum and minimum values given in the foregoing are comparable to those employed in the studies of Helin and Watry[18] and Shih and Ding[19].

In this investigation, emphasis is on global patterns of the instantaneous flow structure, as well as cinema sequences of these patterns, which allow characterization of the timewise evolution of the flow, and its time-averaged characteristics. A technique of high image density particle image velocimetry was employed to generate quantitative flow patterns. The flow was seeded with 12 micron, metallic-coated hollow plastic spheres. The seeding density of these particles was sufficiently large to satisfy the criterion of high image density; a minimum of 15 particle images were contained within the interrogation window, which is described below. Illumination was provided by a dual-pulsed 90 mJ Nd: Yag laser system. The collinear beam was transmitted through a system of cylindrical and spherical lenses attached to the laser head, in order to generate a laser sheet of 1 mm thickness. The maximum uncertainty of velocity was within 2%.

In order to obtain the near-surface flow patterns and topological characteristics, the laser sheet was located parallel, and immediately adjacent to the surface of the wing, as shown in the plan and side views of Figure B1. For all images shown herein, the laser sheet had a thickness of 1 mm at the center of the wing, and its center of the sheet was located a distance of 1 mm from the surface of the wing. This location corresponds to a displacement z normal to the surface of the wing of z/C = 0.01, in which C is the root chord.

Patterns of particle images were recorded on a high-resolution, digital charge-coupled device CCD camera, having 1,024 × 1,024 pixels, and an effective framing rate of 15 cycles per second. During evaluation of the velocity field V, a frame to frame cross correlation technique

was employed, with a 32 × 32 pixel interrogation window. The effective overlap was 50%, in order to satisfy the Nyquist criterion. The spatial resolution of the flow field was optimized by acquiring images over half of the wing. Preliminary experiments, which involved a larger field of view, verified that the flow patterns induced by the trailing-edge blowing were symmetrical. The effective resolution, i.e., grid size, was Δ/C = 0.0281, 0.0286, and 0.0289 respectively for the angles-of-attack α = 5°, 8° and 10°.

Once the instantaneous velocity field V was determined, as described in the foregoing, it was possible to calculate time-averaged patterns of velocity $\langle V \rangle$, surface-normal vorticity $\langle \omega \rangle$, streamlines $\langle \Psi \rangle$, and root-mean-square transverse velocity fluctuation v_{rms}/U, by using the cinema sequence of images. In order to provide a guide for interpretation of these patterns, in relation to classical dye visualization, an excerpt from the investigation of Yavuz et al[9] is given in Figure B1b. It shows near-surface patterns for a wing of similarly low sweep angle as in the present study. For purposes of comparison, reference lines are superposed on each image; they are coincident with the centerline of the dye-visualized vortex cores. These lines pass through the extrema of the surface-normal vorticity $\langle \omega \rangle$ contours, thereby indicating that patterns of $\langle \omega \rangle$ serve as a near-surface footprint of the leading-edge vortex. Patterns of $\langle \Psi \rangle$ show positive bifurcation lines BL^+, which represent lines of attachment, and according to the aforementioned reference lines the vortex cores lie outboard of the attachment lines. Again using reference lines as a guide, extrema of root-mean-square velocity fluctuation v_{rms}/U satisfy two conditions: they are located beneath the unsteady vortex core; and they are close to the attachment line, which represents the approximate location of reattachment of the shear layer emanating from the leading edge of the wing. In fact, Taylor and Gursul[7] and Elkhoury et al.[11], in investigations that observed the leading-edge vortex and its breakdown on wings of low sweep angle, related reattachment of the separated shear layer from the windward side of the wing to the wing surface and the relatively large magnitudes of near-surface fluctuations in the region of reattachment. The foregoing interrelationships can aid in interpretation of the images addressed herein, which show the consequence of trailing-edge blowing on the near-surface patterns.

3. FLOW STRUCTURE AND NEAR-SURFACE TOPOLOGY IN ABSENCE OF TRAILING-EDGE BLOWING: EFFECT OF ANGLE-OF-ATTACK

Figure B2 shows patterns of time-averaged velocity vectors $\langle V \rangle$ (left column) and streamlines $\langle \Psi \rangle$ (right column), in absence of trailing-edge blowing for angle-of-attack α = 5°, 8°, and 10°. At all values of α, the magnitude of $\langle V \rangle$ shows an abrupt decrease immediately downstream of the leading-edge. As the value of α increases from α = 5° to 10°, the spatial extent of the region of very low velocity increases. Furthermore, at α = 8°, the onset of a well-defined swirl pattern of velocity is evident in the region near the apex, and at α = 10°, this swirl pattern has a larger extent and is particularly well-defined. Within the central portion of each of these swirl patterns of α = 8° and 10°, the magnitudes of $\langle V \rangle$ are very small.

The corresponding patterns of streamline $\langle \Psi \rangle$ topology, shown in the right column of Figure B2, have well-defined features, which can be characterized in terms of critical points. At α = 5°, a negative bifurcation line BL^- extends over a substantial extent of the leading-edge. It corresponds to the merging of streamlines towards a single line, and represents a line of separation. In the vicinity of the apex, BL^- terminates in the node N_1, to which streamlines tend to converge. In the outboard region of the wing, a saddle point S_1 is evident; it represents the

apparent intersection of streamlines. Furthermore, a positive bifurcation line BL^+, which is a line from which streamlines tend to diverge, is evident; it represents a line of attachment. In addition, a well-defined focus F_1, which represents the center of an inward swirl pattern of streamlines, occurs immediately downstream of the tip of the wing. An additional saddle point S_2 is also apparent in this region.

At the higher angle-of-attack $\alpha = 8°$ in Figure B2, the node N_1 gives way to a large-scale focus F_2. It has been observed experimentally in surface skin friction visualization, near-surface streamlines and numerical simulations on a variety of planar surfaces, bodies and wings by Legendre[23], Perry and Hornung[24], Perry and Chong[25], Dallman and Schulte-Werning[26], Su, Liu, and Liu[27], Lazos[28], and Taylor and Gursul[7]. All of these investigations show an inward-spiraling surface streamline pattern that culminates in a stable focus. The relationship between this focus at the surface and the flow away from the surface, in particular the development of a three-dimensional vortical structure, has been quantitatively described by Perry and Hornung[24], Perry and Chong[25] and Dallman and Schulte-Werning[26]. Herein, existence of the focus F_2 will be taken as an indicator of three-dimensional separation, with the realization that the initial onset of separation may occur at, for example, a critical point located immediately upstream of the focus.

It is interesting to note that despite the onset of the aforementioned large-scale focus F_2, all of the other critical points, i.e., BL^-, S_1, BL^+, F_1 and S_2 are still identifiable. A further increase to $\alpha = 10°$ yields a still larger-scale inward-swirling pattern of streamlines, which culminates in the focus F_2; it is located further downstream that the F_2 at $\alpha = 8°$. Again, at $\alpha = 10°$, all other critical points are still detectable.

Figure B3 (left column) shows patterns of time-averaged, surface-normal vorticity $<\omega>$, whereby the orientation of positive vorticity is in the direction of the outward surface normal. Dashed and solid lines indicate respectively negative and positive values of $<\omega>$. Along the leading-edge of the wing, well-defined clusters of negative $<\omega>$ occur, due to a three-dimensional instability of the shear layer separating from the windward surface of the wing. Regarding the positive, elongated layer of vorticity at $\alpha = 5°$, its form is generally similar to that characterized by Yavuz et al.[9] for a wing of different, but low sweep angle. Corresponding dye visualization showed that this well-defined region of vorticity is the footprint of the leading-edge vortex, as represented in Figure B1b. At $\alpha = 8°$ and 10°, however, the elongated layer of vorticity moves dramatically closer to the plane of symmetry of the wing and becomes narrower in extent. These patterns suggest that the locus of the vortex emanating from the apex of the wing is close to the plane of symmetry of the wing. In fact, dye visualization (in absence of surface patterns) of Yaniktepe and Rockwell[8] show that, at sufficiently high angle-of-attack, the visualized vortex moves from a well-defined leading-edge vortex to a vortex close to the plane of symmetry of the wing.

Figure B3 (right column) provides contours of constant root-mean-square velocity transverse fluctuation v_{rms}/U as a function of angle-of –attack α. Consider first $\alpha = 5°$. The relation between the visualized leading-edge vortex, the v_{rms}/U contours, the surface-normal vorticity $<\omega>$ and the streamlines $<\Psi>$ on a wing of similarly low sweep angle is given in Figure B1b, based on images of Yavuz et al.[9] The type of v_{rms}/U contour distribution given at $\alpha = 5°$ in Figure B3 is coincident with the footprint of the leading edge vortex, which has undergone breakdown (Compare Figure B1b) and close to the line of attachment. At higher values of $\alpha = 8°$

and 10°, where the large-scale focus forms, the patterns of v_{rms}/U are dramatically broadened and, at the higher value of α = 10°, the peak values of v_{rms}/U are located closer to the trailing-edge than at α = 8°. These much broader patterns of v_{rms}/U occur in accord with the onset of the large-scale swirl pattern of streamlines and the focus F_2 shown in the right column of Figure B2.

Viewing together the patterns of Figures B2 and B3, onset of a large-scale, inward-spiral pattern culminating in the focus F_2 dramatically affects the topology between the positive and negative bifurcation lines BL^- and BL^+. Remarkably, however, other critical points on the planform and in its wake remain relatively unchanged. This major transformation of the near-surface topology is associated with similarly radical transformations of the pattern of $<\omega>$, which, at sufficiently low angle-of-attack, represents the footprint of the vortex, as well as patterns of near-surface velocity fluctuation v_{rms}/U.

4. NEAR SURFACE TOPOLOGY: EFFECT OF TRAILING-EDGE BLOWING

The near-surface flow patterns on the wing of low sweep angle, at angles-of- attack α = 5°, 8° and 10°, are shown in Figures B4 to B9 for a range of dimensionless blowing coefficient extending from C_μ = 0.006 to 1.63. This coefficient C_μ is defined in Section 2. Further values of C_μ were considered within the aforementioned range, in order to allow generalization of the observations.

4.1 PATTERNS BELOW CRITICAL ANGLE-OF-ATTACK

Figures B4 and B5 show patterns of streamline $<\Psi>$ topology, surface-normal vorticity $<\omega>$ and root-mean-square of near-surface velocity fluctuation v_{rms}/U at an angle-of-attack α = 5°, which, in accord with the reference patterns of Figures B2 and B3 lies below the critical angle-of-attack.

The patterns of $<\Psi>$ of Figure B4 show that, up to a value of C_μ = 0.025, the location and form of the nodal point N_1, the negative bifurcation line BL^-, the saddle point S_1, and the focal point F_1 remain relatively the same, in both location and form, as for the case of no blowing C_μ = 0. In the region bounded by the negative bifurcation line BL^- and the positive line BL^+, however, substantial changes in the form of the streamline pattern occurs, even for the lowest value of C_μ = 0.006.

At C_μ = 0.1, the overall pattern of $<\Psi>$ starts to undergo a fundamental change, and at C_μ = 0.4, it is fundamentally different. The node N_1 and the saddle point S_1 have disappeared in favor of a nodal point N_2, which is accompanied by movement of the saddle point S_2 to a location immediately upstream of the trailing-edge of the wing. It is therefore evident that, at sufficiently large C_μ, there is a reduction of the number of critical points along the leading-edge of the wing, and, simultaneously, movement of the saddle point S_2 from the wake region to a location on the surface of the wing.

A still further change of the pattern of $<\Psi>$ at relatively high values of C_μ is the decreasing distance between the negative bifurcation line BL^- along the leading-edge of the wing and the positive bifurcation line BL^+. At values of C_μ = 0.4 and 1.63, they nearly become

coincident. Simultaneously, the focus F_2, which is evident at a location close to the tip of the wing for lower values of C_μ, disappears at these higher values.

Figure B5 (left column) shows patterns of surface normal vorticity $<\omega>$ at two selected values of blowing coefficient in relation to the case of no blowing. At $C_\mu = 0$, a single, well-defined peak (extremum) of $<\omega>$ occurs near the apex, and for larger values of $C_\mu = 0.1$ and 0.4, multiple peaks occur over the entire elongated distribution of $<\omega>$. The onset of these multiple peaks corresponds to substantial changes of the patterns of instantaneous ω, not shown herein and thereby occurrence of substantial unsteadiness. A further feature of the elongated patterns of $<\omega>$ is that the angle of inclination of the pattern with respect to the plane of symmetry of the wing increases with increasing C_μ.

Figure B5 (right column) shows patterns of v_{rms}/U. At $C_\mu = 0.1$, peak values of v_{rms}/U are significantly larger and appear closer to the apex of the wing than the patterns at $C_\mu = 0$. Furthermore, at $C_\mu = 0.4$, even larger magnitudes of v_{rms}/U occur closer to the apex. As was the case for the patterns of $<\omega>$, the angle of inclination of the elongated pattern of v_{rms}/U with respect to the plane of symmetry of the wing increases with increasing C_μ.

The patterns of both $<\omega>$ and v_{rms}/U at $C_\mu = 0.1$ and 0.4 in Figure B5 can be directly compared with the corresponding patterns of streamline $<\Psi>$ topology in Figure B4. At these two values of C_μ, the positive bifurcation line BL^+ is in the process of transformation, whereby the line BL^+ present at $C_\mu = 0$ undergoes substantial broadening. This transformation of the $<\Psi>$ is therefore associated with enhanced unsteadiness and deflection of the pattern of v_{rms}/U, which is thereby consistent with deflection of the new line of reattachment, i.e., the new location of BL^+ away from the plane of symmetry of the wing.

4.2 PATTERNS ABOVE CRITICAL ANGLE-OF-ATTACK

The onset of a well-defined focus, and thereby a region of three-dimensional separation, occurs at an angle-of-attack above a critical value, as defined in the overview of Figure B2. Figure B6 shows the consequence of trailing-edge blowing in this regime for an angle-of-attack $\alpha = 8°$. For the reference case, $C_\mu = 0$, the topology indicates: negative and positive bifurcation lines BL^- and BL^+, which represent lines of separation and attachment; saddle points S_1 and S_2; and focal points F_1 and F_2.

Even for a very small value of blowing coefficient $C_\mu = 0.006$ in Figure B6, the location of the focus F_2 is displaced closer to the apex of the wing and, furthermore, detectable changes in the pattern of streamlines occurs in the region between the negative and positive bifurcation lines BL^- and BL^+. When $C_\mu = 0.025$, the focus F_2 moves even closer to the apex of the wing and, furthermore, a small-scale focus F_3 occurs. Remarkable is the fact that, while these topological changes are occurring at locations upstream of the trailing-edge of the wing for $C_\mu = 0.006$ and 0.025, the alteration of the patterns downstream of the trailing-edge is relatively insignificant. Furthermore, a secondary positive bifurcation line designated as $(BL^+)_2$, which is detectable at lower values of C_μ, becomes clearly evident near the tip of the wing in the image at $C_\mu = 0.025$, and at larger values of C_μ as well.

Increase of the blowing coefficient to a value of $C_\mu = 0.1$ in the series of Figure B6 has the striking effect of eradicating the focus F_2; that is, the occurrence of a large-scale swirl pattern of streamlines no longer exists; rather, it is replaced by the nodal point N_1. In this respect, the topology is very similar to the topology at the lower angle-of-attack $\alpha = 5°$ in absence of blowing, as indicated in Figure B4.

At still higher values of $C_\mu = 0.4$ and 1.63 in Figure B6, the transformation of the topology is similar to that occurring in Figure B4. More specifically, in Figure B6, at $C_\mu = 1.63$, the nodal point N_1 and the saddle point S_1 have disappeared in favor of the single nodal point N_2. Simultaneously, the positive bifurcation line $(BL^+)_2$ becomes more diffuse at $C_\mu = 1.63$. (The line $(BL^+)_2$ is designated at the tip of the wing at $C_\mu = 0.025$.)

Figure B7 (left column) shows patterns of surface normal vorticity $<\omega>$ at representative values of blowing coefficient C_μ. As it is increased to $C_\mu = 0.1$, then to 0.4, it is evident that the pattern of vorticity transforms to a well-defined, elongated form that is characteristic of the wing at lower angle-of-attack in absence of blowing (compare pattern of $<\omega>$ at $C_\mu = 0$ in Figure B3). This process corresponds to re-establishment of the well-defined leading-edge vortex; Yavuz et al.[9] have shown that the type of pattern of $<\omega>$ at $C_\mu = 0.4$ is the footprint of the dye vortex visualized above the wing at sufficiently low angle-of-attack. Direct comparison of patterns of $<\omega>$ at $C_\mu = 0.1$ and 0.4 with the corresponding patterns of $<\Psi>$ in Figure B6 shows that they correspond to disappearance of the focus F_2 associated with large-scale separation.

Figure B7 (right column) shows the patterns of v_{rms}/U. These near-surface patterns, which are an indication of the buffet loading, undergo a transformation in accord with the aforementioned patterns of $<\omega>$ and $<\Psi>$. At $C_\mu = 0$, where large-scale separation exists over the surface of the wing, the pattern of v_{rms}/U is broadly distributed. In the presence of blowing at $C_\mu = 0.1$, the pattern of v_{rms}/U starts to take on an elongated form, and the peak values become somewhat larger. In fact, even for lower values of $C_\mu = 0.006$ and 0.025 (not shown), significant upstream movement of the peak values of v_{rms}/U is evident. At $C_\mu = 0.4$, the pattern of v_{rms}/U is sharply defined and relatively narrow. Furthermore, the peak values have increased substantially. Thus, we have the remarkable observation that eradication of separation over a substantial portion of the wing surface via trailing-edge blowing, which is associated with re-establishment of a well-defined leading-edge vortex, actually results in higher near-surface fluctuation amplitudes over a narrowly defined region. In fact, these regions of high fluctuation are close to the primary (positive) bifurcation line BL^+, i.e., the attachment line.

At a higher angle-of-attack, as shown in Figure B8, the patterns of streamline $<\Psi>$ topology undergo a generally similar transformation during increases of C_μ as for the angle-of-attack $\alpha = 8°$. The disappearance of the focus F_2 at a sufficiently high value of $C_\mu = 0.4$ is the predominant change. It appears that a higher value of $C_\mu = 0.4$ is required to eradicate the focus F_2 involving three-dimensional separation, relative to the case of the lower angle-of-attack $\alpha = 8°$; as shown in Figure B6, the focus F_2 could be eradicated at $C_\mu = 0.1$. Note also that a small-scale focus at F_3 appears at $C_\mu = 0.1$. This type of focus was also evident at $\alpha = 8°$, but at a substantially lower value of blowing coefficient $C_\mu = 0.025$, as indicated in Figure B6.

Furthermore, Figure B9 shows patterns of $<\omega>$ and v_{rms}/U, which follow a generally similar trend as at $\alpha = 8°$ in Figure B7. The pattern of $<\omega>$ transforms, at a sufficiently high value of $C_\mu = 0.4$, to a general form characteristic of a footprint of a well-defined leading-edge vortex. The patterns of v_{rms}/U are generally similar at $C_\mu = 0$, but the peak value is close to the trailing-edge at $\alpha = 10°$ in Figure B9, relative to peak values occurring upstream of the trailing-edge at $\alpha = 8°$ in Figure B7. Furthermore, at $\alpha = 10°$, the pattern of v_{rms}/U remains relatively broadly distributed, whereas at $\alpha = 8°$, $C_\mu = 0.1$ in Figure B7, it has already taken the general form of an elongated distribution. At $C_\mu = 0.4$, $\alpha = 10°$ in Figure B9, the pattern of v_{rms}/U has a very well-defined elongated form with high fluctuation level, very similar to that of the same value of C_μ at $\alpha = 8°$ shown in Figure B7.

Viewing together the near-surface patterns above the critical angle-of-attack, i.e., at $\alpha = 8°$ and 10°, shown in Figures B6 through B9, the transformations of the near-surface topology with increasing values of blowing coefficient C_μ are remarkably similar. Larger values of C_μ are required, however, to induce the topological change at the higher $\alpha = 10°$, relative to $\alpha = 8°$. Nevertheless, the remarkable similarities of the transformed patterns indicate that they are robust, which is further evident by examining the types and locations of the critical points of the topology. In other words, despite the fact that the patterns at $\alpha = 10°$ are less sensitive to this trailing-edge control technique, the topology follows the same sequence of alterations, or transformations, as at lower angle-of-attack at $\alpha = 8°$. Similar statements can be made for the patterns of surface normal vorticity $<\omega>$ and near-surface velocity fluctuation v_{rms}/U; that is, similar types of transformations are evident with increasing C_μ.

5. NEAR-SURFACE PATTERNS: COMPARISON OF DUAL AND SINGLE TRAILING-EDGE BLOWING

In order to determine the sensitivity of the near-surface patterns to location of the blowing slot, the case of a single jet aligned with the plane of symmetry of the wing is compared with the dual jet, which has been the focus of the preceding sections. Figure B10 provides this comparison for two values of blowing coefficient: $C_\mu = 0.1$ and 1.63. For the case of the single jet, at $C_\mu = 0.1$, the pattern of streamline $<\Psi>$ topology is essentially the same as that in absence of blowing (compare Figure B2), except that the location of the focus F_2 is shifted slightly upstream and secondary positive bifurcation line $(BL^+)_2$ becomes apparent. On the other hand, for the case of the dual jet at $C_\mu = 0.1$, the pattern of surface topology is fundamentally transformed; that is, the focus F_2 and thereby the region of large-scale separation are eradicated, as demonstrated in Figure B6.

If the magnitude of the blowing coefficient is increased to a relatively high value of $C_\mu = 1.63$ for the case of the single jet, however, the pattern of $<\Psi>$ is as indicated in Figure B10; that is, the focus F_2 and secondary positive bifurcation line $(BL^+)_2$ are now eradicated. Furthermore, aside from the negative and positive bifurcation lines BL^- and BL^+, no other critical features exist along the surface of the wing. All the critical points on the surface of the wing are eradicated. On the other hand, for the case of the dual jet with blowing at $C_\mu = 1.63$, a node N_2 and a saddle point S_2 remain on the wing surface, in addition to the negative and positive bifurcation lines, BL^- and BL^+. In addition, for this case, secondary positive bifurcation line $(BL^+)_2$ remains and has become diffuse. Thus, remarkably, the single jet yields a much simplified $<\Psi>$ topology

relative to the case of the dual jet at a relatively high value of blowing coefficient C_μ . Furthermore, for the case of the dual jet, the bifurcation line BL^+ is relatively diffused, relative to the well-defined line BL^+ for the case of single jet at $C_\mu = 1.63$; in this case, it persists in a well-defined fashion to the trailing-edge of the wing.

Figure B11 shows contours of constant v_{rms}/U, which correspond to the $<\Psi>$ topology patterns of Figure B10. At the low value of blowing coefficient $C_\mu = 0.1$, the pattern of v_{rms}/U for the single jet is relatively broadly distributed and has low peak values; this observation is in accord with the existence of the focus F_2 shown in Figure B10, and thereby occurrence of three-dimensional separation. On the other hand, for the case of the dual jet at $C_\mu = 0.1$, the peak values of fluctuation are significantly larger, and the overall pattern of v_{rms}/U tends to take an elongated form. This higher level and more ordered form are associated with eradication of the focus F_2 and thereby the region of large-scale separation, designated in Figure B10. At larger values of blowing coefficient $C_\mu = 1.63$, both the single jet and dual jet yield relatively elongated and ordered patterns of v_{rms}/U, but significantly higher values occur for the dual jet. Taking an overview of all of the patterns in Figure B11, it appears that the single jet tends to induce lower values of near-surface velocity fluctuation v_{rms}/U, relative to the dual jet.

6. CONCLUDING REMARKS

The near-surface patterns on a delta wing at low sweep angle have been investigated as a function of both angle-of-attack, and magnitude of localized blowing from slots at the trailing-edge. Patterns of streamline topology, involving several classes of critical points, surface-normal vorticity and root-mean-square velocity fluctuations allow quantitative representations of the sensitivity of the patterns to magnitude of the blowing coefficient. The principal findings are as follows:

1. For the reference case of no blowing from the trailing-edge, there exists a critical value of angle-of-attack, above which large-scale, three-dimensional surface separation occurs. It is defined by a stable focus, i.e., center of an inward-spiraling pattern located immediately downstream of the apex of the wing. When this regime occurs, the pattern of near-surface velocity fluctuation has a substantially larger spatial extent, with peak amplitudes that are shifted towards the trailing-edge of the wing.

2. At an angle-of-attack lower than the critical value, application of trailing-edge blowing, even at a very small magnitude, can significantly alter the topological pattern between the lines of separation and attachment. When the magnitude of the blowing coefficient is sufficiently large, the nature and location of the critical points of the near-surface streamline topology are fundamentally altered, both along the surface of the wing and in its near-wake.

3. Above the critical angle-of-attack, the major consequence of trailing-edge blowing is to move the focus of the inward-spiraling streamline pattern, which represents the locus of three-dimensional separation, towards the apex of the wing, and when the value of the blowing coefficient reaches a critical value, this focus is entirely eliminated. This change in near-surface topology is accompanied by recovery of patterns of surface-normal vorticity and root-mean-square near-surface velocity fluctuations that are characteristic of a well-defined vortex above the surface of the wing. That is, the patterns of root-mean-square velocity fluctuation transform from broadly distributed, lower level contours to highly concentrated,

relatively high level contours of fluctuation magnitude. The consequence of trailing-edge blowing is therefore to transform the patterns to forms very similar to those at lower angle of attack in absence of trailing-edge blowing.

4. When the angle-of-attack is significantly higher than the critical value, the near-surface patterns are generally less sensitive to trailing-edge blowing. Nevertheless, the transformation between successive states of near-surface streamline topology, surface-normal vorticity and root-mean-square velocity fluctuation follow the same sequence and form as for lower angle-of-attack; larger values of blowing coefficient are, however, required to induce these states of the flow.

5. Comparison of blowing from a single slot centered at the plane of symmetry of the wing, with the foregoing cases of dual blowing indicates that, at lower values of blowing coefficient, the dual blowing configuration induces radical changes in the near-surface pattern, whereas the single jet induces almost no change. On the other hand, when the blowing coefficient becomes sufficiently large, the single blowing jet is remarkable effective, and it minimizes the number of critical features occurring on the surface of the wing, relative to the case of dual jet blowing.

7. ACKNOWLEDGMENTS

The support of the Air Force Office of Scientific Research under Grant Number F49620-02-1-0061 is gratefully acknowledged. This AFOSR program was monitored by Dr. John Schmisseur.

REFERENCES

[1]Ol, M. V., and Gharib, M. "The Passage Towards Stall of Nonslender Delta Wings at Low Reynolds Number", AIAA Paper 2001-2843, June, 2001.

[2]Ol, M. V. and Gharib, M. "Leading-Edge Vortex Structure of Nonslender Delta Wings at Low Reynolds Number", *AIAA Journal*, Vol. 41, No. 1, 2003, pp. 16-26

[3]Honkan, A. and Andreopoulos, J., "Instantaneous Three-Dimensional Vorticity Measurements in Vortical Flow over a Delta Wing," *AIAA Journal*, Vol. 35, No. 10, October, 1997, pp. 1612-1620.

[4]Miau, J. J., Kuo, K. T., Liu, W H., Hsieh, S. J., Chou, J. H., and Lin, C. L., "Flow Developments Above 50-Deg Sweep Delta Wings with Different Leading-Edge Profiles," *Journal of Aircraft*, Vol. 32, No. 4, 1995, pp. 787-794.

[5]Gordnier, R. E. and Visbal, M. R. 2003 "Higher-Order Compact Difference Scheme Applied to the Simulation of a Low Sweep Delta Wing Flow", AIAA Paper 2003-0620, 41st AIAA Aerospace Sciences Meeting and Exhibit, Reno, NV, January 2003.

[6]Taylor, G.S., Schnorbus, T., and Gursul, I., "An Investigation of Vortex Flows over Low Sweep Delta Wings", AIAA-2003-4021, AIAA Fluid Dynamics Conference, 23-26 June, Orlando, FL.

[7]Taylor, G.S. and Gursul, I. "Unsteady Vortex Flows and Buffeting of a Low Sweep Delta Wing", AIAA-2004-1066, 42nd AIAA Aerospace Sciences Meeting and Exhibit, Reno, NV, January, 2004.

[8]Yaniktepe, B. and Rockwell, D., "Flow Structure on a Delta Wing of Low Sweep Angle", AIAA Journal, Vol. 42, No.3, March, 2004, pp.513-523

[9]Yavuz, M. M., Elkhoury, M. and Rockwell, D., 2004 "Near-Surface Topology and Flow Structure on a Delta Wing", *AIAA Journal*, Vol. 42, No. 2, February, 2004, pp.332-340.

[10]Elkhoury, M. and Rockwell, D., 2003 "Visualized Vortices on Unmanned Combat Air Vehicle Planform: Effect of Reynolds Number", *AIAA Journal of Aircraft,* Vol.41, No.5, Sept-Oct, 2004, pp.1244-1247.

[11]Elkhoury, M., Yavuz, M.M and Rockwell, D., 2004, "Near-Surface Topology of a UCAV Planform: Reynolds Number Dependence", *AIAA Journal of Aircraft*, Vol. 42, No. 5, September/October, pp. 1318-1330.

[12]Wood, N. J., Roberts, L., and Celik, Z., "Control of Asymmetric Vortical Flow over Delta Wings at High Angles of Attack", *Journal of Aircraft*, Vol. 27, No.5, May 1990, pp.429-435.

[13]McCormick, S and Gursul, I., "Effect of Shear Layer Control on Leading Edge Vortices", *Journal of Aircraft*, Vol. 33, No. 6, November-December 1996, pp.1087-1093.

[14]Gu, W., Robinson, O., and Rockwell, D., "Control of Vortices on a Delta Wing by Leading-Edge Injection", *AIAA Journal*, Vol. 31, No.7, July 1993, pp.1177-1186.

[15]Vorobieff, P. and Rockwell, D., "Vortex Breakdown on Pitching Delta Wing: Control by Intermittent Trailing Edge Blowing", *AIAA Journal*, Vol. 36, No. 4, 1998, pp. 585-589.

[16]Parmenter, K. and Rockwell, D., "Transient Response of Leading Edge Vortices to Localized Suction". *AIAA Journal*, Vol.28, No.6, June, 1990, pp. 1131-1133.

[17]Johari, H., Olinger, D.J. and Fitzpatrick, K.C., "Delta Wing Vortex Control via Recessed Angled Spanwise Blowing", *AIAA Journal of Aircraft*, Vol. 32, No. 4, 1995, pp.804-810

[18]Helin, H. E. and Warty, C. W. "Effects of Trailing Edge Entrainment on Delta Wing Vortices", *AIAA Journal*, Vol. 32, 1994, pp. 802-804.

[19]Shih, C. and Ding, Z., "Trailing Edge Jet Control of Leading Edge Vortices of a Delta Wing", *AIAA Journal*, Vol. 34, No. 7, 1996, pp. 1447-1457.

[20]Mitchell, A.M., Molton, P., Barberis, D., and Delery, J., "Control of Leading Edge Vortex Breakdown by Trailing Edge Injection", AIAA Paper 99-3202, 1999.

[21]Phillips, S., Lambert, C., and Gursul, I., "Effect of a Trailing-Edge Jet on Fin Buffeting", *AIAA Journal of Aircraft*, Vol. 40, No.3, pp. 590 – 599, 2003

[22]Wang, J. J., Li, Q. S. and Liu, J. Y. "Effects of Vectored Trailing Edge Jet on Delta Wing Vortex Breakdown", *Experiments in Fluids*, Vol. 34, 2003, pp. 651-654

[23]Legendre, R. "Lignes de Courent d'un Ēcoulement Continu", *Rech. Aērosp.* 1965, No. 105, pp. 3-9.

[24]Perry, A. E. and Hornung, H. G. 1984 "Some Aspects of Three-Dimensional Separation. Part II. Vortex Skeletons", *Z.Flugwiss.Weltraumforsch.* 8, pp. 155-160.

[25]Perry, A. E. and Chong, M. S. "A Description of Eddying Motions and Flow Patterns Using Critical-Point Concepts", *Annual Review of Fluid Mechanics*, 1987, Vol. 19, pp. 125-155.

[26]Dallman, U. and Schulte-Werning, B. "Topological Changes of Axisymmetric and Non-Axisymmetric Vortex Flows" *Proceedings of the IUTAM Symposium*, Cambridge, 1990, pp. 372-383.

[27]Su, W., Liu, M., and Liu, Z., "Topological Structures of Separated Flows About a Series of Sharp-Edged Delta Wings at Angles-of-Attack up to 90°," in *Topological Fluid Mechanics, Proceedings of the IUTAM Symposium*, Cambridge, 1990, pp. 395-407.

[28]Lazos, B. "Surface Topology on the Wheels of a Generic Four-Wheel Landing Gear," *AIAA Journal,* Vol. 40, No. 12, 2002, pp. 2402-2412.

LIST OF FIGURES

Figure B1a: Overview of experimental setup including delta wing and laser sheet orientation.

Figure B1b: Direct comparison of patterns of dye visualization, near-surface vorticity $<\omega>$, root-mean-square of transverse velocity fluctuation v_{rms}/U, and streamline topology $<\Psi>$ from Yavuz et al[9]. Sweep angle Λ=38.7°, angle-of-attack α = 10°, and Reynolds number Re=10,000.

Figure B2: Near-surface flow patterns of time-averaged velocity $<V>$ and streamlines $<\Psi>$ on wings at different angle-of-attacks α = 5°, 8° and 10°.

Figure B3: Patterns of time-averaged vorticity $<\omega>$ oriented in a direction normal to the surface of the wing and root-mean-square of transverse velocity fluctuation v_{rms}/U on wings at different angles-of-attack α = 5°, 8° and 10°. ($[|<\omega>|]_{min}$ = 2 sec^{-1}, $\Delta[|<\omega>|]$ = 2 sec^{-1}, $[v_{rms}/U]_{min}$ = 0.05, $\Delta[v_{rms}/U]$ = 0.01)

Figure B4: Comparison of near-surface patterns of time-averaged streamlines $<\Psi>$ for dual blowing cases for momentum coefficients C_μ= 0, 0.006, 0.025, 0.1, 0.4, and 1.63 on a wing at angle-of-attack α = 5°. $C_\mu = (V_j^2 * A_j)/(U^2 * A_s)$, in which V_j is the mean velocity of blowing at the trailing edge, A_j is the total area of both blowing slots at the trailing edge, A_s is the surface area of the planform, and U is the freestream velocity.

Figure B5: Comparison of vorticity $<\omega>$ oriented in a direction normal to the surface of the wing and root-mean-square of transverse velocity fluctuation v_{rms}/U for dual-location blowing

cases for momentum coefficients $C_\mu = 0$, 0.1, and 0.4 on a wing at angle-of-attack α = 5°. $C_\mu = (V_j^2 * A_j)/(U^2 * A_s)$, in which V_j is the mean velocity of blowing at the trailing edge, A_j is the total area of both blowing slots at the trailing edge, A_s is the surface area of the planform, and U is the freestream velocity.($[|<\omega>|]_{min} = 2$ sec^{-1}, $\Delta[|<\omega>|] = 2$ sec^{-1}, $[v_{rms}/U]_{min} = 0.05$, $\Delta[v_{rms}/U] = 0.02$)

Figure B6: Comparison of near-surface patterns of time-averaged streamlines $<\Psi>$ for dual blowing cases for momentum coefficients $C_\mu = 0$, 0.006, 0.025, 0.1, 0.4, and 1.63 on a wing at angle-of-attack $\alpha = 8°$. $C_\mu = (V_j^2 * A_j)/(U^2 * A_s)$, in which V_j is the mean velocity of blowing at the trailing edge, A_j is the total area of both blowing slots at the trailing edge, A_s is the surface area of the planform, and U is the freestream velocity.

Figure B7: Comparison of vorticity $<\omega>$ oriented in a direction normal to the surface of the wing and root-mean-square of transverse velocity fluctuation v_{rms}/U for dual-location blowing cases for momentum coefficients $C_\mu = 0$, 0.1, and 0.4 on a wing at angle-of-attack α = 8°. $C_\mu = (V_j^2 * A_j)/(U^2 * A_s)$,, in which V_j is the mean velocity of blowing at the trailing edge, A_j is the total area of both blowing slots at the trailing edge, A_s is the surface area of the planform, and U is the freestream velocity.($[|<\omega>|]_{min} = 2$ sec^{-1}, $\Delta[|<\omega>|] = 2$ sec^{-1}, $[v_{rms}/U]_{min} = 0.05$, $\Delta[v_{rms}/U] = 0.02$)

Figure B8: Comparison of near-surface patterns of time-averaged streamlines $<\Psi>$ for dual blowing cases for momentum coefficients $C_\mu = 0$, 0.006, 0.025, 0.1, 0.4, and 1.63 on a wing at angle-of-attack α = 10°. $C_\mu = (V_j^2 * A_j)/(U^2 * A_s)$, in which V_j is the mean velocity of blowing at the trailing edge, A_j is the total area of both blowing slots at the trailing edge, A_s is the surface area of the planform, and U is the freestream velocity.

Figure B9: Comparison of vorticity $<\omega>$ oriented in a direction normal to the surface of the wing and root-mean-square of transverse velocity fluctuation v_{rms}/U for dual-location blowing cases for momentum coefficients $C_\mu = 0$, 0.1, and 0.4 on a wing at angle-of-attack α = 10°. $C_\mu = (V_j^2 * A_j)/(U^2 * A_s)$, in which V_j is the mean velocity of blowing at the trailing edge, A_j is the total area of both blowing slots at the trailing edge, A_s is the surface area of the planform, and U is the freestream velocity.($[|<\omega>|]_{min} = 2$ sec^{-1}, $\Delta[|<\omega>|] = 2$ sec^{-1}, $[v_{rms}/U]_{min} = 0.05$, $\Delta[v_{rms}/U] = 0.02$)

Figure B10: Comparison of near-surface patterns of time-averaged streamlines $<\Psi>$ for single blowing and dual blowing cases for momentum coefficients $C_\mu = 0.1$ and 1.63 on a wing at angle-of-attack α = 8°. $C_\mu = (V_j^2 * A_j)/(U^2 * A_s)$, in which V_j is the mean velocity of blowing at the trailing edge, A_j is the total area of both blowing slots at the trailing edge, A_s is the surface area of the planform, and U is the freestream velocity.

Figure B11: Comparison of root-mean-square of transverse velocity fluctuation v_{rms}/U for single blowing and dual blowing cases for momentum coefficients $C_\mu = 0.1$ and 1.63 on a wing at angle-of-attack α = 8°. $C_\mu = (V_j^2 * A_j)/(U^2 * A_s)$, in which V_j is the mean velocity of blowing at the trailing edge, A_j is the total area of both blowing slots at the trailing edge, A_s is the surface area of the planform, and U is the freestream velocity. ($[v_{rms}/U]_{min} = 0.05$, $\Delta[v_{rms}/U] = 0.02$)

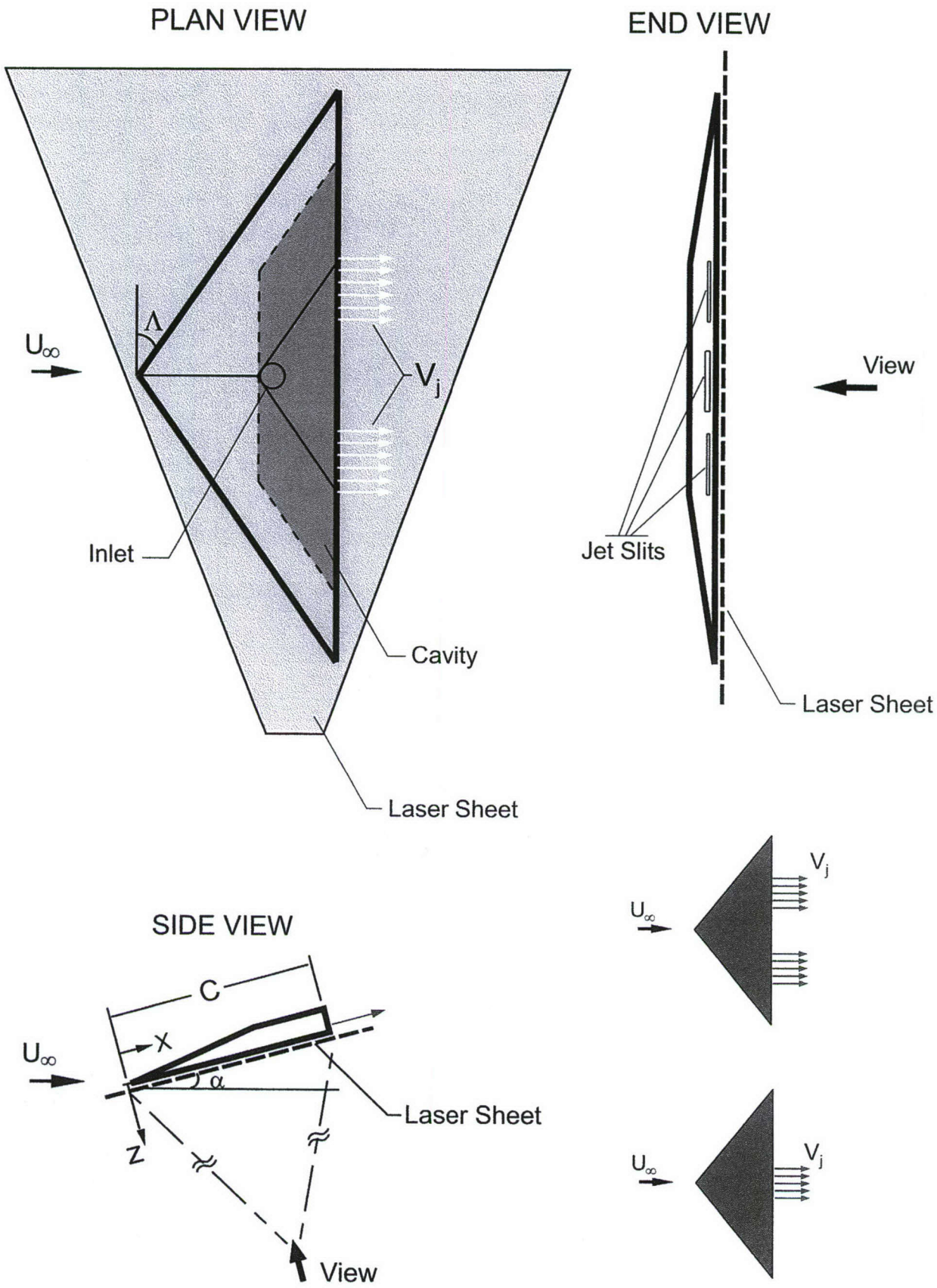


Figure B1a: Overview of experimental setup including delta wing and laser sheet orientation.

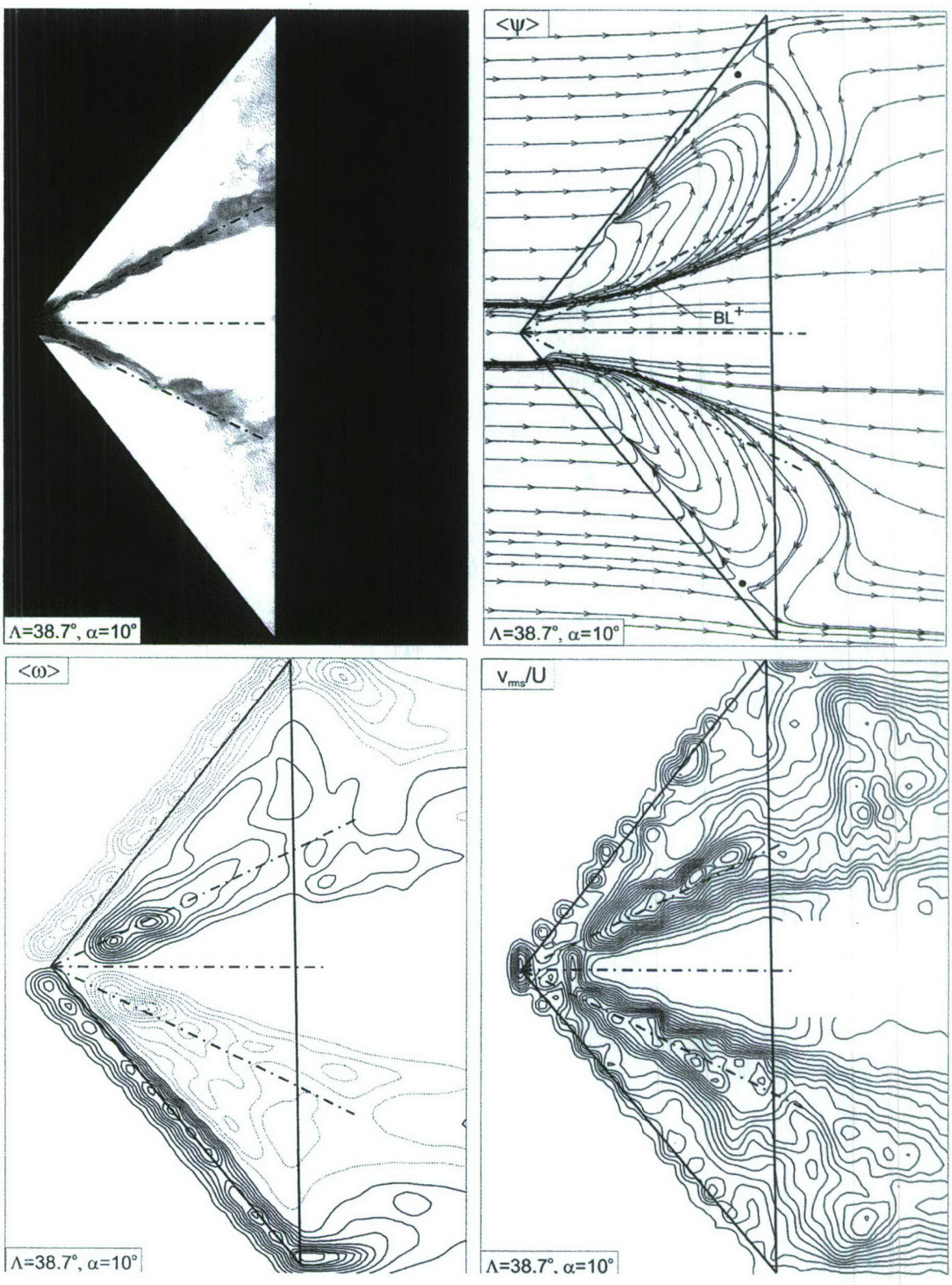


Figure B1b: Direct comparison of patterns of dye visualization, near-surface vorticity $\langle\omega\rangle$, root-mean-square of transverse velocity fluctuation v_{rms}/U, and streamline topology $\langle\Psi\rangle$ from Yavuz et al[9]. Sweep angle $\Lambda = 38.7°$, angle-of-attack $\alpha = 10°$, and Reynolds number Re=10,000.

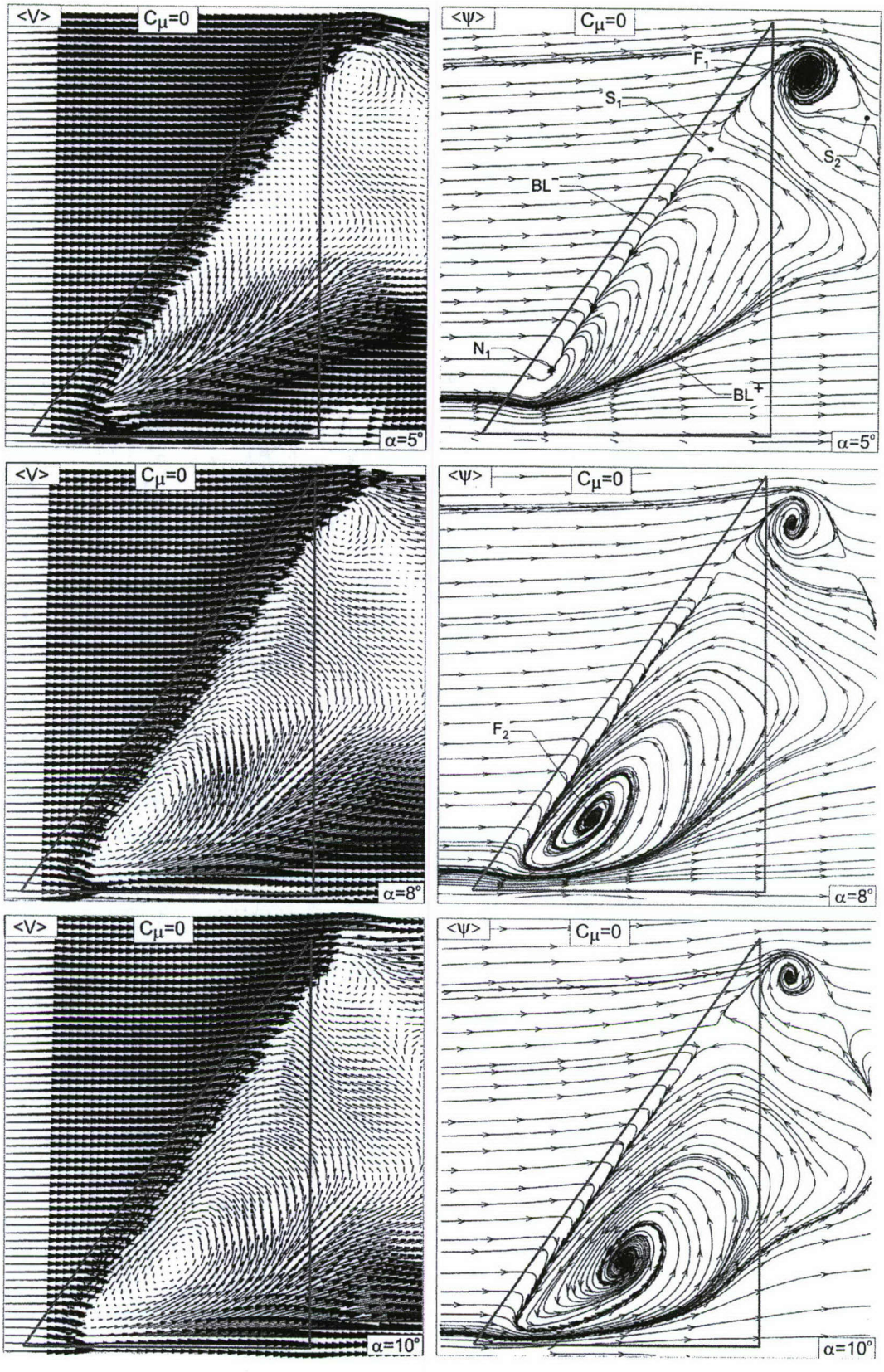


Figure B2: Near-surface flow patterns of time-averaged velocity <*V*> and streamlines <*Ψ*> on wings at different angle-of-attacks $\alpha = 5°$, 8° and 10°.

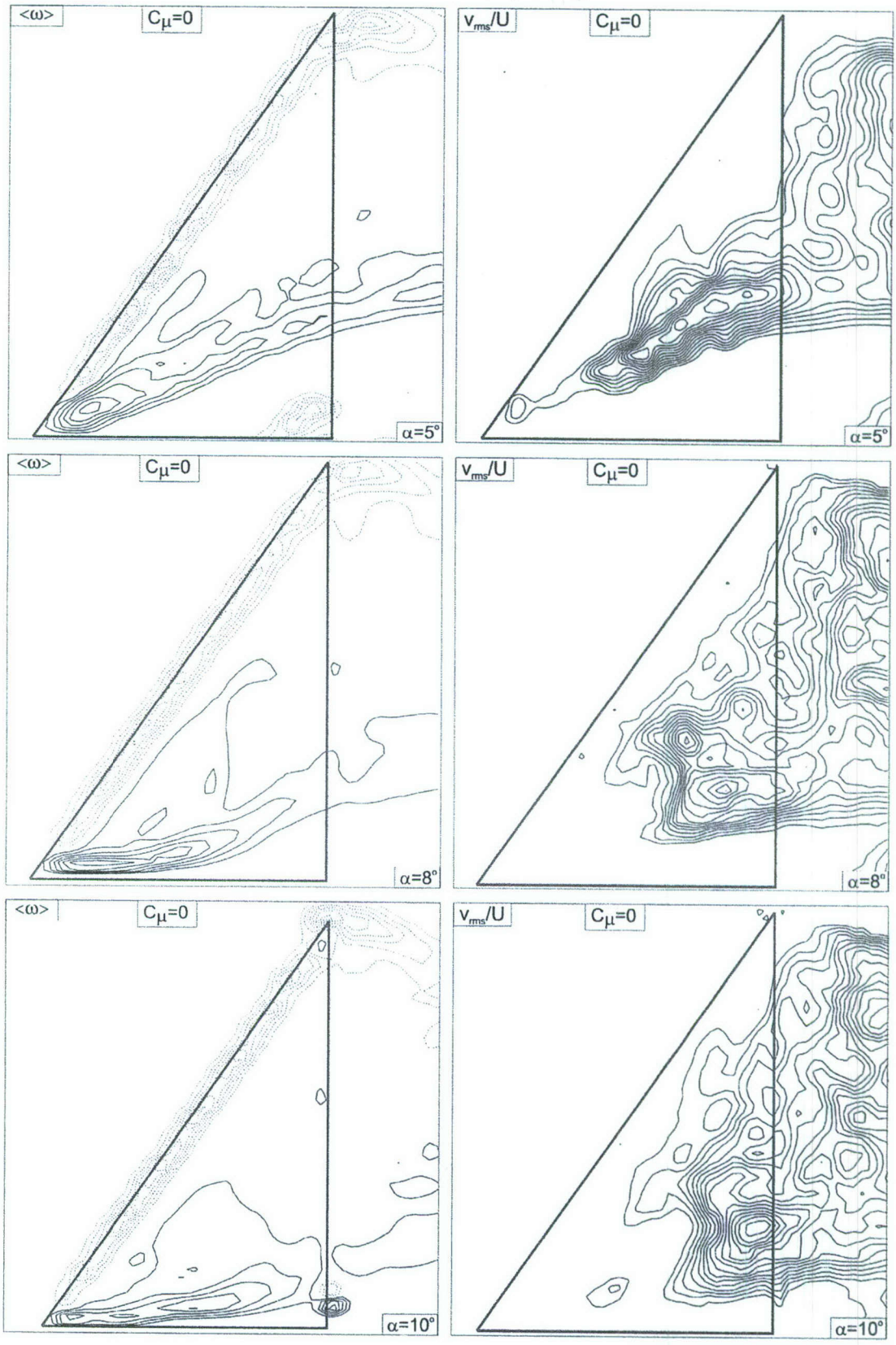


Figure B3: Patterns of time-averaged vorticity $<\omega>$ oriented in a direction normal to the surface of the wing and root-mean-square of transverse velocity fluctuation v_{rms}/U on wings at different angles-of-attack $\alpha = 5°$, 8° and 10°. .($[|<\omega>|]_{min} = 2$ sec^{-1}, $\Delta[|<\omega>|] = 2$ sec^{-1}, $[v_{rms}/U]_{min} = 0.05$, $\Delta[v_{rms}/U] = 0.01$)

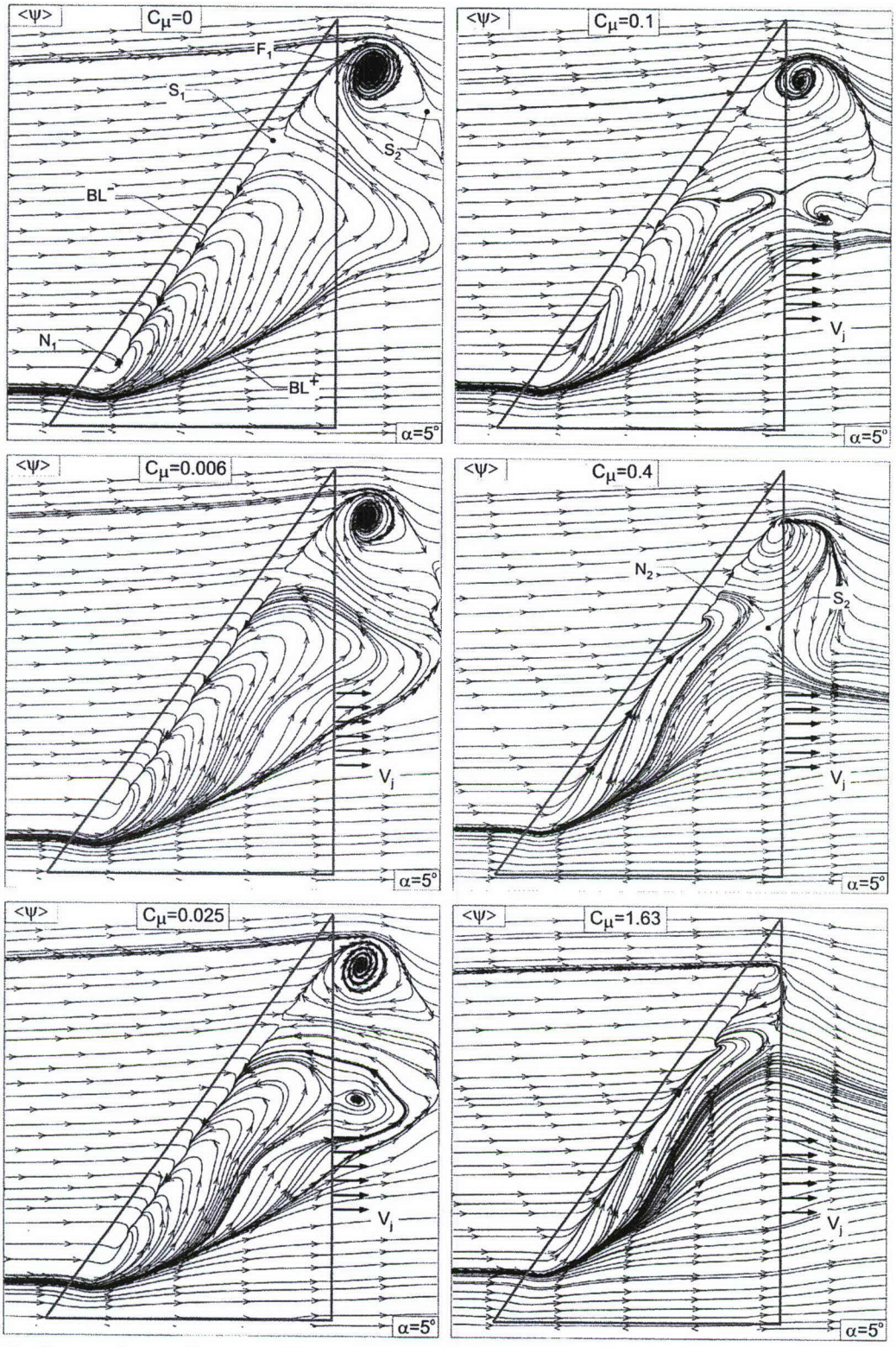


Figure B4: Comparison of near-surface patterns of time-averaged streamlines $\langle\Psi\rangle$ for dual blowing cases for momentum coefficients $C_\mu = 0$, 0.006, 0.025, 0.1, 0.4, and 1.63 on a wing at angle-of-attack $\alpha = 5°$. $C_\mu = (V_j^2 * A_j)/(U^2 * A_s)$, in which V_j is the mean velocity of blowing at the trailing edge, A_j is the total area of both blowing slots at the trailing edge, A_s is the surface area of the planform, and U is the freestream velocity.

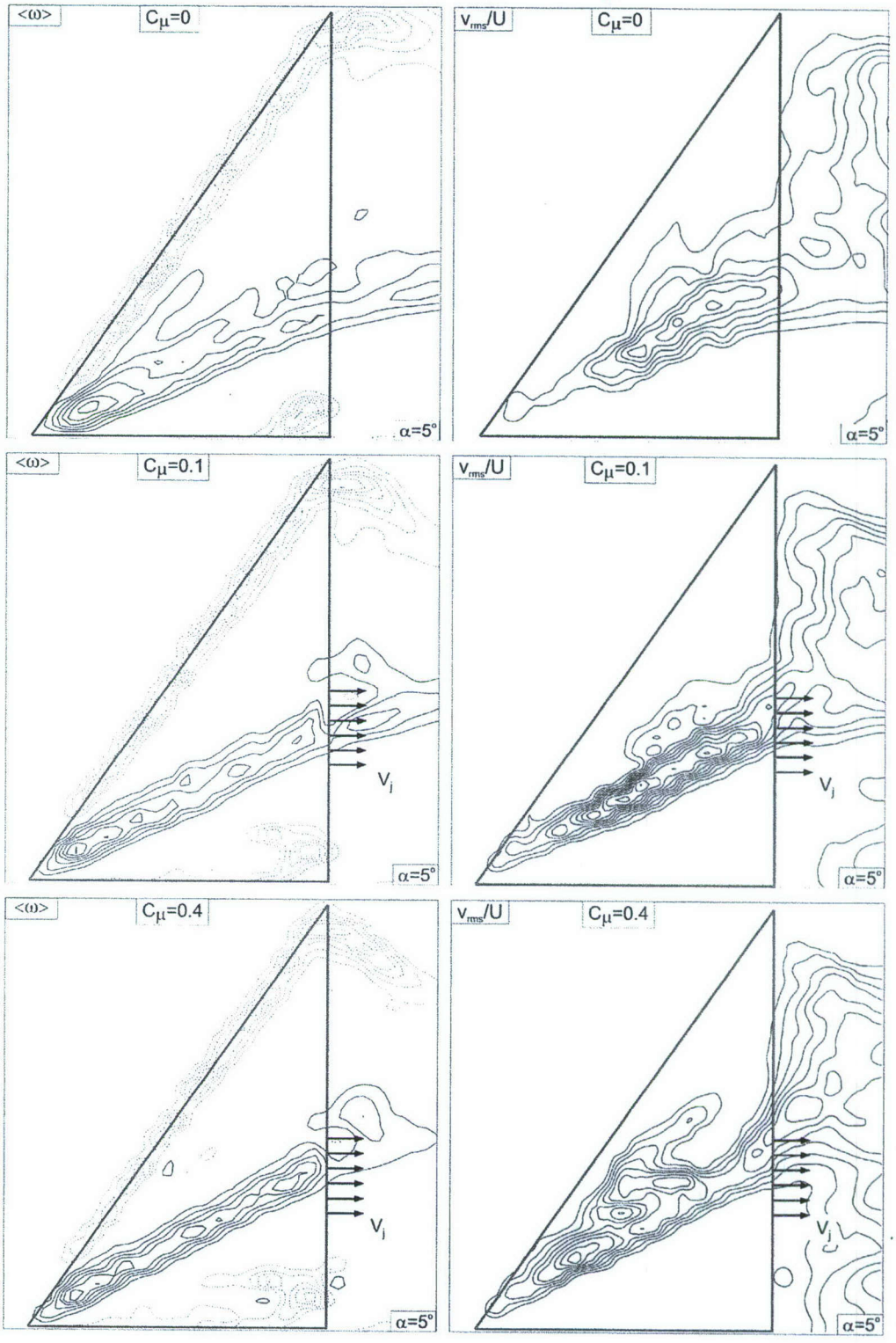


Figure B5: Comparison of vorticity $<\omega>$ oriented in a direction normal to the surface of the wing and root-mean-square of transverse velocity fluctuation v_{rms}/U for dual-location blowing cases for momentum coefficients $C_\mu = 0$, 0.1, and 0.4 on a wing at angle-of-attack $\alpha = 5°$. $C_\mu = (V_j^2 * A_j)/(U^2 * A_s)$, in which V_j is the mean velocity of blowing at the trailing edge, A_j is the total area of both blowing slots at the trailing edge, A_s is the surface area of the planform, and U is the freestream velocity.($[|<\omega>|]_{min} = 2$ sec^{-1}, $\Delta[|<\omega>|] = 2$ sec^{-1}, $[v_{rms}/U]_{min} = 0.05$, $\Delta[v_{rms}/U] = 0.02$)

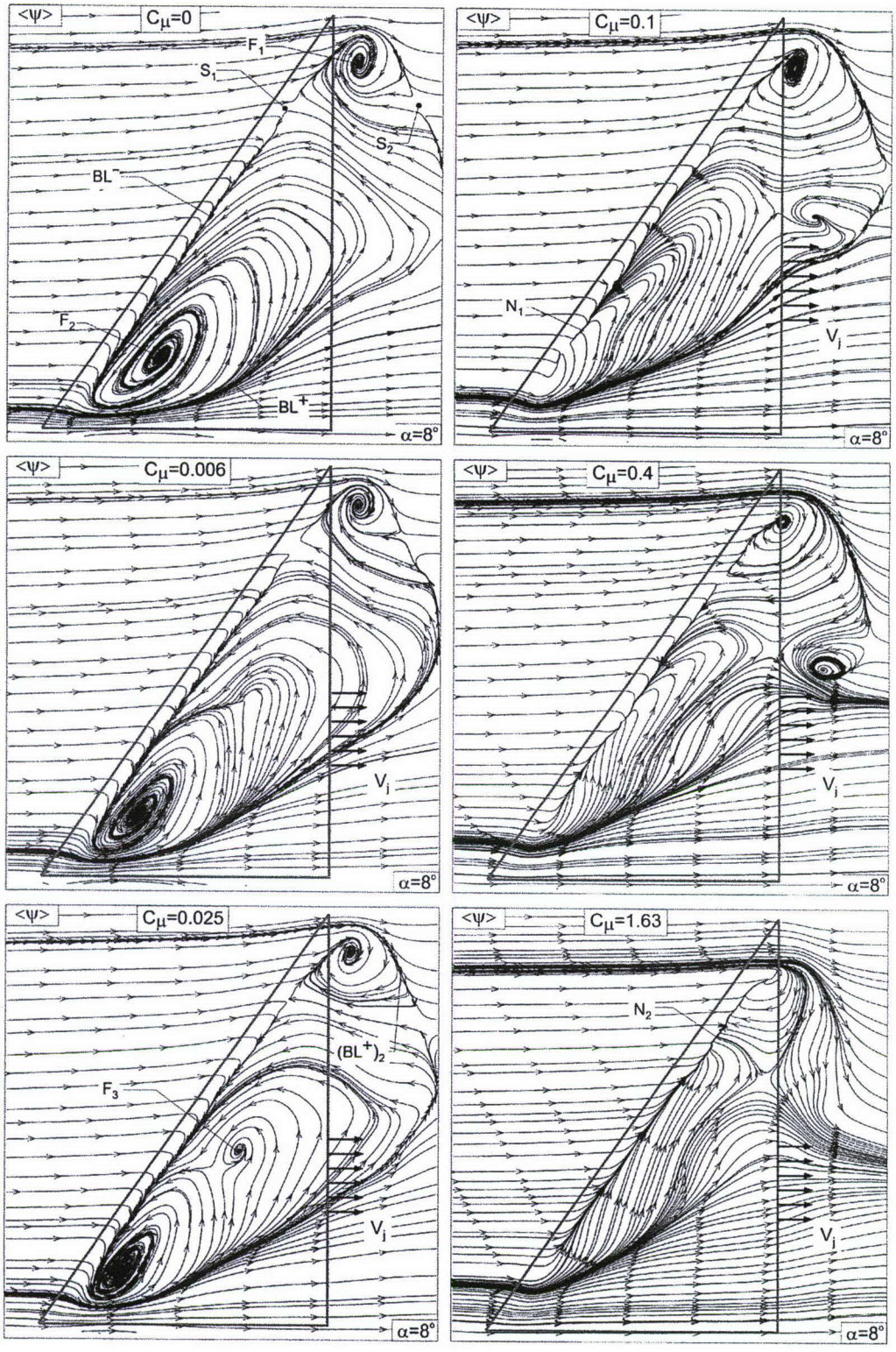


Figure B6: Comparison of near-surface patterns of time-averaged streamlines $<\Psi>$ for dual blowing cases for momentum coefficients $C_\mu = 0$, 0.006, 0.025, 0.1, 0.4, and 1.63 on a wing at angle-of-attack $\alpha = 8°$. $C_\mu = (V_j^2 * A_j)/(U^2 * A_s)$, in which V_j is the mean velocity of blowing at the trailing edge, A_j is the total area of both blowing slots at the trailing edge, A_s is the surface area of the planform, and U is the freestream velocity.

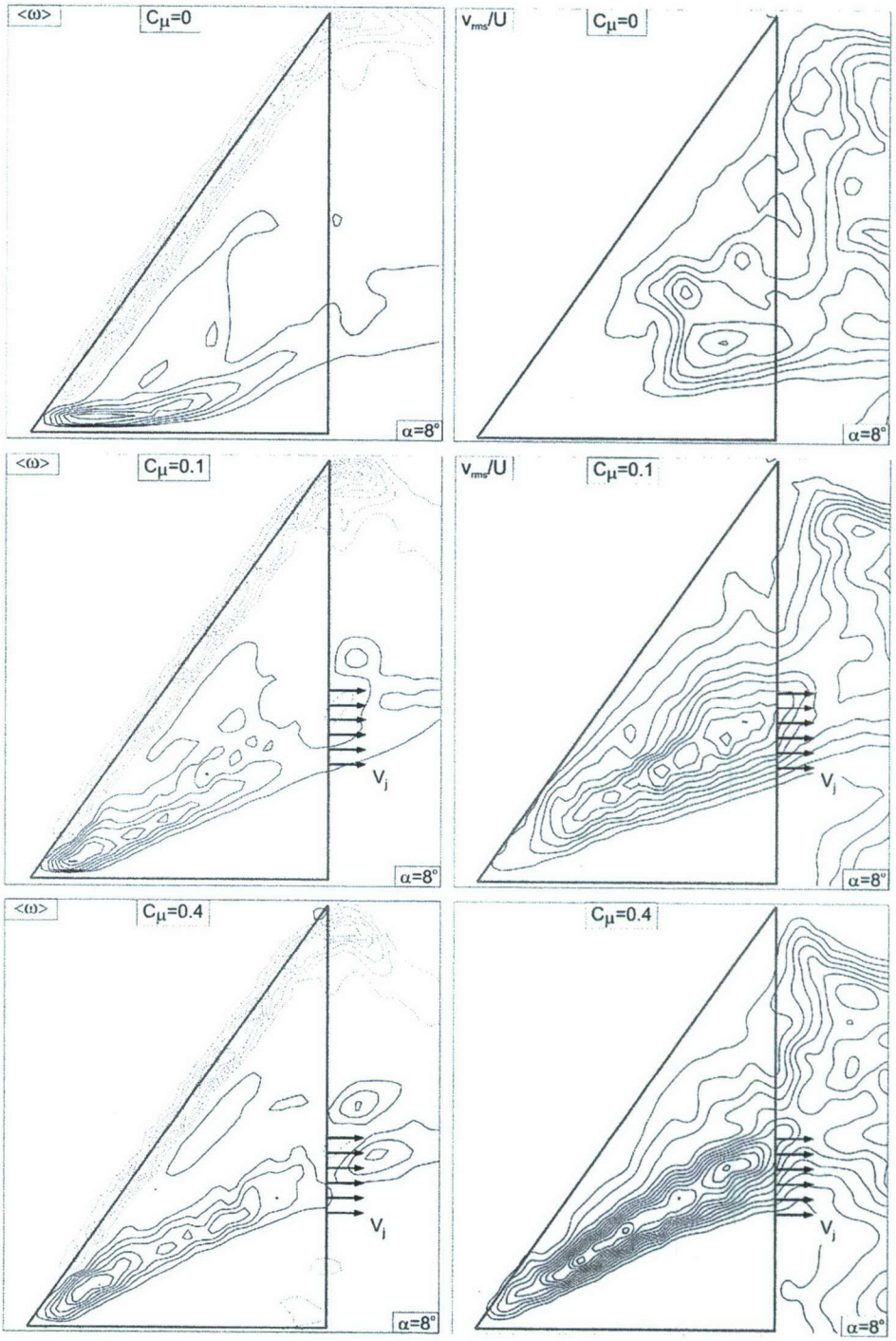


Figure B7: Comparison of vorticity $<\omega>$ oriented in a direction normal to the surface of the wing and root-mean-square of transverse velocity fluctuation v_{rms}/U for dual-location blowing cases for momentum coefficients $C_\mu = 0$, 0.1, and 0.4 on a wing at angle-of-attack $\alpha = 8°$. $C_\mu = (V_j^2 * A_j)/(U^2 * A_s)$,, in which V_j is the mean velocity of blowing at the trailing edge, A_j is the total area of both blowing slots at the trailing edge, A_s is the surface area of the planform, and U is the freestream velocity.($[|<\omega>|]_{min} = 2$ sec^{-1}, $\Delta[|<\omega>|] = 2$ sec^{-1}, $[v_{rms}/U]_{min} = 0.05$, $\Delta[v_{rms}/U] = 0.02$)

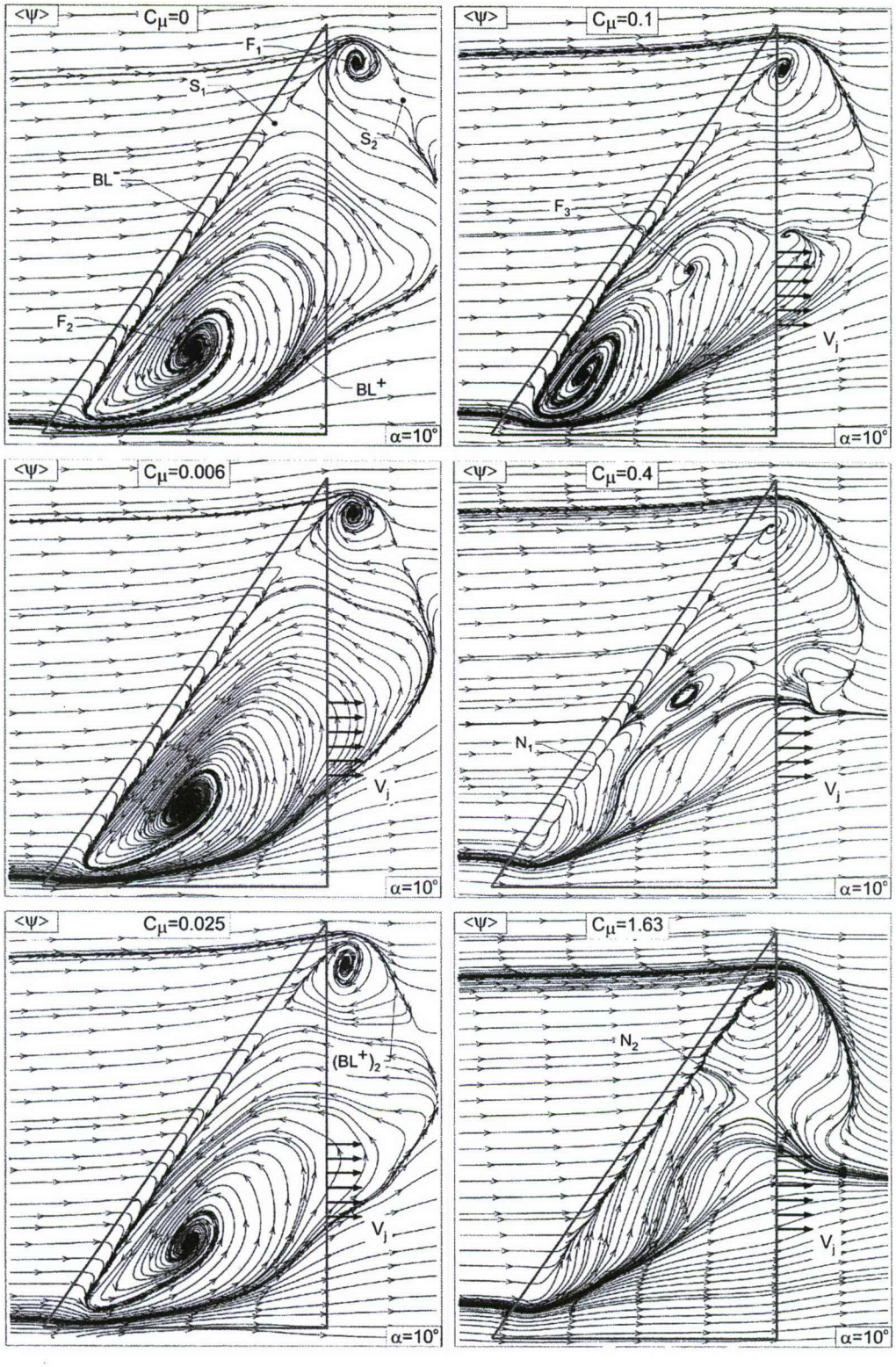


Figure B8: Comparison of near-surface patterns of time-averaged streamlines $<\Psi>$ for dual blowing cases for momentum coefficients C_μ= 0, 0.006, 0.025, 0.1, 0.4, and 1.63 on a wing at angle-of-attack α = 10°. $C_\mu = (V_j^2 * A_j)/(U^2 * A_s)$, in which V_j is the mean velocity of blowing at the trailing edge, A_j is the total area of both blowing slots at the trailing edge, A_s is the surface area of the planform, and U is the freestream velocity.

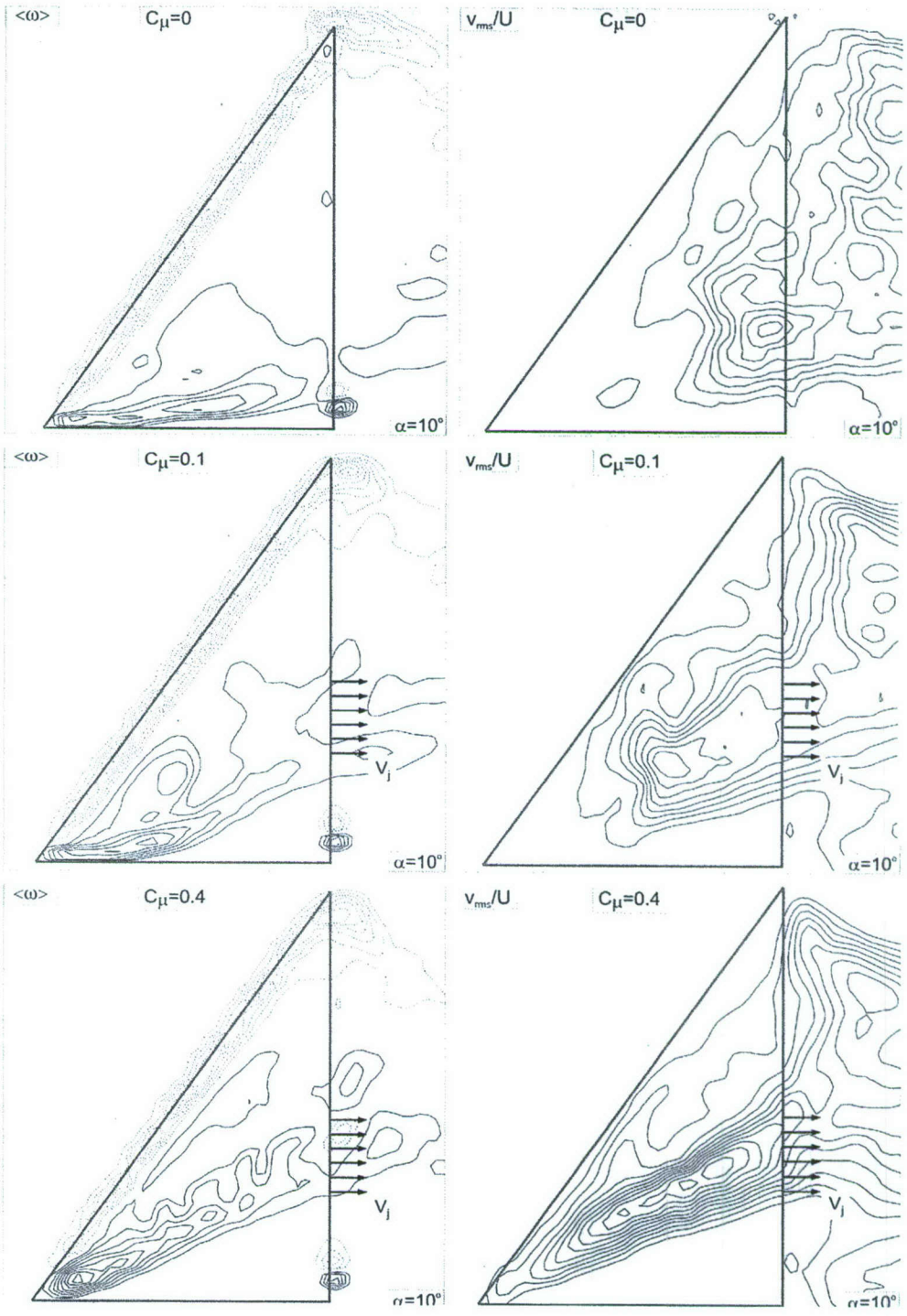


Figure B9: Comparison of vorticity $<\omega>$ oriented in a direction normal to the surface of the wing and root-mean-square of transverse velocity fluctuation v_{rms}/U for dual-location blowing cases for momentum coefficients $C_\mu = 0$, 0.1, and 0.4 on a wing at angle-of-attack $\alpha = 10°$. $C_\mu = (V_j^2 * A_j)/(U^2 * A_s)$, in which V_j is the mean velocity of blowing at the trailing edge, A_j is the total area of both blowing slots at the trailing edge, A_s is the surface area of the planform, and U is the freestream velocity.($[|<\omega>|]_{min} = 2$ sec^{-1}, $\Delta[|<\omega>|] = 2$ sec^{-1}, $[v_{rms}/U]_{min} = 0.05$, $\Delta[v_{rms}/U] = 0.02$)

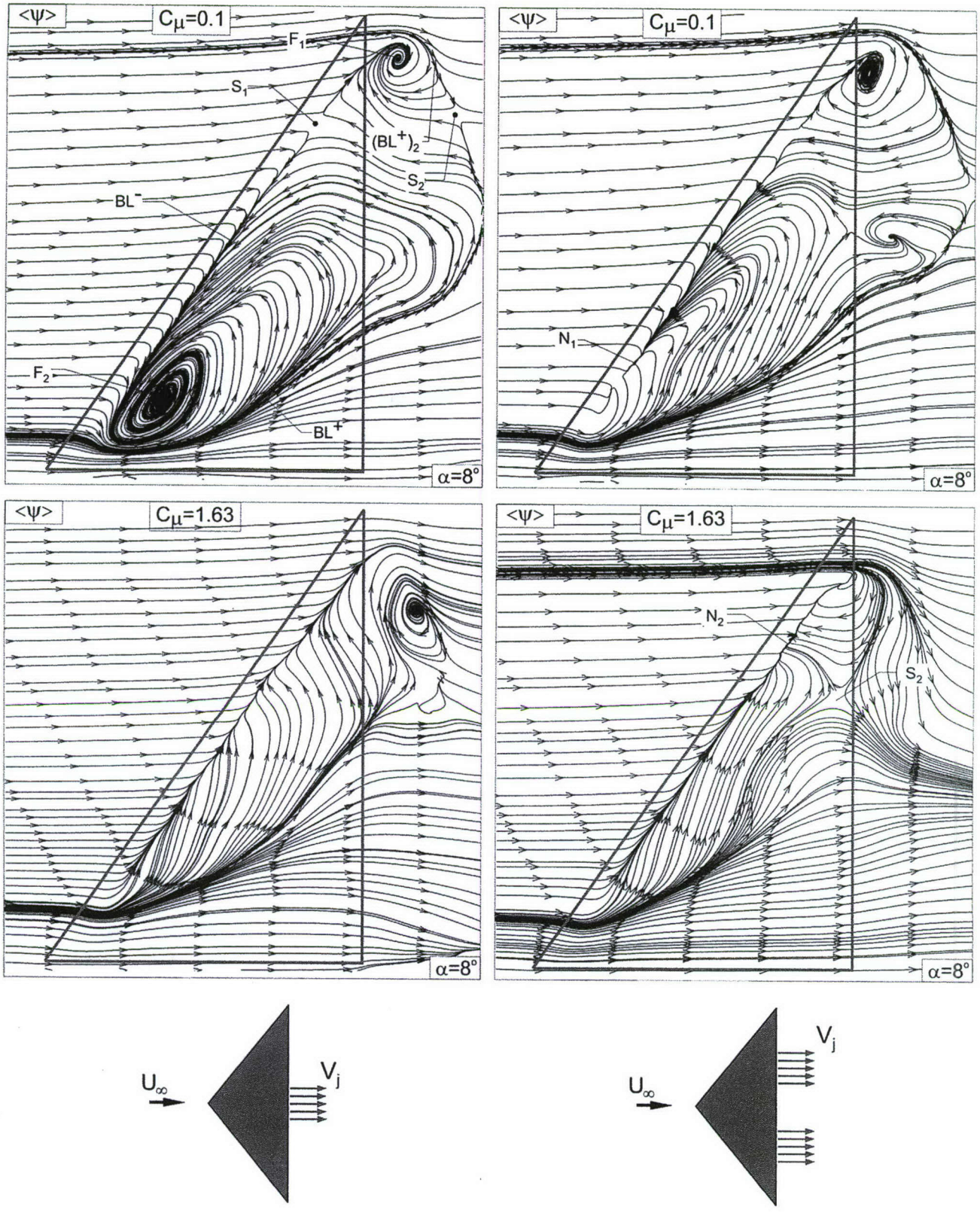


Figure B10: Comparison of near-surface patterns of time-averaged streamlines $<\Psi>$ for single blowing and dual blowing cases for momentum coefficients $C_\mu = 0.1$ and 1.63 on a wing at angle-of-attack $\alpha = 8°$. $C_\mu = (V_j^2 * A_j)/(U^2 * A_s)$, in which V_j is the mean velocity of blowing at the trailing edge, A_j is the total area of both blowing slots at the trailing edge, A_s is the surface area of the planform, and U is the freestream velocity.

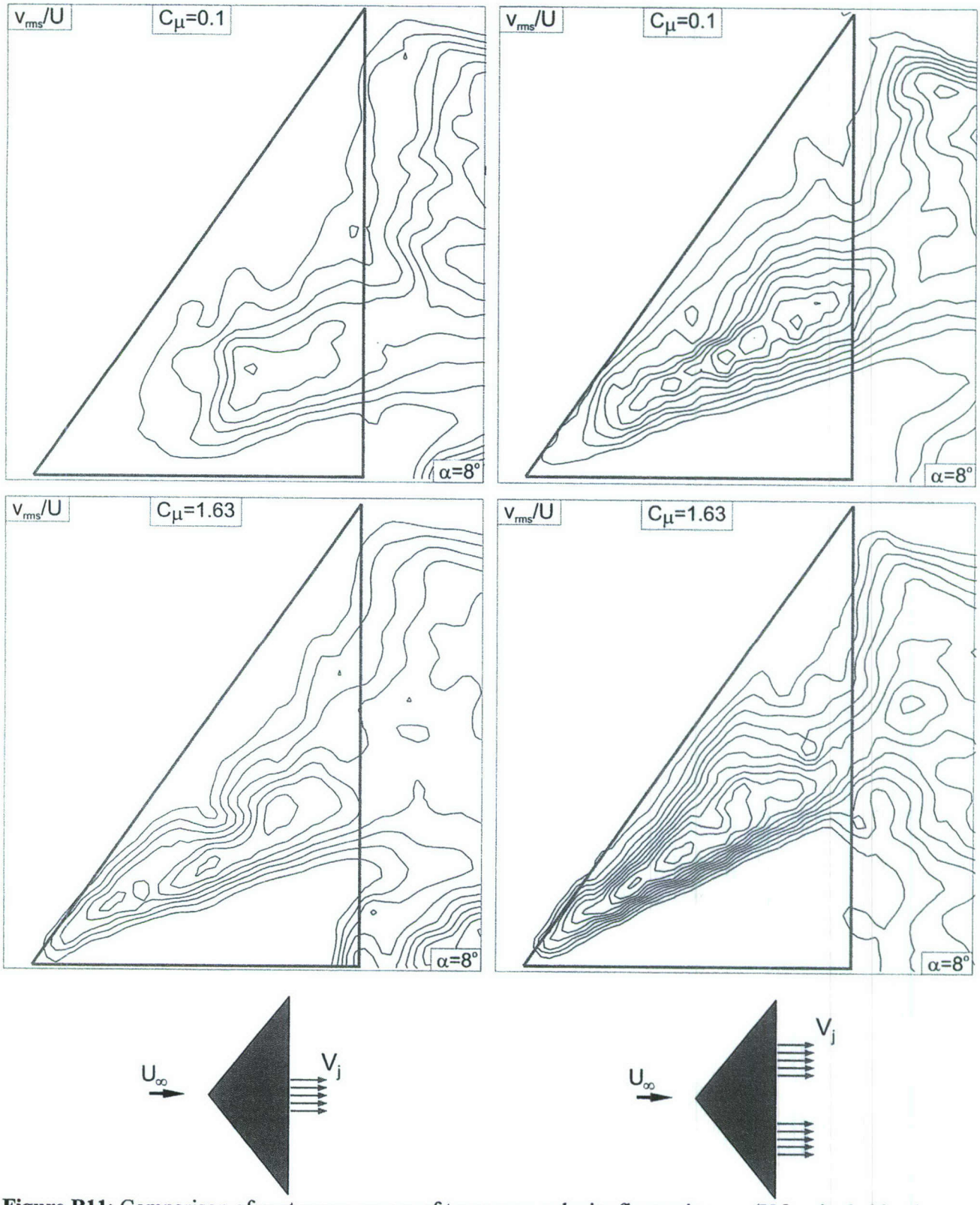


Figure B11: Comparison of root-mean-square of transverse velocity fluctuation v_{rms}/U for single blowing and dual blowing cases for momentum coefficients $C_\mu = 0.1$ and 1.63 on a wing at angle-of-attack $\alpha = 8°$. $C_\mu = (V_j^2 * A_j)/(U^2 * A_s)$, in which V_j is the mean velocity of blowing at the trailing edge, A_j is the total area of both blowing slots at the trailing edge, A_s is the surface area of the planform, and U is the freestream velocity. ($[v_{rms}/U]_{min} = 0.05$, $\Delta[v_{rms}/U] = 0.02$)

Appendix C

IDENTIFICATION AND CONTROL OF THREE-DIMENSIONAL SEPARATION ON LOW SWEPT DELTA WING

by

M. M. Yavuz and D. Rockwell
Department of Mechanical Engineering and Mechanics
Lehigh University
Bethlehem, PA 18015

1. INTRODUCTION

Recent interest in unmanned combat air vehicles (UCAVs) has stimulated investigation of the flow structure, as well as its control, on delta wings having low and moderate values of sweep angle. In addition, micro-air vehicles (MAVs) typically have complex leading-edge forms, including relatively low values of sweep angle. The distinctive features of the instantaneous and averaged flow structure on a delta wing of sweep angle $\Lambda = 50°$ have been numerically computed by Gordnier and Visbal[1]. Taylor, Schnorbus and Gursul[2] employed a dye technique, along with complementary particle image velocimetry, to visualize the vortex development on the moderately swept ($\Lambda = 50°$) wing, and Taylor and Gursul[3] investigated the near-surface topology and buffeting phenomena on the same planform. The foregoing investigations indicate that, at low angle-of-attack, a dual primary vortex system is established, whereas at higher angles-of-attack, this dual structure gives way to a single, larger-scale vortex. Ol and Gharib[4] employed a stereo version of particle image velocimetry to characterize the three-dimensional structure on crossflow planes of wings of sweep angle $\Lambda = 50°$ and 65°. Honkan and Adreopoulos[5] determined patterns of instantaneous vorticity on a delta wing of sweep angle $\Lambda = 45°$ via a pointwise technique, and identified the existence of stationary discrete vortical structures, within the feeding sheet and the primary vortex.

Another possible form of leading-edge vortex, which occurs for a wing of sweep angle $\Lambda = 38.7°$, involves formation of an elongated vorticity layer that tends to reattach to the surface of the wing. This has been characterized by Yaniktepe and Rockwell[6] via particle image velocimetry (PIV). Yaniktepe and Rockwell[7] addressed the flow structure at the trailing edge region on diamond and lambda planforms of low swept wing. Yavuz, Elkhoury and Rockwell[8] investigated the near-surface topology and flow structure for a wing of sweep angle $\Lambda = 38.7°$, including the effect of wing perturbations and transient motion of the wing; a near-surface technique of PIV was employed. Yavuz and Rockwell[9] determined the near-surface flow patterns of a wing of sweep angle $\Lambda = 35°$, and investigated the effect of trailing-edge control mechanism for various angles-of-attack. Such control can take the form of either one or more thrust vector systems, or localized control jets of small cross-sectional area along the trailing-edge. In the case of MAV configurations at low flight velocity, the velocity of the control jet, in a steady state or burst mode, may be relatively large.

The crossflow structure on delta wings of low sweep angle, in absence of a control technique, should be characterized with particular attention to the occurrence of vortex breakdown, or even loss of an identifiable vortex structure. These features should be interpreted

in conjunction with the near-surface flow patterns. This approach can potentially lead to identification of three-dimensional separation from the surface of the wing, in relation to the existence or nonexistence of a leading-edge vortex.

Control at the trailing-edge is known, from the investigation of Yavuz and Rockwell[9], to have a global effect on the near-surface flow structure of a wing of low sweep angle. The effect of this global influence on the flow structure in crossflow planes has not been addressed, and should be determined in terms of patterns of mean and fluctuating parameters. The possibility of recovery of a highly ordered structure of the leading-edge vortex, and a radical transformation of the form of the surface-normal fluctuations should be pursued. The latter has important consequences for buffet loading of the wing surface.

2. EXPERIMENTAL SYSTEM AND TECHNIQUES

Experiments were performed in a large scale water channel, which had a test section of 927 mm width, 610 mm depth and 4,928 mm length. The walls of this section were optically transparent. The value of Reynolds number Re based on chord C was maintained at 10,000. The corresponding value of free-stream velocity was U_∞ = 96.8 mm/sec. The angle-of-attack of the wing was $\alpha = 8°$.

The delta wing had a sweep angle of $\Lambda = 35°$, a chord C of 98 mm and a total span at the trailing-edge of 280 mm. The thickness of the wing was 12.7 mm, and its leading-edges were beveled on the windward side at an angle of 15°. The inside of the delta wing was machined in the form of a cavity, in order to allow generation of uniform blowing from the trailing-edge; this blowing is represented in the schematic of Figure C1. For the jet system, the center of each slit was located 50.8 mm from the plane of symmetry of the wing. Each slit had width of 25.4 mm and thickness of 0.8 mm.. Seven different jet velocities were employed. These velocities corresponded to seven different momentum coefficients, C_μ= 0.006, 0.025, 0.1, 0.23, 0.4, 0.92 and 1.63. To demonstrate the principal effects of trailing-edge blowing, addressed herein, the blowing coefficients C_μ= 0.1, 0.4, and 1.63 are described, relative to the case of no blowing C_μ= 0. The momentum coefficient was calculated as follows: $C_\mu = (V_j^2 * A_j)/(U^2 * A_s)$, in which V_j is the mean velocity of blowing at the trailing edge, A_j is the total area of both blowing slots the trailing edge, A_s is the surface area of the planform, and U is the freestream velocity. The corresponding values of velocity ratio were V_j/U = 5.8, 11.6, and 23.5.

A technique of high-image-density particle image velocimetry was employed. Illumination was provided by a dual-pulsed Nd:Yag laser system, having a maximum output of 90 mJ. Twelve micron metallic coated particles were used for seeding. The laser sheet was located at x/C = 0.34 and 0.8, where x is measured from the tip of the apex and C is the chord length of the planform.

For the PIV technique, the images were recorded by CCD camera and an effective framing rate of 15 cycles per second was used. The pattern of instantaneous velocity vectors was obtained by frame to frame cross-correlation technique involving successive frames of patterns of particle images in an interrogation window 32 × 32 pixels. An effective overlap of 50% was employed, in order to satisfy the Nyquist criterion. The effective resolution, i.e., grid size, was Δ/C = 0.0162, and 0.0264 respectively for the laser sheet locations at x/C = 0.34 and 0.8.

After the instantaneous velocity field V was determined, the time-averaged patterns of velocity $\langle V \rangle$, axial vorticity $\langle \omega \rangle$, streamlines $\langle \Psi \rangle$, and root-mean-square surface normal velocity fluctuation w_{rms}/U were calculated by using the cinema sequence of images. Time-averaged patterns are based on 200 images of the instantaneous velocity field. Preliminary investigations to assess the rate of convergence as a function of the number of images indicated that convergence was essentially attained with 100 images. These patterns were interpreted in conjunction with the foregoing patterns of near-surface streamline patterns taken from Yavuz and Rockwell[9]; as a result, complementary representations of near-surface and crossflow streamline patterns were constructed.

The laser sheet locations for crossflow characterizations were based on the streamline patterns of the near-surface flow topology. A major consequence of trailing-edge blowing is that the large-scale swirl pattern associated with the focus is eradicated. This may be physically interpreted with the aid of previous investigations. Legendre[10], Perry and Hornung[11], Perry and Chong[12], Dallman and Schulte-Werning[13], Su, Liu, and Liu[14], Lazos[15], and Taylor and Gursul[3] showed an inward swirling surface streamline patterns which had a focus point in its center. This focus point was taken as an indicator of three-dimensional separation. The relationship between this focus at the surface and the flow away from the surface is the development of a three-dimensional vortical structure. In order to identify the effect of three-dimensional separation in conjunction with the steady trailing-edge blowing, a location slightly upstream of the focus of separation, $x/C = 0.34$, and a location further downstream of the focus of separation, $x/C = 0.8$, were selected.

3. TIME-AVERAGED STREAMLINE PATTERNS

Time-averaged streamline patterns in crossflow planes. Corresponding patterns of streamline topology of $\langle \psi \rangle$, based on the time-averaged velocity patterns (not shown here), are demonstrated in Figure C2 for the values of blowing coefficients $C_\mu = 0$, 0.1, 0.4 and 1.63, and on the crossflow planes located at $x/C = 0.34$ and 0.8.

Consider patterns of $\langle \psi \rangle$ at $x/C = 0.34$ shown in the left column of images. In the absence of blowing $C_\mu = 0$, the streamlines appear to originate from a common node located close to the leading-edge of the wing. Moreover, the overall pattern of $\langle \psi \rangle$ does not exhibit significant swirl. This distinctive form of the crossflow streamline pattern appears to be due to separation from the leading-edge having relatively low sweep angle. It occurs in presence of a highly separated flow in this region of the wing. Trailing-edge blowing at $C_\mu = 0.1$ induces pronounced swirl of the streamlines. They spiral inward towards the focus and therefore the focus is stable. Furthermore, at the larger values of $C_\mu = 0.4$ and 1.63, the inward spiral persists until a limit cycle is obtained. Within this limit cycle, the focus is associated with an outward spiraling streamline pattern, indicating that an unstable focus is embedded within the limit cycle. Viewing the patterns on the plane $x/C = 0.34$ as a whole, it is evident that increasing C_μ induces a detectable movement in the outboard direction of the focal point. Simultaneously, the overall swirl pattern of streamlines is displaced in the outboard direction. On the plane corresponding to $x/C = 0.8$, given in the right column of images, even for the case of no blowing, $C_\mu = 0$, a well-defined, inward-spiraling pattern of streamlines is evident. This general form of the spiral pattern, which terminates in a stable focus, persists for all values of blowing coefficient C_μ. The spanwise location of the focus, as well as the overall pattern of spiraling streamlines, is displaced

substantially towards the leading-edge for increasing C_μ. Furthermore, at larger values of C_μ, the swirling streamlines appear to coalesce together along the surface of the wing and remain parallel to the surface, before rolling up into the spiral pattern.

Comparison of streamline topology on crossflow planes and along surface of wing. In order to further clarify the overall flow patterns, in relation to the magnitude of trailing-edge blowing, patterns of $<\psi>$ in the crossflow planes and along the surface of the wing (Yavuz and Rockwell[9]) are superposed. These representations are given in Figure C3 for $C_\mu = 0$ and 0.1, and in Figure C4 for $C_\mu = 0.4$ and 1.63.

In Figure C3, for $C_\mu = 0$, at $x/C = 0.34$, the relationship between the streamlines emanating from a node near the leading-edge in the crossflow plane and the focus of the streamline pattern on the surface of the wing, associated with three-dimensional separation, is clearly evident. Further downstream, at $x/C = 0.8$, streamlines emanating from the leading-edge are centered above the negative bifurcation line B_L^-. Streamlines associated with reattachment to the surface of the wing are centered approximately on the positive bifurcation line B_L^+. Furthermore, if the location of the focus (apparent center of the spiral streamline pattern) in the crossflow plane is projected onto the surface of the wing, that location corresponds to the location of turning of the surface streamlines, i.e., the location at which they change direction from predominantly downstream- to upstream-oriented streamlines. By considering both of the planes at $x/C = 0.34$ and 0.8, the relationship between the focus at the surface and the flow away from the surface can be further defined. The development of the three-dimensional vortical structure due to the three-dimensional separation at the surface yields a well-defined swirling pattern at a location downstream of the focus of separation. It is evident that counterclockwise swirl of the separation region at the surface is associated with counterclockwise swirl in the crossflow plane. That is, the three-dimensional separation from the surface gives rise to a "vortex tube" that is deflected in the downstream direction, thereby appearing as the swirl pattern in the plane at $x/C = 0.8$. This concept is very similar to that obtained in the numerical simulation of Dallman and Schulte-Werning[13]. Their representation shows that no swirl pattern is evident in the crossflow plane located upstream of the focus of separation, which is consistent with the present interpretation.

In general, the foregoing observations of the crossflow pattern of $<\psi>$ at $x/C = 0.8$ for $C_\mu = 0$, relative to the corresponding pattern of $<\psi>$ on the surface plane, holds for all values of blowing coefficient, i.e., for $C_\mu = 0.1$ in Figure C3 and $C_\mu = 0.4$ and 1.63 in Figure C4, irrespective of whether one considers the crossflow plane $x/C = 0.34$ or $x/C = 0.8$. That is, compatibility persists between: (i) streamlines in the crossflow plane in the vicinity of the leading-edge and the negative bifurcation line B_L^- on the surface plane; (ii) streamlines associated with reattachment on the crossflow plane and the positive bifurcation line B_L^+ on the surface plane; and (iii) the location of the focus on the crossflow plane in relation to the location of turning of streamlines (from downstream to upstream orientation) on the surface plane.

Generally speaking, for increasing values of C_μ, the focus of the swirl patterns of streamlines in a crossflow plane, as well as the location of streamline turning in the surface patterns of streamlines, move in the outward direction towards the leading-edge.

4. PATTERNS OF AXIAL VORTICITY

Contours of constant axial vorticity $<\omega>$ are given in Figure C5. Solid (dark) and dashed (light) lines represent respectively positive and negative contours of $<\omega>$, in which the positive orientation corresponds to a vorticity vector in the direction of the outward normal vorticity vector, oriented in the streamwise direction. The left and right columns of images represent, respectively, planes at $x/C = 0.34$ and 0.8.

Consider the case of no blowing $C_\mu = 0$ in the first row of images. At $x/C = 0.34$, a concentration of $<\omega>$ is located close to the plane of symmetry of the wing. As visualized by Yaniktepe and Rockwell[6], dye visualization shows that, at sufficiently high angle-of-attack, where large-scale separation/stall occurs on the surface of the wing, the marker originating from the apex is close to the plane of symmetry of the wing. The indicated concentration of $<\omega>$ is therefore indicative of vorticity shed from the apex region. Furthermore, between this concentration of vorticity and the leading-edge of the wing, low level, elongated contours of $<\omega>$ are apparent, and there is no indication of a leading-edge vortex. At the leading-edge, the small-scale concentration is associated with the rapid flow distortion in that region. At $x/C = 0.8$, the inboard concentration of vorticity is hypothesized to be an extension of the foregoing concentration at $x/C = 0.34$, whereas the outboard concentration most likely arises from the three-dimensional separation process from the wing surface.

In the presence of blowing, the patterns of vorticity at $x/C = 0.34$ represent a well-defined, leading-edge vortex(ices). At $C_\mu = 0.1$ and 0.4, a single concentration of vorticity is evident; it is part of an elongated vorticity layer. At $C_\mu = 1.63$, two identifiable concentrations of vorticity occur within the elongated layer. Furthermore, a pattern of positive $<\omega>$ appears between the negative layer of $<\omega>$ and the surface of the wing. It is due to eruption of the boundary layer from the wing surface. Finally, a common feature for all values of C_μ (at $x/C = 0.34$), is occurrence of a well-defined, small-scale concentration of vorticity at the leading-edge; it is present even for the limiting case of no blowing $C_\mu = 0$. This concentration is associated with rapid distortion of flow from the leading-edge.

At $x/C = 0.8$, in presence of blowing over the range $C_\mu = 0.1$ to 1.63, the pattern of negative $<\omega>$ transforms from an elongated layer having a single concentration of vorticity to a layer having two concentrations of vorticity. This transformation is in parallel with the change in flow structure at $x/C = 0.34$ over the same range of C_μ. Moreover, an increase of C_μ results in an increase in magnitude of the peak vorticity, which occurs in the dominant, primary vortex structure. The second concentration of vorticity, of significantly lower magnitude, is, however, readily identifiable at $C_\mu = 0.4$ and 1.63. Furthermore, at larger values of C_μ, at $x/C = 0.8$, the positive concentration of vorticity adjacent to the wing surface is evident.

The existence of two concentrations of vorticity in the vorticity layer, as well as the positive concentration of vorticity adjacent to the surface of the wing, which occur at the highest value of $C_\mu = 1.63$ and in both of the planes at $x/C = 0.34$ and 0.8, are remarkably similar to those first identified in the numerical simulation of Gordnier and Visbal[1] at lower angle-of-attack, and in the experimental observations of Taylor, Schnorbus and Gursul[2], and Yaniktepe and Rockwell[6,7], also at lower angle of attack, and in absence of blowing. We therefore conclude that highly separated flow along a wing of low sweep angle, which is present at moderate angle

of attack, can be transformed to the dual vortex pattern, via localized control at the trailing-edge (in the form of steady blowing). This dual vortex occurs naturally, i.e., in absence of any control, at low angle-of-attack. Furthermore, this dual vortex exists over the entire streamwise extent of the wing.

Direct comparison of the vorticity contours on both planes of interest in presence of blowing, shows significant reduction in the negative vorticity values in the plane further downstream, at x/C = 0.8. This reduction in the magnitude of negative vorticity at the downstream axial location may be due either to: occurrence of vortex breakdown of the leading-edge vortices; or the onset of unsteadiness due to the inherent instability of this system.

5. PATTERNS OF VELOCITY FLUCTUATION

Contours of constant root-mean-square velocity fluctuation w_{rms}/U, defined in the direction normal to the surface of the wing, are given in Figure C6. The layout of these patterns of w_{rms}/U is the same as those of $<\omega>$ in Figure C5. Surface normal velocity fluctuations are directly related to the unsteady pressure at the surface of the wing, which is associated with unsteady loading, i.e., buffeting, of the surface. The relationship between these velocity fluctuations and the buffet loading is addressed by Ozgoren et al.[16]

At x/C = 0.34, for the case of no blowing C_μ = 0, which corresponds to a location immediately upstream of the focus F_2 of the large-scale separation from the surface of the wing, several isolated, low level clusters of w_{rms}/U are evident. On the other hand, at x/C = 0.8, for the case C_μ = 0, significantly large values of w_{rms}/U are evident, and the pattern of contours extends over nearly the entire semi-span of the wing. Comparison of these patterns for C_μ = 0 at x/C = 0.34 and 0.8 therefore indicates that, at a location close to large-scale surface separation (x/C = 0.34), the fluctuation amplitude w_{rms}/U is relatively small, whereas well downstream of this onset of separation (x/C = 0.8), the fluctuation amplitudes are substantial and of large spatial extent.

The effect of trailing-edge blowing on the patterns of w_{rms}/U at x/C = 0.34, for successively larger values of C_μ = 0.1, 0.4 and 0.163, are given in the left column of images of Figure C6. The spanwise locations of the peak values of w_{rms}/U are approximately the same for different magnitudes of C_μ. On the other hand, the overall spatial extent of each pattern of w_{rms}/U becomes smaller, and the peak values larger, with increasing values of blowing coefficient C_μ. This transformation of patterns of w_{rms}/U can be directly compared with the corresponding patterns of vorticity concentrations $<\omega>$ in Figure C5. It corresponds to a change from a single vortex to a dual vortex structure within the elongated vorticity layer above the surface.

Further downstream, at x/C = 0.8, represented in the right column of images of Figure C6, the effect of increasing C_μ is to increase the degree of concentration of the patterns of w_{rms}/U, and simultaneously, to decrease their overall spatial extent along the semi-span of the wing. It should be noted, however, that the peak values of w_{rms}/U are approximately the same for all values of C_μ. In fact, for the largest value of C_μ = 1.63, the pattern of w_{rms}/U covers less than half of the semi-span, which indicates that only a limited extent of the wing surface is exposed to turbulent buffeting. Finally, the evolution of these patterns of w_{rms}/U with increasing C_μ, when compared directly with the corresponding patterns of vorticity $<\omega>$ in Figure C5, indicate that

the substantial decrease in spanwise extent of the pattern of w_{rms}/U corresponds to onset of the dual vortex structure, most evident at $C_\mu = 1.63$. Furthermore, it should be noted that these patterns of fluctuation are in accord with the patterns of transverse velocity fluctuation along the near-surface flow characterized by Yavuz and Rockwell[9], that is, they occur at the same spanwise locations and have equivalent spatial extents.

6. CONCLUDING REMARKS

The flow structure on crossflow planes, located upstream and downstream of the onset of three-dimensional separation from the surface of a delta wing having low sweep angle, has been investigated as a function of the magnitude of localized blowing from slots at the trailing-edge. The principal findings can be listed as follows:

(a) In the absence of control, a region of three-dimensional separation dominates the near-surface flow, and the crossflow structure is characterized by: the vortex shed from the apex; and the three-dimensional vortex structure that emanates from three-dimensional separation from the surface. There is no indication of a leading-edge vortex.

(b) Occurrence of three-dimensional separation/stall causes remarkable patterns of surface normal velocity fluctuations in the region close to the trailing edge of the planform. These patterns are indicative of buffeting/unsteady loading.

(c) In the presence of trailing-edge blowing, eradication of three-dimensional separation from the surface of the wing is associated with recovery of both the swirl pattern of streamlines and the pronounced axial vorticity concentration in the crossflow plane closest to the apex. Further increases of blowing coefficient cause the center of the vortex structure in the crossflow planes to move closer to the leading-edge of the planform.

(d) At sufficiently high blowing coefficients, a dual vortex structure occurs. It involves a secondary concentration of axially-oriented vorticity, which has the same sign as, and is immediately adjacent to, the primary vortex. This structure is very similar in form to that originally identified at lower angle-of-attack in the numerical simulation of Gordnier and Visbal[1], and confirmed in the experimental investigations of Taylor, Schnorbus and Gursul[2], and Yaniktepe and Rockwell[6,7]. In other words, the separated flow along a wing of low sweep angle, at moderate angle of attack, can be transformed, via steady trailing-edge blowing, to the dual primary vortex structure, which occurs naturally, i.e., in absence of any control, at low angle-of-attack.

(e) An increase of blowing coefficient decreases the overall spatial extent of the pattern of surface-normal velocity fluctuations along the semi-span of the wing, at locations close to the trailing-edge. For the largest value of blowing coefficient, this pattern covers less than half of the semi-span, which indicates that only a limited extent of the wing surface is exposed to turbulent buffeting/unsteady loading.

7. ACKNOWLEDGMENTS

The support of the Air Force Office of Scientific Research under Grant Number F49620-02-1-0061 is gratefully acknowledged. This AFOSR program was monitored by Dr. John Schmisseur and Lt. Col. Rhett Jefferies.

8. REFERENCES

[1]Gordnier, R. E. and Visbal, M. R., "Higher-Order Compact Difference Scheme Applied to the Simulation of a Low Sweep Delta Wing Flow", AIAA Paper 2003-0620, Jan. 2003.

[2]Taylor, G.S., Schnorbus, T., and Gursul, I., "An Investigation of Vortex Flows over Low Sweep Delta Wings", AIAA-2003-4021 June 2003.

[3]Taylor, G.S. and Gursul, I., "Unsteady Vortex Flows and Buffeting of a Low Sweep Delta Wing", AIAA-2004-1066, Jan. 2004.

[4]Ol, M. V. and Gharib, M. "Leading-Edge Vortex Structure of Nonslender Delta Wings at Low Reynolds Number", *AIAA Journal*, Vol. 41, No. 1, 2003, pp. 16-26

[5]Honkan, A. and Andreopoulos, J., "Instantaneous Three-Dimensional Vorticity Measurements in Vortical Flow over a Delta Wing", *AIAA Journal*, Vol. 35, No. 10, 1997, pp. 1612-1620.
[6]Yaniktepe, B. and Rockwell, D., "Flow Structure on a Delta Wing of Low Sweep Angle", *AIAA Journal,* Vol.42, No. 3, 2004, pp.513-523.

[7]Yaniktepe, B. and Rockwell, D., "Flow Structure on Diamond and Lambda Planforms: Trailing-Edge Region", *AIAA Journal,* Vol. 43, No. 7, 2005, pp.1490-1500.

[8]Yavuz, M. M., Elkhoury, M. and Rockwell, D., "Near-Surface Topology and Flow Structure on a Delta Wing", *AIAA Journal*, Vol. 42, No. 2, 2004, pp.332-340.

[9]Yavuz, M. M. and Rockwell, D., "Control of Flow Structure on Delta Wing with Steady Trailing-Edge Blowing", *AIAA Journal*, Vol.44, No. 3, 2006, pp.493-501.

[10]Legendre, R. "Lignes de Courent d'un Ēcoulement Continu", *Rech. Aērosp.* No. 105, 1965, pp. 3-9.

[11]Perry, A. E. and Hornung, H. G. "Some Aspects of Three-Dimensional Separation. Part II. Vortex Skeletons", *Z. Flugwiss. Weltraumforsch.* Vol. 8, 1984, pp. 155-160.

[12]Perry, A. E. and Chong, M. S. "A Description of Eddying Motions and Flow Patterns Using Critical-Point Concepts", *Annual Review of Fluid Mechanics*, Vol. 19, 1987, pp. 125-155.

[13]Dallman, U. and Schulte-Werning, B. "Topological Changes of Axisymmetric and Non-Axisymmetric Vortex Flows", *Topological Fluid Mechanics, Proceedings of the IUTAM Symposium*, edited by H. K. Moffat and A. Tsinober, Cambridge Univ. Press, Cambridge, England, U.K., pp. 372-383.

[14]Su, W., Liu, M., and Liu, Z., "Topological Structures of Separated Flows About a Series of Sharp-Edged Delta Wings at Angles-of-Attack up to 90°," *Topological Fluid Mechanics, Proceedings of the IUTAM Symposium*, edited by H. K. Moffat and A. Tsinober, Cambridge Univ. Press, Cambridge, England, U.K., pp. 395-407.

[15]Lazos, B. "Surface Topology on the Wheels of a Generic Four-Wheel Landing Gear," *AIAA Journal,* Vol. 40, No. 12, 2002, pp. 2402-2412.

[16]Ozgoren, M., Sahin, B. and Rockwell, D. 2002 "Vortex Breakdown from a Pitching Delta Wing Incident upon a Plate: Flow Structure as the Origin of Buffet Loading", *Journal of Fluids and Structures*, Vol. 16, Issue 3, April, pp. 295-316.

LIST OF FIGURES

Figure C1: Overview of experimental setup including delta wing and laser sheet orientation.

Figure C2: Comparison of time-averaged streamline patterns for trailing-edge blowing at values of momentum coefficients $C_\mu = 0$, 0.1, 0.4 and 1.63 at the planes of interest $x/C = 0.34$ and 0.8.

Figure C3: Comparison of time-averaged near-surface streamline patterns with crossflow topology for trailing-edge blowing at values of momentum coefficients $C_\mu = 0$ and 0.1 at the planes of interest $x/C = 0.34$ and 0.8.

Figure C4: Comparison of time-averaged near-surface streamline patterns with crossflow topology for trailing-edge blowing at values of momentum coefficients $C_\mu = 0.4$ and 1.63 at the planes of interest $x/C = 0.34$ and 0.8.

Figure C5: Contours of constant axial velocity $\langle\omega\rangle$ for trailing-edge blowing at values of momentum coefficients $C_\mu = 0$, 0.1, 0.4 and 1.63 at the planes of interest $x/C = 0.34$ and 0.8. ($[\|\langle\omega\rangle\|] = 1$ sec^{-1}).

Figure C6: Contours of constant root-mean-square surface normal velocity fluctuation w_{rms}/U for trailing-edge blowing at values of momentum coefficients $C_\mu = 0$, 0.1, 0.4, and 1.63 at the planes of interest $x/C = 0.34$ and 0.8. ($[\omega_{rms}/U]_{min} = 0.04$, $\Delta[w_{rms}/U = 0.01$).

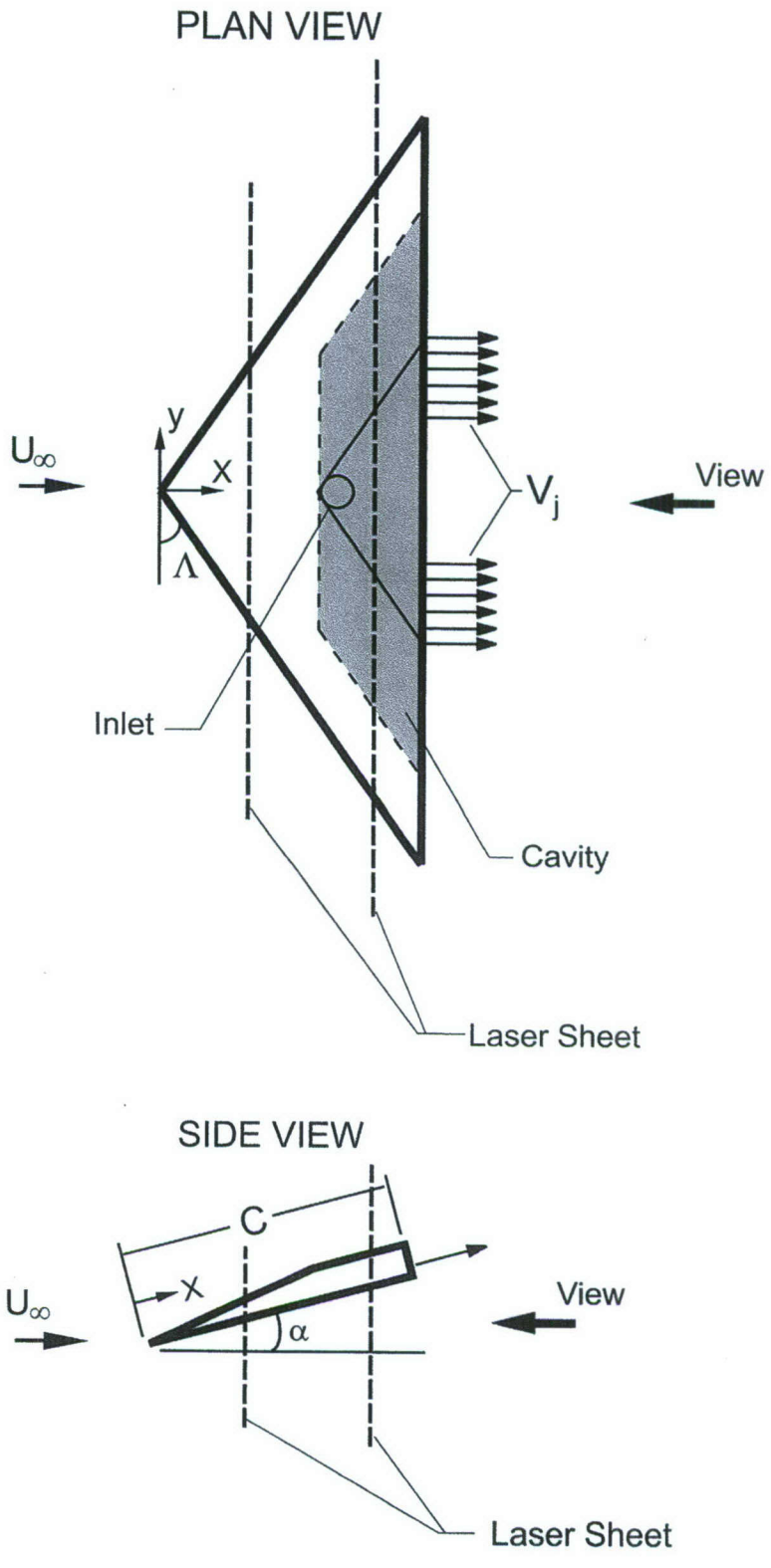


Figure C1: Overview of experimental setup including delta wing and laser sheet orientation.

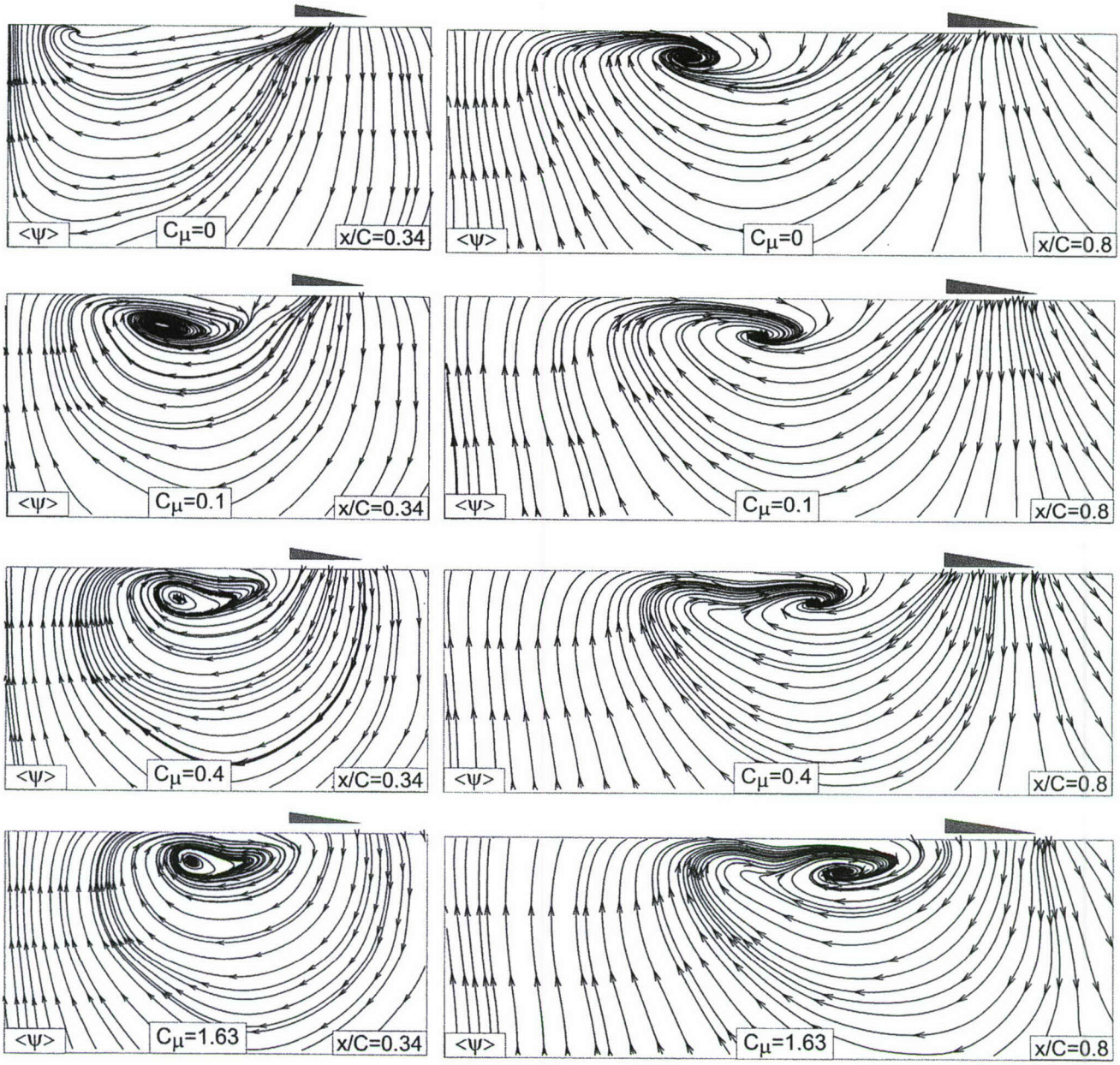


Figure C2: Comparison of time-averaged streamline patterns for trailing-edge blowing at values of momentum coefficients $C_\mu = 0$, 0.1, 0.4 and 1.63 at the planes of interest $x/C = 0.34$ and 0.8.

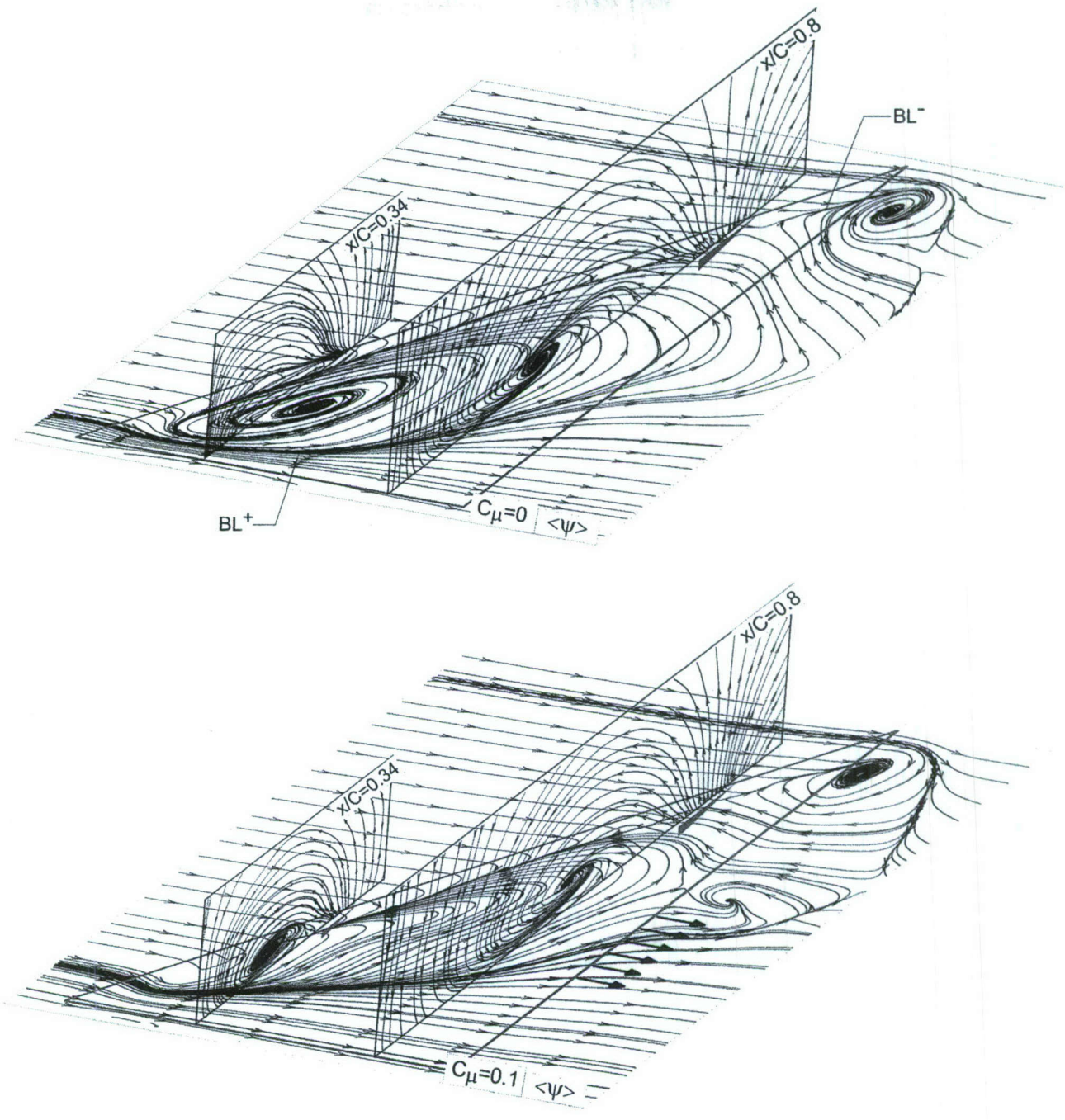


Figure C3: Comparison of time-averaged near-surface streamline patterns with crossflow topology for trailing-edge blowing at values of momentum coefficients C_μ= 0 and 0.1 at the planes of interest x/C = 0.34 and 0.8.

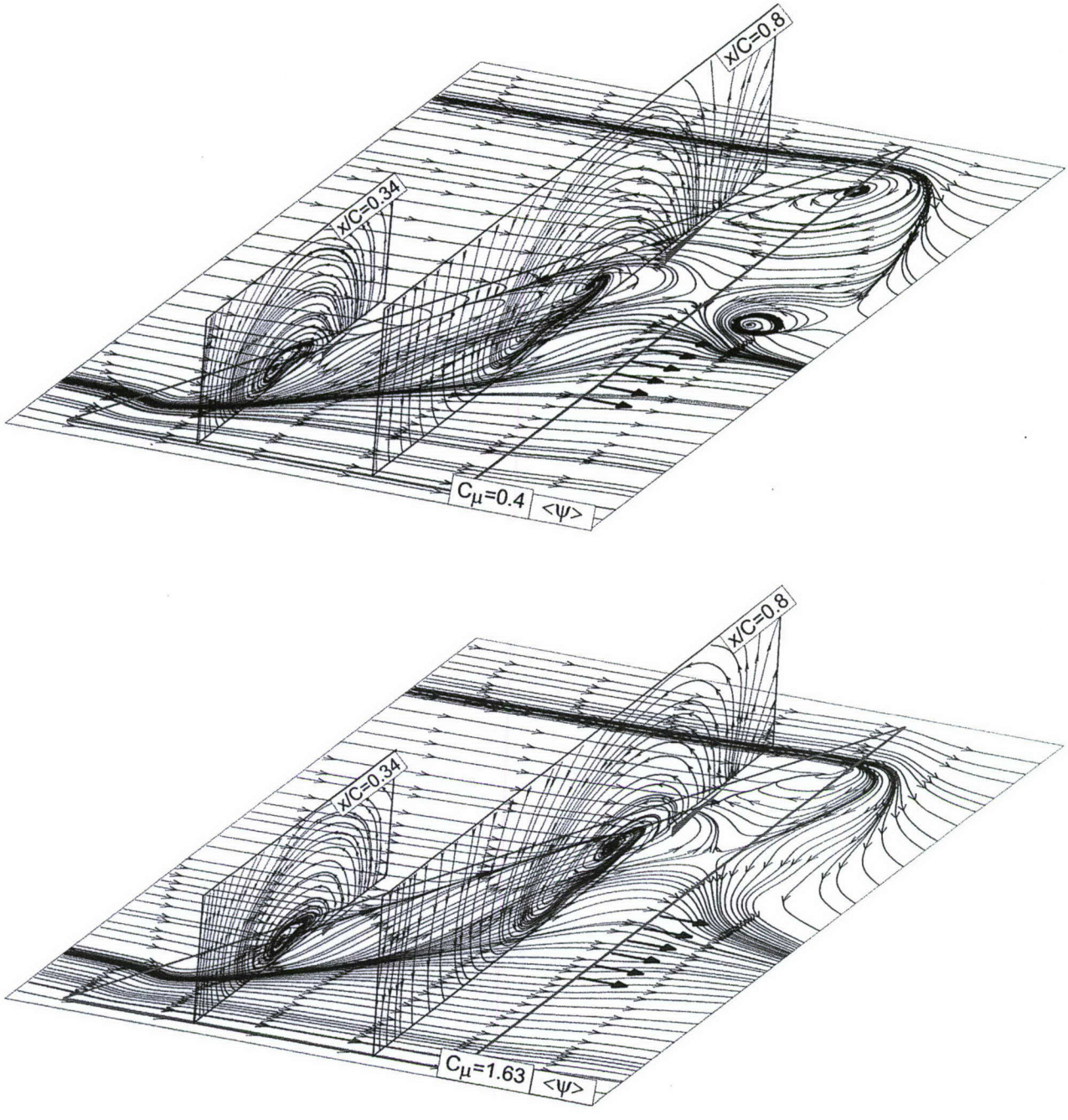


Figure C4: Comparison of time-averaged near-surface streamline patterns with crossflow topology for trailing-edge blowing at values of momentum coefficients C_{μ}= 0.4 and 1.63 at the planes of interest x/C = 0.34 and 0.8.

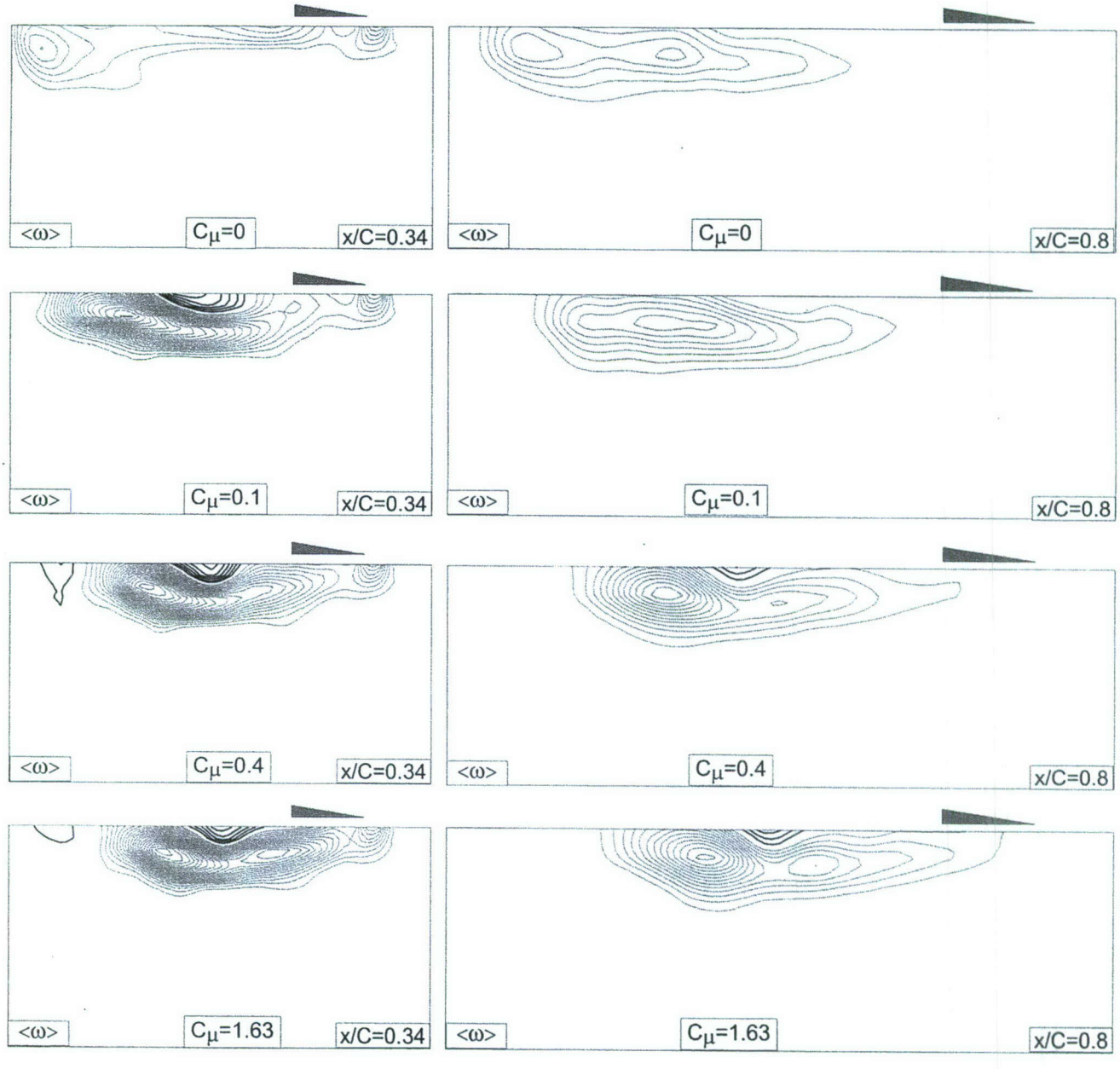


Figure C5: Contours of constant axial velocity $\langle\omega\rangle$ for trailing-edge blowing at values of momentum coefficients C_μ = 0, 0.1, 0.4 and 1.63 at the planes of interest x/C = 0.34 and 0.8. ($[\|\langle\omega\rangle\|] = 1\ \text{sec}^{-1}$).

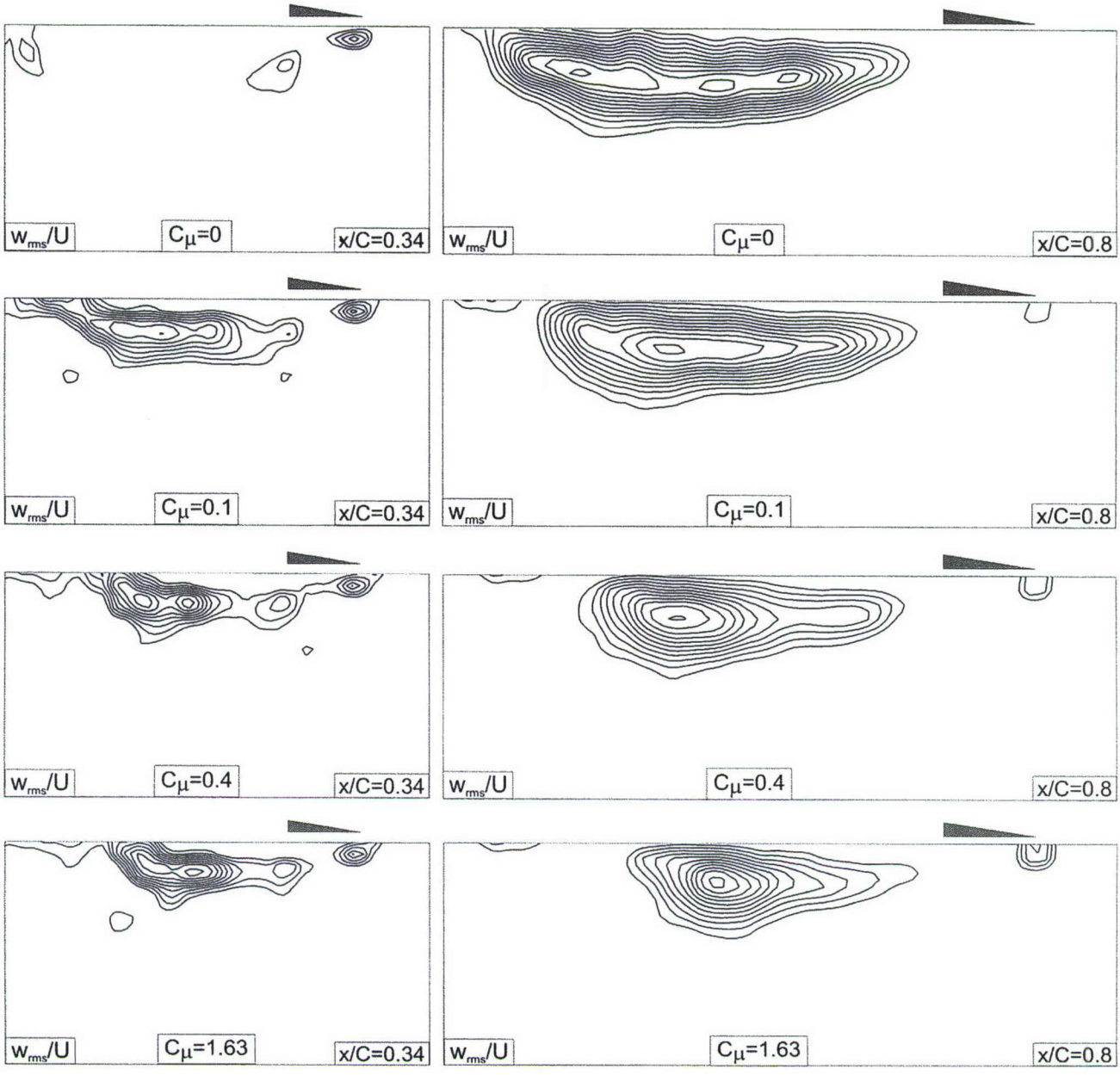


Figure C6: Contours of constant root-mean-square surface normal velocity fluctuation w_{rms}/U for trailing-edge blowing at values of momentum coefficients $C_\mu = 0$, 0.1, 0.4, and 1.63 at the planes of interest $x/C =$ 0.34 and 0.8. ($[\omega_{rms}/U]_{min} = 0.04$, $\Delta[w_{rms}/U = 0.01$).

Appendix D

NEAR-SURFACE TOPOLOGY ON A DELTA WING OF LOW SWEEP ANGLE: RELAXATION PROCESSES FOLLOWING A TRANSIENT MANEUVER

by

T. Goruney and D. Rockwell
Department of Mechanical Engineering and Mechanics
356 Packard Laboratory, 19 Memorial Drive West
Lehigh University
Bethlehem, PA 18055

INTRODUCTION

A wing of defined sweep angle subjected to a prescribed maneuver can give rise to complex forms of the flow physics. This topic has been the subject of a variety of investigations in recent decades, as described in the doctoral dissertation of Goruney (2008), as well as in the literature cited in other sections of this final report.

The focus of the present investigation is to determine the near-surface flow structure and the associated streamline topology during the relaxation process of a wing of low sweep angle subjected to a transient pitch-up motion. Of particular interest are the topological states that occur in an ordered sequence, and the possibility of the same states occurring for various values of pitch rate of the wing. These features of the near-surface flow physics will be characterized using a quantitative imaging technique, which allows quantitative definition of the streamline patterns, and their interpretation in conjunction with critical point theory.

EXPERIMENTAL SYSTEM AND TECHNIQUES

Figure D1 shows a wing of defined sweep angle $\Lambda = 50°$, at his instant, the wing is in its terminal position, i.e., at the instant of completion of the pitch-up motion. The location of the laser sheet relative to the surface of the wing is described in the dissertation of Goruney (2008). For the images shown herein, the displacement of the sheet from the wing surface was at $z/C = 0.005$, where z is the distance measured orthogonally from the wing surface and C is the wing chord. The value of Reynolds number based on chord C is Re = 15,000, and the root chord was $C = 200$mm, while the freestream velocity was $U = 70.92$mm/sec. The magnitudes of the pitch rate were $\dot{\alpha}\,C/U = 0.05$, 0.1, 0.2 and 0.4. Details of the laser system, the seeding of the flow, image acquisition components, and post-processing are described in other sections of this report, in particular in the works of Yavuz and Rockwell (2006a, 2006b). The reader is referred to these works for further details.

FLOW STRUCTURE UPON CESSATION OF WING MANEUVER

Figure D2 shows dye visualization of the leading-edge vortex at cessation of the pitch-up maneuver, for variations in pitch rate $\dot{\alpha}\,C/U$. A schematic of the variation of angle-of-attack α versus time t, as well as definition of other parameters, are given at the bottom of Figure D2. At the lowest pitch rate, $\dot{\alpha}\,C/U = 0.05$, the leading-edge vortex is barely detectable. Except for the region near the apex of the wing, where one can define a vortex of limited extent, the diffused dye pattern suggests that the pattern near the surface of the wing is sufficiently stalled, such that the leading-edge vortex cannot exist. At $\dot{\alpha}\,C/U = 0.1$, however, a well-defined leading-edge

vortex is detectable, but vortex breakdown occurs relatively close to the apex. If the value of pitch rate is increased to $\dot{\alpha}\,C/U = 0.2$, the onset of large-scale vortex breakdown appears to be postponed, or retarded, to a larger distance from the apex of the wing. That is, the vortex has not yet had sufficient time to relax to a fully broken down state, as was the case for the lower pitch rate $\dot{\alpha}\,C/U = 0.1$. Finally, for the highest value of pitch rate $\dot{\alpha}\,C/U = 0.4$, the leading-edge vortex actually seems to be in a developing state, whereby a well-defined front of the vortex appears to occur. It appears that, at this highest value of pitch rate, the complete development of the leading-edge vortex appears not to be attainable, due to the very rapid pitch-up motion.

Figure D3 shows patterns of near-surface velocity vectors. The overall form of these patterns is in accord with the dye visualization shown in Figure D2. A prevalent feature is that, at sufficiently high values of pitch rate, $\dot{\alpha}\,C/U = 0.1$ and larger, the locus of the center of the region of large magnitude velocity vectors actually moves towards the leading-edge of the wing. The consequence is a substantial region of low velocity, that is, a large-scale velocity defect region, near the plane of symmetry of the wing.

The foregoing patterns of near-surface velocity are related to the patterns of near-surface streamline topology shown in Figure D4. At the lowest value of pitch rate, $\dot{\alpha}\,C/U = 0.05$, a number of saddle points S and foci F occur along the leading-edge of the wing. The negative bifurcation line BL^- is of limited streamwise extent and occurs only near the apex of the wing. As the value of dimensionless pitch rate $\dot{\alpha}\,C/U$ is successively increased to larger values, these saddle points S and foci F become smaller in number until, at the largest value of $\dot{\alpha}\,C/U = 0.4$, they are not evident at all in the near-surface topology. Furthermore, the negative bifurcation line BL^- exists along the entire leading-edge of the wing.

RELAXATION OF NEAR-SURFACE FLOW STRUCTURE AND TOPOLOGY

In the preceding section, the near-surface patterns at cessation of the wing motion were compared as a function of pitching rate $\dot{\alpha}\,C/U$. In this section, a representative relaxation process is described for a single value of pitch rate $\dot{\alpha}\,C/U = 0.2$. Figure D5 shows patterns of velocity vectors that occur during successive stages of this relaxation process. The states of the flow structure, defined as State 1 through State 5, are defined on the α vs. t schematic given at the bottom of Figure D5.

State 1, which occurs at $t^* = 0$, corresponding to cessation of the pitch-up motion, shows a well-defined pattern of relatively large magnitude velocity vectors. In State 2, the pattern of vectors becomes somewhat less defined, and complex patterns of low magnitude vectors occur along the leading-edge. In State 3, there is onset of a pronounced flow in the upstream direction along the leading-edge of the wing, and in State 4, this upstream oriented jet-like flow along the leading-edge still persists. In the inboard region of the wing of State 4, the onset of a large-scale swirl pattern is evident. Finally, in State 5, the upstream oriented flow is still evident along the leading-edge, but the flow structure appears to be dominated by the large-scale swirl pattern in the inboard region of the wing.

The sequence of states of velocity vectors shown in Figure D5 corresponds to the patterns of instantaneous streamline topology given in Figure D6. The primary feature of the topological pattern of State 1 is the bifurcation line BL^- that persists along the entire leading-edge, and a saddle point S inboard from the leading-edge. In State 2, a large number of critical points, predominantly foci F and saddle points S, exist in the leading-edge region. In fact, this multiplicity of critical points along the leading-edge is part of the transformation process to State

3, where a well-defined, upstream oriented flow exists along the leading-edge of the wing. The bifurcation line is now oriented towards the apex, rather than away from the apex, as is the case in State 1. In State 4, onset of a large-scale swirl pattern occurs inboard of the leading-edge of the wing, and in State 5, this swirl pattern becomes more distinct and coherent.

The topological states given in Figure D6 have been shown to occur irrespective of the value of pitch rate *C/U* employed, though the delay time for their onset, following cessation of the wing motion, does vary significantly with the pitch rate. These details, as well as other features, including time-averaged patterns of topology during the relaxation process, in comparison with patterns of topology that occur on a stationary wing at lower angle-of-attack, will be described in detail in a subsequent write-up.

LIST OF REFERENCES

Goruney, T. 2008 "Investigation of Flow Structure on a Pitching Delta Wing of Moderate Sweep Angle using Stereoscopic Particle Image Velocimetry: Passive Control of Flow Structure via Leading Edge Protuberances", Ph.D. Dissertation, Department of Mechanical Engineering and Mechanics, Lehigh University, Bethlehem, PA.

Yavuz, M. and Rockwell, D. 2006 "Identification and Control of Three-Dimensional Separation on Low Swept Delta Wing Angle", *AIAA Journal*, Vol. 44, No. 11, November, pp. 2805-2811.

Yavuz, M. and Rockwell, D. 2006 "Control of Flow Structure on Delta Wing with Steady Trailing Edge Blowing", *AIAA Journal*, Vol. 44, No. 3, March, pp. 493-501.

LIST OF FIGURES

Figure D1. Schematics showing the terminal position of the wing after cessation of a pitch-up maneuver in conjunction with the location of the laser sheet for characterization of the near-surface flow structure.

Figure D2. Dye visualization of structure of leading-edge vortex at instant corresponding to cessation of pitch-up maneuver for different values of pitch rate.

Figure D3. Patterns of instantaneous velocity immediately adjacent to surface of wing at the instant corresponding to termination of pitch-up maneuver for four different values of dimensionless pitch rate.

Figure D4. Patterns of near-surface streamline topology at instant corresponding to termination of pitch-up maneuver for four different values of pitch rate.

Figure D5. Relaxation process of near-surface patterns following termination of pitch-up maneuver of wing. Successive images show states of the flow structure for increasing values of time.

Figure D6. Patterns of near-surface streamline topology during relaxation process, following termination of pitch-up motion of wing. Defined states of topology occur at successive values of time following attainment of the maximum angle-of-attack.

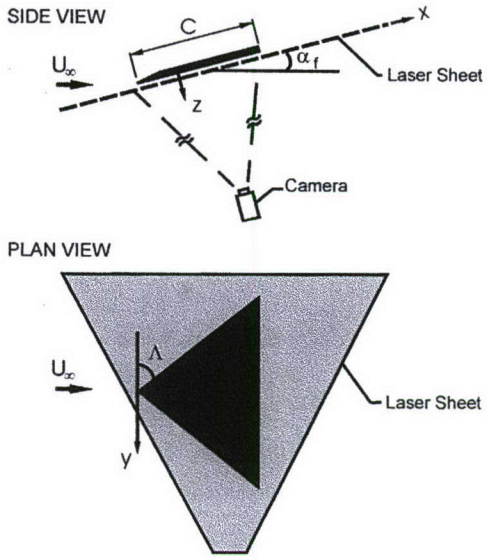


Figure D1. Schematics showing the terminal position of the wing after cessation of a pitch-up maneuver in conjunction with the location of the laser sheet for characterization of the near-surface flow structure.

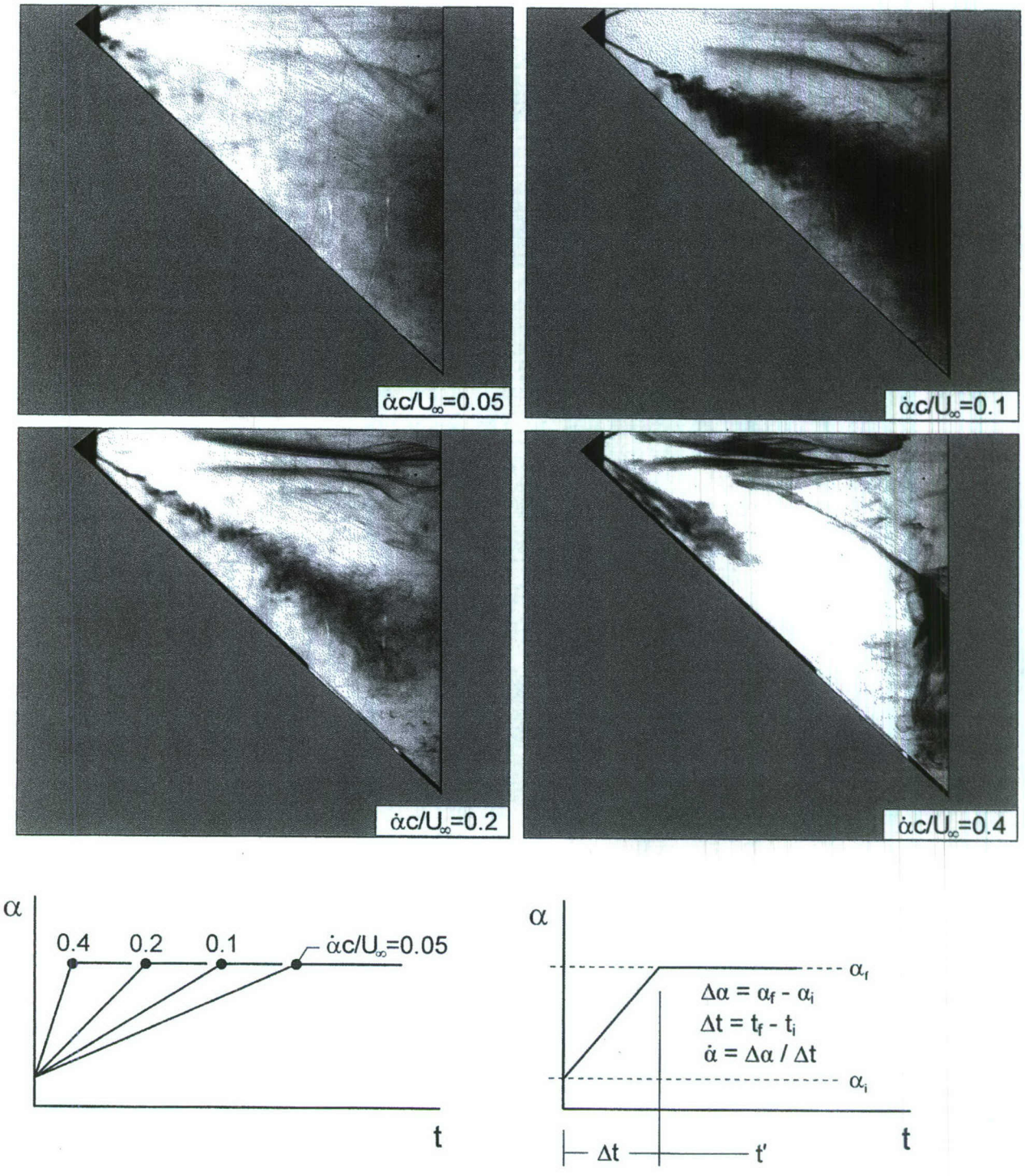


Figure D2. Dye visualization of structure of leading-edge vortex at instant corresponding to cessation of pitch-up maneuver for different values of pitch rate.

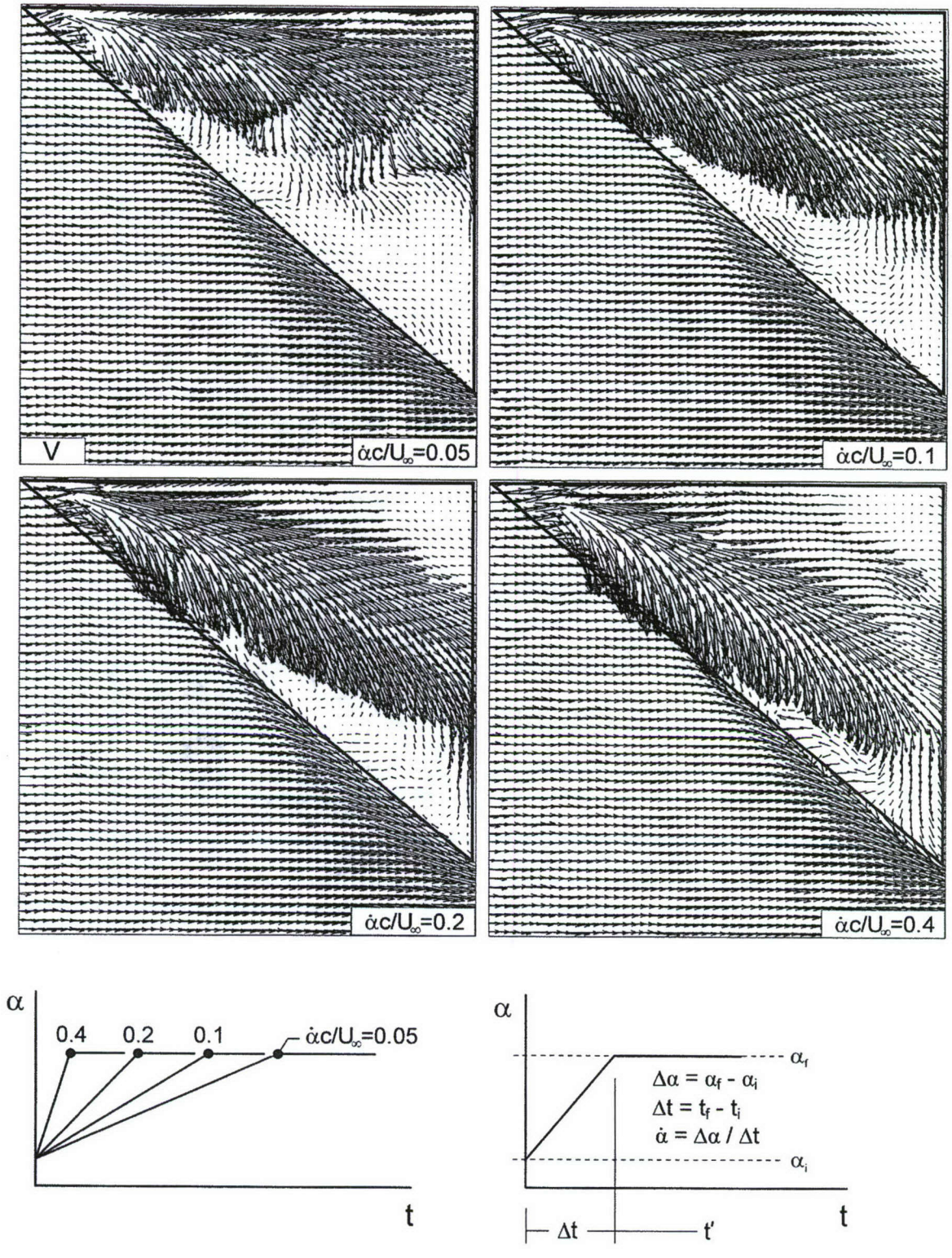


Figure D3. Patterns of instantaneous velocity immediately adjacent to surface of wing at the instant corresponding to termination of pitch-up maneuver for four different values of dimensionless pitch rate.

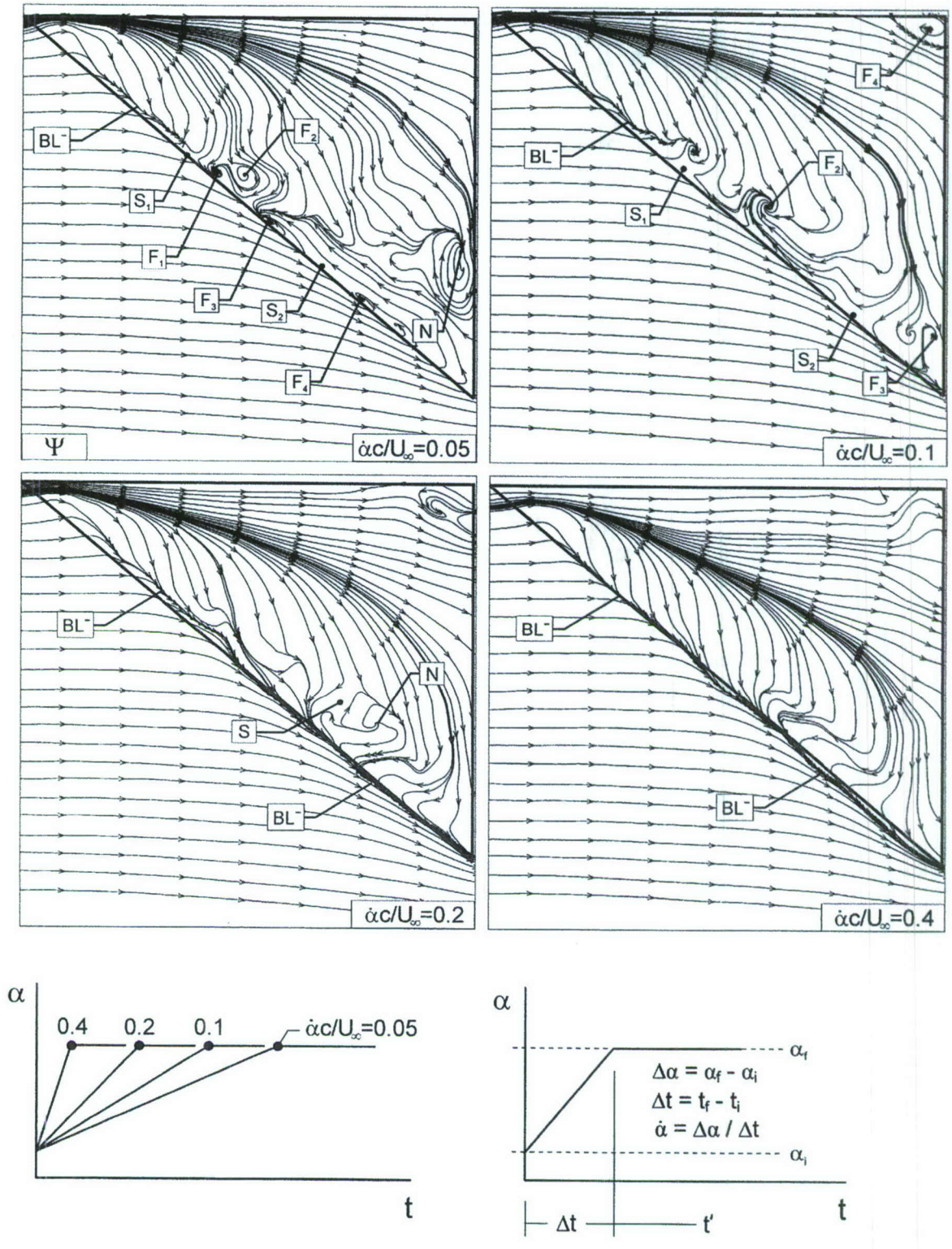


Figure D4. Patterns of near-surface streamline topology at instant corresponding to termination of pitch-up maneuver for four different values of pitch rate.

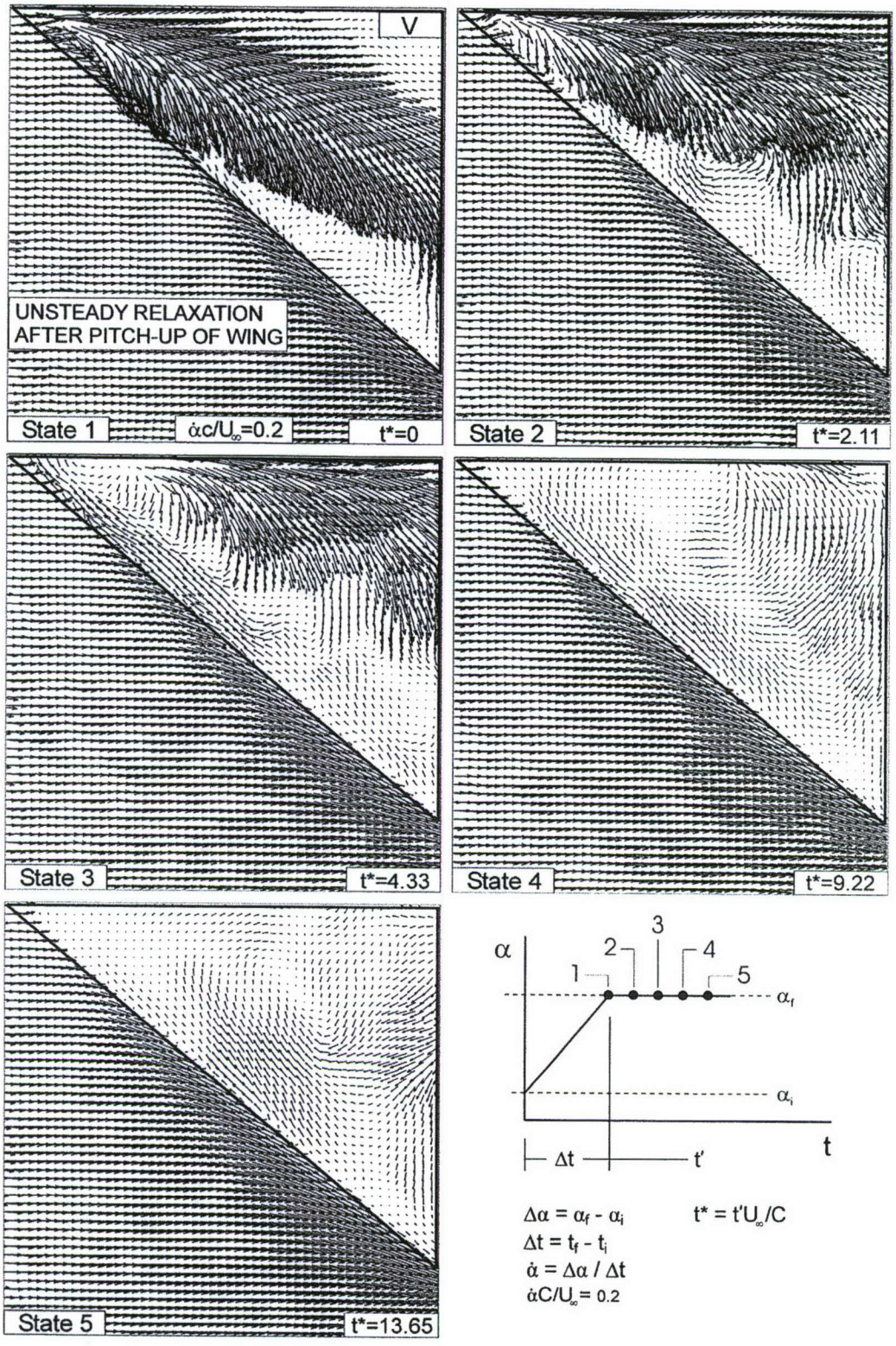


Figure D5. Relaxation process of near-surface patterns following termination of pitch-up maneuver of wing. Successive images show states of the flow structure for increasing values of time.

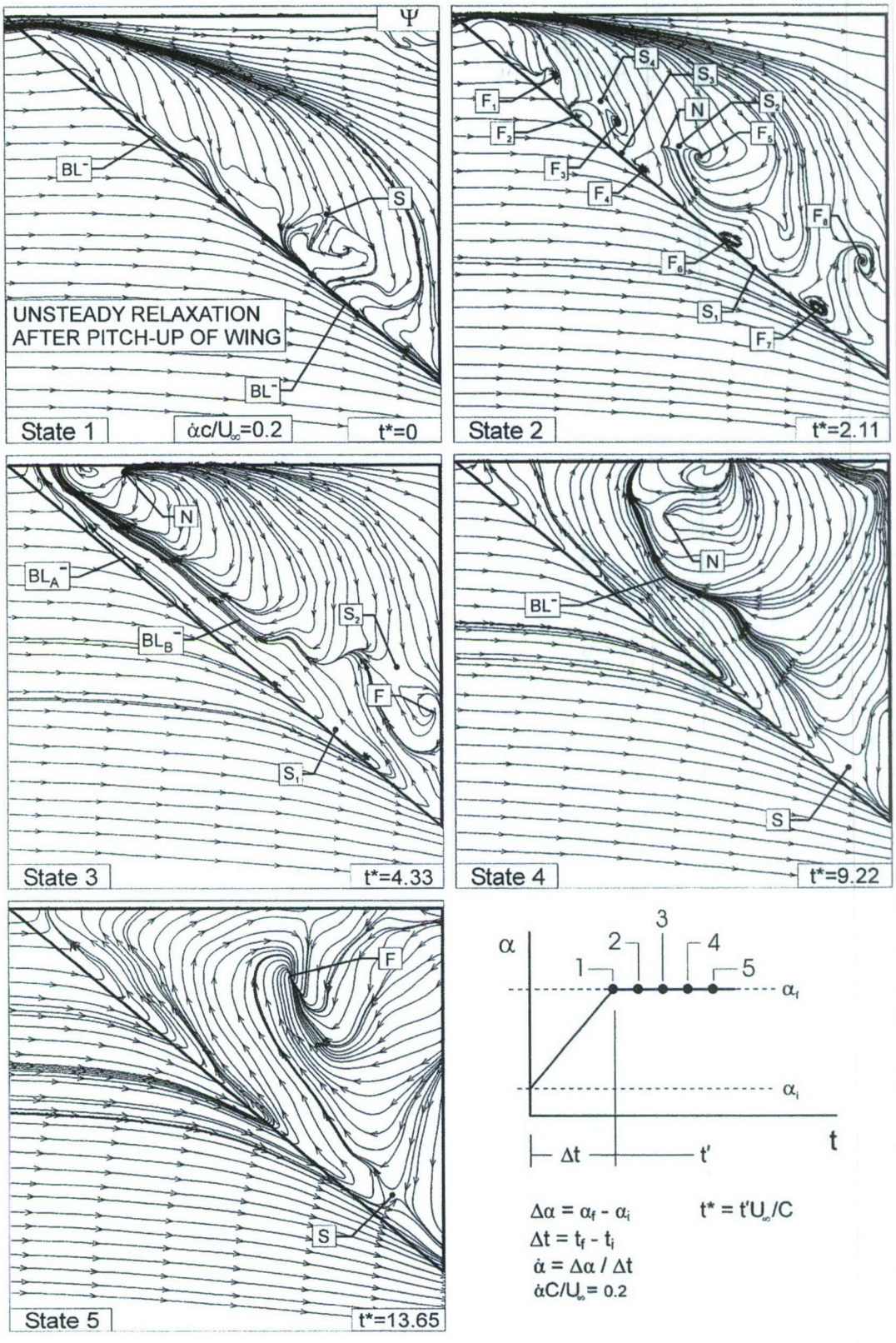


Figure D6. Patterns of near-surface streamline topology during relaxation process, following termination of pitch-up motion of wing. Defined states of topology occur at successive values of time following attainment of the maximum angle-of-attack.

Appendix E

FLOW STRUCTURE ALONG A 1303 UNMANNED COMBAT AIR VEHICLE

by

M. A. Kosoglu and D. Rockwell
Department of Mechanical Engineering and Mechanics
Lehigh University
356 Packard Laboratory
19 Memorial Drive West
Bethlehem, PA 18015

ABSTRACT

The 1303 Unmanned Combat Air Vehicle is representative of a variety of UCAVs with blended wing-body configurations. The flow structure along a scale model of this configuration was investigated using dye visualization and particle image velocimetry, for variations of Reynolds number and angle-of-attack. Both of these parameters substantially influence the onset and structure of the leading-edge vortex (LEV) and a separation bubble/stall region along the tip. The onset of formation of the LEV initially occurs at a location well downstream of the apex, and moves upstream for increasing values of either Reynolds number or angle-of-attack. In cases where a separation bubble or stall region exists, quantitative information on its structure was obtained via PIV imaging on a plane nearly parallel to the surface of the wing. By acquiring images on planes at successively larger elevations from the surface, it was possible to gain insight into the space-time features of the three-dimensional structure of the bubble or stall region, which is highly time-dependent. Both the scale of this region and the corresponding velocity patterns show large variations. Time-averaged images indicate that the maximum velocity defect decreases in magnitude and moves in the downstream direction with increasing elevation from the surface of the wing.

1. INTRODUCTION

Leading-edge-vortices, i.e., LEVs, are the main feature of flow past a simple delta wing of given sweep angle. Their existence enhances the ability of a delta wing to generate substantial lift at higher angles-of-attack. Formation, breakdown and three-dimensional characteristics of LEVs on delta wings have been a subject of research for decades. The focus of the present investigation is on a planform having a more complex configuration than a simple delta wing, and for which the existence and nature of leading-edge vortices is unclear. Moreover, it has a well defined wing tip, and separation and stall may occur in this region. This type of flow pattern may contribute to destabilization of the flight mechanics of the UCAV.

1.1 Practical Aspects of 1303 UCAV

The 1303 UCAV was created at the Boeing Phantom Works, under contract to the Air Vehicles Directorate of Air Force Research Labs (McParlin et al., 2003). The 1303 configuration is representative of a variety of UCAVs with blended wing-body configurations (Ol, 2006). The

US Naval Air Systems Command (NAVAIR) has investigated the low speed characteristics of the 1303 UCAV (McParlin et al., 2003).

The 1303 is an "edge-aligned", "near-lambda" delta wing which has a concave trailing edge crank at or near the mid-semispan and a convex trailing edge crank. These cranks can cause several problems with aerodynamic performance. The local minimum in the chord from the inboard trailing edge crank causes a local maximum in the sectional lift coefficient. Similarly, the outboard crank can generate a local minimum in the local lift coefficient (McParlin et al., 2003). Flow separation may occur at or near either of these local extrema and spread rapidly in the outboard direction. This rapid spreading may lead to fully separated flow over the outboard wing panel and any trailing edge devices installed at that location. The loss of effectiveness of outboard control surfaces is associated with a reduction in lateral control authority (McParlin et al., 2003).

For this configuration, as a result of the onset and development of flow separation over the outer portion of the wing, the centroid of lift of the wing may tend to shift inboard and forward. This can result in an occurrence of rapid and unstable pitch-up. This is also called a pitch break situation, in which the curve of the pitching moment vs. angle-of-attack reverses from stable to unstable at an angle-of-attack far below that of the maximum lift coefficient (Ol, 2006). This phenomenon can impose limits on the useable lift. Lower maximum useable lift coefficient indicates greater landing and take-off speeds, which can be an issue for all UCAVs, especially those intended to be used in carrier based operations (McParlin et al., 2003).

1.2 Previous Investigations of 1303 UCAV

This pitch break phenomena can be very critical, and it is hypothesized that some persistent flow separation is the cause (Ol, 2006). To investigate this, a 1303 UCAV model was tested in the QinetiQ low-speed wind tunnel (McParlin et al., 2003). Pressure tap data from the study demonstrated that the pitch break is due to tip stall with an increase in suction near the apex, possibly from LEV formation from the apex (Ol, 2006). For the "sharp" leading edge case, the pitch break has been shown to occur at $\alpha = 6°$ (Ol, 2006).

The 1303 UCAV configuration with a sharp leading edge was also tested in the AFRL water tunnel in an effort to investigate the possibility of smaller scale water tunnel testing as an alternative to wind tunnels. This study, with the aforementioned pressure distributions in mind, suggests that tip stall may be the main contributor to the "pitch break" phenomenon. LEV formation was not a factor in the water tunnel experiments at $\alpha = 6°$, which is the angle-of-attack for the pitch break onset in the QinetiQ wind tunnel test. It was found that 1303 the UCAV configuration shows signs of tip stall at Re = 32,000, as indicated in the foregoing. Moreover, at this angle-of-attack and Re, the "pitch break" explained earlier is hypothesized to be the result of loss of attached-flow suction at the tip, accompanied by a slight increase in suction near the apex (Ol, 2006). Ol (2006) obtained velocity data from PIV and compared patterns in the tip region with patterns at locations further inboard. He deduced that, at $\alpha = 6°$, the stall region grows from the tip and moves inboard. That is, the flow around the tip is noticeably separated while the flow inboard of the tip is highly attached. It was also stated that a small laminar bubble divides these two regions (Ol, 2006).

Ol (2006) reported that LEV formation was not visualized via dye injection at $\alpha = 6°$, but at $\alpha = 12°$ and Re = 32,000, a distinct LEV was detected in a single realization. This result is given in Figure E1 Ol (2006) found that, at $\alpha = 12°$, LEV formation can occur in accord with outboard branching of the dye visualization immediately downstream of the apex. On the basis of his experiments, Ol (2006) recommended that dye injection ports be located inside the model, and connected to tubes at the aft end, perhaps near the string amount.

Another study of the flow structure on the 1303 UCAV geometry was performed by Nelson et al. (2007). By using a special casting method they were able to place two dye ports inside the wing model. With the dye coming out of two holes on the surface of the wing, located very close to the apex, they were able to visualize the occurrence of a leading-edge-vortex at angles-of-attack $\alpha > 8°$. At lower angles-of-attack, it was concluded that the flow is dominated by a mean flow in the transverse direction. Also there was evidence of considerable reverse flow near the wing tip. This flow structure was referred to as "tip stall" in previous investigations.

1.3. Recent Investigations of Delta Wings of Low-and Moderate-Sweep Angle

Delta wings have been used for several decades in combat and supersonic aircraft. The wings usually have a large sweep angle. However, pure delta wings of small or moderate sweep have been employed less frequently, perhaps due to questions related to the stable and manageable presence of LEVs (Ol and Gharib, 2003). A comprehensive overview of previous related investigations of the flow structure on delta wings of low and moderate sweep angles is beyond the scope of the present study. In the following, selected citations are provided.

Delta wings of low and moderate sweep angles have been researched by Gursul et al. (2002). They used dye visualization to illustrate the flow patterns over moderately swept delta wings with different planforms. PIV was used in order to quantitatively measure the vortex cores in the crossflow planes. Stereo particle image velocimetry (SPIV) was employed by Ol and Gharib (2003) to illustrate three-dimensional features of the flow over 50 and 65 degree swept delta wings. They also demonstrated the upstream progression of vortex breakdown with increasing angle-of-attack. Yaniktepe and Rockwell (2004) and Yavuz et al. (2005) investigated the flow structure in crossflow and near-surface planes for delta wings having relatively low values of sweep angle. The time-averaged flow patterns were accompanied by representations of the flow unsteadiness, including spectral analysis of the structure. Elkhoury and Rockwell (2004) investigated the Reynolds number dependence of vortices on a UCAV planform using dye visualization. The first numerical simulation of the flow structure on delta wings of moderate sweep angle was done by Gordnier and Visbal (2003). Their research illustrated substructures in the shear layer separating from the leading-edge of the wing.

Rullan et al. (2005) investigated the flow on delta wings of 30 and 40 sweep angles and the effect of unsteady blowing at the leading edge of a sharp LE wing. The effect of blowing at the trailing edge was researched by Yavuz and Rockwell (2006).

All of the foregoing investigations, as well as a number of other important, related investigations, provide background for the present study. The planform of the 1303 UCAV is, however, particularly complex, and one expects distinctive features of the flow patterns relative to a simple delta wing.

1.4 Unresolved Issues

The investigations of the 1303 UCAV described in the foregoing have provided an important framework for the present study. Taking into account these investigations, as well as the need for more detailed studies, selected issues may be summarized as follows.

Qualitative visualization using dye injection, extending over a larger extent of the planform, can provide further insight into the flow structure as a function of both angle-of-attack and Reynolds number. In particular, the onset and development of leading-edge vortices, as well as separation bubbles and stall regions, have not been fully clarified.

In cases where a stall region exists, quantitative information on its detailed structure has not yet been obtained. The spatial extent and character of this region along the surface of wing has not been defined in detail. Quantitative representations along a plane oriented nearly parallel to the wing surface would provide a first level of insight. Furthermore, the manner in which the quantitative structure varies as a function of elevation above the surface of the wing has not been characterized, yet this type of information would be helpful to understand the three-dimensional structure of the stall region. Finally, the instantaneous structure of the stall region, relative to its time-averaged structure, would be informative, as it would provide a physical means for interpretation of the flow unsteadiness.

2. EXPERIMENTAL SYSTEM AND TECHNIQUES

A large-scale, low-turbulence water channel in the Fluid Mechanics Laboratories at Lehigh University was used for the experiments in this study. These experiments include dye visualization and near-surface particle image velocimetry for different angles-of-attack and Reynolds numbers of a 1303 UCAV.

Figure E2 gives an overview of the water channel system. It has a test section that is 613 mm wide, 594 mm deep and 5435 mm long. The free surface of the water in the channel is kept at a height of 508 mm. Plexiglas® was used to manufacture the walls of the test section for optical transparency and the reservoirs are made of PVC (polyvinyl chloride). Water that filled the tank was filtered by use of two 1 μm filters to ensure adequate water clarity in the channel for better dye visualization and PIV results.

Upstream of the test section, the flow was conditioned by a honeycomb, a series of four screens and a 3:1 contraction. This conditioning yielded a very low level of free-stream turbulence intensity of less than 0.1%. Perturbations in the flow occurring at locations downstream of the delta wing and sting system were damped by a honeycomb and a settling tank at the downstream end.

The 1303 UCAV model has a leading edge sweep of 47° and a root chord of 177 mm. It has a cranked sharp trailing edge, and aft-rounded tips. This model was made of PVC, and manufactured by a single axis CNC machine in two parts: starboard and port (left and right). The components of the wing were held together by very viscous silicon grease and two 6 mm brass dowel pins.

The rotational speed of the pump motor is controlled with a controller unit in order to achieve various values of Reynolds number for the experiments. Calibration of the revolutions per minute of the motor to the uniform speed of the water at a given temperature in the water channel was done before the start of the experiments. The calibration is given in Figure E3 For a water temperature of 25°C, and freestream velocity $U = 51.66$, the Reynolds numbers based on chord C was 10,000. A floating thermometer was used to measure the temperature of the water in order to track the changes in viscosity.

A support system was designed and manufactured in order to hold the delta wing in position for different angles-of-attack. Side and plan views of the wing, the support system and dye supply are given in Figures E4, and E5. A horizontal, a vertical, and a rotational traverse were used to move the wing in two directions and about a single axis. This allowed the wing to be placed at different angles-of-attack with minimal or no changes of the location of the laser sheet. This is a desired advantage for PIV experiments. The angle-of-attack of the wing was measured from its sharp leading-edge at the starboard side. The alignment laser that is shown in Figures E4 and E5 is generated by a commercially available laser-compass that emits a thin laser sheet at some angle. The angle of the alignment laser is measured by a magnetic protractor, which measures the angle of some object by taking the direction of the gravitational force as a zero reference. When this thin laser sheet exactly matches the leading-edge of the wing the wing, it is assumed to be at the same angle as the alignment laser.

Dye visualization technique was used in order to visualize the flow structures on the 1303 UCAV. A mixture of a generic food dye and tap water with an approximate 1:8 ratio of dye to water was used. The mixture was inserted through the dye ports inside the wing. Dye was carried through these four dye ports and was injected to the flow through the four holes on the surface of the wing. These holes are located at 0.03, 0.1, 0.2 and 0.3 chord-wise locations, and they are placed to be as close to the leading-edge as possible. Each dye hole had a diameter of 1 mm.

A dye supply with flow rate control was used in order to achieve a constant dye flow. During the experiments it was observed that larger flow rates of dye through the dye ports deflected the dye pattern away from the surface of the wing. As one expects, large quantities of dye are needed in order visualize the flow structure, such as leading-edge vortices or tip stall. So, for each experiment, an optimum dye flow was used, while making sure that the injected dye remained sufficiently close to the surface.

Particle image velocimetry technique was used for quantitatively visualizing the flow structure on the 1303 UCAV. This technique consists of generating a sequence of instantaneous velocity fields over the area of interest (field of view) without generating any disturbance in the flow field. Reviews of the advances of this technique have been published by Adrian (1986, 1988) and Westerweel (1993, 1997). In this study, a TSI-based digital particle image velocimetry system was used. Figure 2.4 is a representation of the overview of the experimental components of the DPIV system. It includes a TSI synchronizer (model 610032); a 90 mJ Nd:Yag double-pulsed laser system (532 nm); a CCD digital camera model PowerView^{TM} 2M+ (60057) ; a frame grabber model 600070; and Insight^{TM} software version 6.0. The flow was seeded with 12 micron metallic-coated hollow plastic spheres which have nearly neutral buoyancy. The seeding density was sufficient for high image density PIV. These particles were illuminated with two short duration laser pulses by the dual pulsed Nd: Yag laser. The maximum repetition rate of each laser head is 30 Hz. In this study, a 15 Hz repetition rate was used.

A digital charge-coupled-device (CCD) camera along with a frame grabber card was used to capture and record the particle images. The resolution of the camera was 1600 × 1200 pixels. However, due to the limited capacity of this particular frame grabber, only approximately 40 percent of the capture area could be used for experiments at the 15 Hz sampling rate. If a larger capture area were to be used, the images captured by the frame grabber would be slightly off from the actual pulses of the laser, which resulted in bad velocity fields. However the smaller capture area did not raise an issue about resolution of the PIV because the tip stall region investigated is fairly small, about the size of a 45 mm × 60 mm rectangle. Also the lack of speed of the frame grabber created no problems for dye visualization tests. The camera was equipped with a lens of focal length 28 mm for dye visualization experiments, which gives a larger field of view that encompasses the entire half wing. For the PIV experiments, a lens of focal length 60 mm was used. Figure E6 illustrates the interrelationship of the DPIV components.

Considering that 1303 UCAV configuration is symmetric, flow visualization and PIV were performed only for one half of the wing. In order to obtain a thin laser sheet, two -15 mm focal length cylindrical lenses and a spherical lens of 500 mm focal length were used respectively. The laser sheet was approximately 3/4 mm thick at the center of the half wing. The center of the laser sheet was located at several positions starting at an elevation of 1 mm from the wing surface and extending up to 20 mm in some cases. The laser sheet at 1 mm away from the surface corresponds to $\Delta/C = 0.006$, where C is the chord.

The instantaneous velocity fields are generated by interrogating a pair of single-exposed frames by utilizing a spatial frame-to-frame cross-correlation technique for the time period between the two laser pulses. The Hart correlation technique was used in this study because of the shorter processing time needed to complete the correlations. The interrogation window size was 32 pixels × 32 pixels. In order to satisfy the Nyquist criterion, 50% overlap was used during the interrogation process. The effective grid size in the plane of the laser sheet was approximately 80 mm × 90 mm. A total of 200 instantaneous image couples were obtained for each experiment.

Post-processing of raw velocity fields followed the schematic which is shown in Figure E7. Validation data was done by utilizing the software CLEANVEC. CLEANVEC was utilized in order to perform vector validation according to the following criteria: root-mean-square fluctuation, absolute range, magnitude difference and median magnitudes.

The NFILVB program created by Lin (1994) of the Fluid Mechanics Laboratories was used to fill the missing vectors that were removed by the CLEANVEC program earlier in the post-processing. NFILVB applies a bilinear interpolation technique with a least squares fit. This program also evaluates the instantaneous vorticity fields which were not used in the current study. In addition, data smoothing with an axisymmetric Gaussian smoothing kernel with parameter $\sigma = 1.3$ was utilized to reduce the error-based deviations.

The mean (time-averaged) velocity fields were generated by the in-house program NWENSAV2 which was formulated by Lin (1996).

The data were transformed to the final formats by utilizing Tecplot 360; these formats include velocity vectors, contours of streamwise and transverse velocity both in instantaneous

and averaged form, as well as root-mean-squares of streamwise and transverse velocity. The images in this thesis were prepared using CorelDRAW. The overview of the entire post-processing procedure is given in Figure E7.

In short, the aim of this study was to investigate the flow patterns on a 1303 UCAV. Experimental results are given in the sections that follow.

3. DISCUSSION OF RESULTS

3.1 Dye Visualization

Figures E8 through E12 show the patterns of dye visualization along the scale model of the 1303 UCAV over a Reynolds number range of Re = 1.0×10^4 to 5.0×10^4, and for angles-of-attack α = 4°, 6°, 9° and 12°. Figure 3.1 shows the flow of dye in the transverse direction, from the mid-plane towards the tip of the delta wing, at angles-of-attack α = 4° and 6°, and at Reynolds numbers Re = 10,000, 30,000 and 50,000.

Figure E8 shows that the first formation of a very distinct LEV is at angle-of-attack α = 6° and Reynolds number Re = 50,000. At angles-of-attack α = 9° and 12°, distinctive LEV formation can be seen at a value of Reynolds number Re = 30,000.

Figure E9 demonstrates the Reynolds number dependence of the onset the of LEV formation along a 1303 UCAV. For α = 9° and 12° the onset of formation of the LEV progresses upstream as the Reynolds number increases from 30,000 to 50,000. The LEV formation begins from the apex at 12° angle-of-attack and a value of Reynolds number of 50,000.

Patterns of dye visualization at constant Reynolds number and various values of angle-of-attack are given in Figures E10 through E12. Figure E12 shows the sensitivity of the onset of the LEV formation to changes in the angle-of-attack at a Reynolds number Re = 50,000. While there are no signs of a LEV at angle-of-attack α = 4°, it does occur at α = 6°. For α = 9° and α =12° at Re = 50,000, there is clear evidence of LEVs originating from upstream locations of the leading-edge. From Figure E12, it can be observed that for a Reynolds number Re = 50,000 at α = 6°, the onset location of the LEV is located between the third and fourth holes away from the apex. At 9°, the onset of the LEV formation is at a location between the first and second holes, while at 12° the LEV formation occurs very close to the apex.

As it is shown in Figure E8, signs of tip stall can be seen even at the angle-of-attack α = 4° and Reynolds number Re = 10,000. Figure E8 illustrates that the center of the stall region moves upstream as Reynolds number increases. At α = 4° and Re = 50,000, the flow over the tip region is fully separated. In Figure E10, one can see that the stall region moves upstream and also inboard with increased angle-of-attack, generating a large circulating flow region that can be visualized only at Re = 10,000, which is prior to the occurrence of the LEV.

3.2 Particle Image Velocimetry

Extensive quantitative imaging of the flow structure was undertaken using techniques of particle image velocimetry. A range of angle-of-attack and Reynolds number were considered in

accord with dye visualization indicated in the foregoing section. In the following, a limited number of selected excerpts of this imaging is presented as representative. Further details are available in the M.S. thesis of Kosoglu (2007) and can be obtained by contacting the Department of Mechanical Engineering and Mechanics at Lehigh University.

In the images that follow, the Reynolds number, based on root chord was maintained at 50,000 for all cases. Near-surface PIV was done at different locations away from the surface. The distance from the surface Δ is normalized by chord C. The orientation of the laser sheet and proximity of the laser sheet to the surface are given in Figure E13. The orientation and location of the laser sheet are given in the image layouts described in the following.

Figure E14 shows contours of time-averaged streamwise $\langle u \rangle / U$ for different values of displacement Δ/C of the laser sheet from the surface of the wing at an angle-of-attack $\alpha = 6°$. It is apparent that the maximum magnitude of negative velocity occurs in the laser sheet location closest to the wing, at $\Delta/C = 0.066$. For further elevations from the surface, that is, for increasingly larger values of Δ/C, the extent of the region of negative or low velocity decreases substantially, until, at the largest elevation $\Delta/C = 0.024$, this region represented by the closed contours appears only over a limited extent of the wing, that is, it includes only the small region near the wing tip. This portrayal gives an indication of the overall volume extent of the region of separation.

Figure E15 shows a vertical, stacked arrangement of the patterns of Figure E14. This portrayal of the region of separation/stall provides a good indication of the spatial extent in each plane, as well as in the vertical direction.

The overview of Figure E16 shows patterns of velocity vectors along with other averaged and instantaneous representation of the flow structure on a plane very close to wing surface. All of these images are time-averaged representations, with the exception of the bottom two images at the left, which show instantaneous patterns of streamwise velocity u/U. As is evident, the states of the flow are indeed extreme. In other words, these instantaneous representations differ substantially from each other, and show the rather large variations of the flow structure with time. Patterns of root-mean-square velocity fluctuation associated with these excursions are not included herein, but are available in the M.S. thesis of Kosoglu (2007).

4. CONCLUSIONS

The goal of this investigation is to understand the flow physics associated with the flow along a 1303 UCAV. The focus was on the formation of the LEV and the stall occurring at the wing tip.

It was found that there is an indication of LEV formation as early as an angle-of-attack $\alpha = 6°$. The results of dye visualization showed that tip stall is apparent at all angles-of-attack, and it moves in the upstream direction and inboard as the angle-of-attack or Reynolds number increases.

Near-surface PIV was employed to characterize the physics of tip stall. The scale of the stall region varies with angle-of-attack and the distance from the surface of the wing. The center of the stalled region moves upstream as angle-of-attack increases, and is located further

downstream with the increasing distance from the surface of wing. Moreover, the scale of the stalled region increases with increasing angle of attack, but decreases with increasing distance from the wing. Also, it was shown that the stall region increases in scale in the surface normal direction as the angle-of-attack increases.

This stall region in the vicinity of the tip is also highly time-dependent. That is, its instantaneous structure shows large departures from the time-averaged structure. These departures correspond to relatively large magnitudes of the root-mean-square values of the streamwise and transverse velocities.

LIST OF REFERENCES

Attar, P. J., Gordnier, R. E. and Visbal, M. R. 2006 "Numerical Simulation of the Buffet of a Full Span Delta Wing at High Angle of Attack", Structural Dynamics and Materials Conference, Vol. 8, Collection of Technical Papers – 47th AIAA/ASME/ASCE/AHS/ASC Structures, Structural Dynamics and Materials Conference: 14th AIAA/ASME/AHS Adaptive Structures Conference, 8th AIAA Non-Deterministic APP, pp. 5783-5805.

McParlin, S. C., Bruce, R. J., Hepworth, A.G., and Rae, A. J. 2003 "Low Speed Wind Tunnel Tests on the 1303 UCAV Concept", QinetiQ/fST/tR025502/1.0, QinetiQ, Ltd., Farnborough, UK, March.

Elkhoury, M. and Rockwell, D. 2004 "Visualized Vortices on Unmanned Combat Air Vehicle Planform: Effect of Reynolds Number", *AIAA Journal of Aircraft*, Vol. 41, No. 5, September/October, pp. 1244-1247.

Gursul, I., Taylor, G., and Wooding, C. L. 2002 "Vortex Flows over Fixed-Wing Micro Air Vehicles", AIAA 2002-0698.

Jeon, D. Ph.D. Thesis, California Institute of Technology, 2000.

Kosoglu, M. A. 2007 "Flow Structures along a 1303 Unmanned Combat Air Vehicle", M.S. Thesis, Department of Mechanical Engineering and Mechanics, Lehigh University, Bethlehem, PA.

Miau, J. J., Kuo, K. T., Liu, W. H. Hsieh, S. J., Chou, J. H. and Lin, C. K. 1995 "Flow Developments above 50° Sweep Delta Wings with Different Leading-Edge Profiles", *AIAA Journal of Aircraft*, Vol. 32, No. 4, July-August.

Nelson, R. C., Corke, T. C., He, C., Othman, H. and Matsuno, T. 2007 "Modification of the Flow Structure over a UAV Wing for Roll Control", 45th AIAA Aerospace Sciences Meeting and Exhibit, January 8-11, Reno, NV, AIAA-2007-884.

Ol, M. 2006 "Water Tunnel Velocimetry Results for the 1303 UCAV Configuration", Collection of Technical Papers, 24th AIAA Applied Aerodynamics Conference, 2006, AIAA 2006-2990, 546-557.

Ol, M. V. and Gharib, M. 2003 "Leading-Edge Vortex Structure of Nonslender Delta Wings at Low Reynolds Number", *AIAA Journal*, Vol. 41, No. 1, January, pp. 16-26.

Ol, M., McAuliffe, B. R., Hanff, E. S. Scholz, U., Kaehler, Ch., 2005 "Comparison of Laminar Separation Bubble Measurements on a Low Reynolds Number Airfoil in Three Facilities", AIAA 2005-5149.

Poisson-Quinton, P. and Werle, H. 1967 "Water-Tunnel Visualization of Vortex Flow". *Aeronautics and Astronautics*, June, pp. 64-66.

Rullan, J., Gibbs, J., Vlachos, P., Telionis, D. and Zeiger, M. 2005 "The Aerodynamics of Low-Sweep Trapezoidal Wings", AIAA-2005-0059.

Taylor, G. S. and Gursul, I. 2004 "Unsteady Vortex Flows and Buffeting of a Low Sweep Delta Angle", 42nd AIAA Aerospace Sciences Meeting and Exhibit, January 5-8, 2004, Reno, NV, AIAA-2004-1066.
Taylor, G. S. and Gursul, I. 2004 "Buffeting Flows over a Low-Sweep Delta Wing", *AIAA Journal*, Vol. 42, No. 9, September, pp. 1737-1745.

Tyler, C., Baust, H., Elliott, G. and Crafton, J. 2005 "Multiple Computational Simulations Performed for Comparison with Planar Doppler Velocimetry Measurements", AIAA-2005-0440. January.

Willert, C. E. and Gharib, 1991 M. "Digital Particle Image Velocimetry", *Experiments in Fluids*, Vol. 10, pp. 181-193.

Yaniktepe, B. and Rockwell, D. 2004 "Flow Structure on a Delta Wing of Low Sweep Angle", *AIAA Journal*, Vol. 42, No. 3, March, pp. 513-523.

Yavuz, M. and Rockwell, D. 2006 "Identification and Control of Three-Dimensional Separation on Low Swept Delta Wing Angle", *AIAA Journal*, Vol. 44, No. 11, November, pp. 2805-2811.

List of Figures

Figure E1. Dye visualization of flow structure at angle-of-attack a = 12° and for a value of Reynolds number Re = 32,000 based on chord (Ol, 2006).

Figure E2. Schematic of the recirculating type free-surface water channel facility.

Figure E3. Channel calibration curve.

Figure E4. Side view of experimental system.

Figure E5. Solid model representations of 1303 UCAV and designation of location of laser sheet.

Figure E6. Interrelationship of Digital Particle Image Velocimetry (DPIV) components.

Figure E7. Flow chart of DPIV processing and post-processing.

Figure E8. Dye visualization of flow structure at angle-of-attack $a = 4°$ and $\alpha = 6°$ for values of Reynolds number Re = 10,000, 30,000, 50,000 based on chord.

Figure E9. Dye visualization of flow structure at angle-of-attack $a = 9°$ and $a = 12°$ for values of Reynolds number Re = 10,000, 30,000, 50,000 based on chord.

Figure E10. Dye visualization of flow structure for angles-of-attack $\alpha = 4°$, 6°, 9° and 12° at a value of Reynolds number Re = 10,000 based on chord.

Figure E11. Dye visualization of flow structure for angles-of-attack $\alpha = 4°$, 6°, 9° and 12° at a value of Reynolds number Re = 30,000 based on chord.

Figure E12. Dye visualization of flow structure for angles-of-attack $\alpha = 4°$, 6°, 9° and 12°.

Figure E13. Solid model representations of 1303 UCAV and designation of location of laser sheet at value of Reynolds number Re = 50,000 based on chord.

Figure E14. Contours of time-averaged streamwise velocity $\langle u \rangle / U$ for different values of displacement Δ/C of laser sheet from surface of wing at angle-of-attack $\alpha = 6°$. Reynolds number Re = 50,000 is based on chord.

Figure E15. Stacked arrangement of contours of time-averaged streamwise velocity $\langle u \rangle / U$ for different values of displacement Δ/C of laser sheet from surface of wing at angle-of-attack $\alpha = 6°$. Reynolds number Re = 50,000 is based on chord.

Figure E16. Averaged patterns of velocity vectors $\langle \underline{V} \rangle$, streamwise velocity $\langle u \rangle / U$ and traverse velocity $\langle v \rangle / U$ in comparison with patterns of instantaneous velocity vectors $\underline{V}$, and streamwise velocity u/U. Laser sheet displacement from the surface of the wing is $\Delta/C = 0.006$. Angle-of-attack is $\alpha = 6°$.

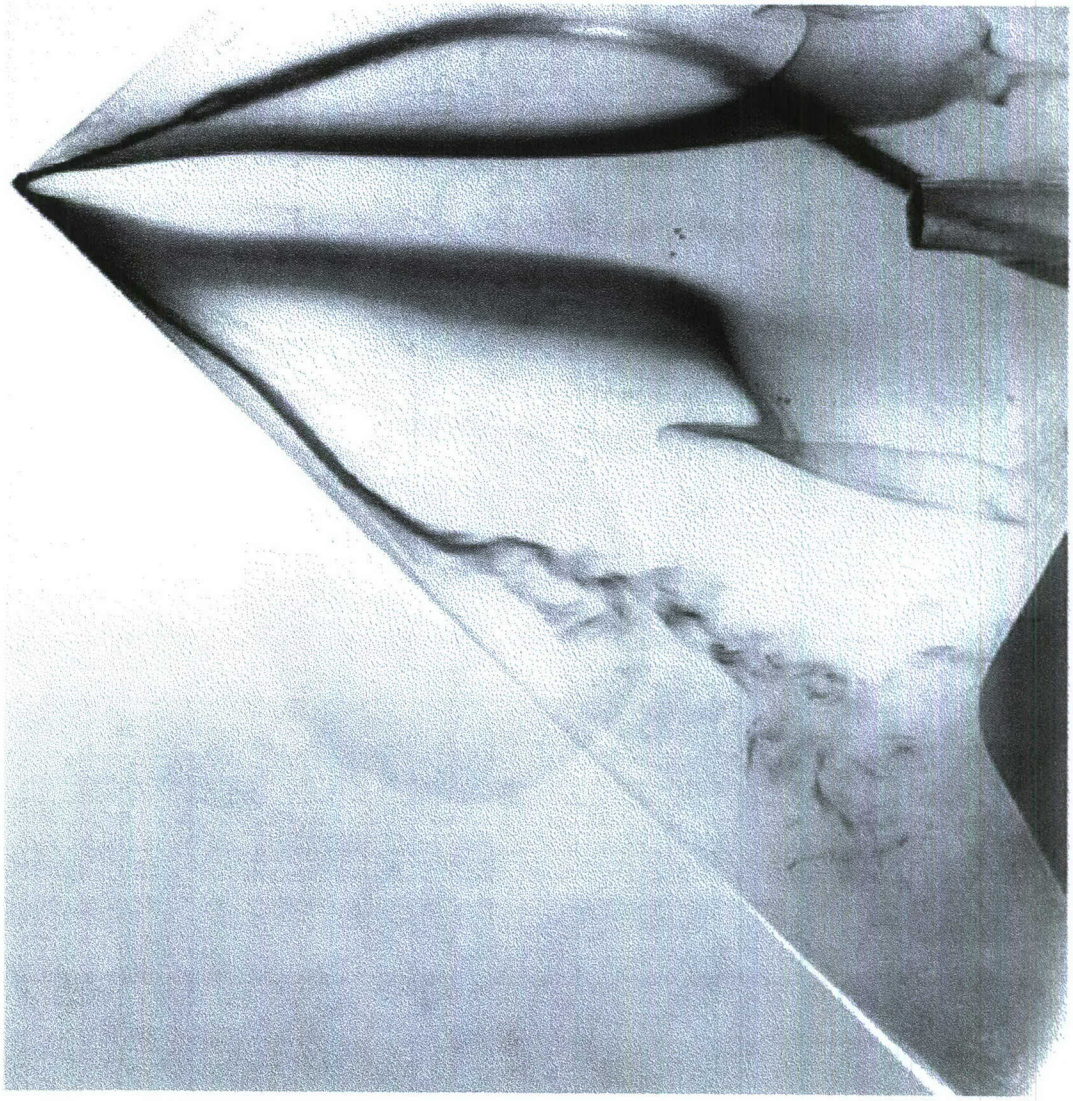


Figure E1. Dye visualization of flow structure at angle-of-attack $a = 12°$ and for a value of Reynolds number Re = 32,000 based on chord (Ol, 2006).

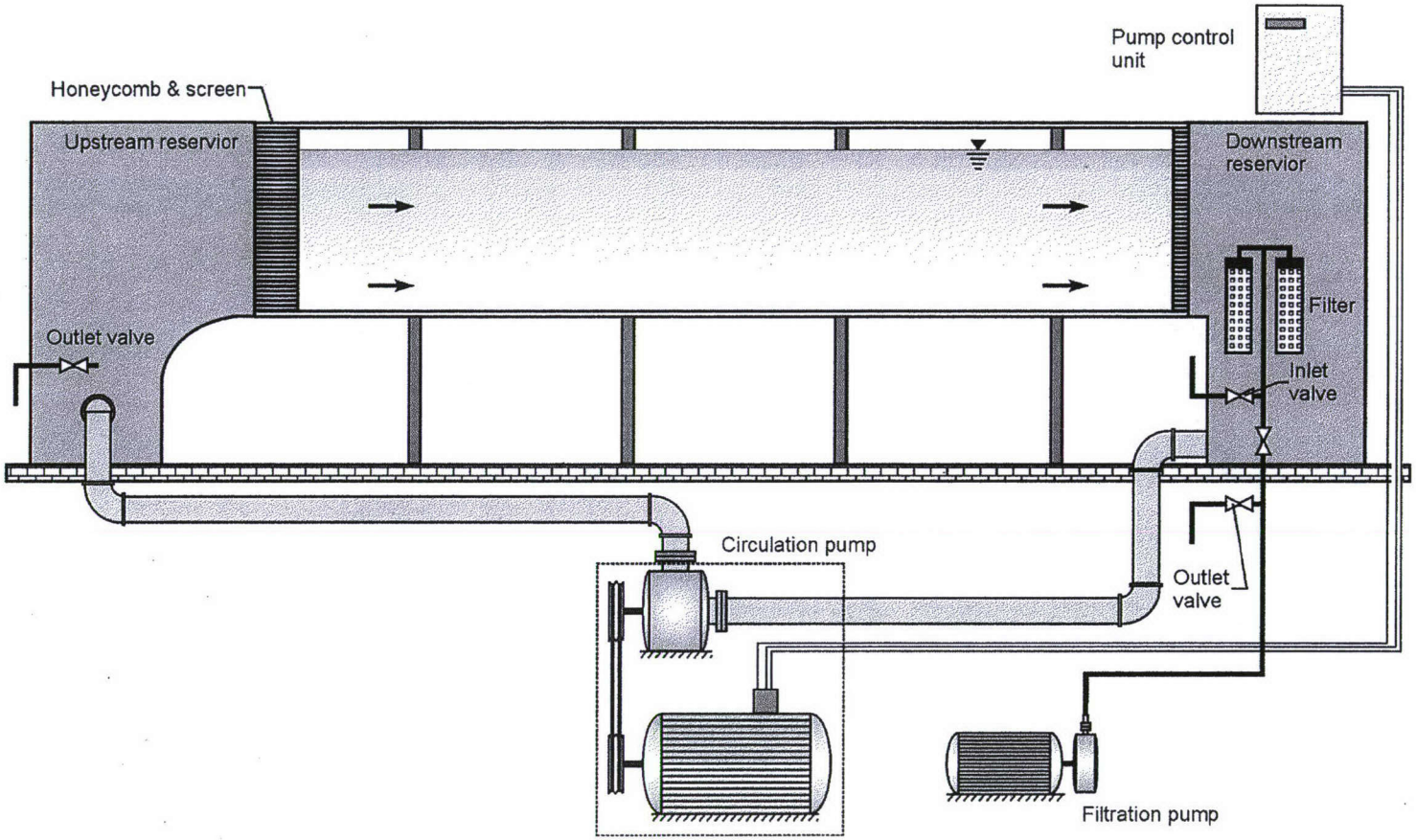


Figure E2. Schematic of the recirculating type free-surface water channel facility.

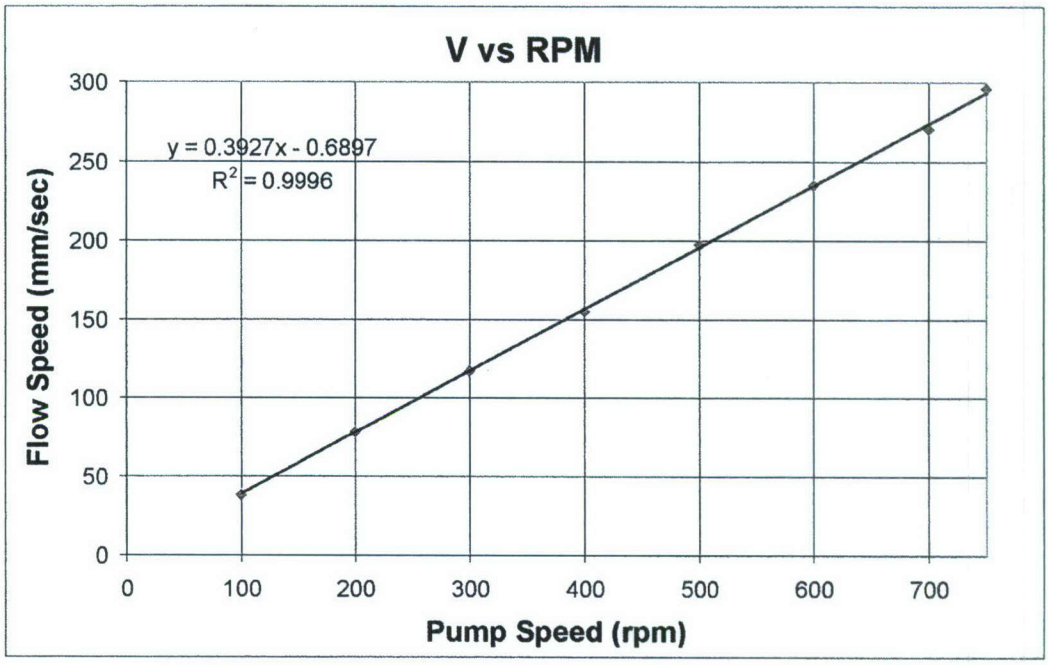


Figure E3. Channel calibration curve.

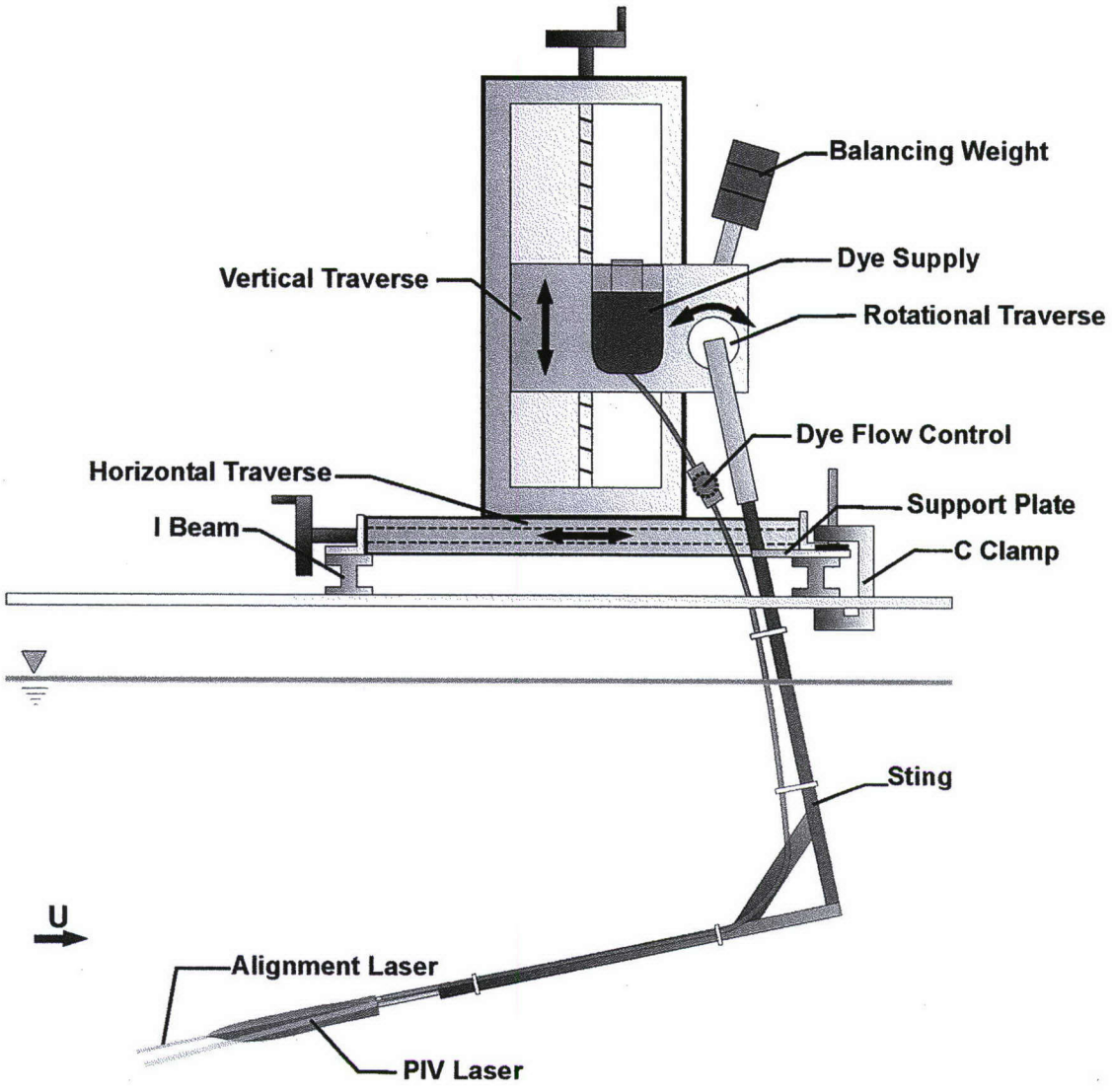


Figure E4. Side view of experimental system.

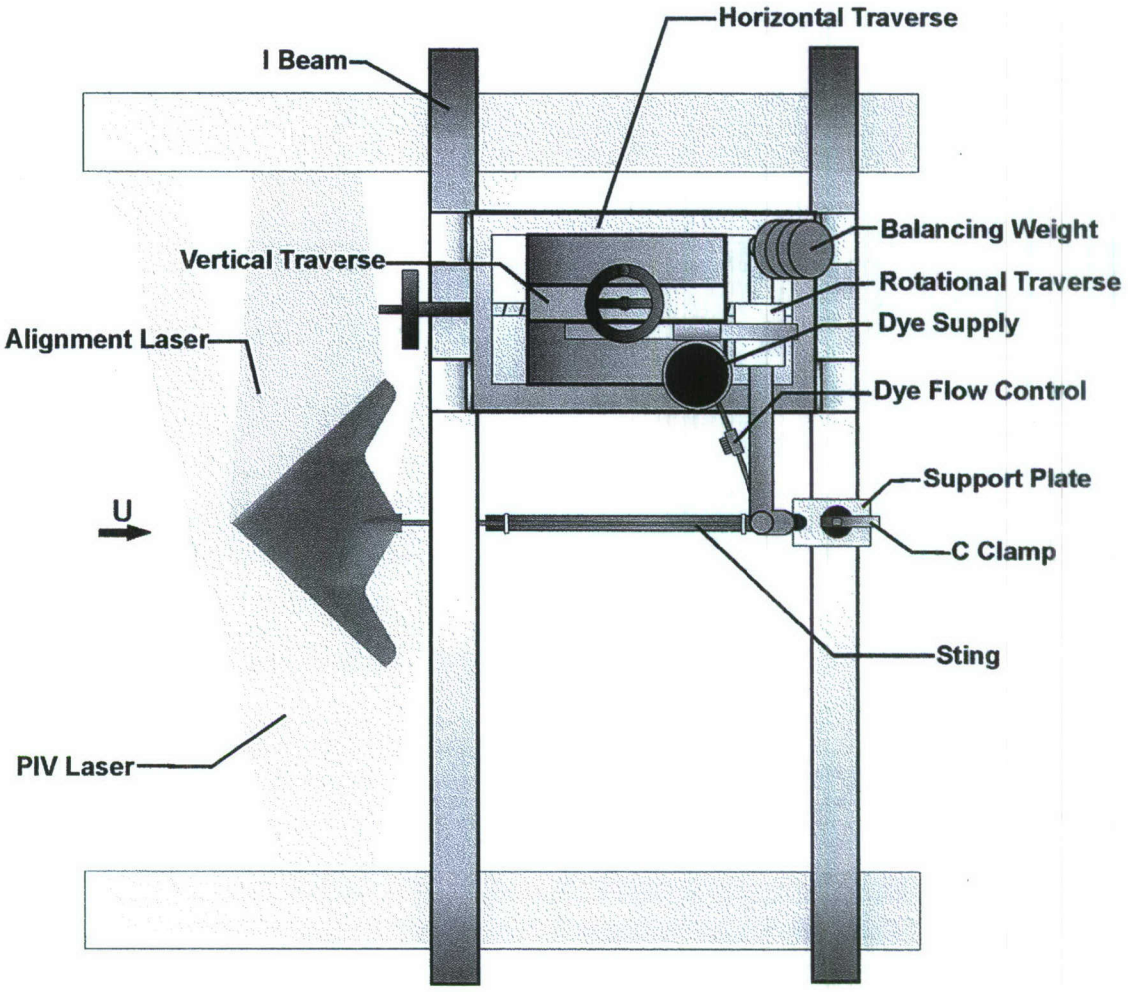


Figure E5. Solid model representations of 1303 UCAV and designation of location of laser sheet.

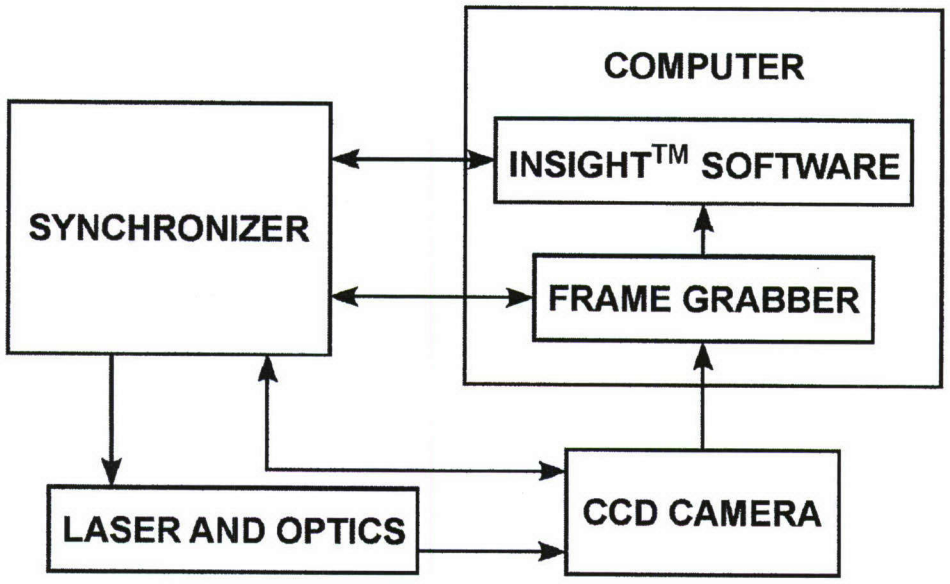


Figure E6. Interrelationship of Digital Particle Image Velocimetry (DPIV) components.

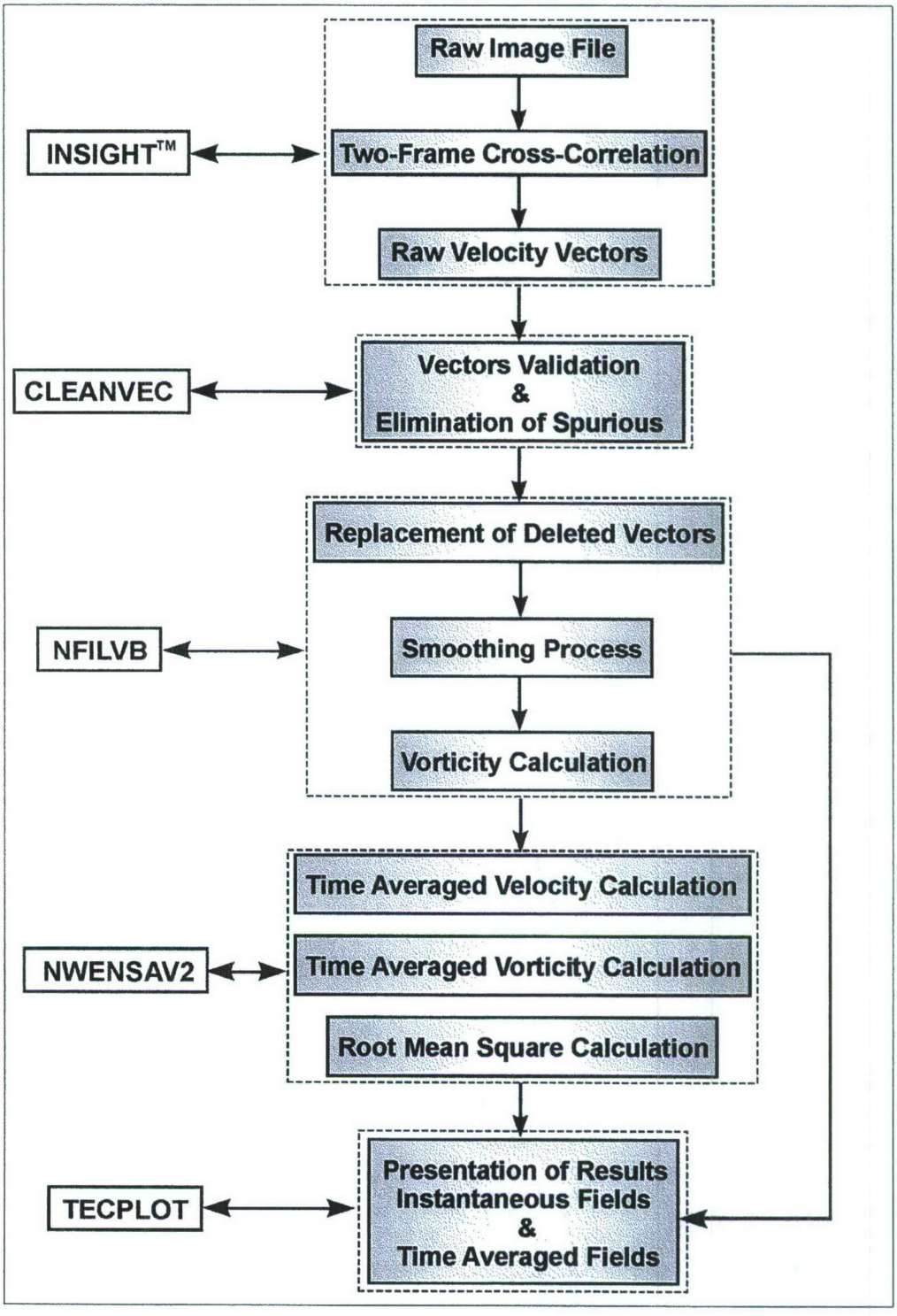


Figure E7. Flow chart of DPIV processing and post-processing.

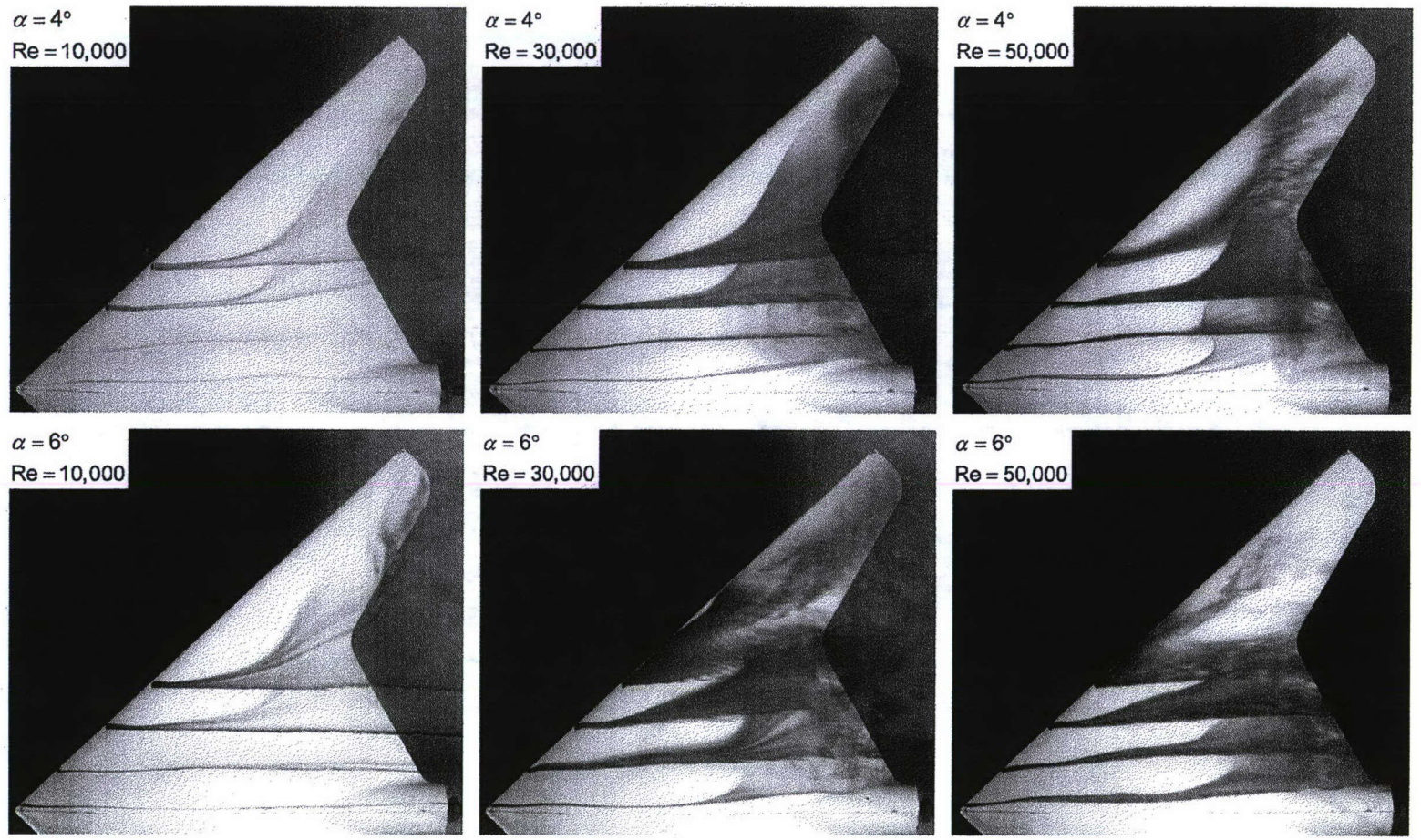


Figure E8. Dye visualization of flow structure at angle-of-attack α = 4° and α = 6° for values of Reynolds number Re = 10,000, 30,000, 50,000 based on chord.

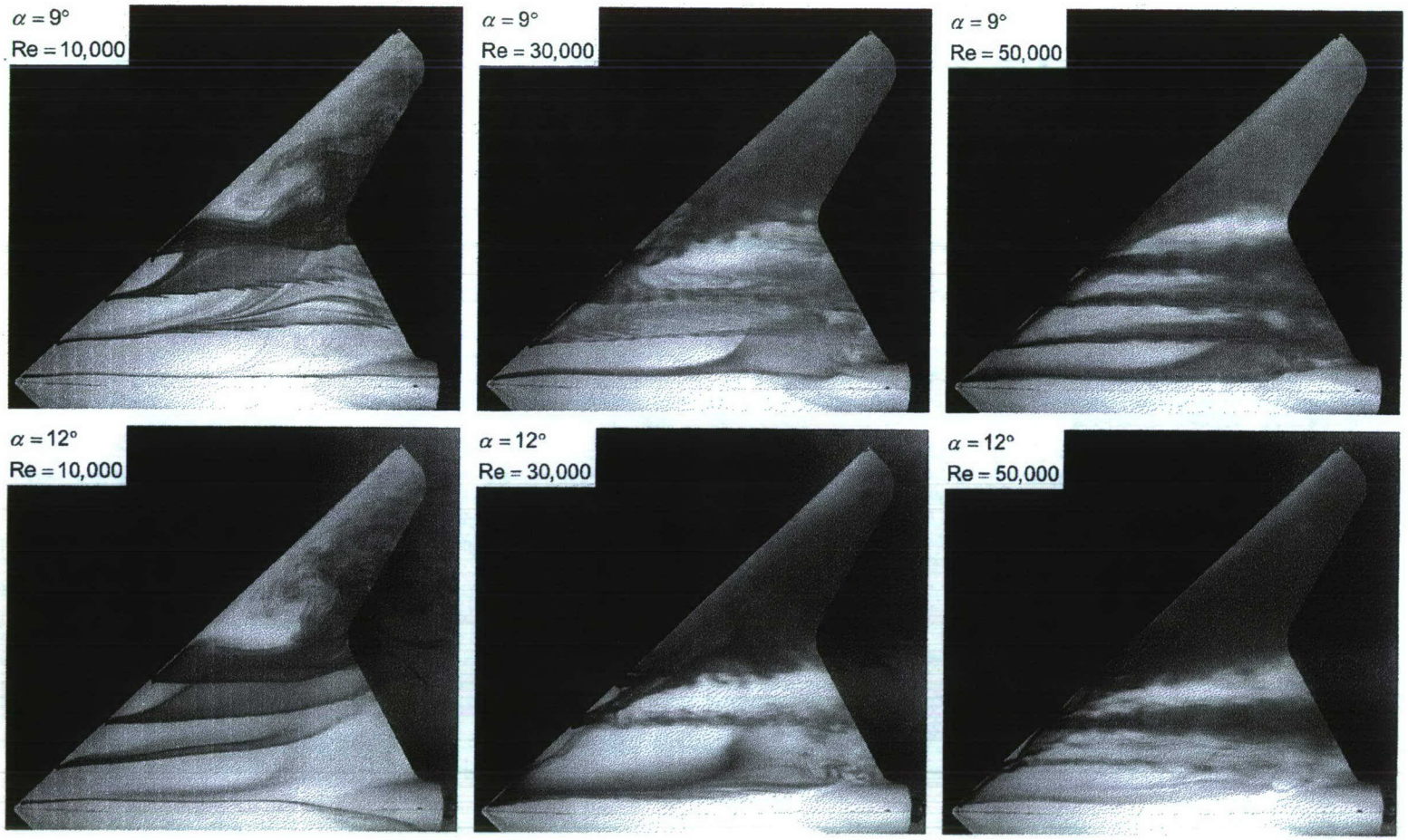


Figure E9. Dye visualization of flow structure at angle-of-attack a = 9° and a = 12° for values of Reynolds number Re = 10,000, 30,000, 50,000 based on chord.

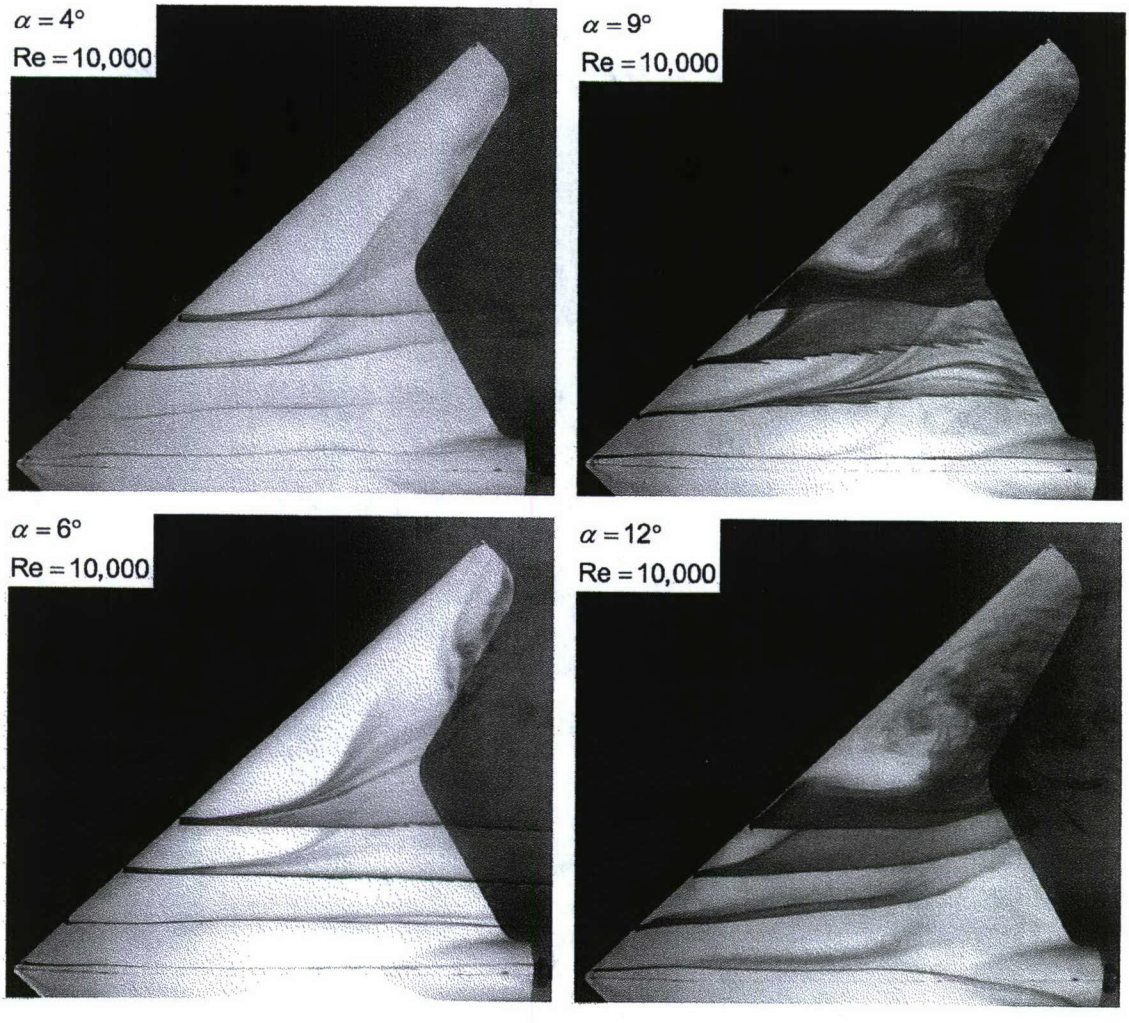


Figure E10. Dye visualization of flow structure for angles-of-attack $\alpha = 4°$, 6°, 9° and 12° at a value of Reynolds number Re = 10,000 based on chord.

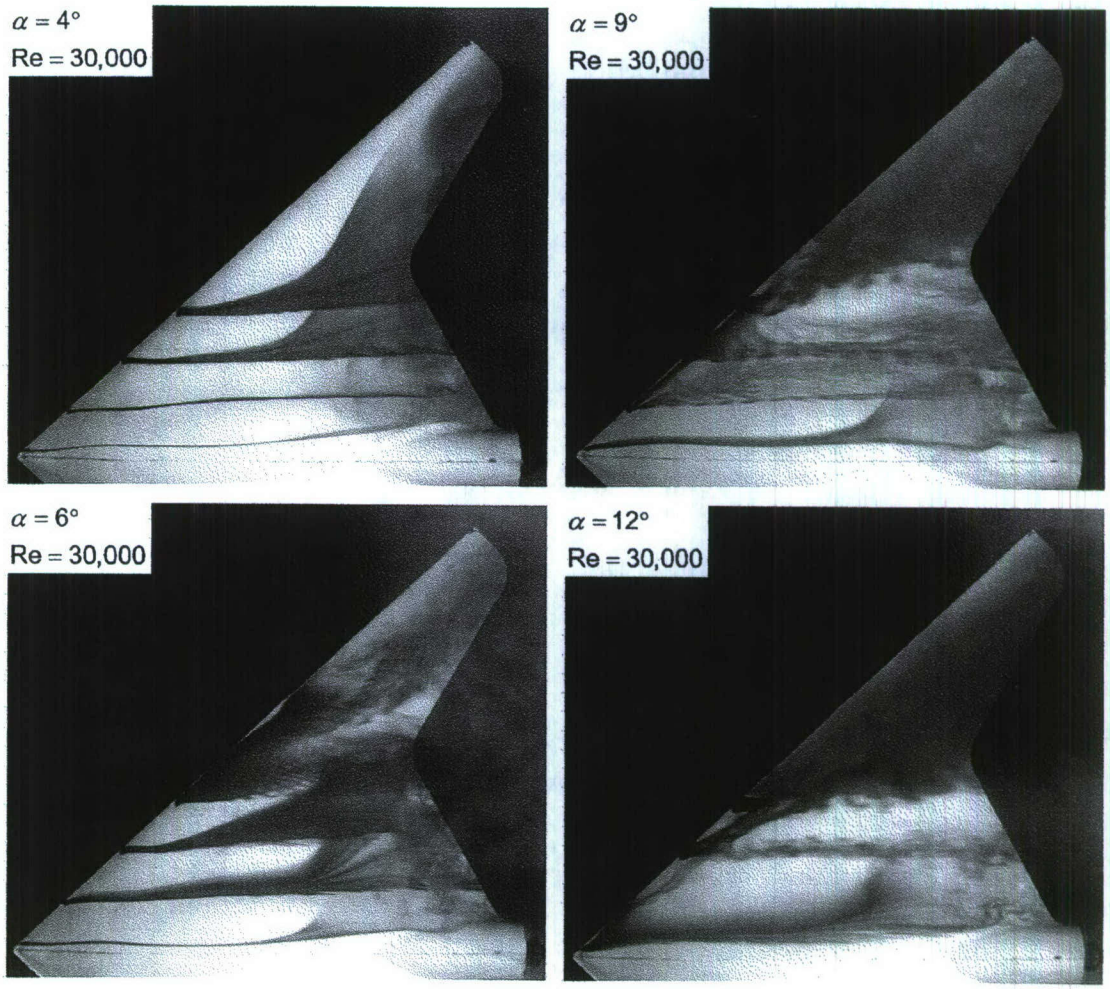


Figure E11. Dye visualization of flow structure for angles-of-attack $\alpha = 4°$, 6°, 9° and 12° at a value of Reynolds number Re = 30,000 based on chord.

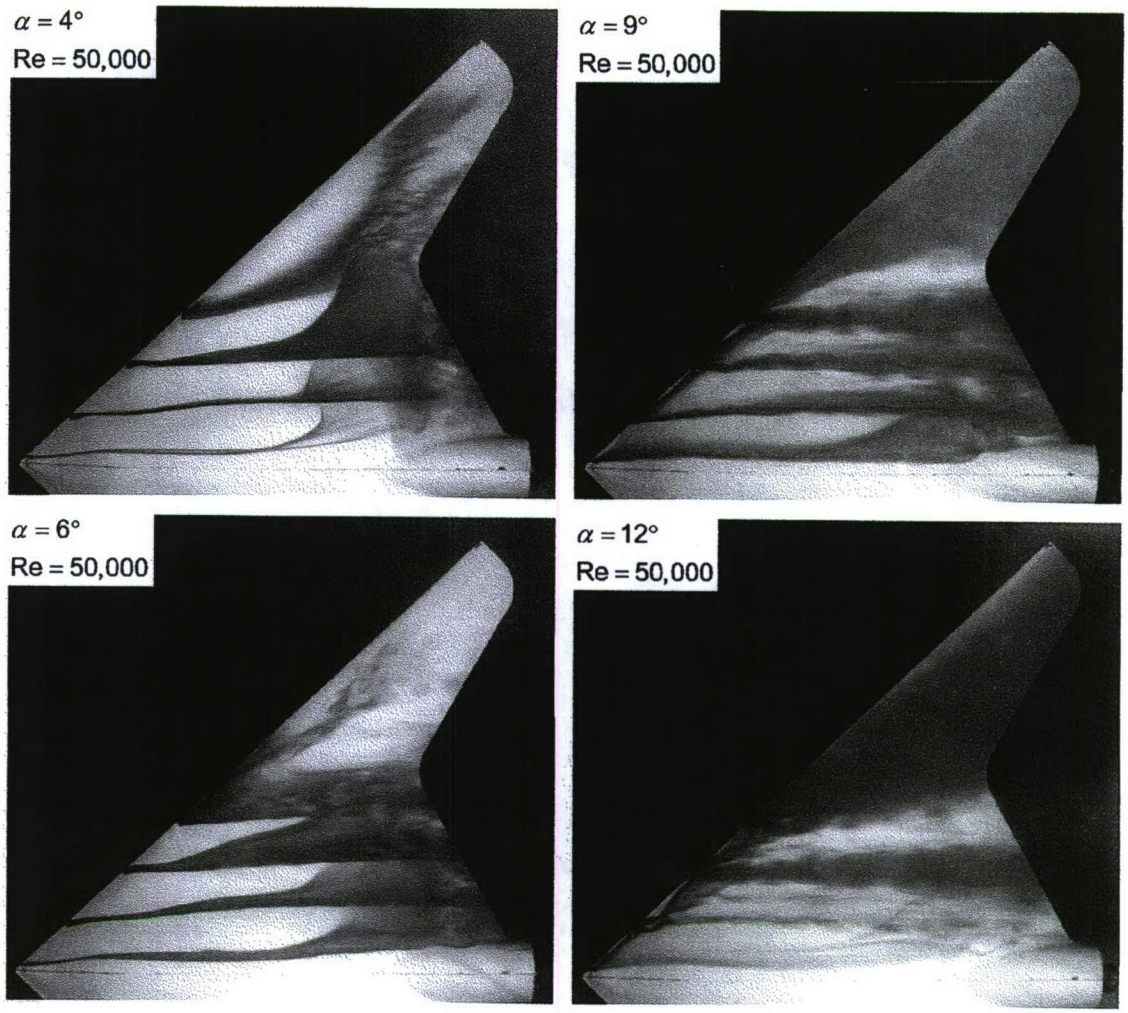


Figure E12. Dye visualization of flow structure for angles-of-attack $\alpha = 4°$, 6°, 9° and 12° at a value of Reynolds number Re = 50,000 based on chord.

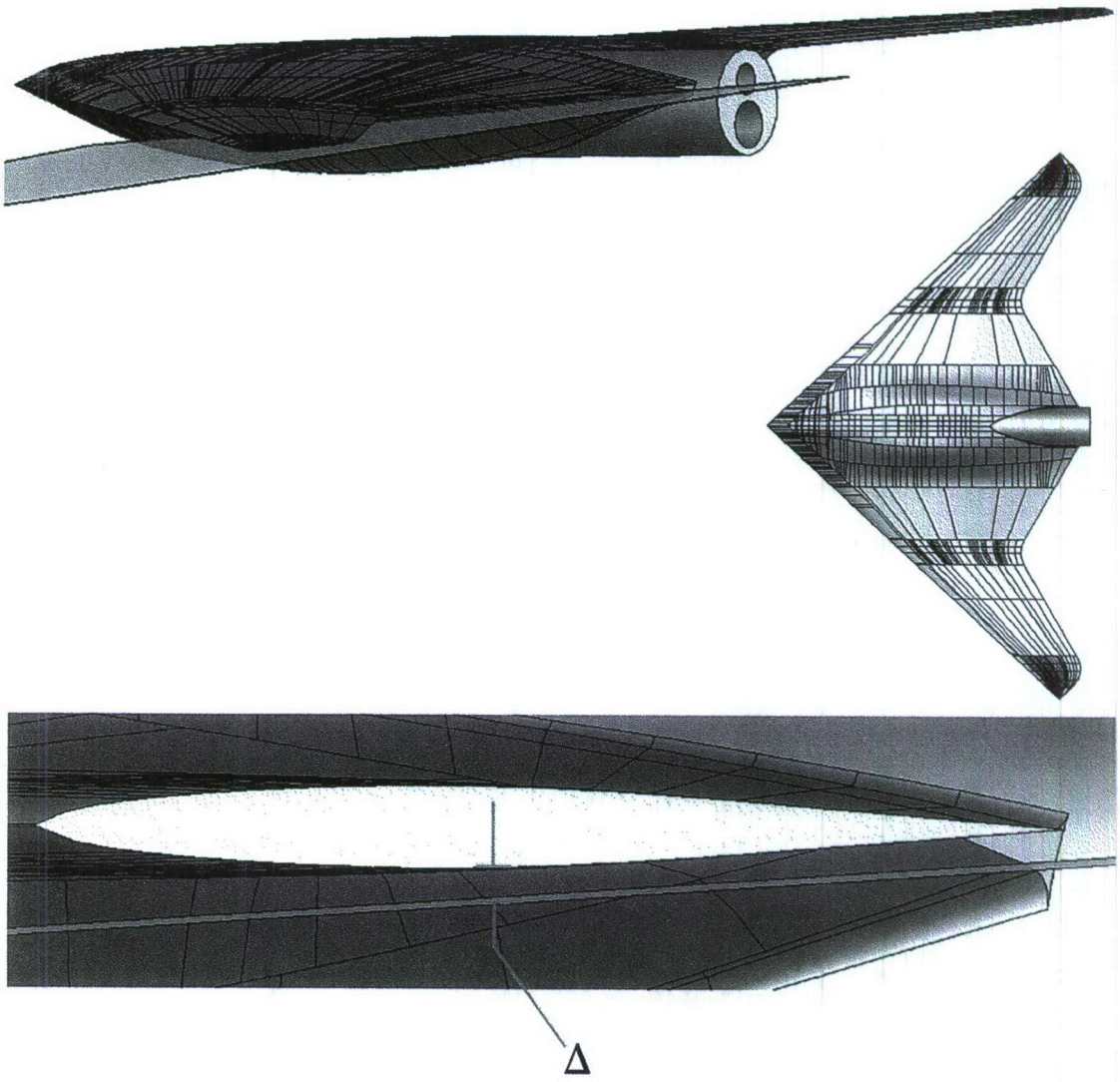


Figure E13. Solid model representations of 1303 UCAV and designation of location of laser sheet.

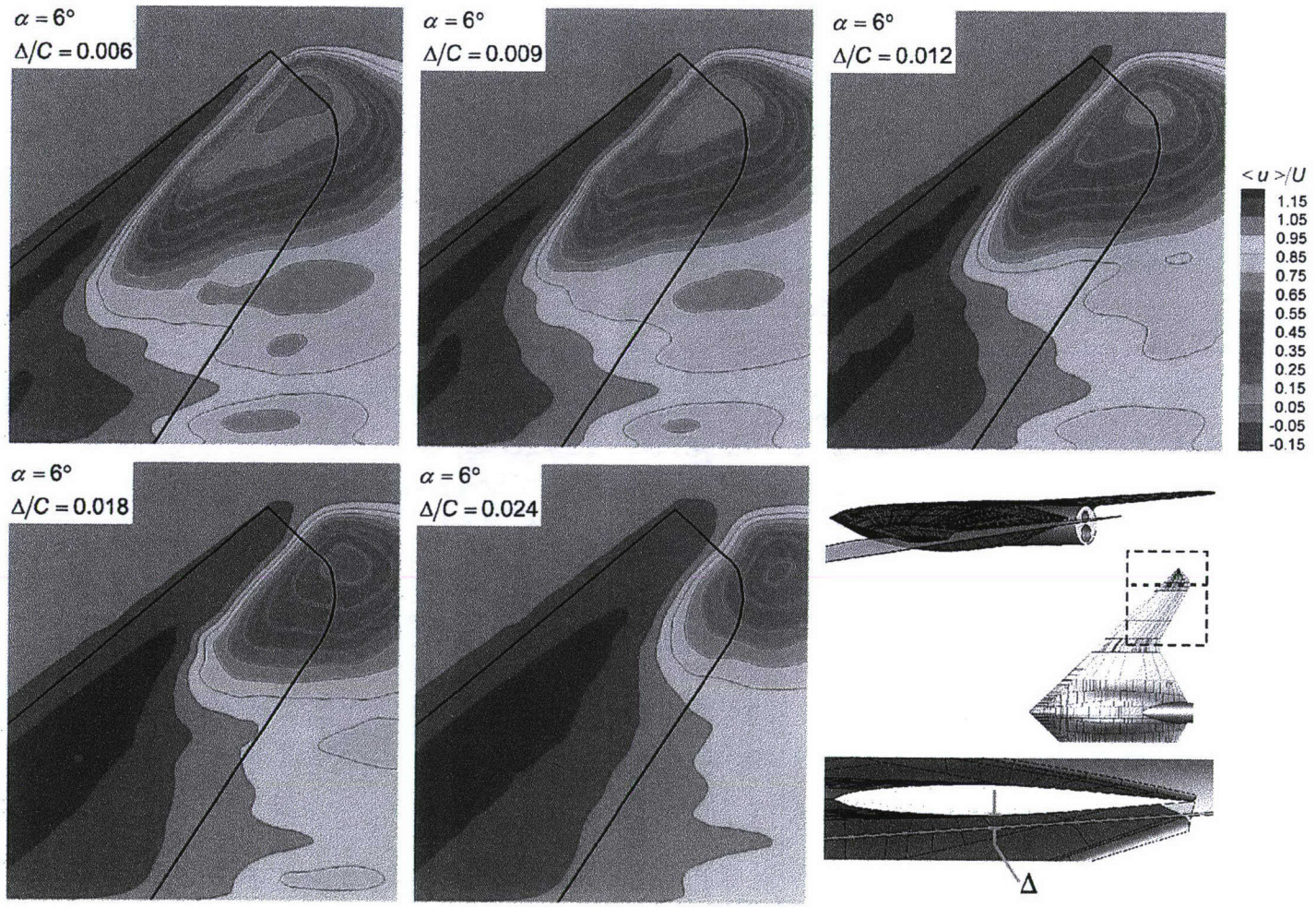


Figure E14. Contours of time-averaged streamwise velocity $\langle u \rangle / U$ for different values of displacement Δ/C of laser sheet from surface of wing at angle-of-attack $\alpha = 6°$. Reynolds number Re = 50,000 is based on chord.

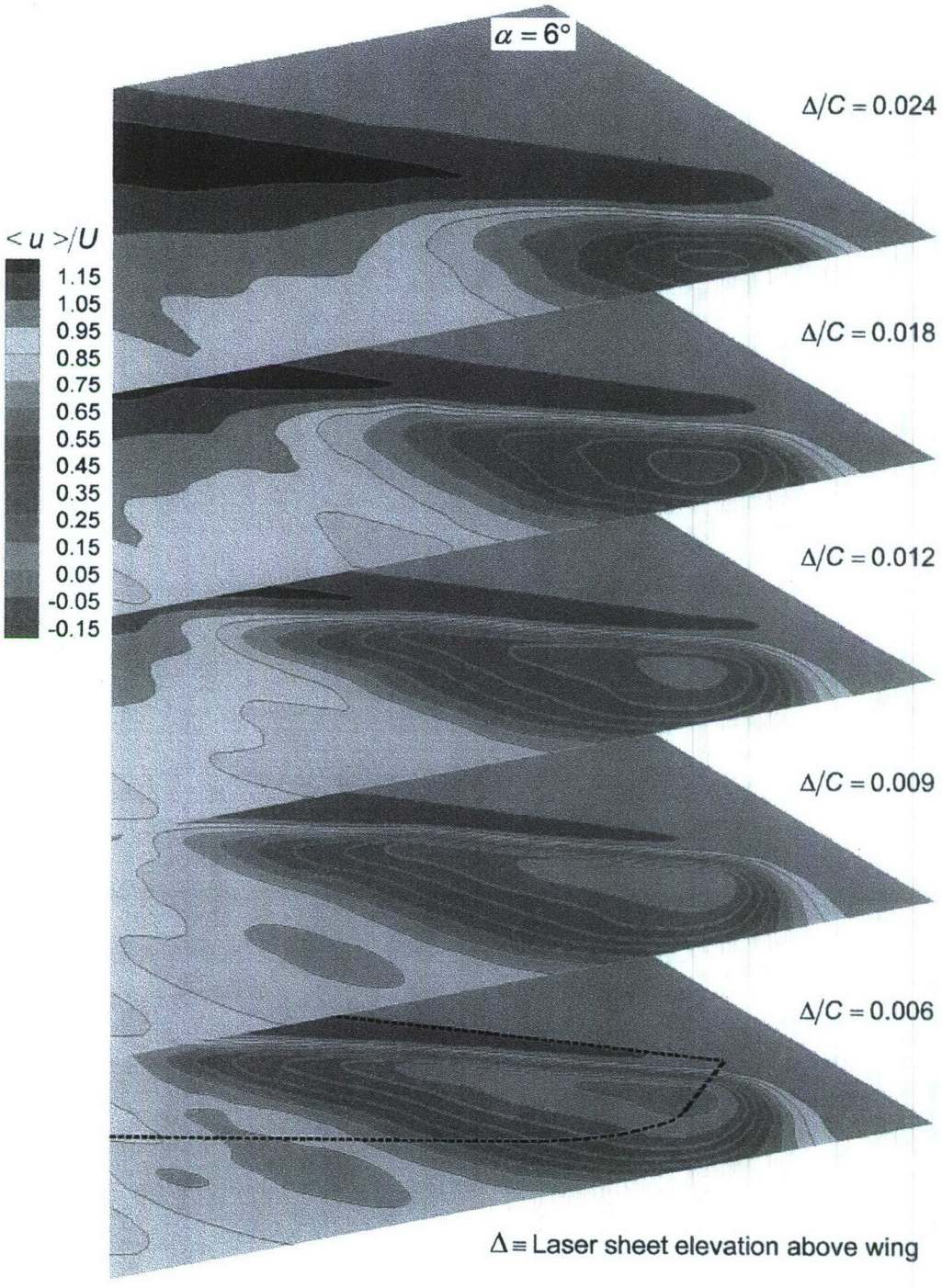


Figure E15. Stacked arrangement of contours of time-averaged streamwise velocity $\langle u \rangle / U$ for different values of displacement Δ/C of laser sheet from surface of wing at angle-of-attack $\alpha = 6°$. Reynolds number Re = 50,000 is based on chord.

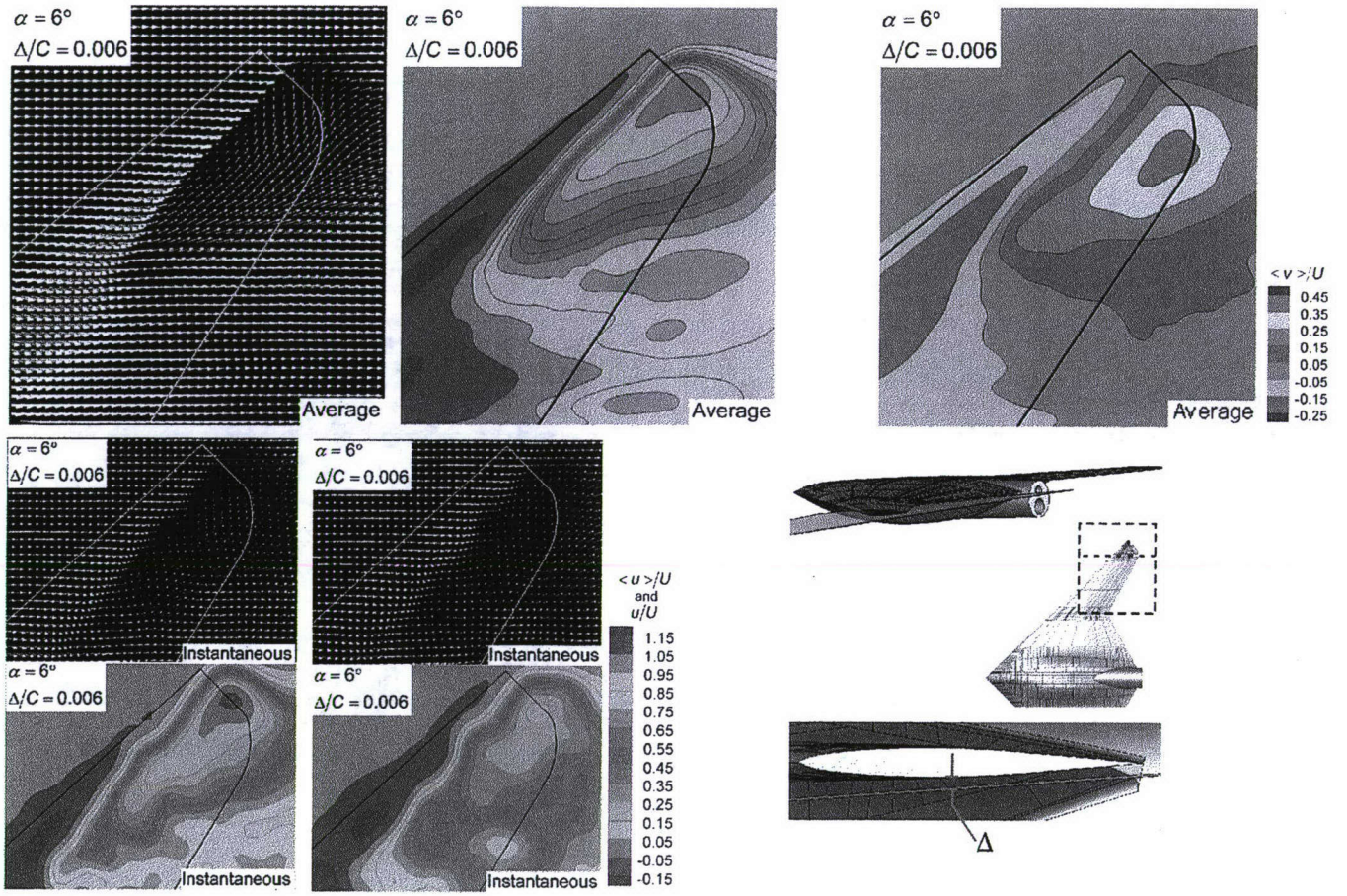


Figure E16. Averaged patterns of velocity vectors $\langle \underline{V} \rangle$, streamwise velocity $\langle u \rangle / U$ and traverse velocity $\langle v \rangle / U$ in comparison with patterns of instantaneous velocity vectors $\underline{V}$, and streamwise velocity u/U. Laser sheet displacement from the surface of the wing is $\Delta/C = 0.006$. Angle-of-attack is $\alpha = 6°$.

Appendix F

QUANTITATIVE FLOW INTERPRETATION OF VORTEX BUFFETING ON AN AIRCRAFT TAIL VIA PROPER ORTHOGONAL DECOMPOSITION (POD)

by

Y. Kim[1], D. Rockwell[2]
Department of Mechanical Engineering and Mechanics
367 Packard Laboratory, 19 Memorial Drive West
Lehigh University, Bethlehem, PA 18015, USA

A. Liakopoulos[3]
Department of Civil Engineering
University of Thessaly
Pedion Areos, 383 34
Volos, Greece

ABSTRACT

The Proper Orthogonal Decomposition (POD) method is applied to PIV data to extract the most energetic flow structures of vortex-tail interaction. The reconstructed flow fields, in conjunction with patterns of vorticity and streamline topology are compared with the original PIV data on a crossflow plane. The reconstructed flow fields using 5 and 10 eigenfunctions can predict the largest-scale features of the original flow field. However, the smaller-scale flow structures, which are evident in the original PIV image, are lost. In other words, the flow features of smaller-scale can be filtered out by employing the first few eigenmodes. By employing 40 eigenmodes, the reconstructed flow field can reproduce most of the smaller-scale flow structures of the original flow field. In terms of the kinetic energy of the fluctuations, about 80% of the total flow energy can be accounted for using 40 eigenmodes. Furthermore, patterns of instantaneous streamline topology clearly show that the reconstructed flow fields from 5 and 10 eigenmodes can represent the most dominant characteristics of the original flow field, while the more complicated streamline topology of the original PIV data can be reproduced by 40 eigenmodes. The future investigation may include the application of the present technique to develop a feedback mechanism for optimization of actual flight controls.

1. INTRODUCTION

1.1 THE PHYSICS OF BUFFET LOADING DUE TO VORTEX BREAKDOWN

The interaction of a broken-down vortex with various types of physical configurations is generally recognized as a major source of the unsteady loading. Of particular interest for buffet loading of an aerodynamic surface is characterization of the frequency and amplitude of velocity and pressure fluctuations. Gursul and Xie (1998) provided representations of the dimensionless frequency of vortex breakdown on delta wings. Detailed consideration of the power spectra of

[1] Research Associate
[2] Paul B. Reinhold Professor, Member AIAA
[3] Professor and Chairman

velocity fluctuations within the region of vortex breakdown has been assessed by Garg and Liebovich (1979) and Gursul and Yang (1995). Moreover, Gursul and Yang (1995) investigated the local pressure fluctuations at specified locations on a delta wing. The classification of pressure fluctuations in terms of dimensionless frequencies, which represent various features of the unsteady flow including vortex breakdown, was provided by Menke, Yang and Gursul (1996). The helical mode of instability of vortex breakdown was viewed to play an important role in determining the unsteady surface loading. The unsteady features of this mode were described by Garg and Leibovich (1979) and Gursul (1994). Reviews and assessments of the flow phenomena of the vortex breakdown include those of Sarpkaya (1971a,b; 1974), Escudier (1988), Brown and Lopez (1990) and Delery (1994).

As reviewed by Rockwell (1998), a number of investigations have assessed the unsteady loading of an aircraft tail due to incident unsteadiness, typically arising from vortex breakdown. Representative investigations include those of Triplett (1983), Brown, Lee and Tang (1990), Komerath *et al.*. (1992a, 1992b). Lee *et al.* (1993) observed the vortical flow above an F/A-18 aircraft. In addition, results for a model F/A-18 with forebody and leading edge extension (LEX) configurations in water tunnel were found to be in accord with the wind tunnel and flight tests (Lee, 2000). The eventual objectives of any of the foregoing types of investigation are to gain an insight into the physical phenomena of the unsteady flow field, in relation to the vortex breakdown and the corresponding loading induced at the aerodynamic surfaces. Numerical investigations of the unsteady loading on tail/fin include those of Kandil *et al.* (1995), Gordnier and Visbal (1997), and Kandil and Sheta (1998). Recent development of quantitative imaging techniques has provided instantaneous global patterns of the flow to allow rational interpretations of the unsteady loading due to the vortex-plate and the vortex-tail configurations. These approaches, which are based on a laser-scanning version of high-image-density particle image velocimetry (HID-PIV), are addressed by Adrian (1991), Rockwell *et al.* (1993), and Westerweel (1997). More recently, Rockwell (2000) assessed case studies of vortex-dominated flows using the technique of PIV.

1.2 PROPER ORTHOGONAL DECOMPOSITION (POD)

The Proper Orthogonal Decomposition (POD) technique was first considered in the field of fluid mechanics by Lumley (1967), in order to identify the dynamical coherent flow structures in turbulent flows. Meteorologists have been referring to the decomposition as the method of orthogonal empirical eigenfunction. Karhunen-Loeve expansion is a term also used widely in the literature. Berkooz *et al.* (1993) have reviewed the important issues in applying POD to turbulent flows. Various unsteady flow configurations have been investigated via POD. They include a turbulent boundary layer (Aubry *et al.*, 1988; Rempfer and Fasel, 1994), a mixing layer (Glezer *et al.*, 1989; Delville *et al.*, 1999; Citriniti *et al.*, 2000), flow past grooved channels and circular cylinders (Deane *et al.*, 1991; Sahan *et al.*, 1997), flow in an enclosure and a vertical channel (Kim, 1996; Liakopoulos *et al.*, 1997), a turbulent jet (Bonnet *et al.*, 1994; Arndt *et al.*, 1997; Gordeyev and Thomas, 2000), and flow past a delta wing (Cipolla *et al.*, 1998).

The POD technique extracts the most energetic eigenmodes by retaining only a small number of modes that capture most of the fluctuation energy. The PIV technique of the present study allows, in effect, acquisition of sequential velocity data at a large number of spatial points simultaneously, so it provides an attractive basis for POD. The snapshot version of POD, which was developed by Sirovich (1987), is particularly relevant to the present investigation. In this

technique, empirical eigenfunctions are extracted from spatio-temporal data sets, obtained from either experiments or numerical computations. In the present study, this snapshot version of POD is applied to the original PIV images of the flow field.

Previous investigations show that the flow field reconstructed via POD can accurately describe the original flow structure even with few empirical eigenfunctions in some cases. Furthermore, this procedure can be used also as a tool for the elimination of some of the extraneous small-scale features of the flow.

Direct numerical simulation of a turbulent flow requires a formidable amount of computing time and memory. Therefore, low-dimensional models are desirable. Deane *et al.* (1991) described low-dimensional models for flows past a grooved channel and circular cylinders. By employing a Galerkin method, a governing partial differential equation can be reduced to a system of first order ordinary differential equations (Gottlieb and Orszag, 1977; Liakopoulos and Hsu, 1984).

2. EXPERIMENTAL SYSTEM AND TECHNIQUES

2.1 TEST FACILITY AND FLOW CONDITIONS

Experiments were conducted in a large-scale free-surface water channel having a cross-section 927 mm wide, 610 mm high, and approximately 5,000 mm long. It is located in the Fluid Mechanics Laboratory of Lehigh University. This recirculating water channel was constructed of optically transparent Plexiglas with water reservoirs at the inlet and outlet ends. In this study, the flow velocity was maintained at 152 mm/sec at a water depth of 559 mm. The corresponding Reynolds number based on the chord length of the delta wing was $Re_c = 52{,}000$.

2.2 EXPERIMENTAL MODEL

The plan and side views of the delta wing-tail system are shown in Figure E1. The laser sheet orientation is indicated. The tail is aligned with, or parallel to, the axis of the leading-edge vortex. The sweep angle of the wing is $\Lambda = 75^\circ$ and the effective sweep angle of the leading-edge vortex is $\lambda_L = 79^\circ$. The chord length of the wing is $C = 342$ mm. Moreover, the distance between the trailing-edge of the wing and the leading-edge of tail is $L_T = 5$ mm or 0.0146C, and the angle-of-attack of the delta wing is $\alpha = 21^\circ$ for the experiment. The distance between the tip of the tail and the laser sheet is indicated by $X_L = 0.965C_T$, where C_T (=105 mm) denotes the root chord length of the tail. Figure E2 shows the dimensions of the rigid tail. The tail had the root chord length of $C_T = 105$ mm, and the ratio of its thickness to chord ratio was $t_T/C_T = 0.12$. The span of the swept leading-edge of the tail was $S_T = 136$ mm. The length of the support system of the tail was $X_T = 51$ mm, while the distance from the tip of the tail to the support system was $Y_T = 60$ mm. The angles of inclination of leading and trailing edges of the tail were $\beta_1 = 70^\circ$ and $\beta_2 = 45^\circ$. In addition, both the leading and tip edges of the tail were beveled at an angle of 30°.

The delta wing geometry is shown in Figure E3. It was of Plexiglas and had a leading-edge sweep angle $\Lambda = 75^\circ$; a chord $C = 342$ mm; a thickness-to-chord ratio $t_w/C = 0.028$. The leading-edges were beveled at an angle of 30° on each side of the wing. Therefore, the sharp leading-edge of the wing provided a stable separation point.

2.3 IMAGE ACQUISITION AND POST-PROCESSING TECHNIQUES

In this study, high-image-density Digital Particle Image Velocimetry (DPIV) was employed by illuminating the flow field to obtain instantaneous images of small scattering particles. Comprehensive reviews of application of the PIV technique are given by Adrian (1991), Rockwell(1993), and Westerweel 1997). For DPIV, the motion of neutrally-buoyant particles in water is analyzed using the image cross-correlation technique to determine the two dimensional velocity fields. The scattering particles are metallic-coated glass spheres with a mean diameter of 14 microns. They are manufactured by Potters Industries Inc. These particles were illuminated by a laser sheet approximately 1mm thick. It was generated from a Nd:Yag (90mJ) double-pulsed laser.

A two-frame cross-correlation technique was employed to determine two-dimensional velocity data for a given interrogation window with a 50% overlap to satisfy the Nyquist criterion. The frame-to-frame cross-correlation technique allows the velocity to be measured without any directional ambiguity. The framing rate of 67 ms, or 15 Hz, between frame pairs was applied throughout the experiment. The magnification factor (MF) of the lens was calculated as the ratio of a length in pixels as it appears on the recorded image to the actual physical length in mm. An image was taken to determine the scale by locating a millimeter scale parallel to the laser sheet. This approach led to the value of the magnification factor (MF). The value of MF was 1:7.54 in this study, which gave an effective grid size of 2.12 mm in the plane of the laser sheet. The grid size in a given image was 61 in x-direction and 62 in y-direction, which yields a total of 3,782 vectors in the field of view.

3. NUMERICAL METHODS: POD

Assuming that M snapshots of the instantaneous velocity field are available from PIV or numerical flow simulation, the Proper Orthogonal Decomposition (POD) methodology proceeds as follows. In the first step, the time-dependent velocity field data are decomposed into time-averaged and fluctuation components, i.e.,

$$\boldsymbol{V}(x,y,t) = \overline{\boldsymbol{V}}(x,y) + \boldsymbol{V}'(x,y,t) \tag{1}$$

where $\boldsymbol{V}'$ and $\overline{\boldsymbol{V}}$ denote the fluctuation and time-averaged velocities, and boldface symbols denote vector quantities. The value of $\overline{\boldsymbol{V}}$ is obtained by calculating the average of M snapshots of the velocity field, i.e.,

$$\overline{\boldsymbol{V}}(x,y) = \frac{1}{M}\sum_{i=1}^{M} \boldsymbol{V}(x,y,t_i) \tag{2}$$

Evidently, the fluctuating component of the velocity is readily available from equations (1) and (2), i.e.,

$$\boldsymbol{V}'(x,y,t) = \boldsymbol{V}(x,y,t) - \overline{\boldsymbol{V}}(x,y) \tag{3}$$

In the next step, the empirical eigenfunctions ($\boldsymbol{\phi_k}$, $k=1, 2, \ldots, M$) are constructed by an appropriate superposition of the fluctuation components of the instantaneous data, as suggested by Sirovich (1987), i.e.,

$$\phi_k(x,y) = \sum_{i=1}^{M} A_{ki} V_i'(x,y,t_i) \tag{4}$$

where V_i' denotes the i^{th} fluctuation velocity field, i.e., the fluctuation velocity at t = t_i and A_k represents the k^{th} eigenvector of the algebraic eigenvalue problem

$$CA = \lambda A \tag{5}$$

In equation (5) C is an $M \times M$ square symmetric real matrix whose elements are given by

$$C_{mn} = \frac{1}{M} \int_{\Omega} F_{mn}(x,y,t) d\Omega \tag{6}$$

Here,

$$F_{mn} = V_m'(x,y,t_m) \bullet V_n'(x,y,t_n) \tag{7}$$

and Ω indicates the processing domain. In equation (7) the dot denotes the inner product between V_m' and V_n'. Having constructed matrix C, the eigenvalue problem, equation (5), is solved and the eigenvalues ($\lambda_1, \lambda_2, \ldots, \lambda_M$) of C and its corresponding eigenvectors ($A_1, A_2, \ldots, A_M$) can be computed. Note that all eigenvalues are real, non-negative and can be arranged in descending order such that $\lambda_1 \geq \lambda_2 \geq \ldots \geq \lambda_M$. Each eigenvalue represents the flow kinetic energy contributed by the corresponding eigenfunction. Note also that $\sum_{i=1}^{M} \lambda_i = 1$, i.e., the sum of all eigenvalues reflects the total fluctuation flow energy. It turns out that the fluctuation velocity field can be approximated by a truncated series expansion of the form

$$V'(x,y,t) = \sum_{k=1}^{N} a_k(t) \phi_k(x,y) \tag{8}$$

where the value of N is usually selected to be much less than the total number of snapshots M and a_k, which is time-dependent, can be determined by using the orthonormality property of eigenfunctions, i.e.,

$$a_k(t) = \int_{\Omega} V'(x,y,t) \cdot \phi_k(x,y) d\Omega \tag{9}$$

Finally, we note that the instantaneous flow field can be reconstructed according to:

$$V(x,y,t) = \overline{V}(x,y) + \sum_{k=1}^{N} a_k(t) \phi_k(x,y) \tag{10}$$

4. ASSESSMENT OF FLOW STRUCTURES VIA POD

In the present study, $M = 137$ snapshots of the velocity data from PIV were employed in the POD analysis.

4.1 PATTERNS OF EMPIRICAL EIGENFUNCTIONS

Figures E4 and E5 exhibit the fluctuating component of velocity and patterns of vorticity of the selected empirical eigenfunctions; ϕ_1, ϕ_2, ϕ_5, ϕ_{10}, ϕ_{20}, *and* ϕ_{40}. These eigenfunctions were obtained from equation (4) in section 3. The first two eigenfunctions represent the large-scale features of the flow, and reflect the most energetic modes. On the other hand, the smaller-scale flow structures can only be captured by computing the high order eigenfunctions, which is also clearly evident in the plots of vorticity. In the plots of vorticity contours, solid lines indicate positive vorticity and dashed lines represent negative vorticity. The patterns of other selected eigenfunctions, ϕ_3, ϕ_4, ϕ_6, *and* ϕ_7 are shown in Figure E6.

4.2 PATTERNS OF INSTANTANEOUS VELOCITY AND VORTICITY

Figure E7 shows comparisons of the original instantaneous PIV flow fields and the reconstructed flow fields using 10, 20, and 40 eigenfunctions. It is clear that the reconstructed flow field using 10 eigenfunctions can predict certain of the largest-scale features of the flow structure, even on the outboard (right) side of the tail. However, the smaller scales of the flow structure, evident in the instantaneous PIV image, are not observed in the reconstructed flow field.

It is evident, however, that the flow field reconstructed with 20 eigenfunctions shows smaller, more detailed features than the previous case using a smaller number of eigenfunctions. The vortical flow structure on the inboard (left) side of the tail is generally predicted in this image.

Furthermore even smaller-scale flow features can be extracted with 40 eigenfunctions. Obviously, the reconstructed flow field does not reproduce all of the characteristics of the original PIV flow structure. The overall form of the secondary (positive) vortex structure on the outboard (right) side of the tail starts to resemble the form shown in the original PIV image.

Figure E8 presents the flow fields reconstructed from 40 eigenfunctions at other instants of time, along with the corresponding original PIV data. It is obvious that the large-scale flow features of the original PIV flow field can, in effect, be reconstructed by employing 40 eigenmodes. However, the small-scale flow structures are only marginally reproduced, as shown in the images.

4.3 COMPARISON OF PATTERNS OF STREAMLINE TOPOLOGY FROM 5, 10, 20, AND 40 EIGENMODES

Figure E9 presents the patterns of the streamlines of the reconstructed flow field using 5, 10, 20, and 40 eigenmodes, respectively. The corresponding streamline pattern of the original PIV data is shown in the image (e). In image (a), the reconstructed flow field involves 5 eigenmodes. The streamline pattern on the inboard (left) side of the tail indicates extended

inward spirals along the tail surface. Moreover, the streamline patterns on the outboard (right) side of the tail show large-scale swirling motion. However, the streamline patterns of the original PIV data (e) have a form quite different from the reconstructed flow field. In the image of original PIV data (e), the streamlines on the inboard (left) side of the tail show concentrated, inward spiraling patterns. On the outboard (right) side of the tail of the original PIV image (e), the original streamline patterns are also characterized by much more complicated topology than shown in the reconstructed flow field. From this comparison between the reconstructed flow field and the original PIV data, it is quite obvious that the reconstructed flow field from 5 eigenmodes in image (a) has insufficient information to represent accurately the original PIV flow field (e).

The patterns of instantaneous streamlines of the reconstructed flow field using 10 eigenmodes are shown in image (b). It is quite evident that the streamline patterns of the reconstructed flow field in the image are somewhat similar to the patterns of the reconstructed flow field from 5 eigenmodes, as shown in image (a). In other words, the reconstructed flow field from 10 eigenmodes in image (b) does not indicate a significant gain, and is not capable of adequately representing the original PIV flow field (e).

In image (c), the patterns of instantaneous streamlines of the reconstructed flow field using 20 eigenmodes yield a more detailed representation of the original PIV flow field (e), relative to the flow field obtained from the lower number of eigenmodes presented in images (a) and (b). Despite this more detailed reconstruction, the complex streamline patterns on the outboard (right) side of the tail in the original PIV image (e) are still not adequately represented. Moreover, on the inboard (left) side of the tail, the streamline patterns are similar to those presented from 5 and 10 eigenmodes cases.

Image (d) presents patterns of the instantaneous streamline patterns of the reconstructed flow field using 40 eigenmodes, in relation to the original PIV data (e). Obviously, the streamline patterns of the reconstructed flow field on the inboard (left) side of the tail clearly start to resemble the patterns of the original PIV data. In addition, the patterns show the complex features on the outboard (right) side of the tail, thereby representing reasonably well the topology of the original PIV flow field.

4.4 PATTERNS OF INSTANTANEOUS AND AVERAGED VELOCITY AND STREAMLINE TOPOLOGY

Figures E10 and E11 show patterns of instantaneous velocity and streamlines of the reconstructed flow field using 5 and 10 eigenmodes in comparison with the time-averaged flow field based on the original PIV data. Interestingly, the streamline patterns of the reconstructed flow field using 5 and 10 eigenmodes in Figure E11 are quite similar to the averaged flow field. Inward spiral patterns are observable on the inboard (left) side of the tail, and the large-scale patterns of the well-organized swirling motion can be clearly found on the outboard (right) side of the tail.

4.5 TIME-DEPENDENT COEFFICIENTS

Figure E12 shows selected time-dependent coefficients $a_k(t)$ which are computed according to equation (9) in the section 3. The first seven most energetic modes are presented.

The first temporal expansion coefficient $a_1(t)$ is randomly distributed throughout the sampling time of the PIV data. The second coefficient $a_2(t)$ and the third coefficient $a_3(t)$ display higher frequency features. Moreover, their amplitudes are smaller; they represent the small-scale structures of the second and third eigenfunctions, respectively. For the higher mode coefficients, a similar trend, at even higher frequency and smaller amplitude, can be clearly observed in the plot.

4.6 RELATIONS OF NORMALIZED EIGENVALUES AND CUMULATIVE FLOW ENERGY TO EIGENMODE NUMBER

Table 1 in the following shows normalized eigenvalues and cumulative flow fluctuation energy according to the eigenmode number. The first two eigenmodes contribute 22.79% of the total flow fluctuation energy, whereas the first six eigenmodes reproduce up to 40.30% of the total energy. The cumulative flow energy level can reach 50.25% of the total with 10 eigenmodes. In addition, with 40 eigenmodes, the reconstructed flow field, which contains 79.56% of flow energy, can predict the major features of the original PIV flow field.

Figure E13a displays the distribution of normalized eigenvalues with respect to the 137 eigenmodes. It can be observed that the eigenvalues decrease very rapidly for the first 10 eigenmodes. However, the eigenvalues decrease gradually and converge to zero value beyond the first 40 eigenmodes.

Figure E13b exhibits the cumulative flow energy according to the 137 eigenmodes. About 84% of flow energy can be captured by employing the first 50 eigenmodes.

Eigenmode Number	Normalized Eigenvalue	Cumulative Flow Energy (%)
1	0.1382	13.82
2	0.0897	22.79
3	0.0644	29.23
4	0.0434	33.57
5	0.0366	37.23
6	0.0307	40.30
7	0.0294	43.24
8	0.0260	45.84
9	0.0231	48.15
10	0.0210	50.25
20	0.0112	64.83
40	0.0052	79.56

Table E1. POD analysis of flow patterns in a crossflow plane: Normalized eigenvalues and cumulative flow energy contribution vs. eigenmode number.

5. CONCLUDING REMARKS

Flow structures associated with vortex-tail interaction, viewed on a crossflow plane, have been analyzed via Proper Orthogonal Decomposition (POD). The POD method is applied to the instantaneous sequential data from PIV experiments to extract the most energetic phenomena of the flow.

Comparisons of patterns of instantaneous velocity and vorticity between the original instantaneous PIV data and the reconstructed flow fields using 5 and 10 empirical eigenfunctions show that the reconstructed flow field can extract the largest-scale features of the flow, while the smaller scales of the flow field are not reproduced in the reconstructed flow field. This is rather expected by noticing (see Figure E13b) that, based on the analysis, the reconstructed flow fields from 5 and 10 eigenmodes contribute respectively about 37% and 50% of the total flow energy.

Furthermore, even the smaller-scale flow features can be predicted with higher eigenmodes by employing 20 and 40 eigenfunctions. However, the reconstructed flow field does not predict all of the flow features of the original PIV data. About 80% of flow energy, in fact, can be accounted for by employing the first 40 eigenmodes. In addition, the amplitudes of the higher-mode, time-dependent coefficients are smaller, which reflect the smaller-scale flow features.

An overall comparison between the streamline patterns of the reconstructed flow field using different eigenmodes and the corresponding original PIV data is also presented. It is quite interesting to observe that the streamline patterns obtained from 10 eigenmodes are of somewhat identical form to the patterns from 5 eigenmodes: extended inward spiral patterns form along the inboard (left) side of the tail, whereas the large-scale features of swirling motion occur on the outboard (right) side of the tail. In the image of the reconstructed field from 20 eigenmodes, the streamline topology on the inboard (left) side of the tail shows similarity to the patterns corresponding to 5 and 10 eigenmodes. However, on the outboard (right) side of the tail, the complex, small-scale features, obvious in the instantaneous original PIV image, can be observed. Moreover, the streamline patterns from 40 eigenmodes can yield more detailed, smaller-scale flow features of the original PIV flow field: extended inward spirals begin to appear along the inboard (left) side of the tail; and more complicated streamline topology becomes apparent on the outboard (right) side of the tail.

In summary, the reconstructed flow structures via POD analysis using the first few eigenmodes can extract successfully the dominant spatial features and the most energetic flow structures of the original PIV data, while more complicated spatial flow features and short-time phenomena can be reproduced by the higher eigenmodes.

ACKNOWLEDGMENTS

The authors gratefully acknowledge support of this research under the U.S. Air Force Office of Scientific Research grants F49620-00-1-0009 and F49620-02-1-0061, monitored by Drs. Steven Walker and John Schmisseur. In addition, supplemental funding for instrumentation was provided by the U.S. Office of Naval Research grants N00014-99-1-0581 and N0014-01-1-0606.

REFERENCES

Adrian, R.J., 1991, "Particle – Imaging Techniques for Experimental Fluid Mechanics", *Annual Review of Fluid Mechanics*, Vol. 23, pp. 261-304.

Arndt, R.E., Long, D.F., and Glauser, M.N. 1997, "The Proper Orthogonal Decomposition of Pressure Fluctuations Surrounding a Turbulent Jet", *Journal of Fluid Mechanics*, Vol. 340, pp. 1-33.

Aubry, N., Holmes, P., Lumley, J.L., and Stone, E. 1988, "The Dynamics of Coherent Structures in the Wall Region of a Turbulent Boundary Layer", *Journal of Fluid Mechanics*, Vol. 192, pp. 115-173.

Berkooz, G., Holmes, P., and Lumley, J.L. 1993, "The Proper Orthogonal Decomposition in the Analysis of Turbulent Flows", *Annual Review of Fluid Mechanics*, Vol. 25, pp. 539-575.

Bonnet, J.P., Cole, D.R., Delville, J., Glauser, M.N., and Ukeiley, L.S. 1994, "Stochastic Estimation and Proper Orthogonal Decomposition: Complementary Techniques for Identifying Structure", *Experiments in Fluids*, Vol. 17, pp. 307-314.

Brown, D., Lee, B.H.K., and Tang, F. C. 1990, "Some Characteristics and Effects of the F/A -18 Lex Vortices", Vortex Flow Aerodynamics, AGARD CP 494, pp. 30-1-30-20.

Brown, G. L. and Lopez, J.M. 1990, "Axisymmetric Vortex Breakdown. Part 2. Physical Mechanisms", *Journal of Fluid Mechanics*, Vol. 221, pp. 553-576.

Cipolla, K. M., Liakopoulos, A. and Rockwell, D. 1998, "Quantitative Imaging in Proper Orthogonal Decomposition of Flow Past a Delta Wing", *AIAA Journal*, Vol. 36, pp. 1247-1255.

Citriniti, J.H. and George, W.K. 2000, "Reconstruction of the Global Velocity Field in the Axisymmetric Mixing Layer Utilizing the Proper Orthogonal Decomposition", *Journal of Fluid Mechanics*, Vol. 418, pp. 137-166.

Deane, A.E., Kevrekidis, I.G., Karniadakis, G.E., and Orszag, S.A. 1991, "Low Dimensional Models for Complex Geometry Flows: Application to Grooved Channels and Circular Cylinders", *Physics of Fluids A*, Vol. 3, No. 10, pp. 2337-2354.

Delery, J. M. 1994, "Aspects of Vortex Breakdown", *Progress in Aerospace Sciences*, Vol. 30, pp. 1-59.

Delville, J., Ukeiley, L., Cordier, L., Bonnet, J.P., and Glauser, M. 1999, "Examination of Large-Scale Structures in a Turbulent Plane Mixing Layer. Part 1. Proper Orthogonal Decomposition", *Journal of Fluid Mechanics*, Vol. 391, pp. 91-122.

Escudier, M. 1988, "Vortex Breakdown: Observations and Explanations", *Progress in Aerospace Sciences*, Vol. 25, pp. 189-229.

Garg, A. K. and Leibovich, S. 1979, "Spectral Characteristics of Vortex Breakdown Flowfields", *Physics of Fluids*, Vol. 22, No.11, November, pp. 2053-2064.

Glezer, A., Kadioglu, Z., and Pearlstein, A.J. 1989, "Development of an Extended Proper Orthogonal Decomposition and its Application to a Time Periodically Forced Plane Mixing Layer", *Physics of Fluids A*, Vol. 1, No. 8, August, pp. 1363-1373.

Gordeyev, S.V. and Thomas, F.O. 2000, "Coherent Structure in the Turbulent Planar Jet. Part 1. Extraction of Proper Orthogonal Decomposition Eigenmodes and their Self-Similarity", *Journal of Fluid Mechanics*, Vol. 414, pp. 145-194.

Gordnier, R.E. and Visbal, M.R. 1997, "Numerical Simulation of the Impingement of a Streamwise Vortex on a Plate", AIAA Paper No. 97-1781,28th AIAA Fluid Dynamics Conference, June 29- July 2, Snowmass Village, CO.

Gottlieb, D. and Orszag, S.A. 1977, *Numerical Analysis of Spectral Methods*, Society for Industrial and Applied Mathematics, Philadelphia.

Gursul, I. 1994, "Unsteady Flow Phenomena over Delta Wings at High Angle-of- Attack", *AIAA Journal*, Vol. 32, No. 2, February, pp. 225-231.

Gursul, I. and Xie, W. 1998, "Physics of Buffeting Flows Over Delta Wings", AIAA Paper No. 98- 0688, 36th Aerospace Sciences Meeting and Exhibit, January 15-18, Reno, NV.

Gursul, I. and Yang, H. 1995, "On Fluctuations of Vortex Breakdown Location", *Physics of Fluids*, Vol. 7, No.1, January, pp. 229-231.

Kandil, O.A., Sheta, E.F., and Massey, S.J. 1995, "Buffet Responses of a Vertical Tail in Vortex Breakdown Flows", AIAA Paper No. 95-3464.

Kandil, O.A. and Sheta, E.F. 1998, "Coupled and Uncoupled Bending-Torsion Responses of Twin-Tail Buffet", *Journal of Fluids and Structures*, Vol. 12, pp. 677-701.

Kim, Y. 1996, "Construction of Low-Dimensional Models of Thermo-Fluid Systems: A Fully Spectral Technique", M.S. thesis, Lehigh University, Bethlehem, Pa., U.S.A.

Komerath, N.M., Liou, S. G., Schwartz, R.J., and Kim, J.M. 1992a, "Flow over a Twin-Tailed Aircraft at Angle of Attack, Part I: Spatial Characteristics", *Journal of Aircraft*, Vol. 29, No. 3, pp. 413-420.

Komerath, N.M., Liou, S. G., Schwartz, R.J., and Kim, J.M. 1992b, "Flow over a Twin-Tailed Aircraft at Angle of Attack, Part II: Temporal Characteristics", *Journal of Aircraft*, Vol. 29, No. 4, pp. 553-558.

Lee,J.W., Cavone, A.A., and Suzuki,K.E. 1993, "Doppler Global Velocimetry Measurements of the Vortical Flow Above an F/A-18", AIAA Paper No. 93-0414, 31st Aerospace Sciences Meeting & Exhibit, January 11-14, Reno, NV.

Lee,B.H.K. 2000, "Vertical Tail Buffeting of Fighter Aircraft", *Progress in Aerospace Sciences*, Vol. 36, pp. 193-279.

Liakopoulos, A. and Hsu, C. C. 1984, "On a Class of Compressible Laminar Boundary-Layer Flows and the Solution Behavior Near Separation", *Journal of Fluid Mechanics*, Vol. 149, pp. 339-353.

Liakopoulos, A., Blythe, P. A., and Gunes, H. 1997, "A Reduced Dynamical Model of Convective Flows in Tall Laterally Heated Cavities", *Proceedings of the Royal Society of London*, Vol. A 453, pp. 663-672.

Lumley, J. L. 1967, in Atmospheric Turbulence and Radio Wave Propagation, (ed. Yaglom, A. M. and Tatarski, V. I.), Navko, Moscow, pp. 160-178.

Menke, M., Yang, H., and Gursul, I. 1996, "Further Experiments on Fluctuations of Vortex Breakdown Location", AIAA Paper No.96-0205, 34th Aerospace Sciences Meeting and Exhibit, January 15-18, Reno, NV.

Rempfer, D. and Fasel, H.F. 1994, "Evolution of Three-Dimensional Coherent Structures in a Flat-Plate Boundary Layer", *Journal of Fluid Mechanics*, Vol. 260, pp. 351-375.

Rockwell, D., Magness, C., Towfighi, J., Akin, O., and Corcoran, T. 1993, "High Image-Density Particle Image Velocimetry Using Laser Scanning Techniques", *Experiments in Fluids*, Vol. 14, pp. 181-192.

Rockwell, D. 1998, "Vortex-Body Interactions", *Annual Review of Fluid Mechanics*, Vol. 30, pp. 199-229.

Rockwell, D. 2000, "Imaging of Unsteady Separated Flows: Global Interpretation with Particle Image Velocimetry", *Experiments in Fluids* [Suppl.], pp. S255-S273.

Sahan, R. A., Liakopoulos, A., and Gunes, H. 1997, "Reduced Dynamical Models of Nonisothermal Transitional Grooved-Channel Flow", *Physics of Fluids*, Vol. 9, No. 3, March, pp. 551-565.

Sarpkaya, T. 1971a, "On Stationary and Traveling Vortex Breakdowns", *Journal of Fluid Mechanics*, Vol. 45, No. 3, pp. 545-559.

Sarpkaya, T. 1971b, "Vortex Breakdown in Swirling Conical Flows", *AIAA Journal*, Vol. 9, No.9, pp. 1792-1799.

Sarpkaya, T. 1974, "Effect of the Average Pressure Gradient on Vortex Breakdown", *AIAA Journal,* Vol. 12, No.5, pp. 602-607.

Sirovich, L. 1987, "Turbulence and Dynamics of Coherent Structures: I-III", *Quarterly of Applied Mathematics*, Vol. XLV, No. 3, pp. 561-590.

Triplett, W.E. 1983, "Pressure Measurements on Twin Vertical Tails in Buffeting Flow", *Journal of Aircraft*, Vol. 20, No. 11, pp. 920-925.

Westerweel, J., 1997, "Fundamentals of Digital Particle Image Velocimetry", *Measurement Science Technology*, Vol. 8, pp. 1379-1392.

LIST OF FIGURES

Figure E1: Schematic of plan and side views of delta wing-tail arrangement.

Figure E2: Schematic of rigid tail.

Figure E3: Schematic of delta wing.

Figure E4: Selected eigenfunctions for the fluctuating component of velocity and vorticity contours. (a) ϕ_1, (b) ϕ_2, and (c) ϕ_5.

Figure E5: Selected eigenfunctions for the fluctuating component of velocity and vorticity contours. (a) ϕ_{10}, (b) ϕ_{20}, and (c) ϕ_{40}.

Figure E6: Selected eigenfunctions for the fluctuating component of velocity; ϕ_3, ϕ_4, ϕ_6, and ϕ_7.

Figure E7: Reconstructed velocity fields and patterns of vorticity using 10, 20, and 40 eigenmodes in association with original PIV data in a crossflow plane. Minimum and incremental vorticity levels are $\omega_{min} = \pm 2s^{-1}$, $\Delta\omega = 1s^{-1}$, respectively.

Figure E8: Reconstructed velocity fields and patterns of vorticity using 40 eigenmodes in association with original PIV data at specific instants (I=1 and I=33) in a crossflow plane. Minimum and incremental vorticity levels are $\omega_{min} = \pm 2s^{-1}$, $\Delta\omega = 1s^{-1}$, respectively.

Figure E9: Comparison of patterns of streamlines using 5, 10, 20, and 40 eigenmodes in association with original PIV data.

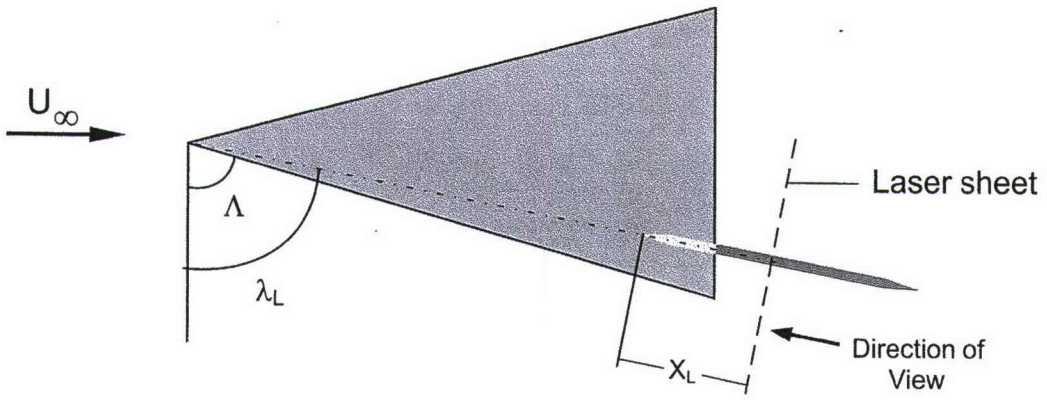
Figure E10: Reconstructed velocity fields and patterns of vorticity using 5 and 10 eigenmodes and corresponding averaged flow field. Minimum and incremental values of parameters are as follows: $\omega_{min} = \pm 2s^{-1}$, $\Delta\omega = 1s^{-1}$; $<\omega>_{min} = \pm 2s^{-1}$, $\Delta<\omega> = 1s^{-1}$.

Figure E11: Reconstructed patterns of vorticity and streamlines using 5 and 10 eigenmodes and corresponding averaged flow field. Minimum and incremental values of parameters are as follows: $\omega_{min} = \pm 2s^{-1}$, $\Delta\omega = 1s^{-1}$; $<\omega>_{min} = \pm 2s^{-1}$, $\Delta<\omega> = 1s^{-1}$.

Figure E12: Expansion coefficients for the seven most energetic modes.

Figure E13: (a) Normalized eigenvalue vs. eigenmode number, (b) Cumulative flow energy distribution (%) vs. eigenmode number.

PLAN VIEW



SIDE VIEW

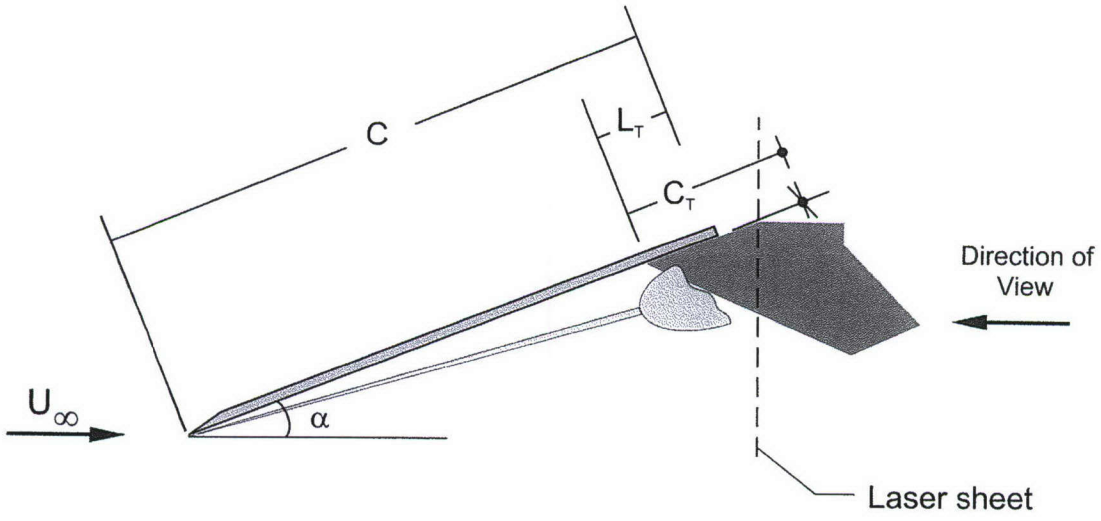


Figure E1: Schematic of plan and side views of delta wing-tail arrangement.

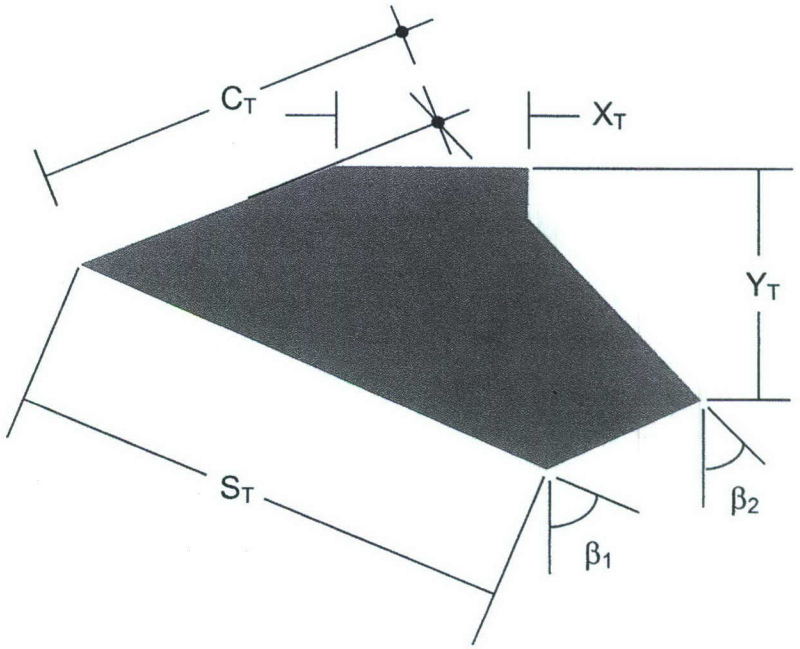


Figure E2: Schematic of rigid tail.

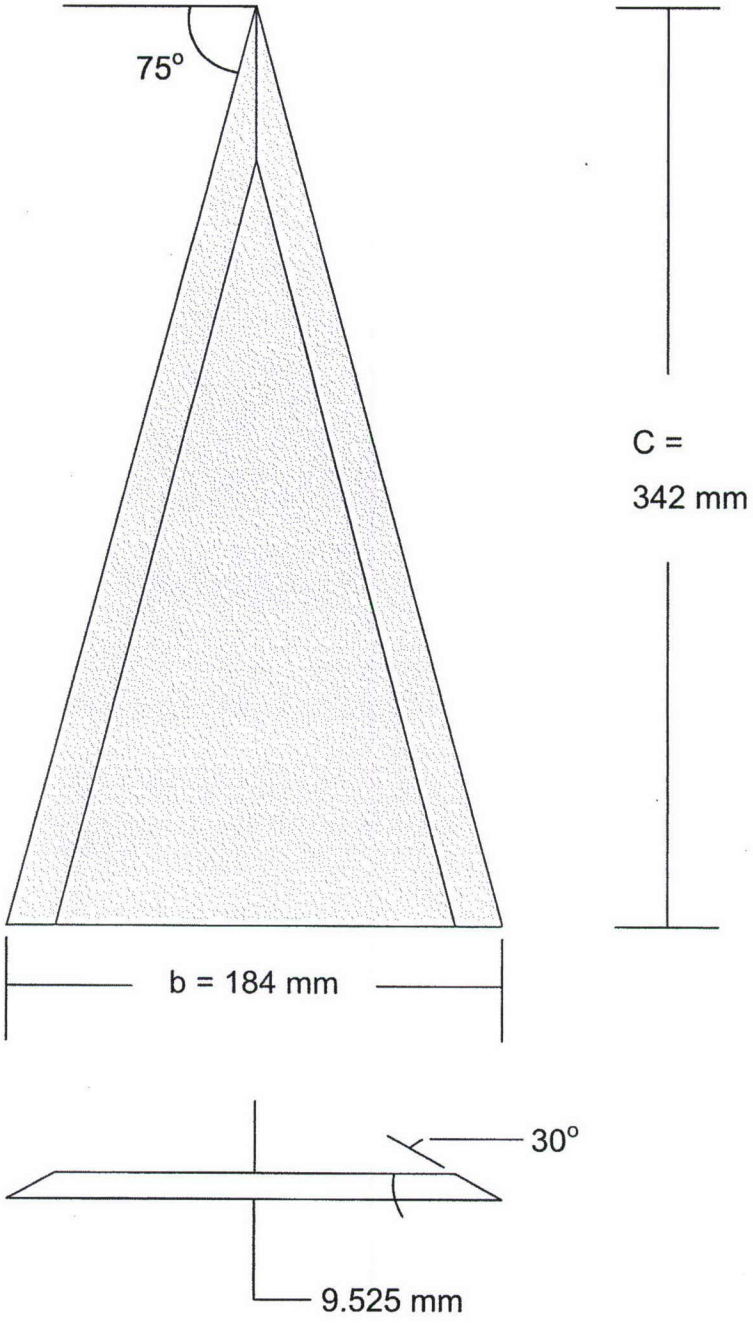


Figure E3: Schematic of delta wing.

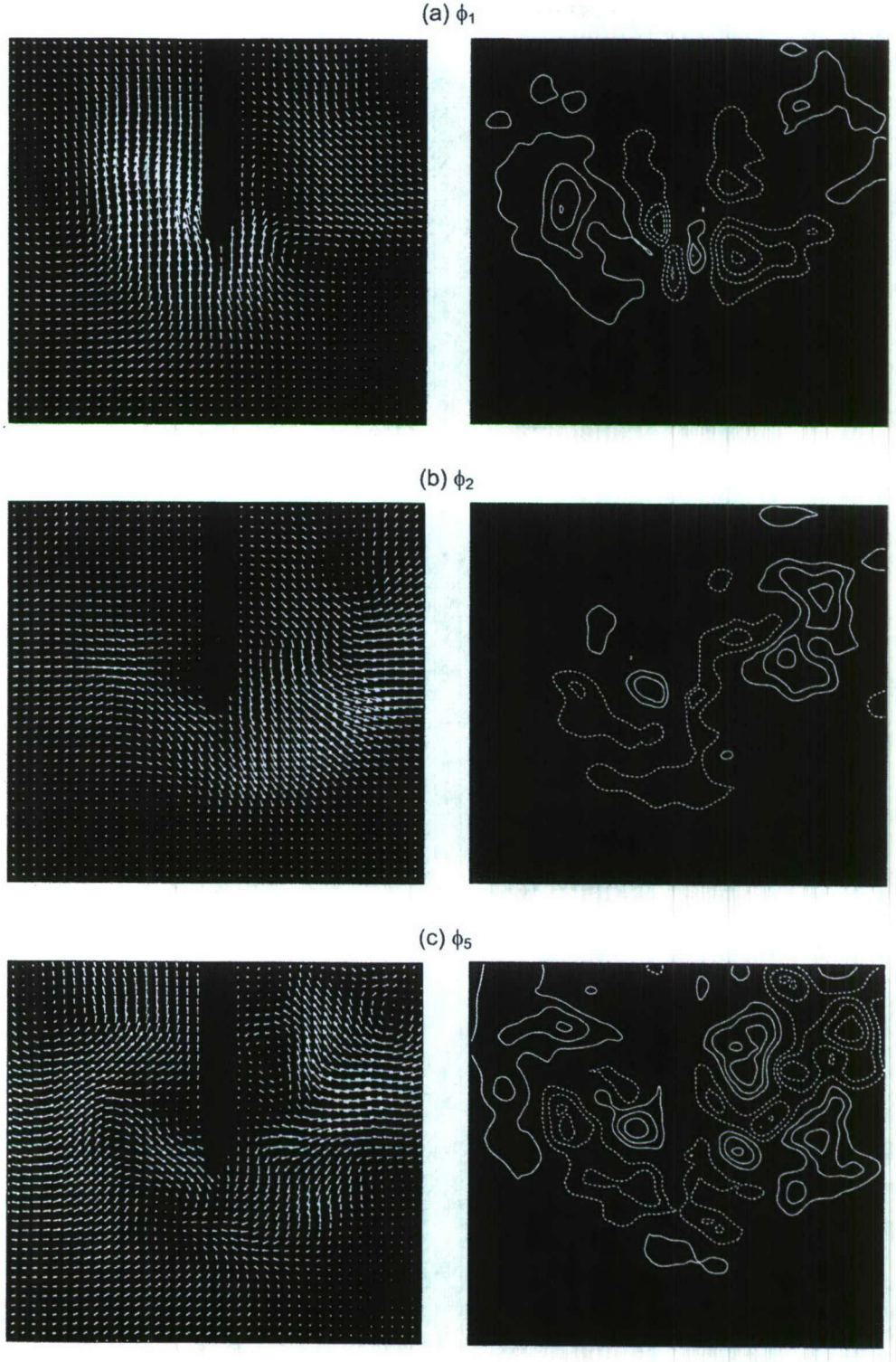
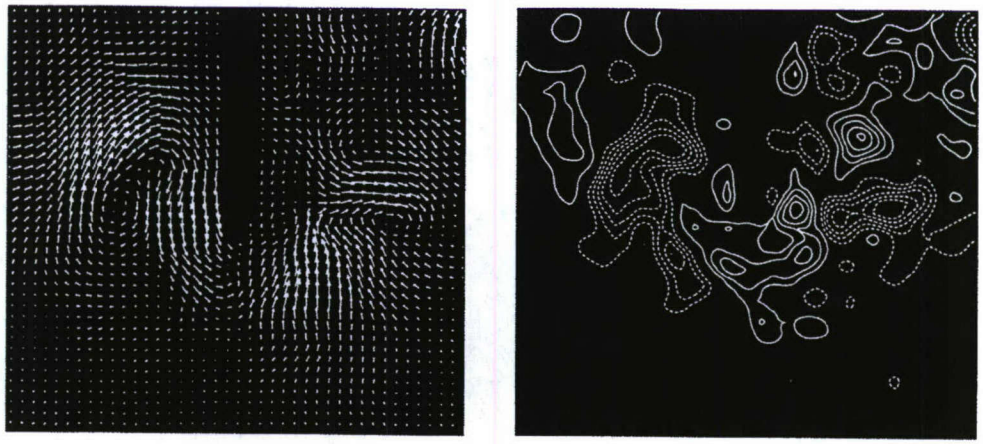
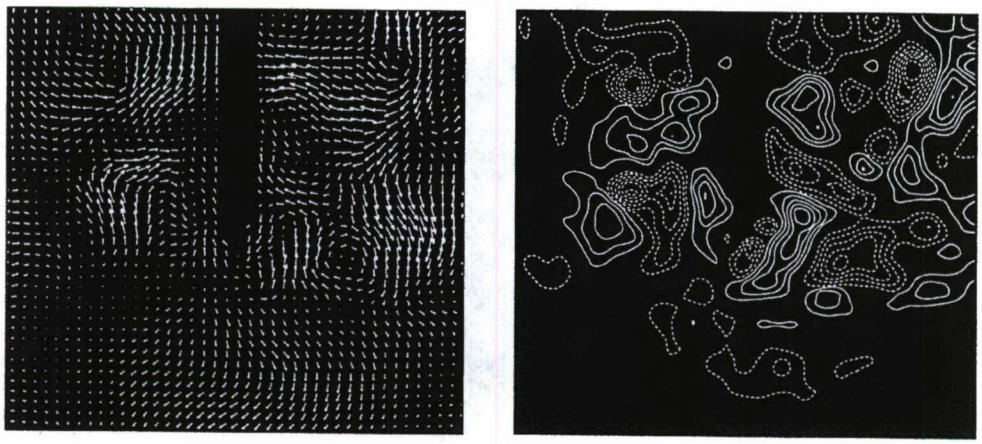


Figure E4: Selected eigenfunctions for the fluctuating component of velocity and vorticity contours. (a) ϕ_1, (b) ϕ_2, and (c) ϕ_5.

(a) ϕ_{10}



(b) ϕ_{20}



(c) ϕ_{40}

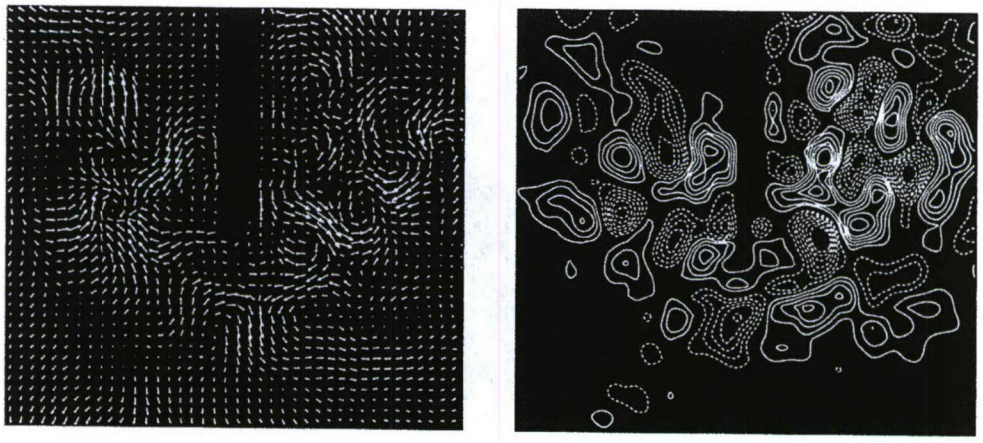


Figure E5: Selected eigenfunctions for the fluctuating component of velocity and vorticity contours. (a) ϕ_{10}, (b) ϕ_{20}, and (c) ϕ_{40}.

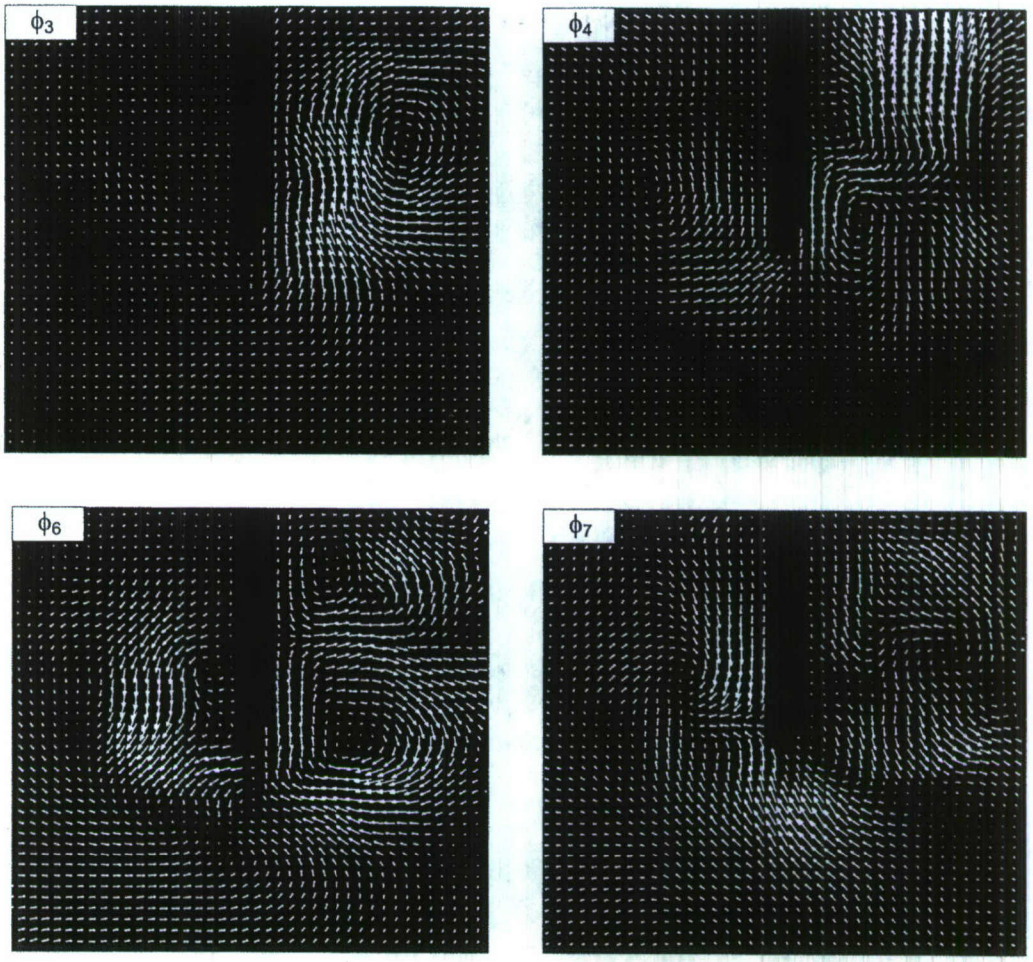


Figure E6: Selected eigenfunctions for the fluctuating component of velocity; ϕ_3, ϕ_4, ϕ_6, and ϕ_7.

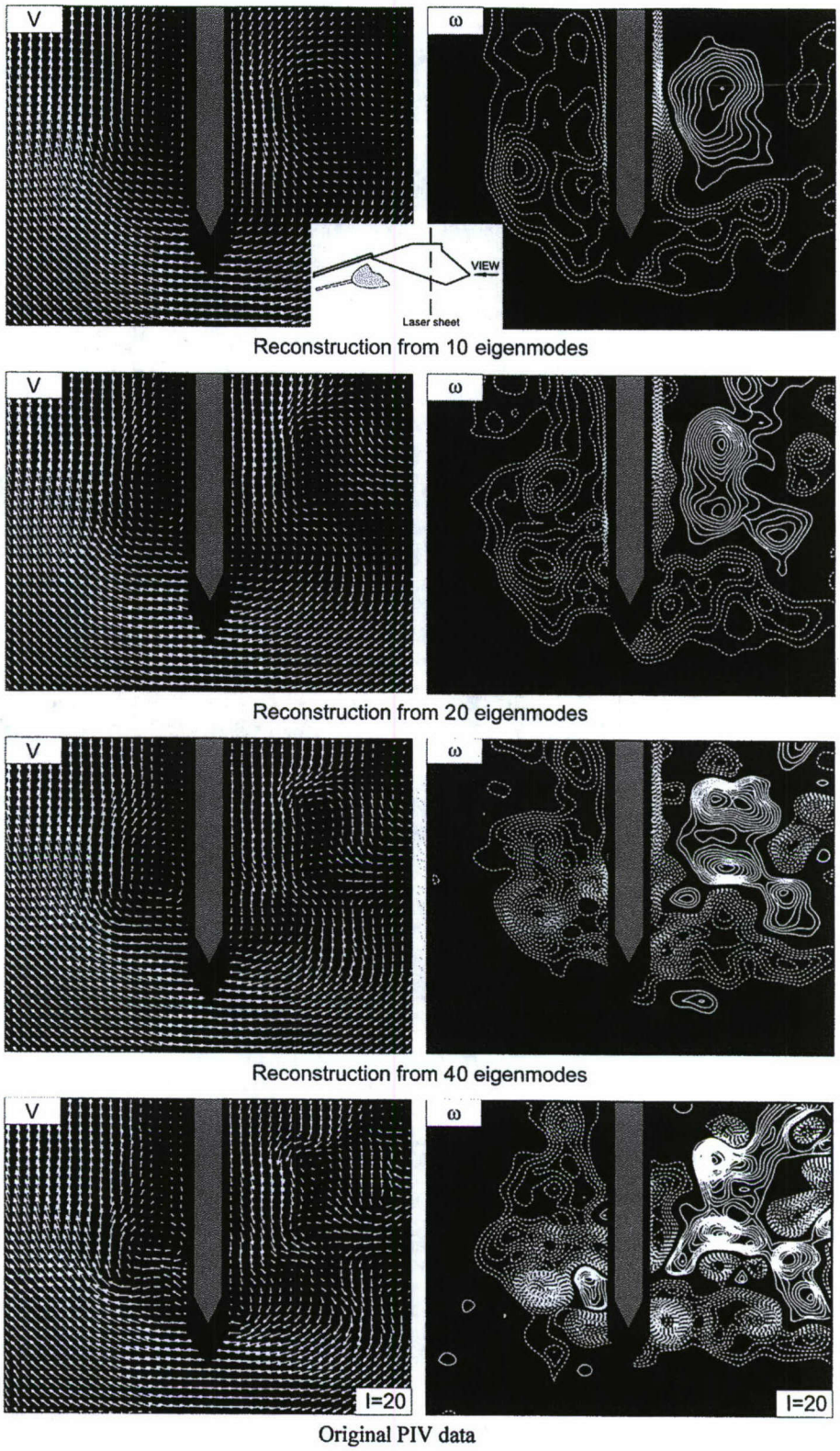


Figure E7: Reconstructed velocity fields and patterns of vorticity using 10, 20, and 40 eigenmodes in association with original PIV data in a crossflow plane. Minimum and incremental vorticity levels are $\omega_{min} = \pm 2s^{-1}$, $\Delta\omega = 1s^{-1}$, respectively.

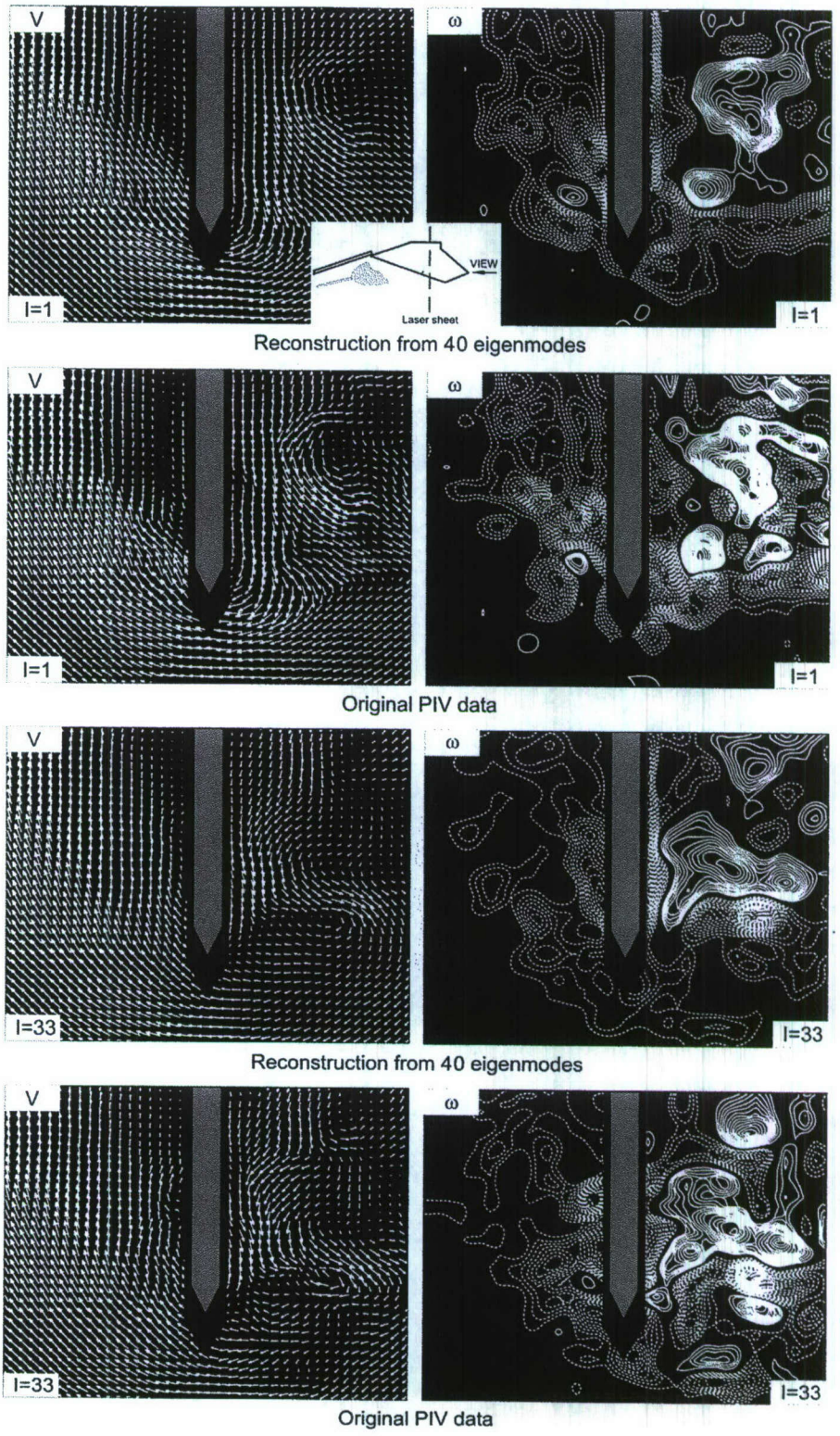


Figure E8: Reconstructed velocity fields and patterns of vorticity using 40 eigenmodes in association with original PIV data at specific instants (I = 1 and I = 33) in a crossflow plane. Minimum and incremental vorticity levels are $\omega_{min} = \pm 2s^{-1}$, $\Delta\omega = 1s^{-1}$, respectively.

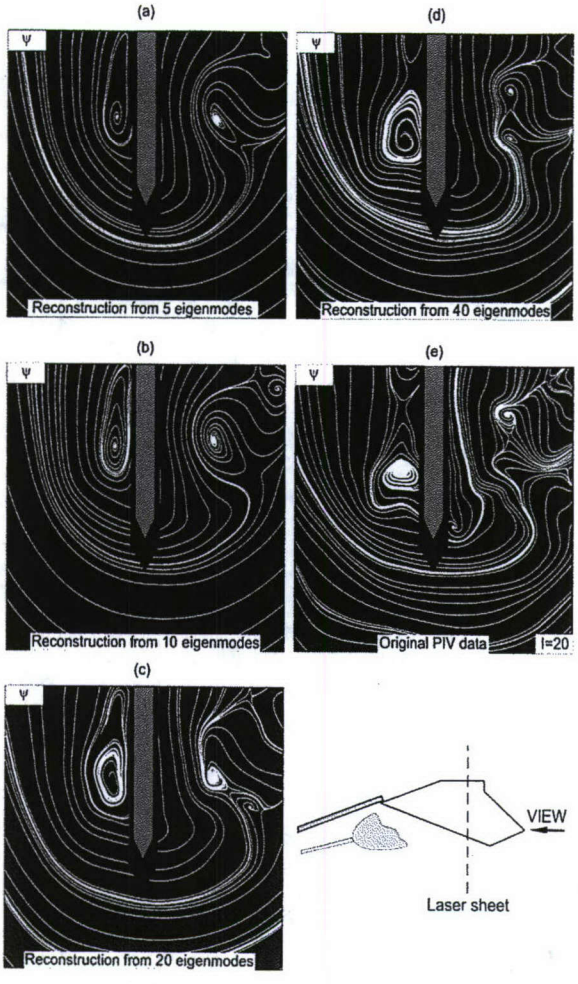


Figure E9: Comparison of patterns of streamlines using 5, 10, 20, and 40 eigenmodes in association with original PIV data.

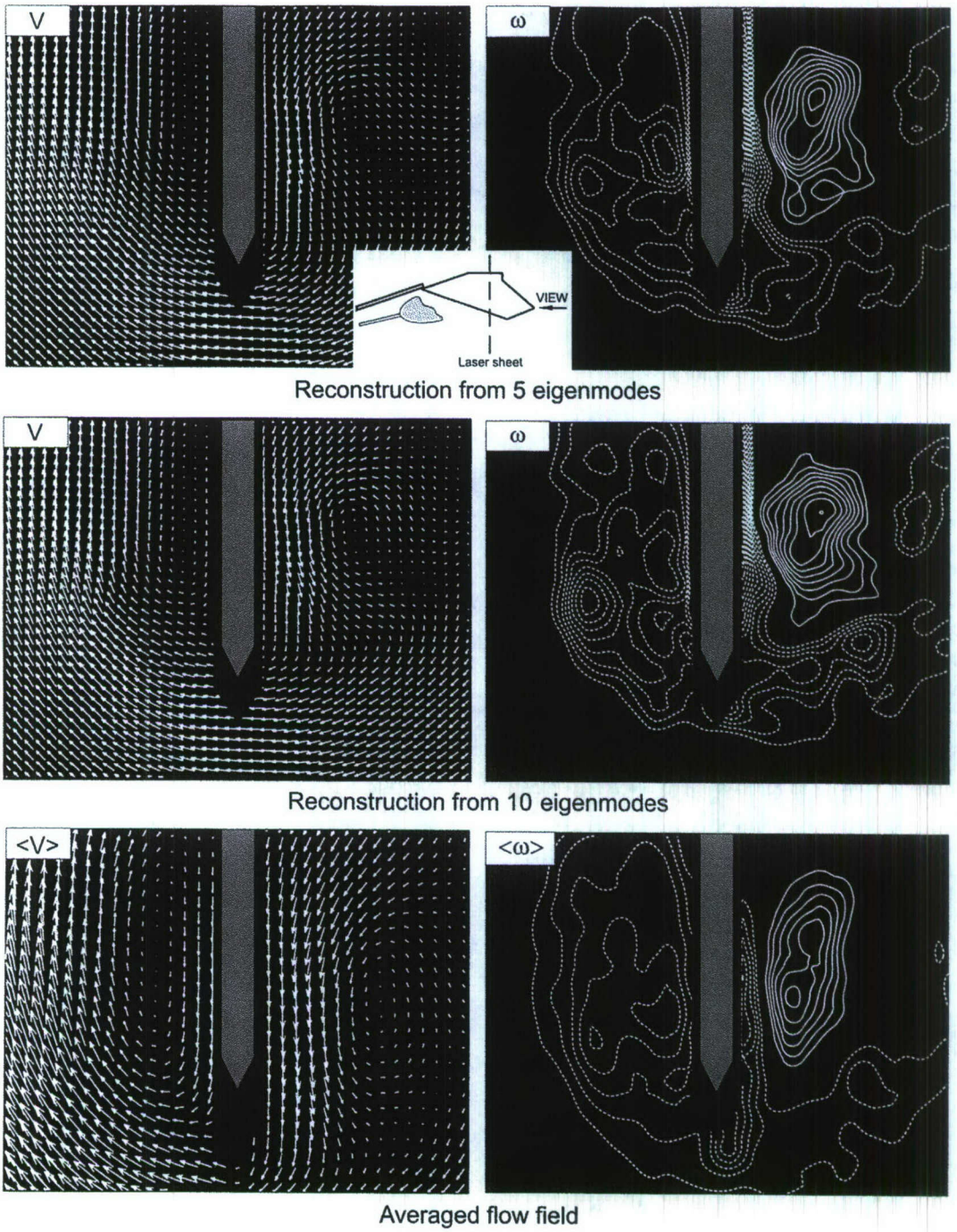


Figure E10: Reconstructed velocity fields and patterns of vorticity using 5 and 10 eigenmodes and corresponding averaged flow field. Minimum and incremental values of parameters are as follows: $\omega_{min} = \pm 2s^{-1}$, $\Delta\omega = 1s^{-1}$; $<\omega>_{min} = \pm 2s^{-1}$, $\Delta<\omega> = 1s^{-1}$.

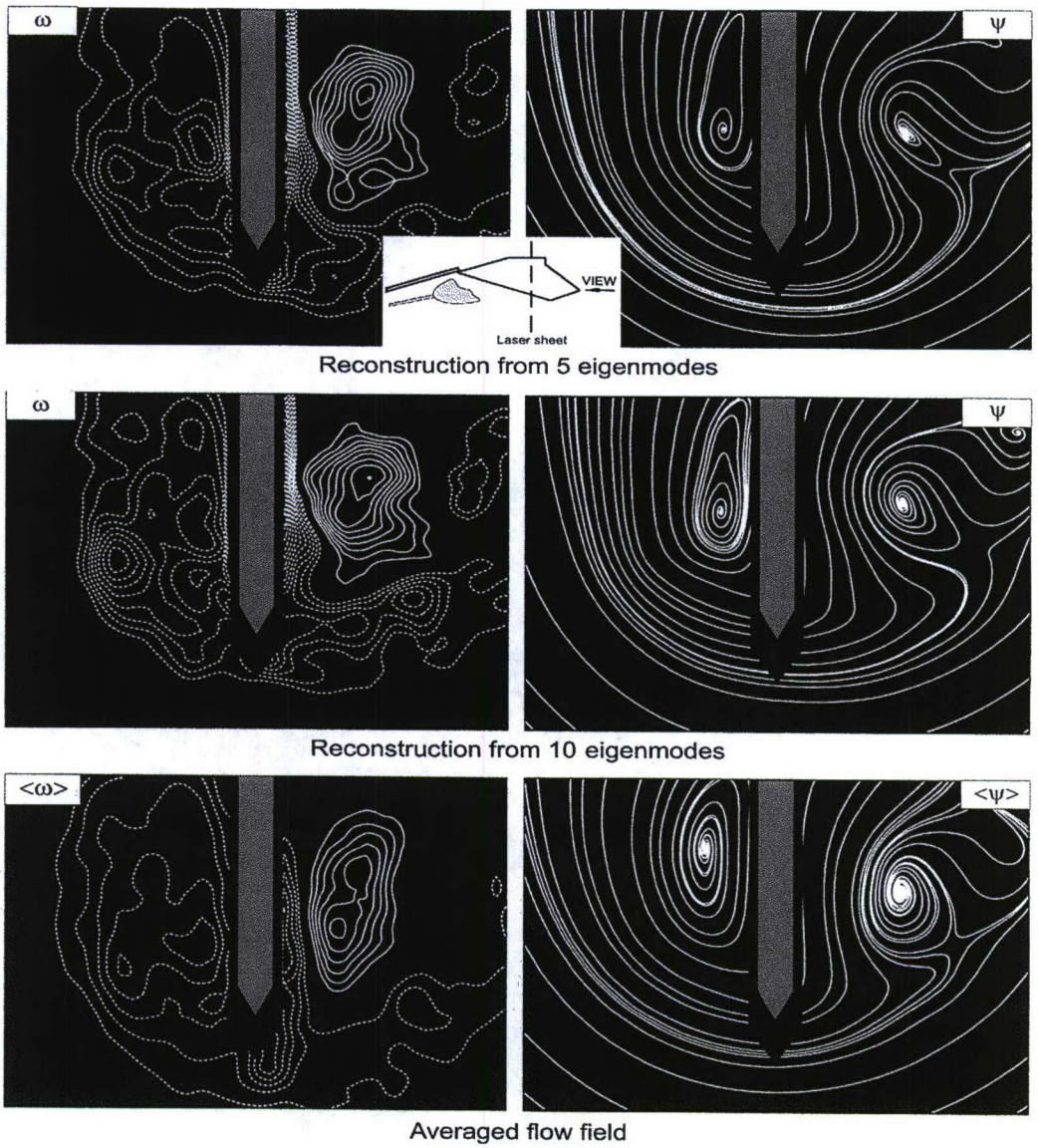


Figure E11: Reconstructed patterns of vorticity and streamlines using 5 and 10 eigenmodes and corresponding averaged flow field. Minimum and incremental values of parameters are as follows: $\omega_{min} = \pm 2s^{-1}$, $\Delta\omega = 1s^{-1}$; $\langle\omega\rangle_{min} = \pm 2s^{-1}$, $\Delta\langle\omega\rangle = 1s^{-1}$.

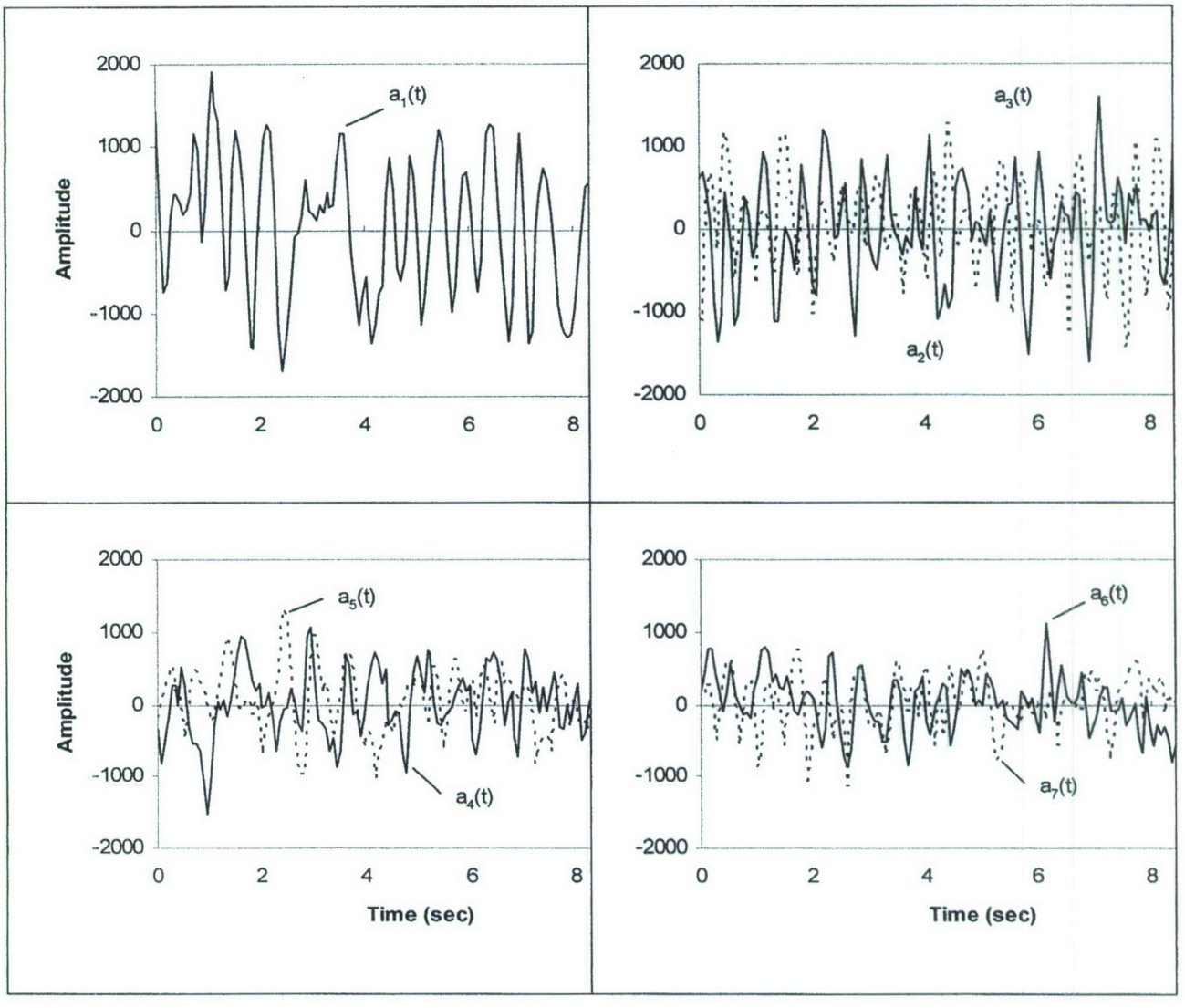


Figure E12. Expansion coefficients for the seven most energetic modes.

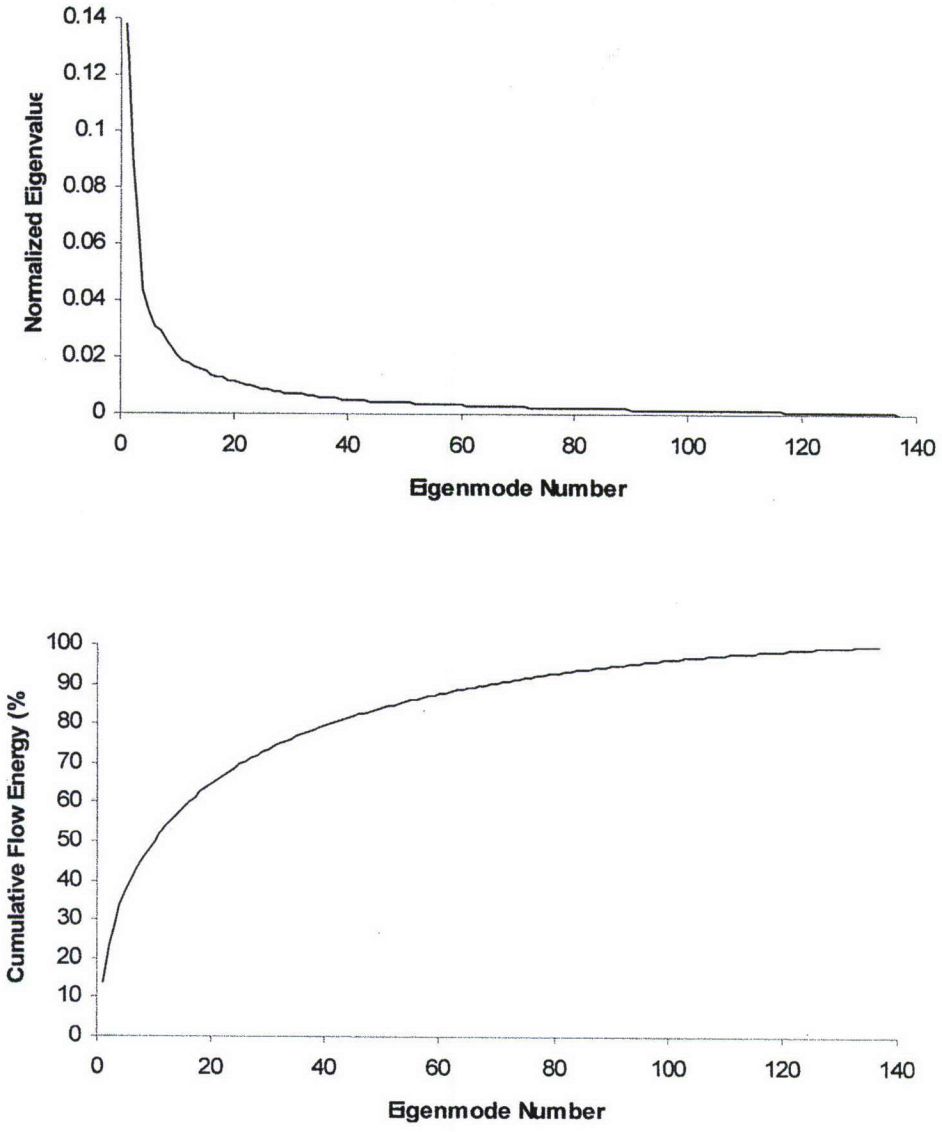


Figure E13: (a) Normalized eigenvalue vs. eigenmode number, (b) cumulative flow energy distribution (%) vs. eigenmode number.